Development of novel probes for high-resolution electron microscopy based on small-sized gold nanoparticle-antibody conjugates

Nadja Groysbeck

UNIVERSITÉ DE STRASBOURG

ÉCOLE DOCTORALE DES SCIENCES CHIMIQUES ED222

UMR7242 Biotechnologie et Signalisation Cellulaire

THÈSE présentée par :

Nadja GROYSBECK

soutenue le : **9 décembre 2020**

pour obtenir le grade de : **Docteur de l'université de Strasbourg**

Discipline/ Spécialité : Chimie biologique

Development of novel probes for high-resolution electron microscopy based on small-sized gold nanoparticle-antibody conjugates

THÈSE dirigée par :

M. ZUBER Guy	Dr., Université de Strasbourg

RAPPORTEURS :

M. LE GUEVEL Xavier	Dr., Université Grenoble Alpes
M. BRAECKMANS Kevin	Prof. Dr., Ghent University

AUTRES MEMBRES DU JURY :

M. KLYMCHENKO Andrey	Dr., Université de Strasbourg
Mme PICHON Chantal	Prof. Dr., Université d'Orléans

Table of contents

Chapter 3: Conjugation to nanobodies and application as electron microscopy probe

Acknowledgement

First of all, I would like to thank Dr. Guy Zuber for having given me the opportunity to perform my PhD studies in his research group under his supervision. I am truly grateful for his patience, creativity and sense of humor that marked his supervision and helped me a lot during the last three years in terms of progressing with my PhD project, as well as maintaining good mood, despite struggles I was facing at several occasions.

I furthermore want to thank Prof. Dr. Étienne Weiss for all the things he explained me about cellular biology during our lab meetings, which was for me as biochemist very helpful, especially in the beginning of my project.

I am grateful for my colleagues Éric Moeglin and Audrey Stoessel, with whom I shared my office and spent many lunch breaks. I really appreciated the good atmosphere in our office, all the discussions we had their support for helping me improving my French.

I would like to thank Dr. Manuela Chiper for introducing me into the lab during my first month of PhD and her help in proof-reading scientific articles. Besides, I would like to thank the rest of my team for their help regarding scientific or technical questions, as well as all other members of our unit for the cheerful atmosphere in the common rooms and during organized events.

I would like to thank Dr. Mariel Donzeau, who I consider very openminded and interested in various directions, for her keenness to build up a collaboration between her and my project, as well as for her generosity of having provided me with various cell lines, plasmids, etc.

Moreover, I am grateful for all my other collaborators, their interest in my project and the effort they made. I want to thank Dr. Danièle Sphener and Dr. Anne-Marie Haeberle for their help in preparing cellular samples for electron microscopy. I would like to thank Dr. Mounib Bahri and Dr. Dris Ihiawakrim for the analysis of various samples by electron microscopy. I want to thank Dr. Jean-Marc Strub for the analysis of gold nanoparticle samples by mass spectrometry. I would like to thank Elisabete Silva and Dr. Maxime Lehmann for their assistance for cellular assays using glioblastoma cells, as well as their help in proof-reading the paper which we published together. Furthermore, I would like to thank Prof. Dr. Patrick Schultz and Dr. Ovidiu Ersen for their interest in continuing our common project.

I also want to thank Dr. Andrey Klymchenko and Dr. Gaëtan Mislin for their helpful role in evaluating my mid-thesis.

I truly want to thank my boyfriend Benjamin Eckert who supported me during challenging times and had a lot of patience and understanding for the time I invested in my PhD studies. Moreover, I want to thank him for all the efforts he made to help me changing my mind when experiments in the laboratory did not work as I wished and I was in an accordingly bad mood.

I also want to thank my old friends from Vienna, Lina Cardozo, Nassim Amiri, Lilly Leitner and Florian Stampfer for keeping contact so closely during my stay in Strasbourg, which always gave me a feeling of being home when we talked on the phone. Furthermore, I am grateful for the people I met here in France, Julián Del Fiore, Melanie Castagno, Sebastián Sampayo, Antonella Zerpa and Jelica Vasiljevic who became good friends and with whom I spent a lot of great moments.

Finally, I would like to give my heartfelt thanks to my mother and my father who always showed a great interest in what I was doing during my PhD studies, as well as my stay in Strasbourg in general. Despite the difficult situation of the last years, they always had an open ear for the problems and achievements I was facing during my research, which gave me strength.

List of abbreviations

APEX	Modified soybean ascorbate peroxidase
AuG	Thionitrobenzoate-, thioaminobenzoate-protected gold nanoparticle of 2.4 nm
AuL	Thionitrobenzoate-, thioaminobenzoate-protected gold nanoparticle of 2.6 nm
AuNC	Gold nanocluster
AuNP	Gold nanoparticle
AuZ	Thionitrobenzoate-, thioaminobenzoate-protected gold nanoparticle of 1.4 nm
Bmab	Bevacizumab
BSA	Bovine serum albumin
BSA-c	Acetylated bovine serum albumin
CDR	Complementarity determining regions
CLEM	Correlative light and electron microscopy
Cmab	Cetuximab
Cryo-EM	Cryogenic electron microscopy
Cys	Cysteine
DAB	3,3’-Diaminobenzidine
DTNB	2,2′-Dinitro-5,5′-dithiobenzoic acid
EDC	N-(3-Dimethylaminopropyl)-N’-ethylcarbodiimide
EDX	Energy-dispersive X-ray
EGFR	Epidermal growth factor receptor
ELISA	Enzyme-linked immunosorbent assay

EM	Electron microscopy
EPR	Enhanced permeabilization and retention
ESI-MS	Electrospray ionization mass spectrometry
Fab	Fragment antigen binding
Fc	Fragment crystallizable
FBS	Fetal bovine serum
FIB	Focused ion beam
FLIPPER	Fluorescent Indicator and Peroxidase for Precipitation with EM Resolution
FT-IR	Fourrier-transform infrared
GFP	Green fluorescent protein
GSH	Glutathione
HAADF-STEM	High-angle annular dark-field scanning transmission electron microscopy
HRP	Horseradish peroxidase
HSAB	Hard and soft acids and bases
IF	Immunofluorescence
IMAC	Immobilized metal affinity chromatography
LSPR	Localized surface plasmon resonance
MALDI-TOF	Matrix-assisted laser-desorption-ionization time of flight
MBA	Mercaptobenzoic acid
MDP	Multidomain peptide
MUA	Mercaptoundecanoic acid
MW	Molecular weight
MWCO	Molecular weight cut-off

NAR	Nurse shark antigen receptor
NBS	Nucleotide binding site
NES	Nuclear export signal
NHS	N-Hydroxysuccinimide
NIR	Near infrared
NLS	Nuclear localization signal
NMR	Nuclear magnetic resonance
PALM	Photoactivated localization microscopy
PAR	Payload-to-antibody ratio
PBS	Phosphate buffered saline
PCNA	Proliferating cell nuclear antigen
PEG	Polyethylene glycol
PFA	Paraformaldehyde
PPTT	Plasmonic photothermal therapy
RNAP II	RNA polymerase II
RT	Room temperature
scFv	Single chain variable fragment
SDS-PAGE	Sodium dodecyl sulfate polyacrylamide gel electrophoresis
SEM	Scanning electron microscopy
SPIA	Sol particle immunoassay
STEM	Scanning transmission electron microscopy
STORM	Stochastic optical reconstruction microscopy
TAB	Thioaminobenzoate
TCEP	Tris(2-carboxyethyl)phosphine-HCl
TEM	Transmission electron microscopy

TEOS	Tetraethyl orthosilicate
TNB	Thionitrobenzoate
TOAB	Tetraoctylammonium bromide
TPPMS	Triphenylphosphine monosulfonate
UV-Vis	Ultraviolet-visible
VEGF	Vascular endothelial growth factor
VIP	Versatile interacting peptide

List of figures

Introduction on gold nanoparticles and their use for biomedical applications

This introductory section provides an overview over the physicochemical, electronic and optical properties of gold nanoparticles and their use for different biomedical applications. A comprehensive review on existing electron microscopy probes based on gold nanoparticles finally leads to the objective of this PhD project and an explanation on how this thesis is structured (three schematic chapters).

1 Gold nanoparticles

Over the last decades gold nanoparticles (AuNPs) have attracted considerable interest in the scientific community, due to their unique optical and electronic properties.[1,2] AuNPs can be prepared in different sizes (typically ranging from one to several hundred nm in diameter) and can display various shapes, such as spherical, cylindrical, pyramidal, triangular, octahedral and tetrahedral particles (examples of AuNP shapes in Figure 1(a)). Most spherical AuNPs consist of an Au(0) core, which is surrounded by Au(I) ions, to which organic species are coordinated. The resulting shell of organic molecules bound to the surface of the AuNP represents the particle's surface coating. Since gold is a high atomic number material (Z = 79), AuNPs have a high electron density and therefore provide opacity to electrons. The physical and chemical properties of AuNPs strongly differ from that of the bulk material and are determined by the AuNP's size, shape and surface coating.[1] Metallic gold does not seem to interfere with biological metabolic pathways and is thus considered as non-toxic[1] and safe to the human body.[2] However, various organic species such as surfactants can associate or absorb onto the AuNPs,[3–5] conferring bioactivity and occasionally even toxicity to these AuNPs. Besides, certain AuNP sizes have been associated with cytotoxicity, such as the ultrasmall triphenylphosphine monosulfonate (TPPMS)-protected Au_{55} cluster, whose irreversible binding to the major groove of DNA has been shown by molecular modeling and *in vitro* studies.[6,7] Interestingly, significantly lower cytotoxic effects were observed for slightly larger, as well as smaller TPPMS-protected AuNPs,[7] suggesting that apart from the AuNPs' biochemical composition, physical considerations play a role in the safety profile of AuNPs. Moreover, it is noteworthy that the AuNP concentration is critical as well, as it has been shown

that massive uptake of AuNPs can lead to significant changes in cell morphology and reduced cell viability.[8]

1.1 Optical Properties

Spherical AuNPs with sizes from 1 – 100 nm change their color from brown to orange over red to purple with increasing particle diameter when dissolved in water. This size-dependent coloration of aqueous AuNP solutions results from a phenomenon called localized surface plasmon resonance (LSPR).[9] Metallic nanoparticles that are smaller than the wavelength of light absorb incident photons, which excite the nanoparticle's conduction band electrons and cause a collective oscillation being resonant with the wavelength of the absorbed light. The LSPR and was theoretically described by Gustav Mie[10] following the experimental approaches of Michael Faraday aimed at explaining how metal particles affect the color of church windows.[11] The LSPR and therefore the color of AuNPs depend on the particle's size, shape and surface ligands, as well as on the distance between the AuNPs.[12] For illustration, Figure 1(b) shows the color and UV-Vis spectra of differently sized spherical AuNPs in aqueous solutions. As seen, the absorption band's maxima shift from about 520 to 560 nm when diameters of AuNPs are increased from 12 nm to 86 nm (sample I: 12 nm, II: 29 nm, III: 45 nm, IV: 63 nm and V: 86 nm). It is noteworthy that only AuNPs of diameters larger than 2 nm produce LSPR (plasmonic AuNPs)[13,14] and consequently the UV-Vis spectra of particles < 2 nm do not display a peak at 500 – 750 nm.

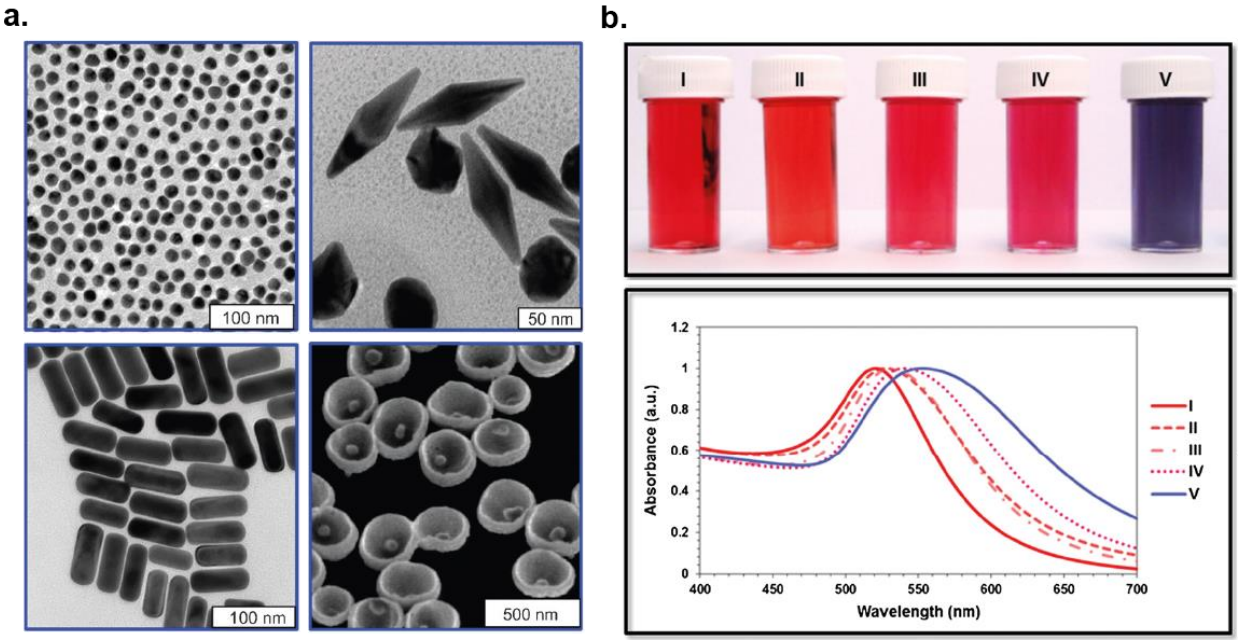

Figure 1. (a) Different shapes of AuNPs: spheres (scale bar: 100 nm), bipyramids (scale bar: 50 nm) rods (scale bar: 100 nm), and bowls with bottom core (scale bar: 500 nm)[15]; (b) Differently sized spherical (plasmonic) AuNPs in aqueous solution and their corresponding UV-Vis spectra. The LSPR absorption maximum and the related color of spherical AuNP solutions depend on the size of the nanoparticles. Image reproduced from Dykman *et al*. 2012 and Ajdari *et al.* 2017.[15,16]

AuNPs being smaller than 2 nm, also referred to as gold nanoclusters (AuNCs), are characterized by a metallic core of a countable number of Au(0) atoms and Au(I) ions that are coordinated by ligands protecting the gold core. Due to their ultrasmall size, AuNCs are placed between isolated atoms/small molecules and plasmonic AuNPs: AuNCs have a well-defined molecular structure, discrete electron transitions and quantized charging.[17] More specifically, AuNCs have dimensions approaching the Fermi wavelength of electrons and therefore the delocalized electrons present in plasmonic AuNPs, as well as bulk gold, are constricted to discrete energy levels. This quantum confinement of electrons provides AuNCs with unique electronic, magnetic and optical properties, including photoluminescence for some AuNCs. Over the last years photoluminescent AuNCs have attracted considerable interest in the scientific community and photoluminescence has been tuned from the UV to the near infrared (NIR) region.[18] At present, it is generally accepted that the photoluminescence of AuNCs results from (i) electronic transitions that are similar to the ones of molecules, (ii) ligand to metal charge transfer and (iii) Au(I) present on the surface of the nanocluster.[19] For instance, Wu and Jin demonstrated that the fluorescence quantum yield of AuNCs is proportional to the Au(I)-coordinated ligand's ability to donate electrons.[20]

1.2 Catalytic properties

For a long time the catalytic properties of gold were not considered of any significance,[21] which presumably resulted from the use of gold foil or wires, instead of AuNPs. Research of the last two decades proved the opposite. The acceptance that gold is catalytically active started with the independent discovery of Haruta[22] and Hutchings[23] that AuNPs on metal oxide supports (e.g. α-Fe_2O_3) efficiently catalyze the oxidation of CO to CO_2.[24] Based on this finding further studies were conducted to investigate the catalytic activity of AuNPs for the hydrogenation of alkenes and alkynes, as well as for photocatalysis.[25] The key element for the catalytic properties of AuNPs has been linked to the fact that gold nanoparticle's surfaces display high curvature and hence facilitate access of substrates and cofactors to Au(0) and Au(I).

2 Biomedical applications of gold nanoparticles

The unique physicochemical properties of AuNPs, as well as their biocompatibility gave rise to the development of numerous AuNP-based applications in the fields of bioimaging, sensing and diagnostics, as well as therapy and delivery. These various applications exploit the possibility to functionalize the AuNP surface with diverse molecules, but also the different intrinsic properties of AuNPs outlined before. Electron microscopy imaging uses the high electron density of gold (19.3 g/mL), relative to the one of proteins (1.35 g/mL), which provides opacity to electrons and a high contrast to biological materials, such as cells or tissue. Sensing and diagnostics usually exploit the LSPR (color) of AuNPs and its sensitivity towards variation in the particles' environment. The photothermal effect uses the ability of AuNPs to produce heat upon irradiation with light and radiation enhancement is assumed to rely on the oxido-reduction ability of AuNPs. Although this thesis is focused on the development of novel probes (immunolabeling agents) based on small-sized AuNPs for electron microscopy, other important biomedical applications making use of AuNPs are summarized in the following sections. Figure 2 gives an overview about the different fields for which AuNPs are explored.

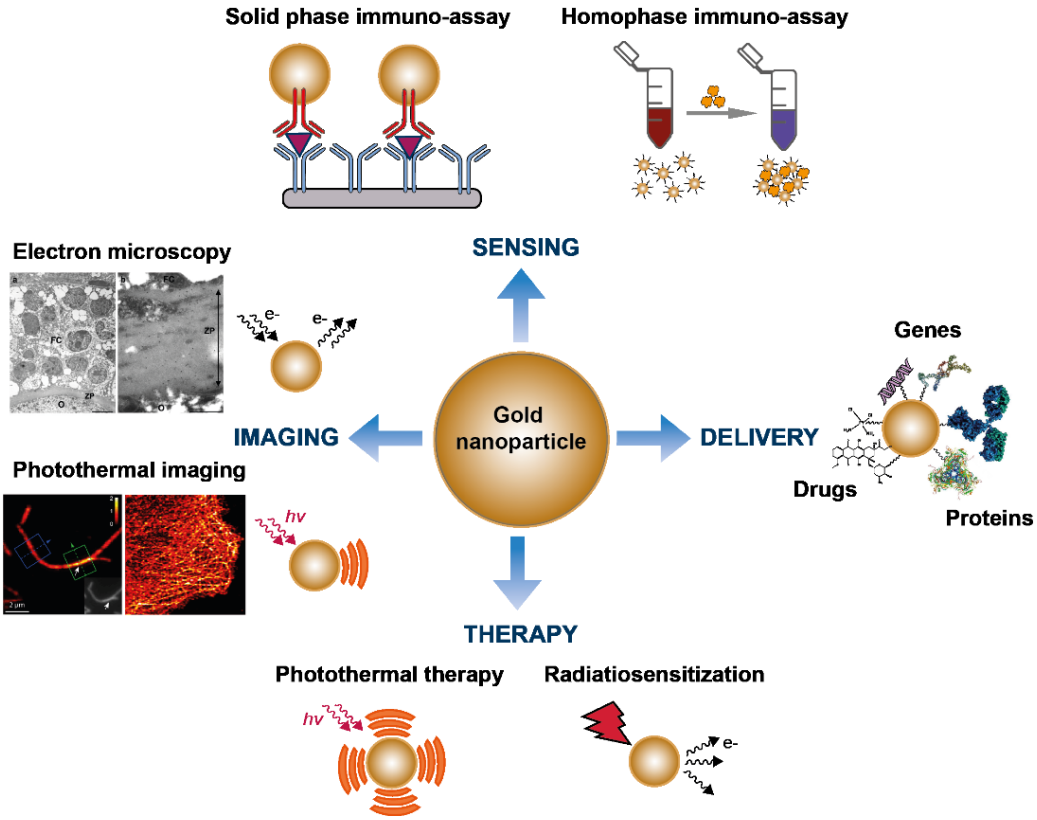

Figure 2. Overview about different applications of AuNPs, divided into the four fields: imaging, sensing, delivery and therapy.

2.1 Health care applications

The first reports of colloidal AuNPs used for medical treatments can be found in Chinese, Arabian and Indian papers from the 5th – 4th century BC. In the middle age colloidal gold was studied by alchemists and used for the treatment of mental diseases, syphilis and diarrhea.[26] In the late 1990's AuNPs have been then explored for the treatment of rheumatoid arthritis, due to the anti-angiogenic effects of gold.[27] Nowadays, most researchers explore AuNPs for the development of anti-cancer therapies, due to the need for new alternative treatments.[26] Approaches for such alternative therapies include AuNP-based platforms for the delivery of small molecules or high molecular weight proteins,[28] plasmonic photothermal therapy[29] and radiosensitization.[30] To date, no AuNP-based therapies or diagnostics are approved by the FDA/EMA. However, as of 2019 three AuNP formulations are undergoing clinical trials: the Aurimune CYT-6091 (*CytImmune*), the AuroLase (*Nanospectra Biosciences*) and the NU-0129 (*Northwester*).[31] All Aurimune products from *CytImmune* are based on 27 nm spherical AuNPs that are PEGylated to prevent clearance by the reticuloendothelial system and contain TNF-α. CYT-6091 is the first generation Arimune product currently undergoing phase II clinical trials

in pancreatic cancer patients. Second generation Aurimune nanomedicines are designed to deliver anticancer agents. Aurolase from *Nanospectra Biosciences* is based on 150 nm PEG-coated silica-gold nanoshells for near infrared facilitated thermal ablation, applied for solid primary and metastatic lung tumors. NU-0129 from *Northwester* is a nucleic acid platform consisting of spherical AuNPs onto which nucleic acids targeting the Bcl2L12 gene are arranged. NU-0129 is designed for treating glioblastoma patients by blocking the Bcl2L12 gene, thus promoting apoptosis of tumor cells. While only these three gold-based nanodrugs have reached the clinical stage, there is a plethora of potential AuNP-based therapeutic applications reported from researchers around the globe. A selection of potential AuNP-based therapeutics will be reviewed in the following paragraphs addressing platform-based approaches, plasmonic photothermal therapy and radiosensitization.

2.1.1 Platforms

Due to the possibility to easily functionalize AuNPs with a variety of molecules, AuNPs have been explored as drug carriers. The purpose of drug delivery is to modify the *in vivo* solubility, stability and biodistribution of small organic molecules (i.e. cytotoxic drugs), as well as high molecular weight proteins, such as therapeutic antibodies.[28] Several studies demonstrated that AuNP-drug conjugates successfully enable selective accumulation of water-insoluble chemotherapeutics to targeted cells and favor endocytosis of the nanomaterial, as reviewed by Dreaden *et al*.[32] AuNPs have been conjugated either by adsorption or using Au-S coordination to numerous anti-cancer agents, such as doxorubicin (11 nm spherical AuNPs),[33] methotrexate (13 nm spherical AuNPs),[34] 5-fluorouracil (2 nm spherical AuNPs),[35] or herceptin (gold nanorods)[36]. Moreover AuNPs hold promises for the delivery of multiple therapeutic agents to non-homogeneous solid tumors.[37] In 2006, Paciotto and coworkers reported the conjugation of TNF-α and paclitaxel to 26 nm spherical AuNPs coated with polyethylene glycol for targeting solid cancers.[37] Although spherical AuNPs are currently most commonly used for the generation of delivery platforms, there is an increasing recognition that non-spherical particles having cylindrical shapes (e.g. gold nanorods) are preferential for drug delivery purposes.[38] In fact, it has been demonstrated that cylindrical shaped nanoparticles have an increased capacity for evading the immune system, passing through tubular pores,[38] penetrating into tumors[39] and internalizing into cells.[40] It needs to be noted that these advantageous characteristics of rod-shaped AuNPs do not always apply, but a general trend has been observed throughout the

literature and it is hence expected that future therapeutic approaches will be more and more based on non-spherical AuNPs.[38]

Apart from antitumor substances, AuNPs are explored as platforms for the delivery of antibiotics and other anti-microbial agents,[41] as well as for gene therapy by linking genetic material to the AuNP and tuning its properties to allow penetration into cells and delivery of the genetic material into the nucleus.[42,43]

2.1.2 Plasmonic photothermal therapy

Spherical AuNPs with diameters > 2 nm, as well as differently shaped AuNPs strongly absorb light from the visible to the infrared spectrum (see Figure 1 (b) for spherical nanoparticles). The energy of the absorbed visible-near infrared (NIR) light is subsequently transformed into heat and this property of AuNPs is explored for a medical approach, named plasmonic photothermal therapy (PPTT). During PPTT the heat generated by the irradiation of the AuNPs causes lethality to cells that are in close proximity to the irradiated (thus heated) AuNPs.[29] In 2003, AuNPs were for the first time explored for PPTT by Hirsch and colleagues, who incubated human breast carcinoma cells *in vitro* with gold nanoshells (110 nm in diameter, 10 nm shell thickness) and observed cell death upon irradiation with near infrared light (NIR).[44] Light in the NIR is particularly useful for therapeutic applications, as it can penetrate 2 – 3 cm into biological tissues, which are highly transparent in this optical window.[45] Pitsillides *et al.* described another PPTT approach for selectively damaging lymphocytes with the use of 20 nm and 30 nm spherical AuNPs.[46] To ensure selective binding of the plasmonic AuNPs to the target cells, isolated lymphocytes were first incubated with anti-CD45 mouse antibodies (CD45 antigen common to all lymphocytes), then excess antibodies were removed and subsequently the cells were incubated with 30 nm and 20 nm AuNPs conjugated to anti-mouse antibodies. After a 30 min incubation time to ensure binding and internalization of the AuNPs into the living cells, 20 ns laser pulses at 532 nm were applied resulting in heat production and highly localized cell damage. For *in vivo* applications non-spherical particles, such as gold nanorods, gold nanostars and gold nanocages are most commonly employed, since they can be tuned to maximally absorb in the NIR window. Furthermore, non-spherical AuNPs usually have a higher photoconversion efficiency, than their spherical counterparts.[47]

One big advantage of PPTT using AuNPs is that the particles, in contrast to photosensitizers, are stable and inert inside cells for an extended period of time.[46] For accumulating AuNPs at the tumor site, researchers address two strategies – passive and active targeting. For the passive

targeting strategy, the surface-coating of the AuNPs is tuned to increase the circulation time in the blood (e.g. by coating the AuNP with high molecular weight polyethylene glycol). This extended residence time in the blood in turn favors passive accumulation at tumor sites, where abnormal vasculature causes the enhanced permeabilization and retention effect (EPR).[48,49] In case of active targeting, AuNPs are conjugated to targeting biomolecules, such as antibodies, directed against tumor-specific antigens to enable binding to cancerous cells, while sparing healthy tissue.[50] For instance, Loo *et al*. conjugated anti-HER2 antibodies to gold nanoshells for active targeting and thermal ablation of HER2-overexpressing breast cancer cells.[51]

Besides photothermal approaches for the treatment of tumors, the plasmon properties and photoconversion ability of AuNPs were recently explored for the photoablation of human vitreous opacities by Sauvage *et al*.[52] Vitreous opacities result from collagen aggregation inside the vitreous body and one current, hazardous treatment option is the destruction of these collagen aggregates by using high energy laser pulses. As an alternative approach the authors injected AuNPs coated with hyaluronic acid into the vitreous body, resulting in the binding of the AuNPs to the collagen aggregates and upon laser irradiation using 1000 times less energy, compared to the standard treatment, the aggregates could be efficiently destroyed.

2.1.3 Radiosensitization

In analogy to the absorption of visible light, AuNPs have a high X-ray absorption coefficient.[53] Upon X-ray irradiation of AuNPs secondary electrons and photons are emitted *via* the photoelectric effect, Auger effect or ionization effect, causing severe damage to cells in the vicinity of the nanoparticles[54]. More precisely, the generated low dose secondary electrons promote radical reactions that finally result in DNA damage causing cell death.[55] For cancer treatment, the radiosensitization of tumor tissue using radiosensitizing material (e.g. AuNPs) can reduce damage to healthy tissues if the radiosensitizer preferentially accumulates at the lesion sites.[56] In 2004 Hainfeld *et al.* described for the first time the radiation dose enhancement properties of AuNPs in tumor-bearing mice.[30] The authors reported that the administration of 1.9 nm AuNPs in combination with 30 Gy irradiation (250 kVp X-rays) resulted in 86% one-year survival of tumor-bearing mice, representing a drastic improvement when compared to 20% long-term survival for X-ray irradiation alone.[30] This pioneering work was followed by several studies on the radiosensitization properties of AuNPs which mostly confirmed the initial results.[57–60] However, the translation of AuNP radiosensitizers into the clinic remains problematic, as the current X-ray instruments used in clinic (operating at megavoltage) are not

well adapted for AuNP radiosensitization, since AuNPs strongly absorb X-rays in the kilovoltage spectrum, but not in the megavoltage range.[53,55] Moreover, many AuNP formulations do not display enough colloidal stability in the blood, requiring intra-tumoral injection to minimize potential side effects caused by nanoparticle aggregation.[53] To overcome these limitations, researchers focus today on the development of multi-functional AuNPs, AuNP-drug conjugates, as well as on actively targeted AuNPs to reduce long term toxicity. For instance, Hainfeld and coworkers explored the synergistic effect of hyperthermia (photothermal effect) and radiosensitization using 15 nm AuNPs that aggregate at acidic pH.[61] This aggregation occurring at pH < 6.5 (corresponding to the pH of the tumor environment) is due to the surface coating of the AuNPs consisting of lipoic acids which diminished AuNP's solubility upon protonation (e.g. when the pH decreases < 6.5) and PEGs for adjusting particle's furtivity. While isolated particles at physiological pH (pH 7.4) absorb visible light, the absorption maximum of aggregated particles lies in the NIR. After intratumoral injection of the AuNPs, the tumor site was exposed to NIR light resulting in a temperature increase of the AuNPs to 48°C, which was maintained for 5 min, followed by an irradiation with 100 kVp X-rays. This combination of hyperthermia and radiosensitization enabled to reduce the applied X-ray dose to <15 Gy versus 55 Gy and increased the long-term survival (> 250 days) of the treated mice to 71% from 33% for the control (X-ray treatment alone).[61] Hence, the synergetic effect of AuNP-based radiosensitization and hyperthermia appears promising. Besides, the synergistic combination of AuNP-based radiation enhancement and cytotoxic drugs was explored by several research groups, which is reviewed by Her and colleagues in *Advanced Drug Delivery Reviews* 2017.[53]

As an alternative approach, AuNPs can be made to contain radioactive ^{198}Au for carrying therapeutic doses of radiation to tumors.[39,62,63] ^{198}Au undergoes β-decay to stable ^{198}Hg with a half-life of 2.7 days, whereby the emitted β-radiation has an efficient radius on 1 mm in tissue. First studies using ^{198}Au-containing gold nanostructures for radiation therapy of tumors produced promising results, however it needs to be noted that the preparation of radioactive AuNPs remains an expensive technology.

2.2 Bio-sensing

In the 1980's AuNPs conjugated to targeting biomolecules (such as antibodies or antibody fragments) started to be used in analytical methods for diagnostics.[15] The principle behind these analytical methods is the change in coloration of AuNP solutions upon binding to biomolecules

and subsequent aggregation. One of the first described analytical methods making use of this principle was the sol particle immunoassay (SPIA) described by Leuvering *et al.*[64] This assay relies on the detection of antigens by specific binding to AuNPs, causing aggregation and a subsequent color change of the solution, which can be followed by eye, as well as by UV-Vis spectroscopy. SPIA is a homophase technique, meaning that the analyte and detection agent are in one phase (solution). Techniques like SPIA were applied for the detection of various tumor antigens,[65] as well as hepatitis B in blood.[66] Besides, colorimetric AuNP-based sensors were developed for the detection of DNA using either unmodified AuNPs,[67,68] or AuNPs conjugated to single strand DNA.[69] Apart from homophase techniques AuNPs conjugated to antibodies, antibody fragments or single chain variable fragments have also proven valuable for solid phase assays, such as dot immunoassays and ELISA.[15] It has been shown that the use of AuNP markers can enhance the sensitivity of a standard ELISA up to single molecule detection limit.[70]

2.2.1 Immunochromatographic assays

In the 1990's immunochromatographic assays for hand-held diagnostics became popular. The principle of such assays is the formation of specific immune complexes at preset membrane sites (deposition of sample's fluid) followed by the lateral movement of the immune complexes along a membrane (test strip) driven by capillary forces. For the visualization of these immune complexes, enzymes can be used to transform substrates in colored products. An alternative possibility is the use of red AuNPs, which remains popular due to their intense coloration.[71] One famous example for immunochromatographic assays using AuNPs are the cost-effective pregnancy tests. In a typical immunochromatographic assay, the test strip includes two "colorizable" positions (test zone and control zone) to verify that (i) the sample was correctly deposited, (ii) the device functioned properly and (iii) whether the antigen was present or absent in the sample. After depositing the sample (containing the antigen) the AuNP-antibody conjugate binds to the antigen in the sample and this immuno-complex migrates towards the test zone. The test zone contains immobilized antigen, but as the AuNP-antibody conjugates are already bound to the antigen present in the deposited sample, the immobilized antigens remain unbound and the test zone consequently unlabeled (assuming the antigen concentration of the sample exceeds a certain threshold). The AuNP-antibody-antigen complex migrates further towards the control zone, in which anti-species antibodies are immobilized. These anti-species antibodies bind the AuNP-antibody-antigen complex, resulting in a red coloration of the control zone, thereby validating the assay. Consequently, a positive test (antigen present in

the sample) is characterized by a signal in the control zone and no signal in the test zone. In case the deposited sample does not contain the antigen, the AuNP-antibody conjugate migrates towards the test zone and binds to the immobilized antigen, resulting in a red coloration of the zone. Driven by capillary forces the AuNP-antibody conjugate migrates further towards the control zone, where it bound by the immobilized anti-species antibodies, thus validating the assay. Hence, a negative test (antigen absent in the sample) is characterized by a signal in the test zone, as well as a signal in the control zone. An invalid test (indicating a failed device) is characterized by either a signal in the test zone and no signal in the control zone, or no signal at all (schematic illustration in Figure 3).

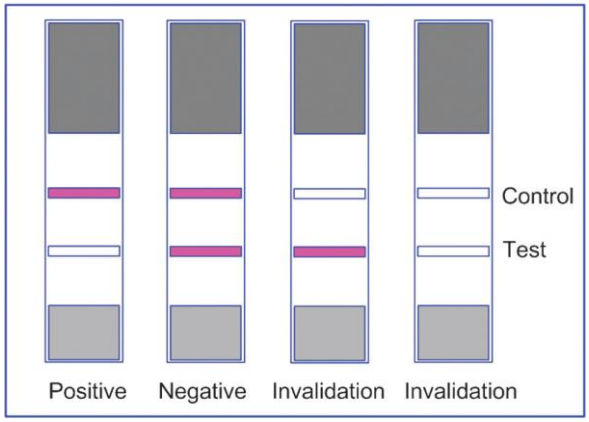

Figure 3. AuNP-based immunochromatographic assay showing positive, negative and invalid results.[15] Antigen immobilized in the test zone, anti-species antibodies (binding the AuNP-antibody conjugate) immobilized in the control zone. Image reproduced from Dykman *et al.* 2012.[15]

Immunochromatographic assays using AuNP-antibody conjugates for the visualization are widely applied to test for narcotics, toxins and infectious diseases, such as tuberculosis and helicobacter.[72] The company nanoComposix developed and commercialized a Borrelia Detection Kit (BDK) Home Tick test intended to evaluate whether a tick encounter posed a risk for Lyme disease. The BDK test is a lateral flow immunoassay using gold nanoshells for the visualization of *Borrelia burgdorferi,* the bacterium causing Lyme disease. The limit of detection was determined at 10 ng/mL of *B. burgdorferi* (corresponding to 57 cells). In 2000 Beck *et al*. developed an immunochromatographic assay for the detection of amphetamines and metamphetamines from clinical and forensic specimens (Frontline R).[73] Red colored AuNPs functionalized with anti-analyte antibodies allow the visualization of the drugs on the test strip in a concentration range of 150 ng/mL to 1 µg/mL (sensitivity cut-off was set to 300 ng/mL).

2.2.2 Plasmonic Biosensors

Since the LSPR of AuNPs is not only dependent on the AuNP's size, shape and surface coating, but also on the interparticle distance and the interaction with other molecules, AuNPs are highly attractive for the development of plasmonic biosensors. All AuNP biosensors are based on spectral (LSPR) shifts upon the binding of molecules to the AuNP surface.[15] Such biosensors are very sensitive and allow the detection of single molecular interactions near to the AuNP's surface. LSPR biosensors are valuable tools for biology (e.g. detection of genes and proteins), as well as for medicine allowing drug screening and the analysis of antibodies, antigens and infectious agents.[15] Thus far, AuNP-aided biosensors have not been commercialized, but the high number of publications in the field underscores the potential of the approach.[74–76]

2.3 AuNPs for imaging of biological specimens

The first application of colloidal AuNPs and antibody-gold conjugates for bio-imaging were developed for electron microscopy observation, more precisely for immunogold labeling of protein targets in biological specimens.[15] As mentioned before, AuNPs provide high contrast in electron microscopy thanks to their opacity to the electron beam, given by the high electron density of the metallic AuNP core containing more than 3800 Au atoms for a 5 nm AuNP. Today, AuNPs are also used in various other imaging techniques that allow the visualization of biological systems and interactions.[9,77–79] The high scattering cross section of AuNPs facilitates observation using dark field microscopy[80] and the characteristic of plasmonic AuNPs to convert absorbed light into heat are used for photothermal imaging.[81] Moreover, AuNPs are employed in state-of -the-art bio-imaging methods, such as optical coherence tomography,[82] X-ray and magnetic resonance tomography,[83] photoacoustic microscopy[84]/tomography[85] and correlative fluorescence and electron microscopy.[86] These imaging techniques will not be discussed in here, but a detailed review on AuNP-based imaging modalities was written by Dykman and Khlebtsov and can be found in *Chemical Society Reviews* in 2012.[15] Instead, the next section will provide a comprehensive review on electron microscopy imaging of biological specimens with a particular emphasis on the development of immunogold labels, the technical advances in electron microscopy technologies of the last decades and a final point elucidating the need for novel immunogold labeling agents. This final point will lead to the objective of this PhD thesis and an explanation on the structuration of the manuscript.

3 Electron microcopy imaging of biological specimens – immunogold labeling

Since the construction of the first electron microscope in 1933 by Ruska and Knoll, the resolution of electron microscopes has drastically increased and reaches today the atomic range for hard materials and purified proteins and the nanometer range for cellular samples. With regards to cellular biology, electron microscopy (EM) has majorly contributed to our understanding of the complex organization of proteins inside cells at the ultrastructural level.[87] For any EM observation of biological specimens, samples need to be fixed and converted into a solid form, since the high vacuum in the electron microscope column quickly dehydrates and consequently destroys the highly hydrated biological specimens.[88] In traditional TEM experiments cells are hence chemically fixed, dehydrated and embedded into resins.[89] The resin blocks containing the specimen are then sectioned into thin slices to ensure collection of the electron beam after passage through the sample. Since biological specimens (cells and tissue) consist of elements with low atomic number, the difference in electron density is low, resulting in weakly contrasted images. Besides the vacuum, organic materials can be severely damaged by electrons. In order to increase the specimen's stability and contrast, biological samples are traditionally stained with heavy metal salts, such as osmium tetroxide, lead citrate and uranyl acetate.[90] Osmium interacts with lipids, uranium binds to phosphate and amino groups and lead interacts with negatively charged groups. Altogether, these metallic stains allow differential staining of organelles and compartments of mammalian cells, as well as microorganisms including viruses. For labeling selected proteins inside cells or tissue sections, immunogold labeling has been established.[91] In analogy to immunofluorescence, antibodies are used to target the epitope of interest and the gold domain, which is conjugated to the antibody, provides the detected contrast due to the high atomic number of Au (Z = 79).[92]

Immunogold labeling can be performed either before, or after embedding the specimen in resin, accordingly referred to as pre-embedding and post-embedding immunogold labeling.[93] Pre-embedding immunolabeling requires cell permeabilization, leading to a compromised ultrastructure, but offers the advantage that the cells are only fixed with paraformaldehyde prior to the immunolabeling, which does not destroy the antigenicity of proteins as easily as glutaraldehyde.[92] In post-embedding techniques immunolabeling is performed on resin embedded cell/tissue sections and therefore does not require permeabilization resulting in an improved ultrastructural preservation. Yet, the sample preparation for post-embedding immunolabeling, notably the fixation using glutaraldehyde, often impairs the antigen binding

and consequently limits possible targets.[94] In the 1970's Kiyoteru Tokuyasu developed a cellular sample preparation procedure for EM yielding ideal substrates for immunogold labeling.[95] This technique, named "Tokuyasu-method", relies on the use of low concentrations of glutaraldehyde (hence "mild" denaturation) and the infiltration of the fixed cells with sucrose as cryo-protectant. The fixed and sucrose infiltrated cells are then frozen in liquid nitrogen permitting cryo-sectioning into ultrathin slices. Thanks to the cryo-protectant the sectioned specimens can be thawed without destroying their ultrastructure, thus permitting immunogold labeling at room temperature and subsequent high resolution transmission electron microscopy (TEM) observation.[96]

3.1 History of immunogold labeling

The first use of colloidal gold-antibody conjugates for the labeling of selected proteins for EM observation was reported in 1971 by Faulk and Taylor.[97] The authors described a protocol for conjugating antibodies targeting the *Salmonella* surface antigen to AuNPs having a mean diameter of 5.2 nm (coefficient of variation 60%) using strong non-covalent interactions, as well as a labeling protocol for observing the targeted structure by TEM. Three years later Romano and coworkers reported the preparation of colloidal gold conjugates with purified secondary antibodies and set up the indirect immunogold labeling methodology.[98] The introduction of the protein-A gold labeling technique made by Roth together with Bendayan and Orci in 1978 was another important milestone in immuno-EM.[99] Instead of preparing colloidal gold conjugates with secondary antibodies, the authors linked the *staphylococcal* protein A to the gold particles, which likewise permits the use as secondary probe, since protein A binds to the Fc region of antibodies with high affinity. Electron micrographs of AuNPs with and without protein A coating produced by Roth and colleagues,[99] as well as immunolabeled pancreatic tissue section are depicted in Figure 4.

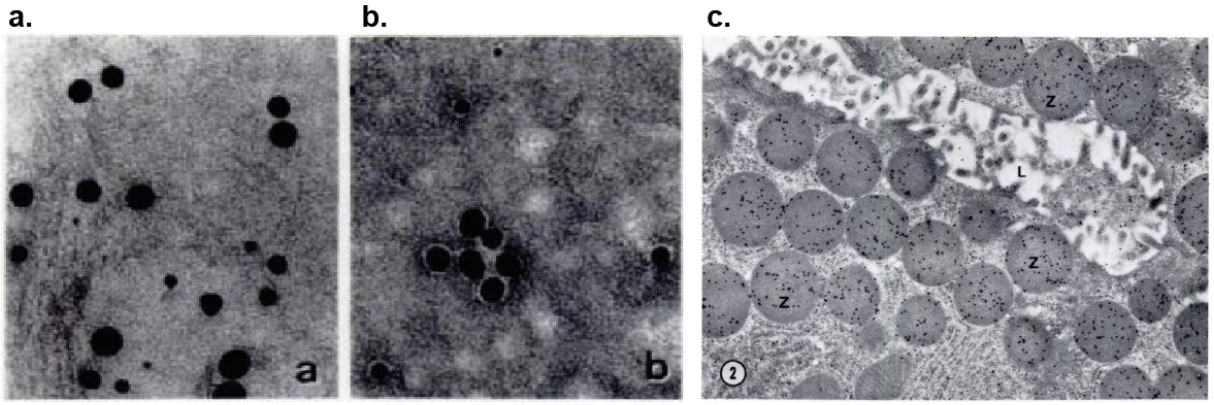

Figure 4. Protein A-colloidal gold conjugates prepared by Roth and colleagues in 1978 for immunolabeling of amylase in rat pancreatic tissue. (a) Naked AuNPs visualized after negative staining using uranyl acetate (x165000); (b) Protein A-AuNP complex after negative staining (x165000), halo around the particles indicates the presence of protein A coating; (c) Rat pancreatic tissue immunolabeled with anti-amylase serum and protein A-colloidal gold conjugate (x23000) showing high density of amylase in zymogen granules (Z). Image reproduced from Roth *et al.* 1978[99]

The colloidal gold particles used for making these first generation of immunogold probes are mainly in the size range of 5 – 15 nm and the conjugation of the biomolecules to the AuNPs is accomplished by physical adsorption.[100,101] Since the quality of EM images relies on the quality of the probes, which is apart from AuNP uniformity, based on controlling the amount of biomolecules (antibody/protein A) that adsorb to the surface of the nanoparticles, researchers established procedures for identifying the right protein/AuNP ratio for the conjugation. Practically, a constant concentration of AuNPs was mixed with increasing protein concentrations and the stabilization of the AuNPs is evaluated by salt induced flocculation.[102] In 1985 Baschong *et al.* published the synthesis of 2.6 nm AuNPs having a relatively discrete size distribution (coefficient of variation 15%) and described the complex formation with protein A.[100] This small-sized probe developed by Baschong and colleagues proved useful for immunolabeling of resin-embedded tissue sections, applying primary antibodies or antiserum as a first step and the 2.6 nm AuNP-protein A conjugates as a second step. Based on the successful results of Baschong *et al*. several other groups reported the synthesis of small-sized AuNPs for the generation of immunogold labeling probes by exploiting the ability of AuNPs to bind various macromolecules by non-covalent electrostatic and hydrophobic interactions.[94,103,104]

In the late 1980's Hainfeld and coworkers introduced another approach for generating immunogold probes by synthesizing discrete gold clusters having a countable number of Au atoms ranging in size from 0.8 – 1.4 nm.[105,106] The cluster compounds possess a well-defined coordination shell of organophosphines, into which specific functionalities can be introduced

(e.g. amino or maleimido group), permitting to covalently link these clusters to biomolecules in a controlled manner (structure of 0.8 nm gold cluster "Undecagold" reported by Hainfeld *et al.* depicted in Figure 5). Besides the covalent conjugation to antibodies, the clusters proved useful for the linkage to Fab' fragments, thereby reducing the spatial distance between the target structure and the gold label.

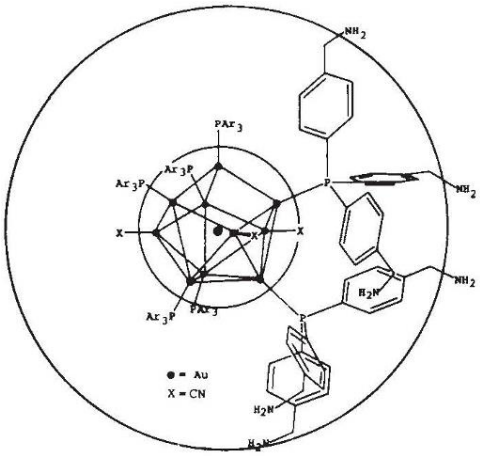

Figure 5. Structure of 0.8 nm Undecagold cluster consisting of 11 Au atoms, to which 7 triphenyl phosphine ligands are coordinated. Triphenyl phosphines bear amino groups in the para position, resulting in 21 amino groups per cluster that can be used for functionalization. Image obtained from Hainfeld *et al.* 1988.[106]

Due to an enhanced diffusion ability, small-sized immunogold probes are advantageous in terms of labeling efficiency, which is particularly useful for sparse antigens.[101] However, non-aggregated (single) AuNPs having sizes of 1.4 nm and below are not easy to pinpoint when embedded in sections of biological samples, since the decreased size of AuNPs is accompanied by decreased opacity to electrons, thus resulting in lower contrasting ability. One solution to this obstacle is to enlarge the AuNPs using a silver enhancement protocol prior to the EM observation.[101,102,107] While it is generally accepted that AuNPs being smaller than 1.4 nm need to be silver enhanced for EM visualization when embedded in cell sections, Sousa *et al.* reported that 2 nm AuNPs coated with glutathione and the cell-penetrating peptide TAT can be detected as single particles inside cell sections without any heavy metal staining by high-angle annular dark-field scanning transmission electron microscopy (HAADF-STEM).[108]

Today there are two main companies providing probes for immunogold labeling: *Nanoprobes* (created by Dr. James F. Hainfeld, website: https://www.nanoprobes.com) and *Aurion* (created by Dr. Jan Leunisse, website: https://aurion.nl/). While both companies offer classical labeling agents consisting of colloidal gold particles ranging in size from 3 – 30 nm, to which secondary antibodies, protein A, Fab' fragments, as well as streptavidin are adsorbed, they also

commercialized small-sized gold clusters. *Nanoprobes* sells the 1.4 nm Nanogold®[105] and 0.8 nm Undecagold®[106] that are functionalized with maleimide, amino and sulfo-NHS-groups to label thiols, carboxylic acids and amine groups. Moreover, *Nanoprobes* sells certain IgG- and Fab-Nanogold® conjugates. *Aurion* has likewise developed AuNPs of 0.8 nm (the Ultra Small Immuno Gold) and corresponding conjugates, which are, unlike the covalent conjugates of *Nanoprobes*, made by physically adsorbing the 0.8 nm AuNPs to antibodies. As already mentioned before, AuNPs below 1.4 nm are advantageous in terms of diffusion and accessibility to antigens,[92,109] but suffer from low detectability, which needs to be palliated using silver enhancement methods. Silver enhancement is a critical step in the EM sample preparation and when improperly performed causes the aggregation of the growing particles into large clumps. However, if the procedure is carried out correctly, excellent images with higher labeling efficiency can be obtained, when compared to images labeled with probes made with larger gold particles.[92] Figure 6 shows the immunogold labeling of synaptic vesicle integral membrane proteins using 1.4 nm Nanogold (*Nanoprobes*) followed by silver enhancement.[110]

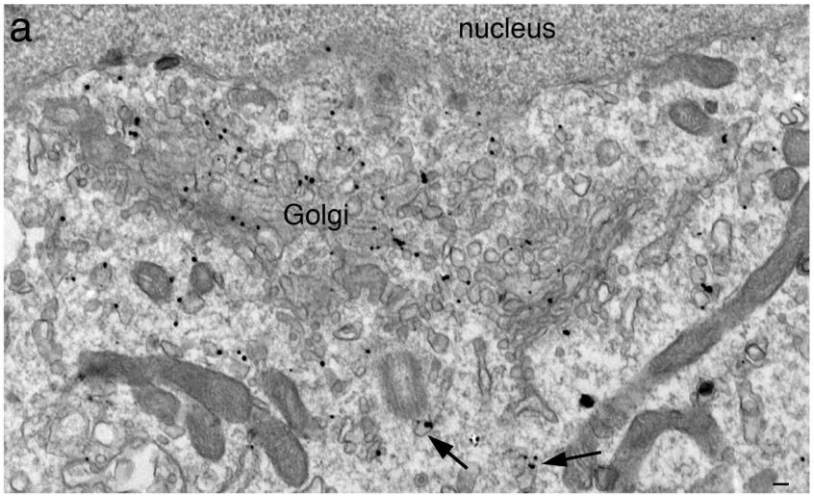

Figure 6. Immunogold labeling of synaptic vesicle (SV) integral membrane proteins and in developing hippocampal neurons. Immunogold labeling with anti-SV2 antibody (targeting SV integral membrane proteins) and secondary antibody coupled to 1.4 nm Nanogold (*Nanoprobes*), followed by silver enhancement. Immunogold labels are localized at the Golgi complex and membranous structures. Figure obtained from Tao-Cheng *et al.* 2020.[110]

Apart from immunogold labeling, labeling techniques based on peroxidases[111] and ferritin[112] have been developed. As for AuNP-based immunolabeling, peroxidase and ferritin are linked to antibodies to target them to the protein/structure of interest. In case of peroxidase an electron dense product is generated through oxidation of 3,3'-diaminobenzidine (DAB) with H_2O_2, forming a brownish precipitate, and subsequent exposure to osmium tetroxide, which deposits

on the DAB oxidation product.[111] In contrast to immunogold labeling, the electron dense DAB product is not bound to the antibody (thus the targeted structure) and can therefore drift away from the target site. Ferritin is a ca. 20 kDa protein that stores iron when grown under iron-rich condition and consequently the electron dense signal in ferritin immunolabeling is provided by the protein itself, not requiring conversion of any substrate.[113] Although both, ferritin and peroxidase have proven useful for immunogold labeling, they have not received as much attention as immunogold methods, due to the advantage of the latter methodology to generate signals with discrete electron dense particles.[92]

3.2 Cryo-electron microscopy and new trends

In 1984, Dubochet and colleagues (Nobel Prize in Chemistry 2017) set up a procedure for cryogenic fixation and cryogenic electron microscopy (cryo-EM) observation of biological specimens.[114,115] In cryo-EM samples are fixed by rapid freezing,[88,116] which does not permit the arrangement of water molecules into ice crystals but results in the formation of amorphous ice – a process called vitrification – yielding frozen hydrated specimens.[117] It is of uttermost importance during cryo-fixation that the cooling rate is faster than the rate of water crystallization (10^5 K/s for samples < 10 µm thickness), since the formation of ice-crystals damages the structure of any biological specimen.[118] Practically, samples that are thinner than 10 µm, such as isolated proteins, viruses, bacteria and thin cells, are plunged into liquid ethane or propane, which is cooled by liquid nitrogen to approximately 100 K. Following this procedure, which is called plunge freezing and was developed by Dubochet *et al.*, the cryo-fixed sample needs to be directly transferred into the cryo-electron microscope without allowing the sample to warm above the devitrification temperature (140 K).[114] For samples that are thicker than 20 µm cryo-fixation cannot be performed by plunge freezing, since the low conductivity of water does not permit attaining the required cooling rate in the center of the sample and as a consequence distorting water crystals can form. This limitation can be overcome by freezing thick samples under high pressure (2100 bar) – a method called high pressure freezing, which can be applied for cell and tissue samples of up to 200 µm thickness.[119]. The increased pressure alters the physical properties of water, thereby reducing the rate of water crystallization and consequently the required cooling rate is lowered as well.

Purified proteins, supramolecular complexes, viruses or bacteria can be directly imaged after cryo-fixation, because they are thin enough to permit the electron beam to pass through the vitrified objects. In contrast, specimens that are thicker than 500 nm, such as mammalian cells

and tissue, do not allow transmission of the electron beam and therefore need to be thinned.[88,118] Traditionally, the thinning of frozen-hydrated cells was accomplished by cryo-ultramicrotomy. In analogy to classical ultramicrotomy, the samples are cut into thin sections using a diamond knife and subsequently deposited onto grids. To avoid thawing of the samples the whole procedure is performed at cryogenic temperatures. Cryo-ultramicrotomy allows to routinely section cells and tissue into lamellas of 10 – 150 nm, thus covering a wide area. However, the process of sectioning using a knife relies on mechanical forces that can deform the soft and fragile biological specimen. The resulting artifacts include anisotropic compression, crevasses and chatter, which strongly affect the quality of the sample.[88] In recent years cryo-focused ion beam (FIB) milling has been developed, which represents an attractive alternative for the thinning of frozen-hydrated samples. Cryo-FIB milling generates thinned sections of frozen cells or tissue by abrading material above and below the area of interest in a stepwise fashion, typically with the use of gallium ions. The lamellas that are classically produced have a thickness of 200 nm and the biological material within the section usually remains intact, as it does not interact with the ion beam throughout the process. The described workflow for cryo-EM sample preparation is depicted in Figure 7.

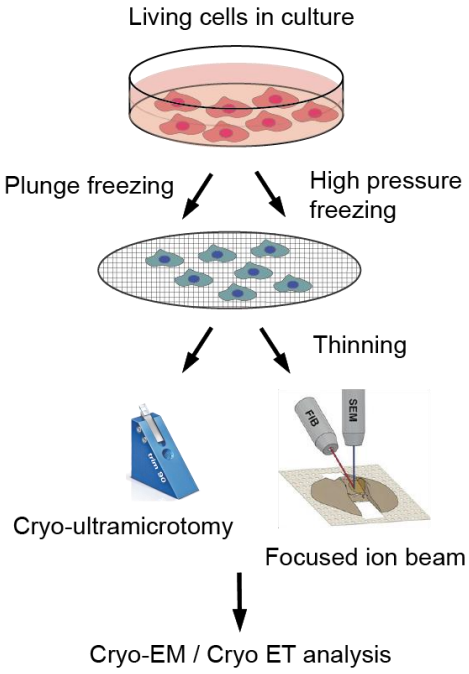

Figure 7. Sample preparation workflow for cryo-EM. Biological specimen is cryo-fixed by plunge freezing or high pressure freezing, cryo-fixed cells (or other specimens that are thicker than 500 nm) are thinned by cryo-ultramicrotomy or focused ion beam milling and finally the specimen is transferred into cryo-electron microscope for analysis.

Besides the resolution of the sectioning issue, the development of direct electron detectors and Volta phase plate has considerably enhanced the contrast of biological samples. In fact, these technical advances facilitate imaging of cryo-fixed biological samples with low electron dosage, yielding high-quality images at nanometer resolution.[88] Moreover, improved data analysis methodologies allow nowadays extremely precise 3D reconstruction of isolated proteins, supramolecular complexes, as well as cellular compartments.[120–122] Figure 8 shows a comparison of electron micrographs of vitrified virus solutions from 1986 and 2018, demonstrating the results of the technological advances.

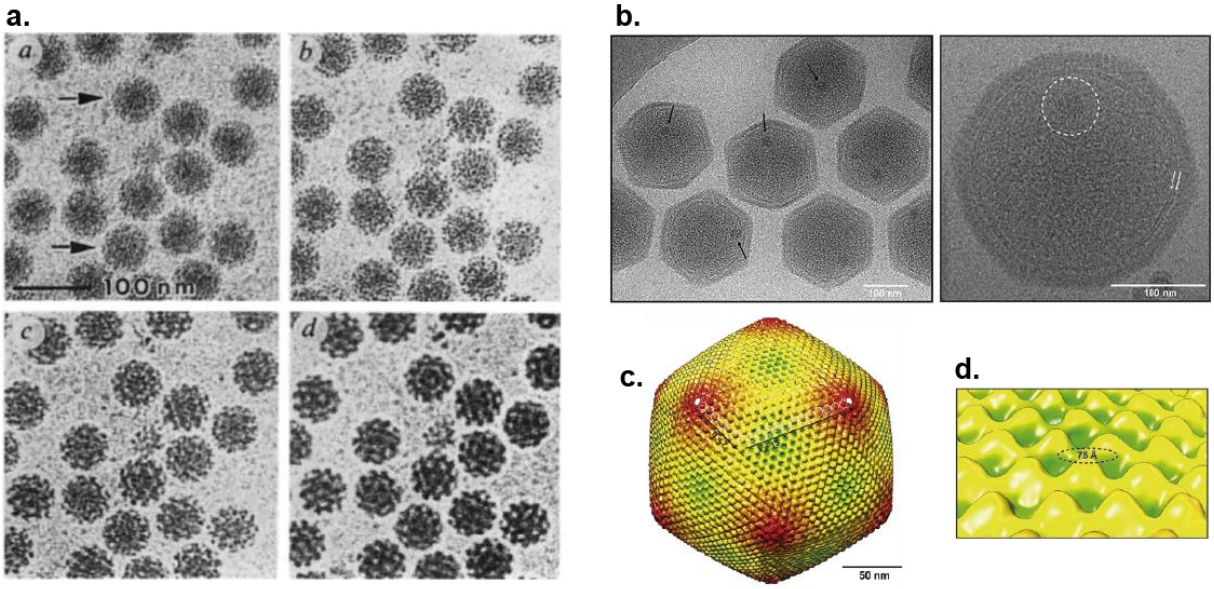

Figure 8. Comparison of electron micrographs of vitrified and unstained Semliki Forest virus published in 1986 (a) and cryo-fixed Melbournevirus published in 2018 (b). Scale bars in (a) and (b): 100 nm. 3D reconstructed capsid of Melbournevirus in (c), scale bar: 50 nm and close-up view of surface protrusions of viral capsid in (d).

Currently, only few research laboratories, amongst them the group of W. Baumeister, make use of these advanced techniques to tackle the challenge of imaging supramolecular complexes within cryo-fixed cells.[123,124] Indeed the production of high resolution images of these complexes within their natural environment in close to native conditions is time consuming and the possibility of labeling selected intracellular proteins within these specimens remain elusive. Figure 9 shows an electron tomographic slice of the nuclear periphery of a HeLa cell and the corresponding 3D reconstructions made in laboratory of W. Baumeister.[125] HeLa cells were sectioned by FIB milling and the 3D reconstructions reveal the nuclear pore complex, ribosomal subunits, microtubules, actin and intermediate filaments. Imaging of nuclear protein complexes by cryo-EM of frozen-hydrated cells is particularly challenging, which presumably results from

the high protein/DNA density inside the nucleus of cells and the resulting low difference in electron density.[126] For this issue, the pinpointing of nuclear proteins with electron dense AuNPs inside cryo-fixed cells would be highly useful and eventually the solution to this bottleneck.

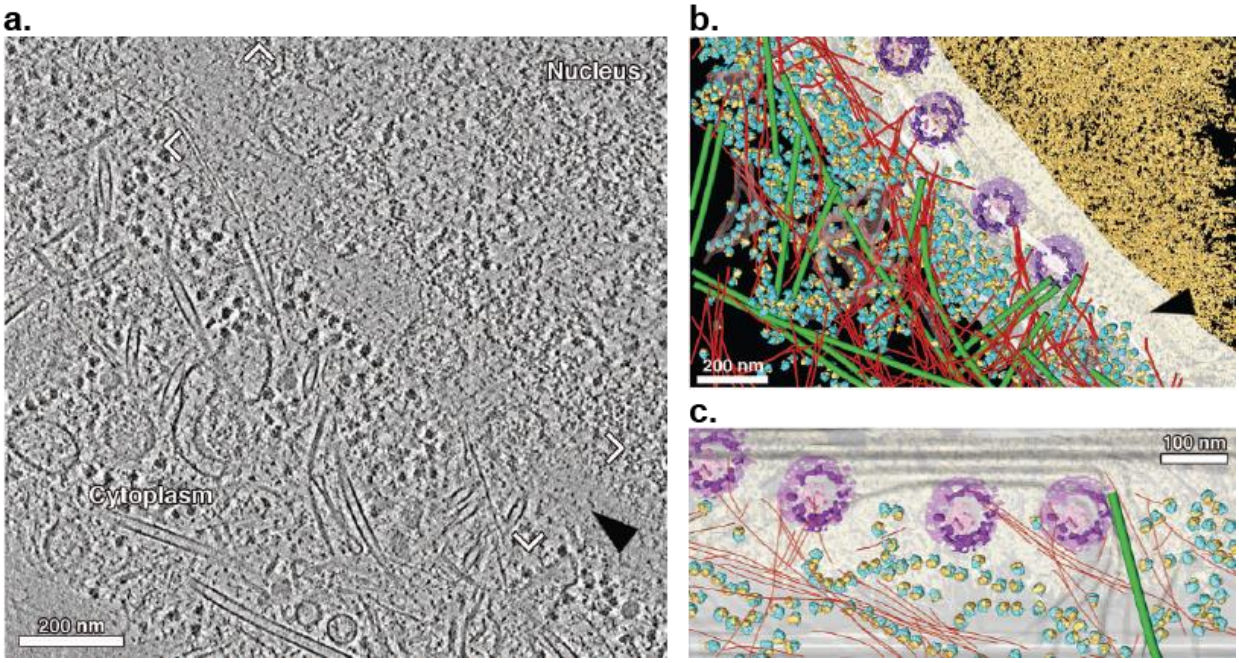

Figure 9. HeLa cell nuclear periphery. (a) Tomographic slice of HeLa cell thinned by FIB. Arrow points at the nuclear envelop; (b) Annotated view of tomographic data; (c) Cross section view in vicinity of nuclear envelop (nuclear pore complex in purple). Image reproduced from Mahamid *et al.* (Group of W. Baumeister).

In 2015, Orlov *et al*. approached the immunogold labeling of nuclear proteins inside living cells by functionalizing an antibody targeting the nuclear enzyme RNA polymerase II with ultrasmall 0.8 nm AuNPs (*Aurion*) and demonstrated that the antibody probe can be delivered into living cells using a cationic lipid system.[127] FIB/SEM imaging revealed that the functionalized antibody was localized inside the cellular nucleus, suggesting that the probe specifically binds to its nuclear target. As a proof of concept Orlov also conjugated the RNA polymerase II-targeting antibody to 6 nm AuNPs (*Aurion*) and attempted the delivery of the conjugate into living cells. In contrast to the ultrasmall particles, the antibody conjugate was not detected inside the nucleus, but only found in cytoplasmic vesicles at the periphery of the cell membrane. Hence, it was evident that the antibody probe based on 0.8 nm AuNPs has beneficial diffusion properties and even permits the labeling of nuclear proteins in live cells. Yet, it needs to be noted that the system reported from Orlov is not perfect. First, the linkages between the antibody and the nanoparticles, as well as the site of attachment are not defined (random physical adsorption of the ultrasmall AuNPs onto the antibody) and therefore an exact

pinpointing of the target is impossible. Second, the 0.8 nm AuNPs need to be enlarged by silver enhancement, which precludes the system from being employed for non-denaturating cryo-EM studies.

3.3 Objective

Considering the workflow of cryo-EM of frozen hydrated specimens there is neither the possibility for performing classical immunogold labeling, nor the possibility for silver enhancing ultrasmall AuNPs that have been delivered into live cells, since these procedures cannot occur under cryogenic conditions. Due to this reason, as well as due to the aforementioned instrumental improvements of EM, allowing to image cellular proteins with nanometer resolution, we believe that there is a need for new immunogold probes. The facts listed hereafter summarize the main shortcomings of traditional EM probes with regards to the technical advances of the last decades. First, the distance between target and signal, resulting from the use of primary and secondary antibodies/protein A, is too large compared to the resolution of novel EM apparatuses. Second, the size of the AuNPs used for immunogold labeling, being either 5 – 15 nm AuNPs or ultrasmall 0.8 – 1.4 nm AuNPs that are silver enhanced finally also reaching a diameter of 10 – 25 nm, is also not adapted for the improved resolution limit. Third, the dependence on cell fixation and permeabilization, restricts the use to cells having a compromised ultrastructure.

To generate immunogold labeling agents that are adapted to state-of-the-art EM technologies the novel immunogold probes should be (i) as small as possible, (ii) chemically defined and easily producible, (iii) applicable as primary probe and (iv) deliverable into living cells, thus allowing the binding to the target in native conditions and the observation of the labeled structure by cryo-EM, thereby avoiding the use of destructive detergents or chemical fixatives. Figure 10 illustrates these novel small-sized immunogold probes compared to traditional immunogold labeling agents. For producing such new EM probes, it is hence necessary to develop uniform AuNPs that are as small as possible, but still directly detectable by EM when embedded in the cellular ultrastructure. Moreover, they should enable the formation of a precise link between the gold and the antibody domain to control the distance between the target and the detectable AuNP. Finally, the surface coating of the AuNPs needs to be tuned to prevent unspecific binding to cellular components, allowing for free diffusion throughout the interior of living cells.

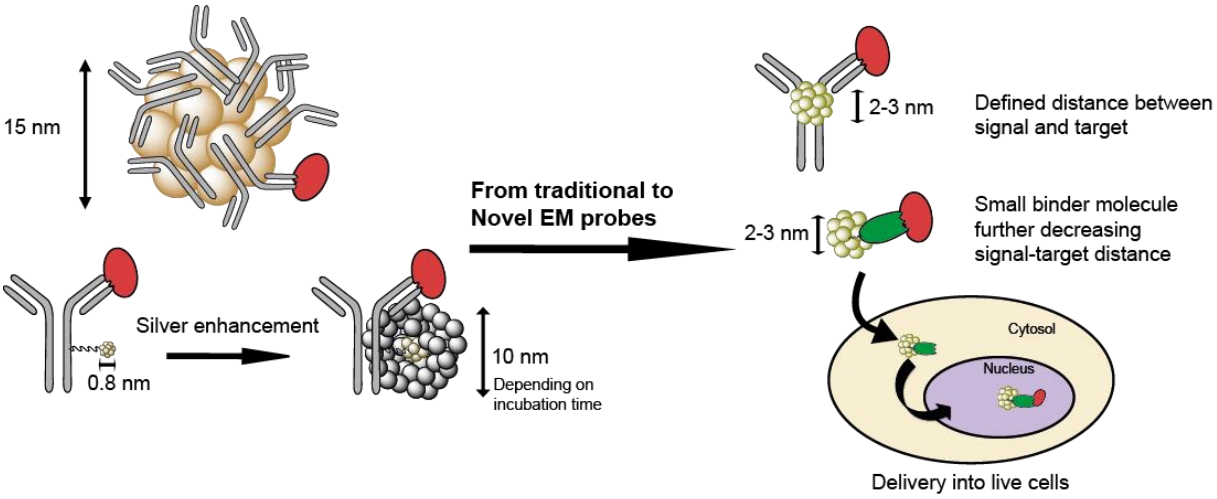

Figure 10. Schematic illustration of the objective of this PhD project: Generation of novel immunogold probes being smaller and more precise than traditional immunogold labels, as well as applicable for delivery into live cells. On the left: traditional 15 nm colloidal gold conjugated with antibodies *via* adsorption and ultrasmall 0.8 nm AuNPs covalently linked to antibody before and after silver enhancement. On the right: novel immunogold probes consisting of a 2 – 3 nm AuNP site-selectively conjugated to an antibody (1 particle per antibody) and 2 – 3 nm AuNP linked to a small binder molecule, allowing to further decrease the distance between the target and the signal, as well as the delivery into living cells.

This thesis describes the synthesis of novel EM probes based on small and monodispersed organothiolate-protected AuNPs for which different conjugation strategies have been developed to link them in a precise and controlled manner to antibodies and nanobodies. Moreover, the thesis covers the evaluation of their binding ability and compatibility with EM procedures. The thesis is organized in three chapters. Chapter 1 entitled "Synthesis and functionalization of small-sized thiolate-protected gold nanoparticles" describes the development of uniform thionitrobenzoate- thioaminobenzoate-protected AuNPs of three different sizes (ranging from 1.4 – 2.6 nm) and their reactions with protective and bioactive molecules. Moreover, this chapter covers the impact of the AuNP surface coating on the behavior of the AuNPs inside living cells after delivery by electroporation. Identifying protective ligands that do not promote unspecific interactions with cellular components but allow for free diffusion throughout the interior of the cell is crucial for the generation of EM probes, since their interactions and binding should solely be dictated by the binder (antibody) moiety. Chapter 2 entitled "Conjugation of gold nanoparticles to antibodies and biological evaluation" presents the site-specific conjugation of the AuNPs to different antibodies, at the hinge area, including the therapeutic antibodies Cetuximab and Bevacizumab, as well as an antibody targeting the nuclear RNA polymerase II. Furthermore, the chapter describes the evaluation of the conjugates' binding ability using fixed and living cells, with an excursus on

the biological function of the AuNP-Cetuximab probe. Chapter 3 entitled “Conjugation to nanobodies and application as EM probes” covers different conjugation approaches for linking the AuNPs to a nanobody targeting the green fluorescent protein (GFP) and the use of these probes for the labeling of GFP-tagged proteins by light and electron microscopy.

Chapter 1

Synthesis and functionalization of small-sized thiolate-protected gold nanoparticles

For the generation of precise immunogold probes to be used inside living cells, the gold nanoparticle domain and the conjugation strategy are of uttermost importance. Firstly, our aim was to select the most suitable type of gold particles. These gold particles should ensure stable conjugation to biomolecules, high opacity to electrons and inertness (e.g. should not interact with biological compounds or modify the biological activity of the attached biomolecule). Previous investigations of our laboratory indicated that a 1.4 nm thiolate-protected AuNP (AuZ) looks extremely promising for this purpose. The aims of our first investigation were (i) to comprehensively investigate the synthetic procedure of AuZ in order to make monodispersed particles of various sizes and (ii) to evaluate the biocompatibility of surface modified AuNPs after intracellular delivery.

Before exposing our investigations, we introduce the peculiar properties of gold and review existing methods to synthesize and functionalize gold nanoparticles.

1 Introduction

1.1 Atomic properties of gold

Gold is a transition metal placed in group 11 and period 6 of the periodic table of elements with the electron configuration $[Xe]4f^{14}5d^{10}6s^{1}$. Gold has an atomic number of 79, thus making the metal a high atomic number material with a molecular weight of 196.97 g/mol and a mass density of 19.3 g/mL. Chemically, gold is inert and can only be oxidized by aqua regia (a mixture of nitric acid and hydrochloric acid in a stoichiometric ratio of 1:3). The oxidation states of gold range from -1 to +5 and Au(I), referred to as aurous, and Au(III), named auric, are the most common oxidation levels. The standard reduction potential of gold (see formula below) indicates that Au(I) disproportionates in aqueous solutions (according to the equation shown below) unless the aurous ion is stabilized in complexes.

Standard reduction potential $\mathrm{Au(0)} \xrightarrow{+1.69\ \mathrm{V}} \mathrm{Au(I)} \xrightarrow{+1.4\ \mathrm{V}} \mathrm{Au(III)}$

Disproportionation reaction $3\mathrm{Au(I)} \rightarrow 2\mathrm{Au(0)} + \mathrm{Au(III)}$

Aurous ions ($4f^{14}5d^{10}$) are preferentially complexed with soft ligands, such as thiolates and tertiary phosphines, thereby forming linear complexes, whereas auric ions ($4f^{14}5d^{8}$) have a strong tendency for forming square planar complexes. In its metallic Au(0) form, electrons freely diffuse throughout the metal making gold very ductile and conductive. This flexibility enables the production of gold leaf having a thickness down to 0.1 µm. The availability of free electrons at the atomic surface of gold, the co-existence of different oxidation states, as well as the ability of gold to coordinate with organic species, facilitate moreover the formation of stable nanostructures.[128]

1.2 Synthesis of gold nanoparticles

For generating AuNPs two types of strategies have evolved – the top down and bottom up approach. In top down techniques the bulk state of gold is broken down to produce AuNPs,[1] whereas the bottom up approach is based on the arrangement of gold atoms to form nanosized particles.[129] The top down strategy can be accomplished using different methods, including grinding or mechanical milling, sputtering, laser ablation, thermal decomposition and lithography. The bottom up approach is by far more common and effective, than top down

techniques,[24] and comprises several methods, among which the chemical method (also named liquid phase synthesis method) is most widely used for the generation of AuNPs.

In the chemical method Au(III) ions of chloroauric acid ($HAuCl_4$) are reduced with reducing agents, e.g. sodium borohydride ($NaBH_4$) or sodium citrate, which results in a process involving the nucleation of Au(0) atoms (nucleation phase) and the growth into nanoparticles (growth phase). The reducing agents or other molecules that are added to the starting material ($HAuCl_4$) participate to the growth process by coordinating to the formed gold clusters and finally build a layer around the generated AuNPs, whose stability varies according to the chemical nature of the coordinating ligands. Common ligands know to stabilize the formation of AuNPs are phosphines, thiols, amines, as well as carboxylates of sodium citrate.[129] The case of sodium citrate is unique, because it enables the reduction of Au(III) to Au(0) and its oxidized and decarboxylated form stabilizes the generated nanoparticles.[130,131] In 1951, Turkevich proposed the synthesis of AuNPs by heating an Au(III) salt in aqueous solution containing sodium citrate. Until today this synthesis procedure (Turkevich method) remains one of the most frequently used methods for generating AuNPs.[132] The gold nanoparticles obtained by the Turkevich method are generally spherical and the particles can be tuned to range in size from 10 – 20 nm in diameter.[133] In 1973, the Turkevich method was revised by Frens and co-workers, who reported that the AuNP size range can be expanded (16 – 150 nm) by varying the ratio between the Au(III) salt and the reductant trisodium citrate.[134] Moreover, the authors studied the effect of the concentration of $HAuCl_4$ and sodium citrate on the nucleation and growth phase of AuNPs and found that the final AuNP size depends on the number of nuclei which form and grow into particles.[134] This seminal study was followed by several other publications proposing to improve the quality of the AuNP preparation with regards to size, dispersity and shape of AuNPs.[135–137] In 2007, Kumar and colleagues moreover conducted studies to unravel the reaction mechanism underlying the AuNP formation through citrate reduction.[138,139] The authors proposed a model comprising the following steps: (i) oxidation of citrate yielding dicarboxy acetone (release of CO_2), (ii) reduction of Au(III) to Au(I), (iii) Disproportionation of Au(I) to Au(0) and (iv) assembly of Au(I) on Au(0) nuclei, forming AuNPs stabilized with dicarboxy acetone (simplified synthesis scheme in Figure 11).[131]

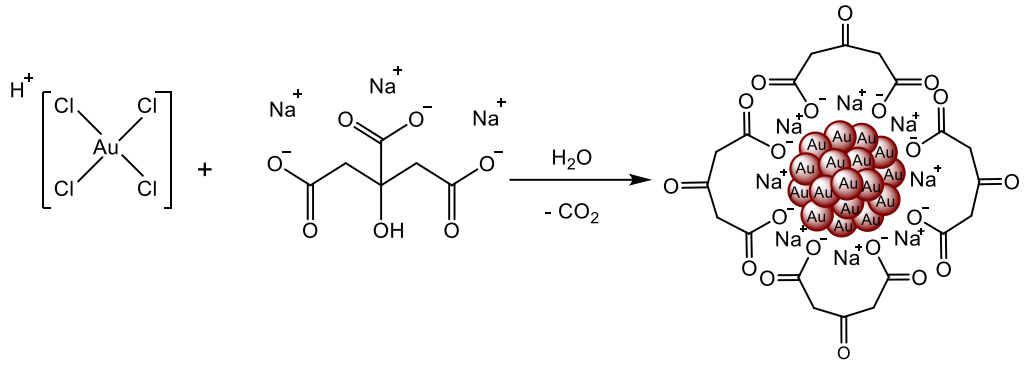

Figure 11. AuNP synthesis according to Turkevich method. Reduction of $HAuCl_4$ with sodium citrate yielding AuNPs stabilized with dicarboxy acetone.[129]

In 1981, Schmid reported the synthesis of a phosphine protected AuNP of 1.4 nm (gold cluster) with the chemical formula $Au_{55}[(C_6H_5)_3P]_{12}Cl_6$.[140] This small-sized cluster was generated by dissolving the Au(I) complex $[(C_6H_5)_3P]AuCl$ in benzol, followed by a reduction with diborane. The produced clusters had a discrete size distribution, but due to the exothermic reaction of diborane with oxygen, the reaction needed to be conducted under anaerobic conditions, making the procedure cumbersome. Moreover, the Au_{55} clusters were insoluble in water. Several years after the initial publication, the authors developed a method to transfer the clusters into the aqueous phase[141] by covering the phosphine protected gold clusters, being dispersed in dichloromethane, with an aqueous solution of mono-sulfonated triphenyl phosphine. This bi-phasic solution was then stirred for three days, resulting in an equilibrium of the gold clusters between the organic and aqueous phase. In 2000, Weare and Hutchison presented a modified, more convenient version of the Schmid synthesis that can be performed under ambient conditions.[142] The authors employed chloroauric acid as the Au precursor and sodium borohydride for the reduction in the presence of triphenyl phosphine, yielding 1.5 nm gold clusters. The synthesis of phosphine-protected AuNPs was further exploited by several research groups using different Au(0) sources and reducing agents.[143,144] Prominent examples for phosphine-stabilized AuNPs are the 1.4 nm Nanogold and 0.8 nm Undecagold clusters developed by Hainfeld *et al.*, today commercially available at *Nanoprobes* (patent: Hainfeld J. F., Leone R. D., Furuya F. R., Powell R. D., 1994, *Small Organometallic Probes*, 5521289). Nanogold is made from chloro(triphenylphosphine)gold(I), which is reduced by sodiumborohydride. Undecagold is synthesized by mixing Au(I)CN with triaryl phosphine ligands yielding an Au(I)-phosphine complex, which is subsequently reduced with $NaBH_4$.

1.2.1 Thiol-coated methods

The publication of the Brust-Schiffrin two-phase synthesis of thiol-derivatized AuNPs in 1994 was a milestone in the field of AuNP synthesis.[145] The reaction is performed in a solvent mixture of water and toluene and the gold salt ($AuCl_4^-$) is transferred into the organic phase using tetraoctylammonium bromide (TOAB). In the organic phase Au(III) and is then reduced by $NaBH_4$ in the presence of dodecanethiol, leading to alkanethiol-protected AuNPs (synthesis scheme depicted in Figure 12). The obtained spherical nanoparticles have sizes of 1.5 – 5.2 nm, are thermally- and air-stable and display a reduced polydispersity. Furthermore, the ligands of alkanethiol-protected AuNPs can be exchanged with other thiol-containing molecules, allowing for straightforward nanoparticle surface functionalization. One year later, in 1995 Brust and colleagues reported a modified synthesis procedure for preparing stable 2 nm AuNPs using *p*-mercaptophenol as stabilizing ligand in a single phase system with methanol in the presence of acetic acid.[146] Due to the synthetic control over particle size and dispersity, the synthesis of thiol-derivatized AuNPs was exploited by several groups during the last decades and a multitude of modifications was reported.[130,147–149]

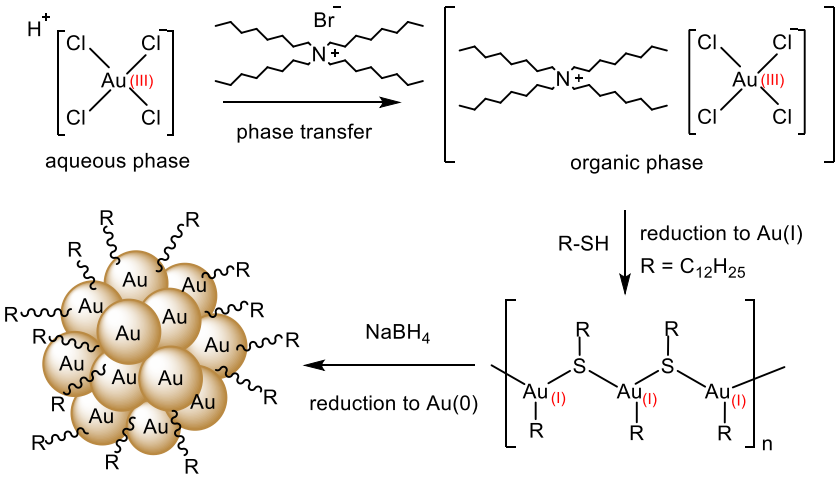

Figure 12. Synthesis scheme of AuNP formation according to Brust synthesis method. 1st step: Phase transfer of $HAuCl_4$ from aqueous to organic phase using tetraoctylammonium bromide. 2nd step: Reduction of Au(III) to Au(I) and formation of Au-S intermediate by coordination of dodecanethiol (R-SH). 3rd step: Reduction of Au(I) to Au(0) by $NaBH_4$ resulting in nucleation and clustering to form AuNPs.

To tighten the size dispersity of thiolated AuNPs soluble in organic solvents, procedures, such as etching,[150] annealing and size-focusing[151] have been reported as effective. In several cases, stable particles displaying exact molecular formulas have been obtained. The occurrence of certain formulas has been attributed to an inherent stability of these AuNPs, which are often referred to as “magic-sized” clusters, and it is widely accepted that their production results from electronic or geometric shell filling.[152] Another but less explored way to tighten the size

dispersity of AuNPs is to optimize the synthesis protocol.[153]. The group of Ackerson conducted substantial work in this field. In a seminal study, Ackerson and coworkers identified 13 organothiolate ligands promoting the synthesis of water-soluble AuNPs following the Brust single phase synthesis in a water/methanol system and deduced minimal ligand requirements.[154] According to their investigation, small and positively charged ligands impede the formation of water-soluble AuNPs, whereas negatively charged organothiolates promote the AuNP production. Mercapto-propionic acid was identified as the smallest negatively charged organothiolate ligand and 3-mercapto-1,2-propanediol was found to be the smallest uncharged organothiolate ligand able to produce stable water-soluble gold particles. In 2010, Ackerson *et al.* reported the synthesis of *p*-mercaptobenzoic acid (*p*-MBA)-protected AuNPs of 2 and 3 nm with discrete size distributions using $HAuCl_4$, *p*-MBA and $NaBH_4$ in a solvent mixture of methanol and water.[149] For identifying reaction conditions yielding homogeneous particle populations, the following parameters were varied: the pH (2 – 13), the *p*-MBA:$HAuCl_4$ ratio (0.5:10 – 10:1) and the proportion of methanol in water (5% – 95%). After an initial screen, reactions were performed at pH 13 using a *p*-MBA/$HAuCl_4$ ratio of 3.4. Interestingly, the methanol/water ratio had the most pronounced impact on the final particles' size. A relative methanol/water concentration of 27% promoted the synthesis of 2 nm particles, whereas a relative concentration of 87% yielded 3 nm AuNPs. Moreover, the authors demonstrated that both *p*-MBA-coated particles could be readily linked to thiolated proteins and thiolated oligonucleotides *via* thiolate-for-thiolate exchange[149] – a straightforward process that was studied in many laboratories.[148,149,155,156] This exchange reaction will be explained in more detail in section 1.3 of Chapter 1. In the meantime, Jadzinsky *et al*. (group of Ackerson) reported the crystallization and X-ray structure determination of a 1.3 nm *p*-MBA-protected AuNP revealing the composition of 102 Au atoms and 44 *p*-MBA ligands.[157] Several years later a modified synthetic procedure for preparing this Au_{102}(*p*-MBA)$_{44}$ cluster with increased yield and purity was published by Levi-Kalisman *et al*.[147]

1.2.2 Seed growth method and other classes of gold nanostructures

In contrast to Turkevich and Brust methods, the seed growth technique allows not only the production of spherical AuNPs, but also the generation of particles having other shapes, such as ovals and rods.[130,158] In the first step $HAuCl_4$ is reduced with $NaBH_4$ (strong reductant) to produce Au salts (seeds) and in the second step these seeds are added to a fresh solution of $HAuCl_4$ in the presence of a mild reducing agent (e.g. ascorbic acid). Since the mild reducing

agent reduces Au(III) only in the presence of the formed seeds (catalyst), reduced Au(0) assembles on their surface.

In the late 1990's Halas and colleagues developed the synthesis of core-shell gold particles, due to the predicted tunability of their optical resonance properties through variation in the relative dimensions of core (consisting of silicon dioxide) and shell (consisting of Au).[159] In the first step, small-sized negatively charged AuNPs are adsorbed to the surface of amine-coated silica nanoparticles. In the second step these silica-core AuNPs then serve as seeds for further reduction of $HAuCl_4$ leading to the growth of the AuNP shell.

Gold nanocages are another class of gold nanostructures.[32] Solution-phase techniques for synthesizing these hollow core metal structure have been reported from Xia *et al.*[160] Briefly, a template nanoparticle consisting of another noble metal having a more negative reduction potential than gold (e.g. silver) is added to Au(III) ions. Since the reduction of gold is energetically more favorable, silver atoms of the template will reduce Au(III) to Au(0), resulting in return in the oxidation of Ag(0) to Ag(I). This oxido-reduction leads to the replacement of the template structure, promoting the formation of gold nanocages.

In general, reactions for synthesizing AuNPs involve the use of chemicals, which are hazardous to the environment and humans. In order to overcome this limitation, green method syntheses have been developed. The principle of this type of syntheses is based on using phytoconstituents present in plants and microorganisms (e.g. bacteria, yeast, fungi) for the reduction of gold salts and stabilization of the nanoparticle.[1] Apart from their environmental friendliness, green method syntheses are generally rapid and technically simple to perform. However, the control over shape and size uniformity is not yet optimized for most of the synthesis protocols and consequently, these types of AuNPs are at the current stage not adapted for the generation of novel immunogold probes that should be as precise and characterizable as possible.

1.3 Functionalization and passivation of gold nanoparticles

The high affinity of AuNP surfaces for various electron-donating groups has led to the development of different AuNP passivation and functionalization methods.[161] For accuracy, we defined the words stabilization, passivation and functionalization in here as follows.

Stabilization is the surface coverage of AuNPs allowing the suspension of the nanoparticles in solution. This process is classically accomplished by electrostatic

repulsions using charged ligands. Often, certain ligands are privileged over others because they consistently promote the formation of the desired AuNPs. However, these ligands might not be suited for a specific application, or for the dispersion of the AuNPs in a certain buffer. It is a well-known fact that most AuNPs get immediately covered with proteins when added to biological fluids containing cells, proteins and solutes (e.g. serum, blood) driven by electrostatic, hydrophobic and van der Waals forces.[4] This coverage of the AuNP surface is referred to as protein corona, which strongly influences the behavior and fate of the nanoparticles, and is not prevented by the stabilization of AuNPs.

Passivation is the process of exchanging the initial (stabilizing) ligands of the AuNP for less reactive molecules that (i) have an increased binding strength to the nanoparticle surface and (ii) do not contain reactive terminal groups. The passivated nanoparticles hence display minimized unwanted ligand substitution and if the passivation agent was chosen appropriately, the formation of protein corona onto the AuNPs upon contact with biological fluids can be limited effectively. Early work employing Brust synthesis has revealed that linear alkane chains of minimum five C-atoms must be used to significantly hamper access of external thiolates to the coordinated ones in aqueous solution.[154,161] Besides, ligands with multiple denticity as well as the pentapeptide CALNN demonstrated efficiency for passivation.

Functionalization is the addition of a molecule or entity to the AuNP's surface to confer a novel activity/function to the system. Importantly, since the thickness, as well as type of protein corona is largely dictated by the surface chemistry of AuNPs,[5] it is of uttermost importance to carefully chose both, the functionalization and passivation agent for AuNPs that will be employed for biological applications, herewith including immuno-EM probes.

Most AuNP synthesis procedures directly yield stabilized nanoparticles, since the stabilizing ligands are mixed with the educts and the resulting stabilizing layer is formed during the nanoparticle formation. Passivation and functionalization of AuNPs are usually performed post-synthetically and involve the formation of a tightly bound surface layer of organic molecules *via* adsorption, or coordination. In the latter case molecules containing thiol-, amine-, phosphine-, silica- and carboxy-terminated groups are coordinated to Au(I) present on the surface of the nanoparticles.[128] According to the Pearson's HSAB (Hard and Soft Acids and Bases) concept, the binding strength of the ligands to Au(I) follows the order O < N < P < S.[162]

The Au-S coordination bond strength is estimated at 210 kJ/mol, corresponding to 2.07 eV.[163] In the literature this bond is often referred to as "quasi covalent", since the coordination of sulfur to gold is almost as strong as a covalent linkage.[164] Accordingly, O- or N-containing AuNP ligands readily exchange with thiolates, which are the most widely used ligands for passivation and functionalization. Phosphines displaying a lower binding energy to AuNPs than thiolates are also commonly used as ligands for the particle's surface coating, typically in the form of aryl phosphines, as their bulkiness provides extra stability to the nanoparticles. Although the Au-N bond is by far less stable than Au-S, amine-capped AuNPs can find some usefulness as sensors as they are pH-sensitive and tend to aggregate upon pH fluctuation.[128] Interestingly, it is also possible to perform a thiolate-for-thiolate exchange on the surface of thiolate-coordinated AuNPs *via* an associative S_N2 like mechanism.[165,166] Important to note, the exchange kinetics of AuNP-coordinated thiolate ligands are determined by (i) their electron withdrawing/electron donating groups and (ii) the location on the AuNP surface. It has been demonstrated that AuNP ligands with electron withdrawing groups have a higher reaction rate (i.e. exchange faster with incoming thiolates), than AuNP ligands with electron donating groups.[165,167] Concerning the surface location, AuNPs offer different ligand binding sites (edges, vertexes and terraces), which differ in electron density and steric accessibility and consequently ligands at different surface sites are differently prone to thiolate-for-thiolate exchanges.[166]

An alternative approach to the post-synthetic passivation and functionalization is to tune the AuNP surface coating from the beginning of the synthesis by exchanging the stabilizing ligands present in the reaction mixture with passivation agents, drugs, or other functional ligands.[1,128] A well-known possibility is the reduction of Au(III) with $NaBH_4$ in the presence of thiolated functional molecules, yielding AuNPs coated with the respective functional ligands. A less traditional and more unique approach is the concerted reduction, stabilization and functionalization of AuNPs by using bio-active molecules accomplishing all these tasks in a one-pot reaction. In 2004, Pal *et al.* reported for the first time the synthesis of dopamine-capped AuNPs (0.5 – 3 nm) by reducing Au(III) to Au(0) with dopamine, an important neurotransmitter, without the use of any other reduction or stabilization agents.[168] This concept of dopamine reduction was extended by Gulsuner and coworkers, who reported the generation of AuNPs functionalized with dopamine-containing multidomain peptides (MDPs) in a single step reaction by simply mixing the MDPs with auric acid.[169] The MDPs used in this study were composed of a unit containing dopamine, a linker site and a domain with the amino acid sequence RGD permitting binding to $\alpha_v\beta_3$ integrin present on many types of cancer cells.

Moreover, the preparation of AuNPs using biopolymers, such as chitosan, dextran and glucose have been reported either with, or without additional reducing agents.[170]

Altogether, substitution and tuning of AuNP ligands enables the preparation of a multitude of AuNPs having mixed monolayers of O-, N-, P- or S-coordinated functional molecules, such as organic dyes,[128] biomolecules and drugs.[28,128,171] If required, secondary modifications of the O-, N-, P- or S-coordinated ligands can be accomplished by different strategies including chemical coupling, polymerization, electrostatic interactions and selective intermolecular interactions.[128] Among these methods chemical coupling and polymerization are most commonly used. In case of chemical coupling, AuNPs are generally functionalized with carboxylate-terminated or hydroxyl groups, hence permitting carbodiimide chemistry or esterification (schematic illustration of mixed monolayer formation *via* chemical coupling in Figure 13).

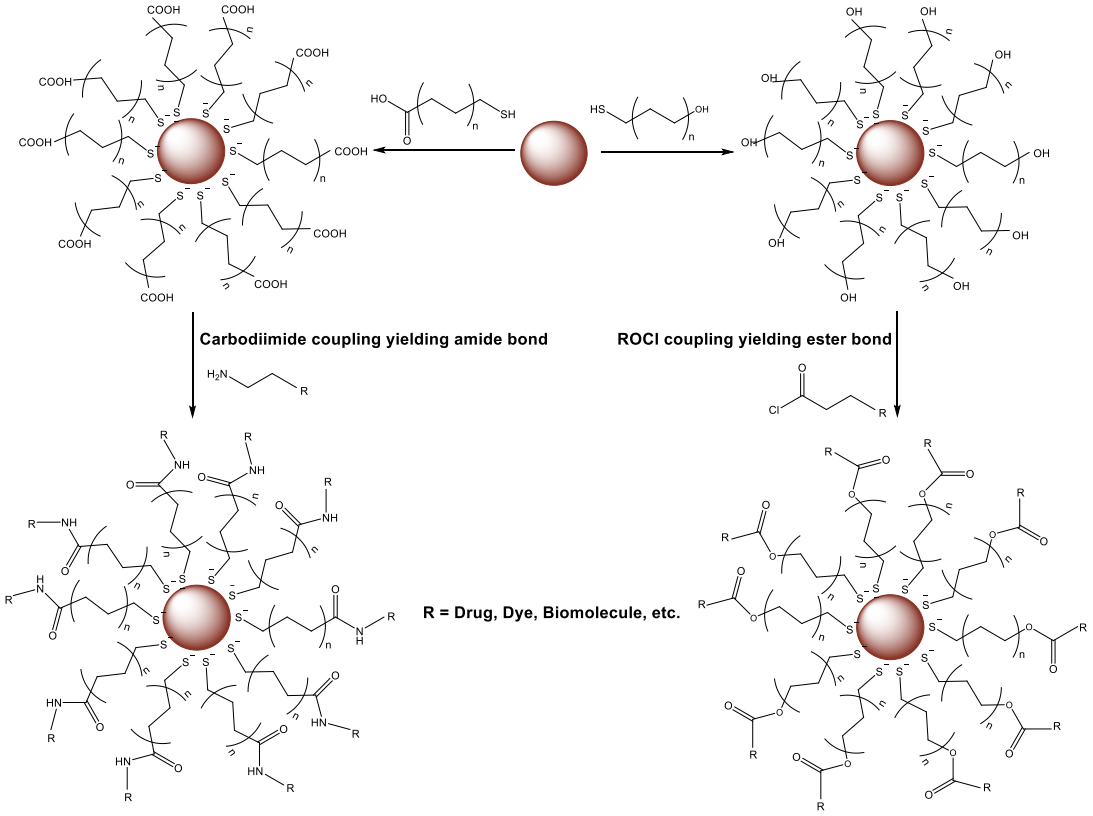

Figure 13. Mixed monolayer formation of AuNPs *via* chemical coupling. Functionalization with carboxylate group (on the left) allowing for carbodiimide coupling and functionalization with hydroxyl group (on the right) permitting esterification with acyl chloride.

The use of polymers for AuNP surface modifications is very popular, as polymers provide steric hindrance and furtivity.[128] Examples of polymers commonly used for improving the stability of AuNPs in biological fluids are polyethylene glycol, poly(N-vinylpyrrolidone), poly(vinyl

alcohol) and poly(methyl methacrylate). In order to equip AuNPs with polymers three procedures have been developed: (i) the grafting-from technique, (ii) the grafting-to technique and (iii) post-synthetic modifications (illustration of the three techniques in Figure 14).[128] During the grafting-from technique polymer chains are grown from scaffolds that are covalently linked to the AuNP. This method, which mainly uses alkylthiol-passivated AuNPs as precursor, allows control over the thickness, density and structure of the polymer layer. Moreover, the generated AuNPs are very robust.[172] Using the grafting-to technique AuNP cores are synthesized in polymer aggregates.[128] The advantage of this method is the compatibility of numerous polymers with this procedure, as well as the simple preparation *via* one-pot synthesis. The polymers that are used for grafting-to techniques either possess, or do not possess a terminal sulfhydryl group.[173,174] The third method used for equipping AuNPs with polymers, the post-synthetic modification technique is either performed like a classical passivation of AuNPs using thiolated polymers to exchange with stabilizing ligands on the AuNP surface, or by simple adsorption of non-thiol containing polymers.[128]

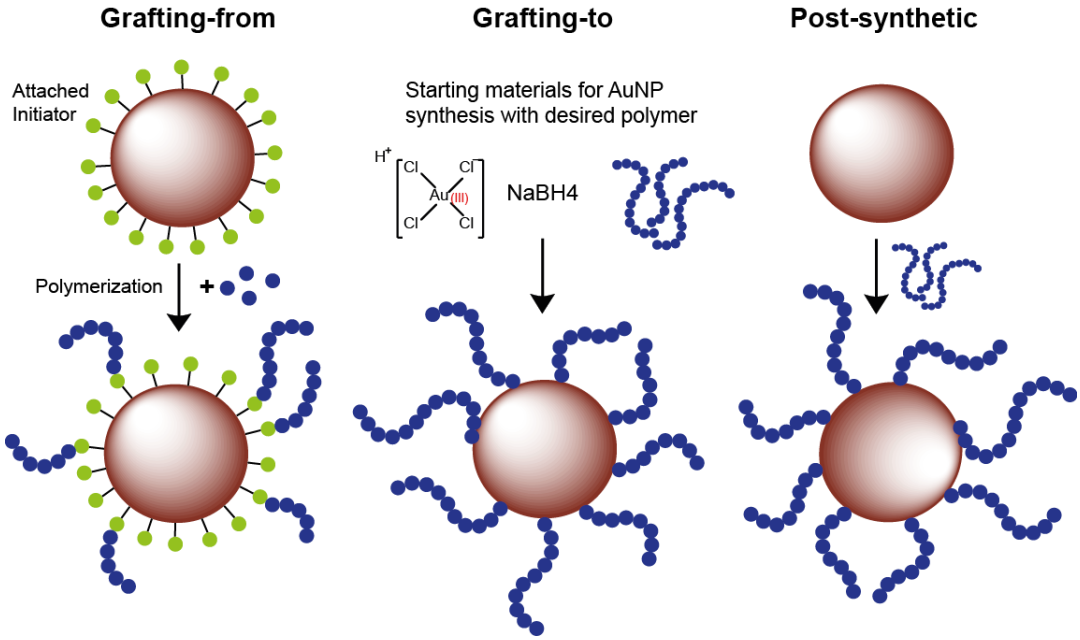

Figure 14. Schematic illustration of the three procedures for equipping AuNPs with polymers: Grafting-from technique (left), Grafting-to technique (middle) and Post-synthetic modification (right).

A completely different but effective possibility for preventing unspecific interactions between AuNPs and proteins, as well as nanoparticle aggregation is the growth of a thin silica layer around the AuNP core. This surface modification is usually performed following the Stöber method using alkylsilicates.[175] Modern methods commonly apply tetraethyl orthosilicate

(TEOS), which gets hydrolyzed, followed by the condensation of silicic acid and the deposition of a silica layer on the AuNP surface. TEOS is dissolved in a mixture of water and ethanol and by varying the water/ethanol ratio the thickness of the silica shell can be controlled.[163] Moreover, the silica shell can be made of amino-, mercapto- and carboxy-terminated silanes to allow for secondary surface modifications.[128]

Taken together, there is a vast number of methods for generating spherical AuNPs of different sizes and for equipping them with organic shells allowing the preparation of functionalized nanomaterials with properties almost at will. Our aim was to make immunogold probes for labeling selected molecules within a living cell. Since the AuNP domain is of uttermost importance for the diffusion ability of the probe inside cells, the AuNP has to be carefully selected and designed. The mercaptobenzoic acid-coated AuNPs[147,148,149,176] appeared particularly suited for our purpose, due to their size-tunability, solubility in water and possibility to be functionalized with various thiolated biomolecules.

Before my arrival, my laboratory underwent preparation of mercaptobenzoic acid-coated AuNPs and discovered that the Ellman's reagent (the 2,2′-dinitro-5,5′-dithiobenzoic acid (DTNB)) can be advantageous for the synthesis of intracellularly-compatible organothiolate-protected AuNPs counting ca. 102 gold atoms (named AuZ).[155] Comprehensive investigation of AuZ showed that the AuNP was not only covered with thionitrobenzoate (TNB) but also contained thioaminobenzoate (TAB), which are incidental reduction products of DTNB. This mixed coverage offers two main advantages. Firstly, the electron withdrawing properties of the TNB's nitro group speed up the ligand exchange with other thiol-containing molecules. Secondly, TAB is zwitterionic at neutral pH and this property has been reported to favor aqueous solubility and colloidal stability of nanoparticles,[177] as well as to prevent unspecific interactions with biomolecules.[178]

In a first step towards application of these AuNPs for EM probes, it was demonstrated that AuZ equipped with nuclear localization sequence (NLS) or nuclear export signal (NES) peptides can be delivered into the cytosol of living cells, where the AuZ-NLS or AuZ-NES were shown to be taken in charge by the NLS and NES specific cellular machineries.[155] Having demonstrated that AuZ is biocompatible inside cells (following delivery), we aimed at optimizing AuZ for EM labeling. For that purpose, the size of AuZ needed to be increased at a first stage, in order to facilitate direct detection of the nanoparticle inside living cells by EM, not relying on silver enhancement. Moreover, it was of uttermost importance to carefully investigate the impact of

different surface coatings on the physicochemical properties of the AuNPs, since an increased nanoparticle size not only increases the opacity to electrons, but also the interaction with biological compounds. It is important to clarify that the work presented in here is not aimed at developing fluorescent AuNPs. Fluorescent AuNPs are usually below 2 nm in diameter and consist of a core counting only a few Au(0) atoms that is surrounded by Au(I),[179] thus likely do not provide enough opacity to electrons when embedded in the cellular ultrastructure, making them poorly suitable as immunogold labels. Considering the advent of correlative light and electron microscopy (CLEM), it would obviously be highly desirable to generate a fluorescent AuNP that can be imaged by EM as well, but due the ultrasmall size of fluorescent gold clusters, we did not pursue this objective in this project.

2 Materials and Methods

2.1 Materials

Centrifugation of 50 ml tubes was performed in an Eppendorf 5810 R centrifuge equipped with an A-4-81 rotor. Smaller volumes (0.2–2ml) were centrifuged using an Eppendorf 5415 R centrifuge. A HI 2210 pH meter was used for measuring the pH of solutions. Gold reaction solutions were mixed using a Heidolph Rotamax 120 rocking platform. Passivated and functionalized AuNPs were separated from low MW compounds and concentrated using Amicon Ultra 0.5ml centrifugal filter devices (MWCO 10 kDa) if not stated otherwise. UV–Vis spectroscopy was carried out on a Varian Cary 100Bio spectrometer.

2.2 Chemicals

Chemicals were purchased from Sigma Aldrich, Carl Roth, Iris Biotech, VWR Chemicals and Honeywell, and used without further purification unless stated otherwise. Peptides were obtained from GeneCust and alpha-Methoxy-omega-mercapto poly(ethylene glycol) 2000 Da was ordered from Iris Biotech. Glutaraldehyde (25% solution) was of electron microscopy grade purchased from Electron Microscopy Sciences. Solutions and buffers were made with water purified with a Millipore Q-POD apparatus. For SDS-PAGE analysis Precision Plus Protein Standard Dual Xtra (BioRad) was used as protein ladder.

2.3 AuNP syntheses

A 0.4 M solution of $HAuCl_4*3H_2O$ (90 µL, 36 µmol) was added to 10.8 mL of a mixture of double-distilled water and an organic solvent (nature and amount of solvent varied for tuning AuNP size as described in results section 3.1.2 and section 3.1.3 of Chapter 1). The mixture was vigorously stirred and 50 mM DTNB (5,5'-dithionitrobenzoic acid) in 0.3 M NaOH was added (volume of DTNB solution varied for tuning AuNP size). The reaction mixture was stirred at RT for at least 6 h before a freshly prepared 0.75 M $NaBH_4$ (240 µL, 180 µmol) was added for reducing the gold ions and inducing the formation of the nanoparticles. The addition of $NaBH_4$ resulted dependent on the reaction conditions (type of solvent, amount of DTNB) either in an immediate color change of the yellow-orange solution to a black colored solution, or in a progressive change of color taking up to 10 min. The reaction mixture was stirred overnight at RT and the next day the AuNPs were recovered by centrifugation, if the AuNPs

precipitated during the overnight stirring (typically AuNP of diameters > 1.4 nm). If AuNPs remained in solution (e.g. particle of about 1.4 nm), precipitation of the AuNPs was promoted the next day by addition of 2 M sodium acetate (1.2 mL, 2.4 mmol), excess methanol and incubation at -20°C. The solid nanoparticles were separated from remaining educts and reduced DTNB by re-suspension in methanol and subsequent precipitation, before being dried as a black powder. For further reactions and characterization, the powder was dissolved in double-distilled water and stored at 4°C.

2.4 AuNP concentration determination

Concentrations of AuNPs were determined spectrophotometrically by measuring the absorbance at 520 nm. The extinction coefficient of the AuNP was determined from the formula $\ln(\varepsilon) = k \cdot \ln(D) + a$, reported from Liu *et al.*[180](ε = extinction coefficient, D = AuNP core diameter, k= 3.32111, a = 10,80505).

2.5 Reactions of AuNPs with passive and bioactive ligands

42 µM AuNP solutions were reacted with thiol-containing molecules (cysteine, glutathione, thiolated NLS peptide [CALNNGAGPKKKRKVED], peptide Cap [CALNNG] and alpha-methoxy-omega-mercapto poly(ethylene glycol) (HS-PEG-OCH_3 MW = 2015 g/mol, HS-PEG-OCH_3 = 300 g/mol). Thiolated molecules were freshly dissolved in 100 mM HEPES buffer pH 7.4 to yield concentrations between 0.5 – 10 mM, depending on the desired surface coverage and size of AuNP, and quickly mixed with the AuNP solutions (volume of AuNP and thiol solutions depending on scale of reaction). For complete exchange of the AuNP-coordinated ligands, 50 eq. of thiolated molecule were added to 1.4 nm AuNPs, 80 eq. were added to 2.4 nm AuNPs and 100 eq. were added to 2.6 nm AuNPs. The thiolate exchange reactions were performed at 25°C overnight. The next day the surface decorated particles were analyzed by SDS-PAGE and removed from the exchanged TNB-/TAB-ligands, as well as excess thiol-containing molecules using Amicon Ultra centrifugal filter devices.

2.6 Cell culture

HeLa cells (ATCC CCL2) were cultured in a humidified incubator at 37°C supplied with 5%CO_2 and maintained in Dulbecco's modified eagle medium containing 2 mM L-glutamine,

10 mM HEPES buffer, pH 7.0, 10% heat-inactivated fetal bovine serum (FBS) and 50 µg/mL gentamycin.

2.7 Electroporation

AuNP solutions were transduced into HeLa cells according to a published protocol using the Neon transfection system (3 ms pulses at 1550 V).[181] For each transduction 10^5 cells suspended in 11 µL PBS were mixed with 1 µL of a 80 µM AuNP solution (80 pmol). Electroporated cells were diluted in pre-warmed cell culture medium not containing antibiotics and harvested by centrifugation. Then, cells were again diluted in cell culture medium not containing antibiotics and led to adhere on glass coverslips of 24-well plates overnight and analyzed the following day by optical microscopy.

SDS-PAGE analysis of AuNPs, mass spectrometry, FT-IR analysis, high-angle annular dark-field scanning transmission electron microscopy (HAADF-STEM), EDX analysis and preparation of cell specimens for AuNP detection by optical microscopy were performed as described in Groysbeck *et al.* 2019 attached to the thesis in the appendix.[156]

3 Results

3.1 Synthesis of gold nanoparticles of variable sizes

Inspired by the work of Ackerson and Kornberg,[147,148,154,157] demonstrating that MBA-protected AuNPs can be directly synthesized with tight size distribution, functionalized with organic ligands and might prove useful as anchoring platform,[182] as well as imaging probes,[127] our laboratory developed a novel type of organothiolate-protected AuNPs counting ca. 102 gold atoms with a diameter of 1.4 nm (named AuZ) by reducing $HAuCl_4$ with $NaBH_4$ in the presence of DTNB.[155] DTNB was chosen as the stabilizing agent, as its reduced forms TNB and TAB were expected to offer a twofold advantage: (i) TNB represents a good leaving group and therefore makes the nanoparticle reactive towards thiolated molecules, (ii) TAB is a zwitterionic molecule, which has been reported to promote aqueous stability and inertness of AuNPs in biological media. The synthesis of the 102 atoms AuNPs was accomplished in a 47% aqueous solution of methanol using $HAuCl_4$ and DTNB at a ratio of 1:1.5 and 3 eq. of $NaBH_4$ based on the number of moles of $HAuCl_4$ (schematic illustration of the AuNP synthesis strategy is depicted in Figure 15). In an initial stage of the project, the effect of using different amounts of $NaBH_4$ on the reduction and reproducibility of the 102 atoms AuNPs was evaluated. Then, the reaction conditions were systematically varied to generate monodispersed AuNPs having the same type of surface coating but a larger diameter for providing increased opacity to electrons. Based on the study of Wong *et al.*, who showed that the type and concentration of water-miscible solvents influences the size, as well as polydispersity of thiolate-protected AuNPs,[152] we screened different solvent/water mixtures for the AuNP synthesis. Thereafter, we varied the thiol/Au ratio, as it is widely accepted that this parameter influences the core size of the generated AuNP as well.[183,184]

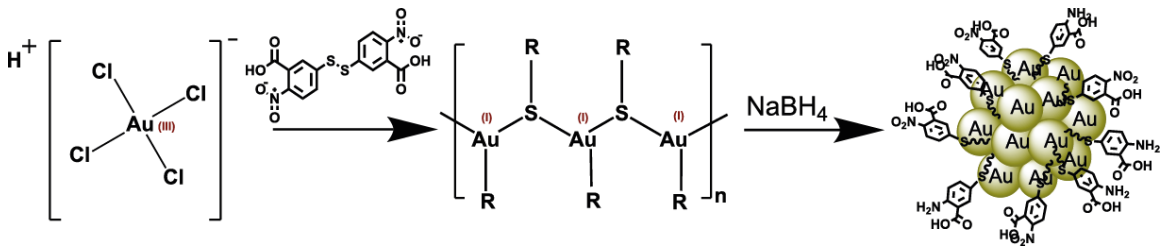

Figure 15. Synthesis strategy for generating TAB-/ TNB-protected AuNPs by reducing $HAuCl_4$ in the presence of DTNB with $NaBH_4$.

3.1.1 Impact of $NaBH_4$ reduction on polydispersity of 1.4 nm AuNP

Briefly, the 1.4 nm AuNPs (AuZ composed of circa 102 gold atoms) were produced by rapidly mixing $HAuCl_4$ with DTNB in 47% methanol/water (6 h of vigorous agitation) followed by addition of different amounts of $NaBH_4$, as a freshly prepared aqueous solution (3, 5 and 10 eq. of $NaBH_4$ relative to $HAuCl_4$).[155] After precipitation of the generated AuNPs, the nanoparticles were analyzed by SDS-PAGE (Figure 16 (a)). The results revealed that the use of 5 eq. $NaBH_4$ led to highest degree of monodispersity, as can be seen from the appearance of only one discrete band on the SDS gel in lane 2. The use of 3 eq. $NaBH_4$ led to the production of the same type of nanoparticle, but the reaction product additionally contained a larger AuNP species, as can be seen from the additional faint band in lane 1 (Figure 16 (a)) having a lower electrophoretic mobility. The use of 10 eq. $NaBH_4$ led to a mixture of AuNP species with smaller size and higher polydispersity compared to the published 102 atoms AuNP. Based on these results, the use of 5 eq. $NaBH_4$ was from then on implemented in the synthesis of the 1.4 nm AuNP, AuZ. Since $NaBH_4$ hydrolyzes in water ($NaBH_4 + 2\ H_2O \rightarrow NaBO_2 + 4\ H_2\uparrow$) and the effective concentration of $NaBH_4$ might vary dependent on the speed of adding the $NaBH_4$, freshly dissolved in water, we tested whether the addition of $NaBH_4$ (5 eq.) as powder alters the nanoparticle formation. Figure 16 (b) shows the SDS-PAGE analysis of the 1.4 nm AuNPs generated by adding 5 eq. $NaBH_4$ as aqueous solution (lane 1) and as powder (lane 2). It can be noted that there is no significant difference in the size and polydispersity of the AuNPs and it was concluded that by rapidly adding the freshly dissolved $NaBH_4$ solution, the rate of hydrolysis is not sufficiently high to result in a remarkable effect.

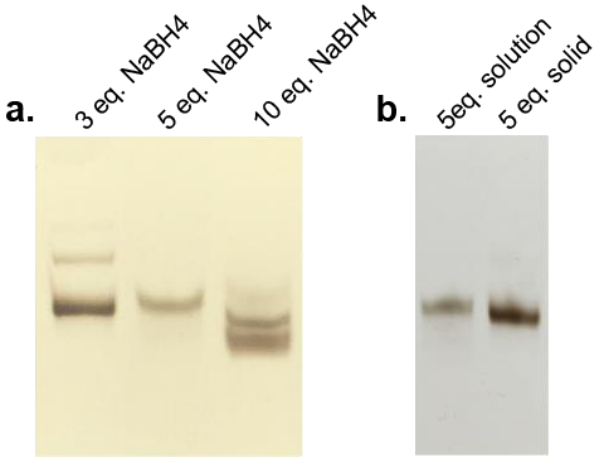

Figure 16. SDS-PAGE analysis of 1.4 nm AuZ analogues synthesized by modifying the reduction using $NaBH_4$. (a) Different equivalents of $NaBH_4$ added to the reaction mixture (eq. based on the number of moles of $HAuCl_4$); (b) 5 equivalents of $NaBH_4$ added to the reaction mixture as aqueous solution (left) and as solid (right).

3.1.2 Impact of water-miscible solvents on AuNP size

As it was demonstrated that the type of solvent or solvent mixture used throughout the synthesis of AuNPs largely impacts the nanoparticle size, we performed the synthesis of AuNPs in the following water miscible solvents at the indicated concentration in water: methanol (40% and 60%), ethanol (60% and 70%), n-propanol (30%, 40% and 50%), 2-propanol (50%, 56%, 60%, 70% and 80%), n-butanol (20%, 35%, 50% and 70%), acetonitrile (80%), dioxane (50% and 60%) and tetrahydrofuran (40%). Out of the tested conditions the reaction in 40% methanol and 40% n-propanol led to particles having the same electrophoretic mobility and nearly the same polydispersity as the 1.4 nm AuZ (Figure 17 (a)) and the reaction in 80% acetonitrile and 80% 2-propanol resulted in monodispersed AuNPs having a lower electrophoretic mobility than AuZ, suggesting an increased size of the generated nanoparticles (Figure 17 (b)).

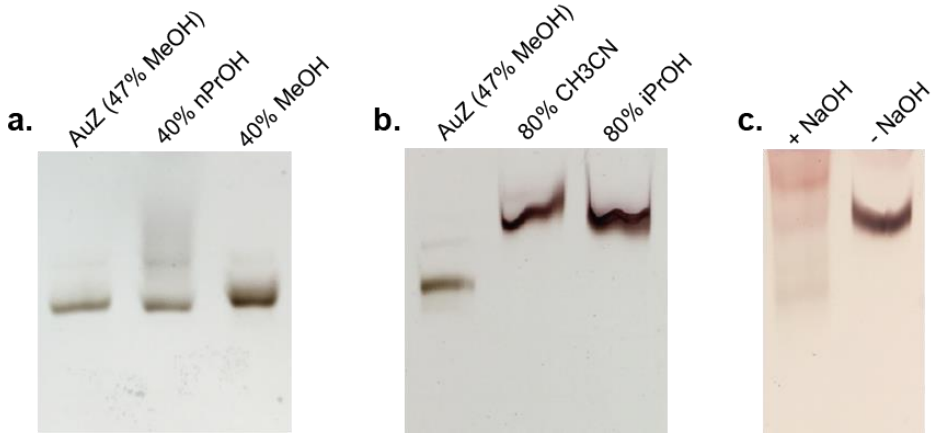

Figure 17. SDS-PAGE analysis of AuNPs generated in different organic solvent/water mixtures following the synthesis protocol that was established for the 1.4 nm AuZ. (a) From left to right: AuNPs produced in 47% methanol (AuZ as control), 40% n-propanol (nPrOH) and 40% methanol (MeOH); (b) From left to right: AuNPs produced in 47% methanol (AuZ as control), 80% acetonitrile (CH_3CN) and 80% 2-propanol (iPrOH); (c) From left to right: AuNPs produced in 80%CH_3CN with addition of NaOH, AuNPs produced in 80%CH_3CN without addition of NaOH.

In both cases (AuNPs of 1.4 nm and AuNPs > 1.4 nm) the solvent/water ratio seems to be a determining factor for the formation of discrete particles independent of the type of solvent. During the AuNP syntheses using 80% acetonitrile and 80% 2-propanol the addition of DTNB to the $HAuCl_4$ solution caused the formation of a white precipitate, which could be resuspended by adding 10 M sodium hydroxide (0.5 mL, 5 mmol). We assumed that the precipitation was due to an insufficient stabilization of the Au(I)-S intermediate in the solvent mixture and that the addition of the base (leading to the deprotonation of the COOH moiety of the reduced TNB- / TAB-ligands) resulted in electrostatic repulsions between the Au(I)-coordinated organothiolates, thus re-dissolving the intermediate again. Interestingly, the monodispersed AuNPs > 1.4 nm (shown in Figure 17 (b)) were only obtained when the formed precipitate was

not re-dissolved by addition of sodium hydroxide (SDS-PAGE of AuNPs produced in 80% acetonitrile with and without addition of NaOH in Figure 17(c)). The AuNP synthesis in 80% acetonitrile was reproduced several times, during which only marginal batch to batch alterations regarding the dispersity of the nanoparticles were observed and this type of AuNP, supposedly having a larger diameter as AuZ, is hereafter referred to as AuG. Apart from the mentioned co-solvent systems (80% acetonitrile, 80% 2-propanol, 40% methanol and 40%, n-propanol), the other solvent/water mixtures that were tested did not produce particles that migrate as discrete bands into polyacrylamide gels and were therefore not further pursued.

3.1.3 Impact of $HAuCl_4$/DTNB ratio on AuNP size

Next, the influence of the ratio between the gold complex $HAuCl_4$ and the organothiolate ligand DTNB on the size, as well as polydispersity of the AuNPs was investigated with the aim to identify a reaction condition that allows the production of nanoparticles being larger than AuG. All reactions (independent of the $HAuCl_4$/DTNB ratio) were performed in 80% acetonitrile/water and 47% methanol/water in parallel, according to the initially described procedure in terms of reaction time and reduction conditions. The ratios of DTNB/$HAuCl_4$were set at 2, 3, 4, 5, 6 and 7. Among these six ratios, each performed in the two solvent mixtures, only the DTNB/$HAuCl_4$ ratio of 4 performed in 80% acetonitrile resulted in the generation of monodispersed AuNPs having a lower electrophoretic mobility, thus larger particle diameter than AuG. Figure 18 shows the SDS-PAGE analysis of the new AuNP, hereafter referred to as AuL, produced in 80% acetonitrile using a $HAuCl_4$/DTNB ratio of 1:4 compared to the electrophoretic mobility of AuZ and AuG.

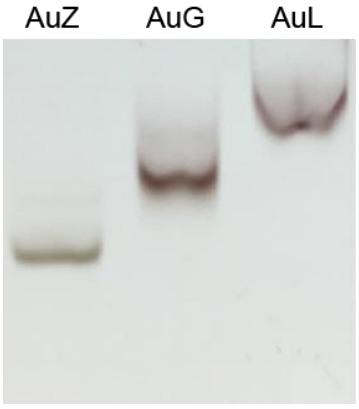

Figure 18. SDS-PAGE analysis of the AuL synthesized in 80% acetonitrile using a DTNB/$HAuCl_4$ ratio of 4, compared to AuZ and AuG.

When the amount of DTNB was further increased (DTNB/$HAuCl_4$ ratio > 4) no particles could be precipitated from the solution in most of the cases. For the remaining conditions tested the degree of polydispersity was not satisfying and comparable with the one of AuZ, AuG and AuL and therefore we did not further pursue these reactions. The synthetic procedures of AuL, was reproducible and the nanoparticles could be prepared in high quantity, as it was the case for AuZ and AuG.

3.2 Characterization of the gold particles AuZ, AuG and AuL

To further characterize the two novel organothiolate-protected AuG and AuL and to confirm whether AuZ generated with increased amounts of $NaBH_4$ displays the same characteristics as the previously published AuZ,[155] we analyzed the nanoparticles by HAADF-STEM, MALDI-TOF mass spectrometry and UV-Vis spectroscopy. AuG was moreover characterized for its elemental composition by EDX analysis.

The HAADF-STEM analysis of the AuNPs revealed that the particle populations are homogeneous and have a spherical shape (HAADF-STEM images depicted in Figure 19) with a diameter of 1.4 nm ± 0.35 for AuZ (n = 40), 2.4 nm ± 0.28 for AuG (n = 61)and 2.6 nm ± 0.99 (n = 58) for AuL. The particle diameters of AuZ, AuG and AuL were in agreement with our hypothesis that the electrophoretic mobility of particles on SDS gels is inverse to the particle size. The high-resolution image of AuG (inset image in Figure 19) shows a crystalline lattice, which confirms that the AuNP's core is composed of metallic Au(0).

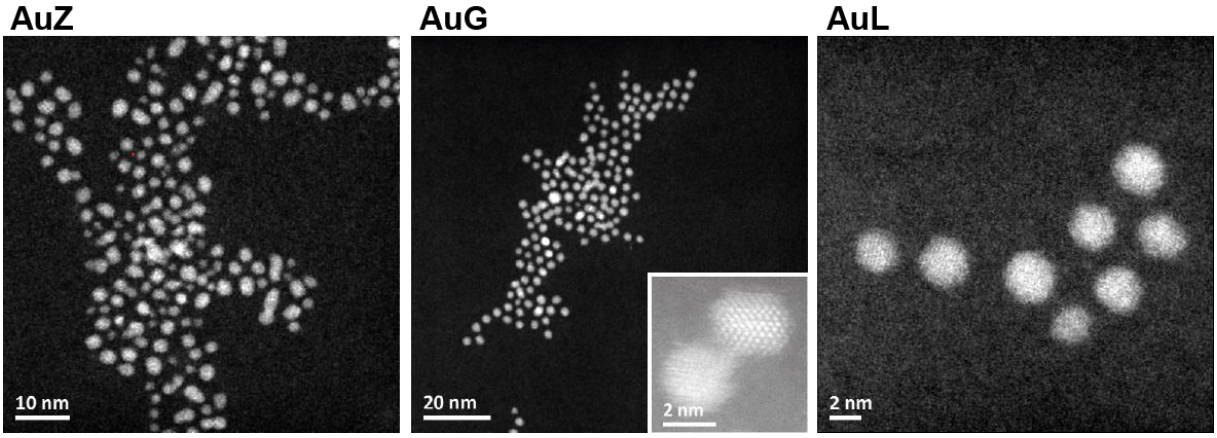

Figure 19. HAADF-STEM images of organothiolate-protected AuNPs AuZ (1.4 nm), AuG (2.4 nm) and AuL (2.6 nm) reveal that each nanoparticle population consist of spherical particles, which are homogenous with regards to size distribution. The inset image in right corner in the middle image shows AuG at higher magnification, displaying the crystalline lattice of the metallic (Au(0)) core. Scale bar for AuZ: 10 nm, scale bar for AuG: 20 nm, scale bar for AuG at higher magnification (inset image): 2 nm, scale bar for AuL: 2 nm.

Next, the molecular weight (MW) of the three AuNPs was evaluated by mass spectrometry (MS). The MS analyses of the three AuNPs revealed an average MW of 21 kDa for AuZ, 80 kDa for AuG and 99 kDa for AuL, confirming the size proportions between the three AuNPs assessed from SDS-PAGE and HAADF-STEM (mass spectra depicted in Figure 20 (a)). Regarding AuZ, it must be noted that the determined MW of 21 kDa matches with the one of the 1.4 nm AuNP recently published,[155] revealing that the altered $NaBH_4$ reduction conditions did not impact the AuNP size. By comparing the mass spectra of AuZ, AuG and AuL it is obvious that the background signals increase with increasing particle diameter. Taking the STEM images and particle bands on SDS gels into account, it is unlikely that the high background signals in the mass spectra of AuG and AuL result from more heterogeneous particle populations, or impurities, but are presumably due to the difficulty in ionizing these heavy particles (laser pulses of high intensity were necessary to get spectra for AuG and AuL).

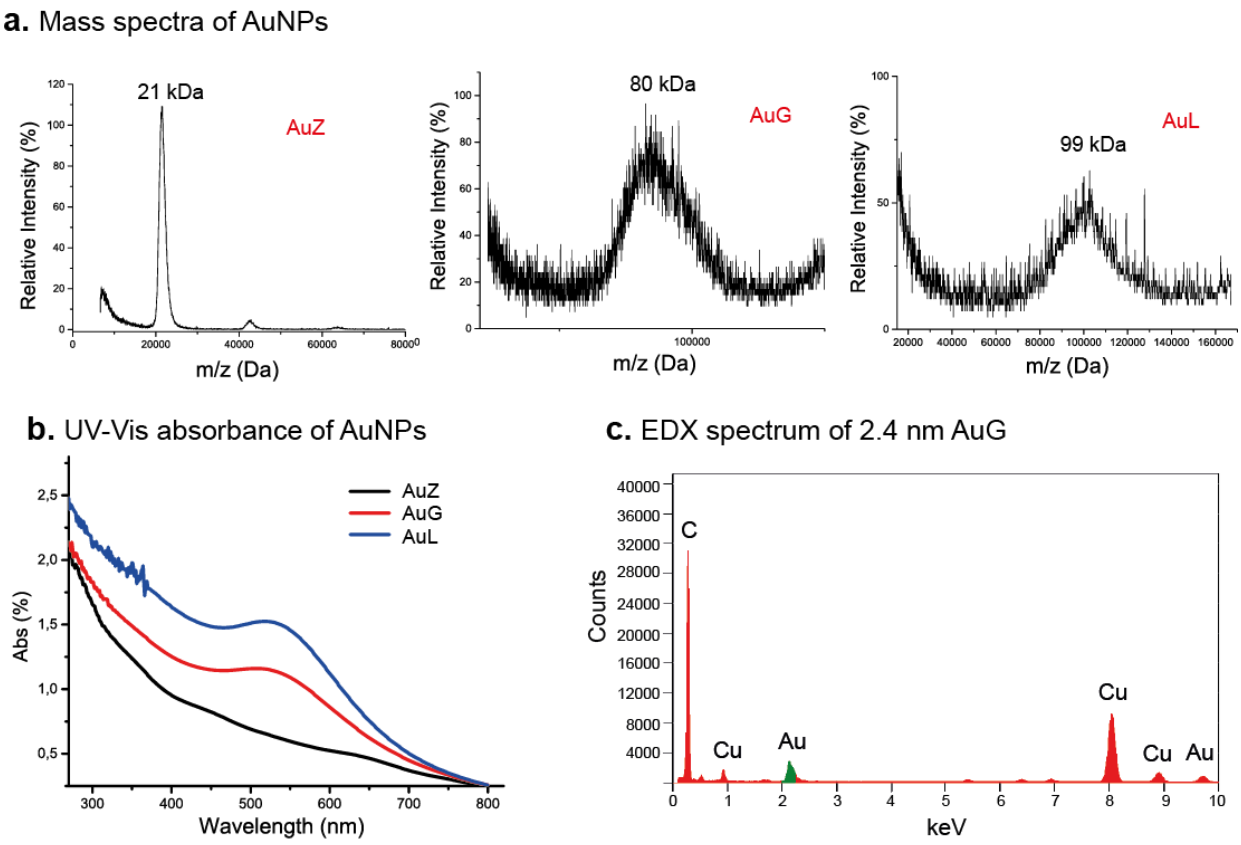

Figure 20. Characterization of AuZ, AuG and AuL by mass spectrometry (a) and UV-Vis spectroscopy (b), as well as elemental analysis of the 2.4 nm AuG by energy dispersive X-ray (EDX) spectroscopy (c). (a) MS analysis reveals a MW of 21 kDa for AuZ, 80 kDa for AuG and 99 kDa for AuL; (b) UV-Vis absorbance demonstrates the absence of any plasmonic properties for AuZ and increasing LSPR peaks for AuG and AuL according to increase in size; (c) EDX spectrum of AuG confirms that the AuNP is composed of gold ($Au_{M\alpha}$ at 2.12 keV; $Au_{L\alpha}$ at 9.712 eV).

Based on the information on nanoparticle diameter, MW and the volumetric density of gold (19.3 g/mL), we estimated that AuG is composed of 420 Au atoms and AuL is composed of 480 Au atoms. We did not precisely determine the number of ligands on the surface of AuL and AuG. However, we estimated them by assuming that the density of ligands on the surface of AuNPs is independent of the AuNP size. Knowing that AuNPs consisting of 102 Au atoms are coated with 44 thiolate ligands,[157] we deduced by a rule of three that AuG and AuL display 130 and 150 ligands, respectively.

To assess whether the absorption (plasmonic/non plasmonic) properties of the three AuNPs correlate with their difference in size, the UV-Vis absorbances of AuZ, AuG and AuL were recorded (Figure 20 (b)). As expected for AuNPs below 2 nm in diameter,[185] the absorbance of AuZ decreases steadily with increasing wavelengths without displaying any LSPR properties (absorption with a maximum between 500 – 600 nm). The UV-Vis spectra of the 2.4 nm AuG and 2.6 nm AuL likewise show a gradually decreasing absorbance with increasing wavelengths, but moreover the spectra display humps with maximum absorbances at 510 nm and 520 nm respectively, demonstrating that these AuNPs have plasmonic properties in accordance with the reported size to LSPR relationship.[77,185]

The elemental analysis of 2.4 nm AuG confirmed that the AuNP consists of gold, as the EDX spectrum (Figure 20 (c)) displays two characteristic peaks of gold ($Au_{M\alpha}$ at 2.12 keV; $Au_{L\alpha}$ at 9.712 eV). The other signals in the spectrum are assigned to carbon and copper ($C_{K\alpha}$ at 0.277 keV, $Cu_{L\alpha}$ at 0.93 keV, $Cu_{K\alpha}$ at 8.04 keV and $Cu_{K\beta}$ at 8.9 eV) belonging to the carbon-coated copper grids onto which the AuNP sample was deposited.

3.3 Functionalization and passivation of gold nanoparticles

To study the reactivity of the organothiolate-protected AuNPs with thiolated molecules (*via* thiolate-for-thiolate exchange), as well as to identify a surface coating that prevents the nanoparticles from unspecific binding to (intra)cellular components, the three AuNPs were reacted with the following thiolated molecules: cysteine, glutathione, thiolated peptide Cap of the sequence [CALNNG], thiolated NLS peptide of the sequence [CALNNGAGPKKKRKVED], as well as thiolated polyethylene glycol (PEG) of high and low MW (PEG 2000 Da and PEG 300 Da). The reason for using these molecules is as follows: Cysteine and glutathione are small natural molecules and glutathione has been used at several occasions to coat AuNPs.[108,148,182] The peptidic sequence [CALNN] was selected from a peptide library for its property to effectively prevent AuNPs from aggregation.[186] For our study we

added an additional glycine to the C-terminus of the peptide leading to the hexapeptide [CALNNG] (referred to as Cap in this thesis). The NLS peptide of sequence [CALNNGAGPKKKRKVED] (fusion of CALNN with the NLS of the SV40 large T antigen)[187] was used to verify that the AuNPs diffuse inside the cytosol, since the NLS-assisted nuclear import cell machinery only shuttles molecules that are in proximity to the nucleus. [188] PEG is well-known to limit the formation of protein corona on AuNPs, to reduce unspecific interactions with cells, as well as to improve the pharmacokinetic profile.[49,189] We hence wanted to investigate, whether the stealth properties of PEG are necessary to render the small-sized AuNPs inert in the presence of biological fluids and cells. Moreover, we wanted to find out whether the polymer length impacts the diffusion properties of the passivated nanoparticles, as the passivation with polymers having different lengths leads to AuNPs with different hydrodynamic diameters

We first assayed the functionalization and passivation of the smallest 1.4 nm AuNP with the NLS peptide, as we assumed that the size and positive charge of the peptide (17 amino acids, five of them being cationic, MW approximately 2000 Da) facilitate distinguishing the unmodified AuZ from AuZ linked to NLSs by SDS-PAGE. It is important to bear in mind that the modification of the AuNP surface occurs *via* thiolate-for-thiolate exchange and that the final MW of the modified AuNP does not correspond to the sum of the unmodified particle plus the attached molecules, but to the sum of the reactants minus the leaving TNB-/ TAB ligands, having a MW of 198 Da and 168 Da, respectively. Reaction mixtures containing the NLS peptide and the AuNP (42 µM in 100 mM HEPES buffer pH = 7.4) at various molar ratios were analyzed by SDS-PAGE after a 4h incubation time at 25°C (Figure 21 shows the SDS-PAGE analysis of the products obtained from the reaction of AuZ with increasing amounts of NLS peptide. AuZ was loaded in sufficiently high amounts to be visible as a black band. The gel was further stained with Coomassie blue to detect the peptide as well.

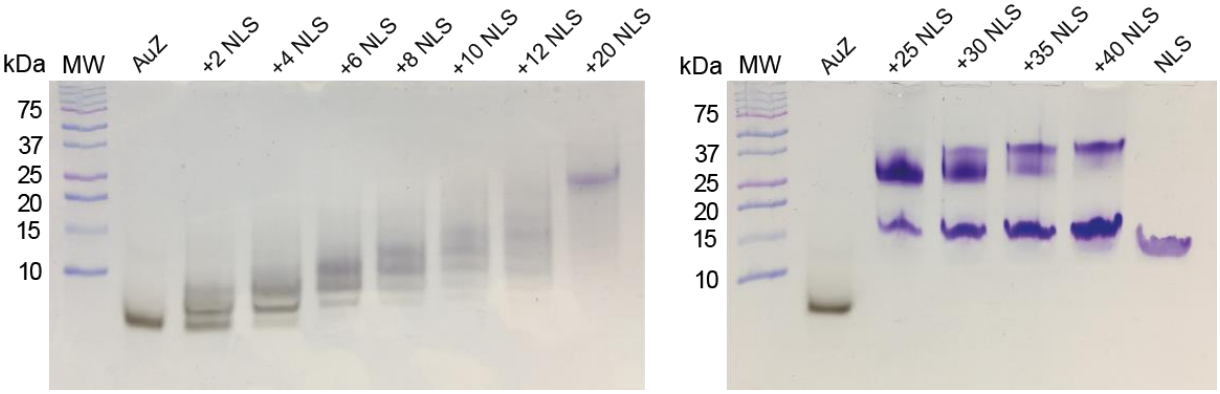

Figure 21. SDS-PAGE analysis of thiolate-specific reaction of AuZ with increasing amounts of NLS peptide. (a) AuZ reacted with 2 eq. – 20 eq. NLS permitting to count the new AuZ species (number of NLS peptides per particle); (b) AuZ reacted with excess NLS (25 eq. – 40 eq. NLS) demonstrating the saturation of the AuNP surface.

AuZ alone was seen as a single black band and the reaction with the thiolated NLS peptide promote the appearance of new bands with lower electrophoretic mobility in a relationship dependent to the NLS/AuZ ratio, indicating that the NLS for TNB exchange occurred smoothly at different surface sites of AuZ. By counting the AuNP bands appearing through the reactions, we could estimate that the product, made by using an NLS/AuZ ratio of 20, is equipped with an exact number of NLS peptides (i.e. 9 peptides). Interestingly enough, when large excess of NLS peptide is used, it is possible to push the surface coverage further, as seen by a discrete band with even higher electrophoretic mobility in the lanes of 35 eq. and 40 eq. NLS, corresponding to 10 NLS peptides (Figure 21).

Next, AuZ was reacted with cysteine, glutathione, and thiolated PEG (2000 Da and 300 Da) and peptide Cap using an excess of 50 molar equivalents to ensure full particle coverage in all cases. Figure 22 (a) shows the SDS-PAGE analysis of the passivated AuZ. In agreement with the MW and negative charge of cysteine (Cys) and glutathione (GSH), the resulting Au-Cys and Au-GSH had higher electrophoretic mobilities than AuZ, whereas peptide Cap did not lead to a change in AuZ's migration pattern on the SDS gel. Products of the reaction between AuZ and PEG(300) and AuZ and PEG(2000) resulted in a retarded and smeary band for Au-PEG(300) and a fully retained band for Au-PEG(2000), suggesting that the PEG(2000) is grafted in enough amount to mask the negative charge of the AuNP.

The possibility of dual functionalization of AuZ was assayed by sequential reaction of AuZ with the NLS peptide and then the peptide Cap. Figure 22 (b) shows the SDS-PAGE analysis of AuZ reacted with 2 and 3 molar equivalents NLS and 50 molar equivalents Cap. The results show that the addition of excess Cap peptide did not majorly modify the electrophoretic

mobility pattern of the products obtained by reacting NLS with AuZ, indicating that the thiolated NLS peptides coordinated to the AuNP's surface are not exchanged. Although not very striking, the addition of Cap resulted in light shift of bands, indicating that the initial organothiolate ligands were substituted. When looking closely at the lanes showing the reaction products for the reactions of AuZ with NLS and Cap (+2/3 eq. NLS + Cap), it is noticeable that the bands are less distinct than the ones detected after the reaction with NLS only. This observation might be explained by the fact that the remaining TNB-/ TAB-ligands of the NLS-functionalized AuZ might not exchange with the exact same amount of peptide Cap for each AuNP, consequently resulting in minor heterogeneity of the particle populations.

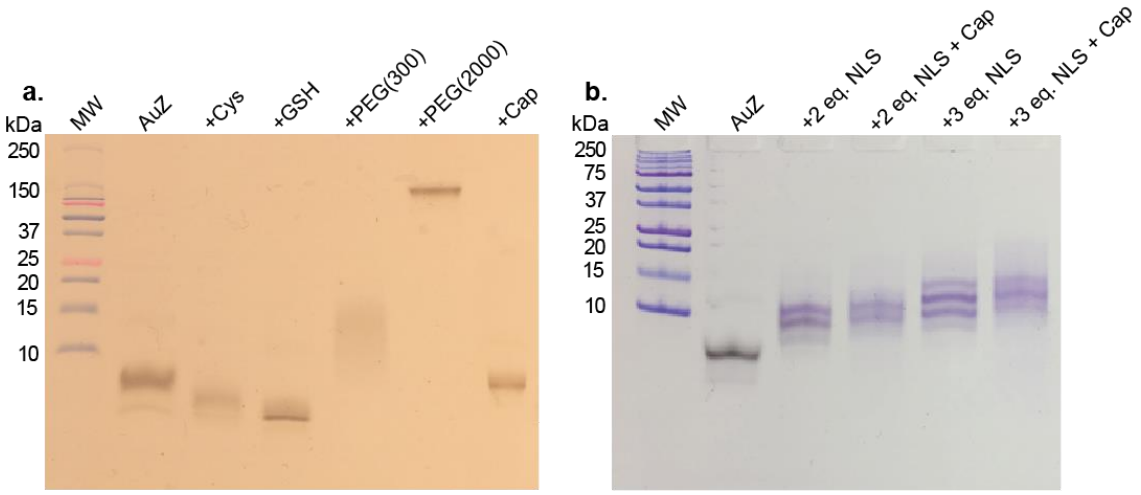

Figure 22. SDS-PAGE analysis of AuZ passivated with different thiolated molecules. (a) From left to right: AuZ, AuZ after reaction with cysteine (+Cys), glutathione (+GSH), polyethylene glycol having a MW of 300 Da (+PEG(300)), polyethylene glycol having a MW of 2000 Da (+PEG(2000)) and Cap peptide (+Cap); (b) from left to right: AuZ, AuZ functionalized with 2 eq. NLS, AuZ functionalized with 2 eq. NLS and excess Cap, AuZ functionalized with 3 eq. NLS and AuZ functionalized with 3 eq. NLS and excess Cap.

Having shown that AuZ (composed of 102 atoms and 44 Ligands) can be equipped with various and mixed ligands through thiolate-for-thiolate exchange, we next assayed the reactivity of AuG (supposedly composed of 420 Au atoms, 130 ligands) and AuL (supposedly composed of 480 Au atoms, 150 ligands) in a similar way. Since AuG and AuL coordinate more ligands than AuZ, higher NLS/AuNP ratios were used for investigating the reactivity of the two larger nanoparticles (10 to 100 molar equivalents of NLS based on AuG and AuL). After a 4h incubation time, the reaction products were analyzed by SDS-PAGE. Figure 23 shows the SDS-PAGE analysis of the reaction products obtained after the addition of the NLS peptide to the 2.4 nm AuNP (AuG) at various NLS/AuG ratios. Results indicate that AuG reacts with the NLS as seen by the formation of new bands that are stainable with Coomassie Blue. In contrast to

AuZ, we did not observe the formation of discrete bands. Nonetheless, the trend was similar with a maximum of thiolate-for-thiolate exchange intervening at an NLS/AuG ratio of 50.

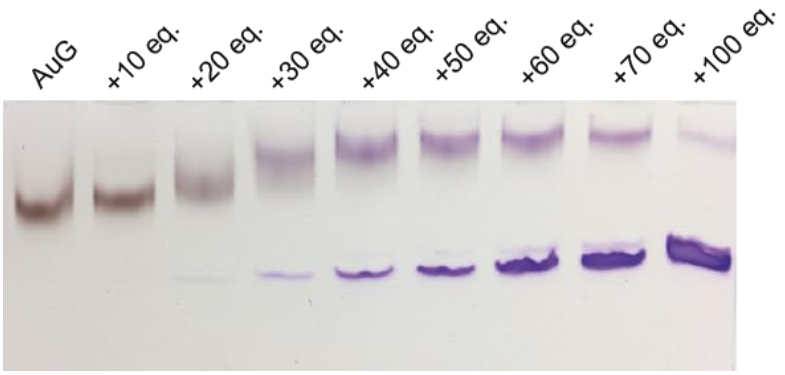

Figure 23. SDS-PAGE analysis of 2.4 nm AuG functionalized with increasing amounts of NLS peptide. From left to right: AuG, AuG mixed with 10 eq. NLS,. 20 eq. NLS, 30 eq. NLS, 40 eq. NLS, 50 eq. NLS, 60 eq. NLS, 70 eq. NLS and 100 eq. NLS

The 2.6 nm AuNP (AuL) was likewise reacted with the mentioned thiolated molecules using an excess of up to 100 molar equivalents. The passivation and functionalization products were run on SDS gels as it was performed for modified AuZ and AuG, but as expected from the large size and low electrophoretic mobility of AuL, the surface modification of the 2.6 nm AuNP could not be tracked by SDS-PAGE.

As performed for AuZ, AuG and AuL were reacted with excess (80 molar equivalents) cysteine, glutathione, peptide Cap and thiolated PEG (300 Da and 2000 Da). The reaction products from AuG were analyzed by SDS-PAGE and are depicted in Figure 24 (a)). Moreover, AuG was reacted with 10 eq., 20 eq. and 80 eq (excess) NLS and further passivated with the high molecular weight PEG(2000) (Figure 24 (b) and (c)). The reason for choosing PEG (2000 Da) for saturating the surface of NLS-functionalized AuG over peptide Cap, which was used in case of NLS-modified AuZ, was that we observed that AuG has a higher tendency to aggregate, when functionalized with positively charged molecules, than AuZ and PEG is known to efficiently counteract aggregation even in case of larger particles.[190]

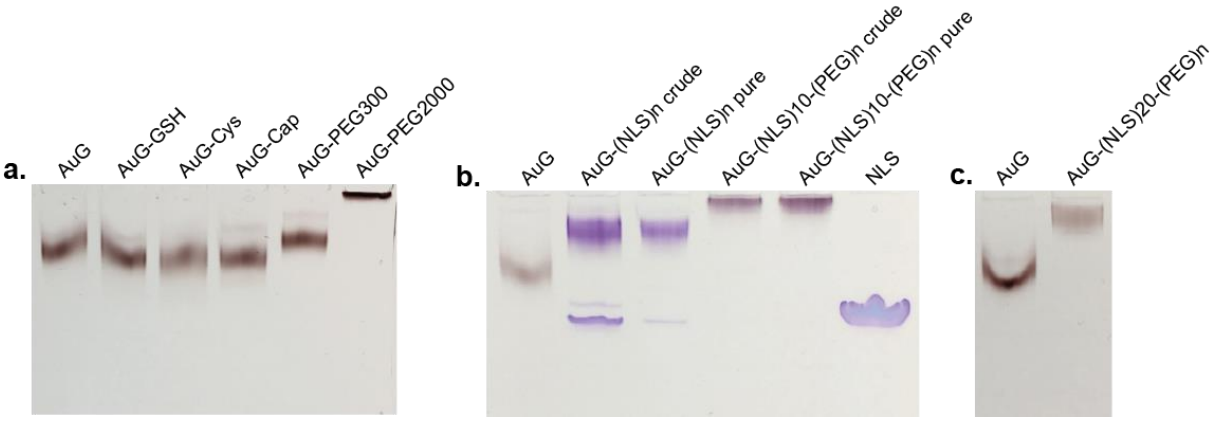

Figure 24. Passivation and functionalization of 2.4 nm AuNP AuG. (a) Passivation of AuG with glutathione (AuG-GSH), cysteine (AuG-Cys), peptide Cap (AuG-Cap), PEG with MW of 300 Da (AuG-PEG300), PEG with MW of 2000 Da (AuG-PEG2000); (b) Functionalization of AuG with NLS. Either AuG surface fully coated with NLS using 80 eq. of the peptide (AuG-(NLS)n) or only 10 eq. of NLS linked to AuNP and remaining surface passivated with PEG2000 (AuG-(NLS)10-(PEG)n); (c) AuG functionalized with 20 eq. NLS and passivated with excess PEG (AuG-(NLS)20-(PEG)n).

For AuL, images of SDS-PAGE analyses are not shown, because AuL and modified AuL barely migrated into SDS gels. This fact was unfortunate, but thanks to the yellow color of the TNB-/TAB-ligands that are released upon the thiolate-for-thiolate substitution, we were able to monitor the effectiveness of the exchange with cysteine, glutathione, peptide Cap, thiolated PEG(300), thiolated PEG(2000) and NLS peptide.

Next, the kinetic profile of the thiolate-for-thiolate exchange was investigated by following the release of TNB whose absorption coefficient at 412 nm is known and used for quantifying free thiols.[191] A solution of each AuNP (2.5 µM in 0.1 M HEPES buffer pH 7.2) was reacted with 60 equivalent of peptide Cap (150 µM final concentration) in a quartz cuvette. The absorbance at 412 nm was recorded over time and data were collected and used to evaluate the released TNB. Effective release of TNB was verified by separating the small MW molecules from the larger AuNPs using an ultracentrifugal filter device with a 10 kDa cut off and by analyzing the low MW fraction by UV-Vis spectroscopy. Figure 25 (a) shows the UV-Vis spectrum of the released ligands showing a spectrum similar to TNB with its maximum absorbance at 412 nm. Figure 25 (b) shows the normalized absorbance at 412 nm as a function of time for AuZ, AuG and AuL after addition to peptide Cap. By comparing this normalized absorbance as a function of time, corresponding to the kinetic profile of the thiolate-for-thiolate exchange on the surface of the three differently sized AuNPs, it is apparent that the passivation of AuZ proceeds much faster, than the one of AuG and AuL. In case of AuZ the normalized absorbance at 412 nm reaches its maximum after 10 min (600 s), whereas the absorbance of AuG only starts to be

saturated after 100 min (6000 s) and in case of AuL the release of TNB is still increasing after 100 min (6000 s). Very surprisingly, the curve of AuZ decreases after having reached its maximum at 600 s (black line in Figure 25 (b)). As this pattern was invariably observed during repeated experiments, we believe that the decrease of the normalized absorbance at 412 nm of AuZ might result from re-oxidation of the released TNB-ligands forming DTNB, which does not absorb at 412 nm. The fact that this proposed re-oxidation of TNB was not detectable for AuG and AuL is puzzling but might be explained by the fact that the redox properties of AuNPs vary with particle size. Despite this inconsistency, the recorded absorbance of the first 500 s provides a clear picture about the different kinetics of the three AuNPs, revealing that the thiolate-for thiolate exchange occurs much faster on the surface of the 1.4 nm AuZ, compared to the larger particles AuG (2.4 nm) and AuL (2.6 nm).

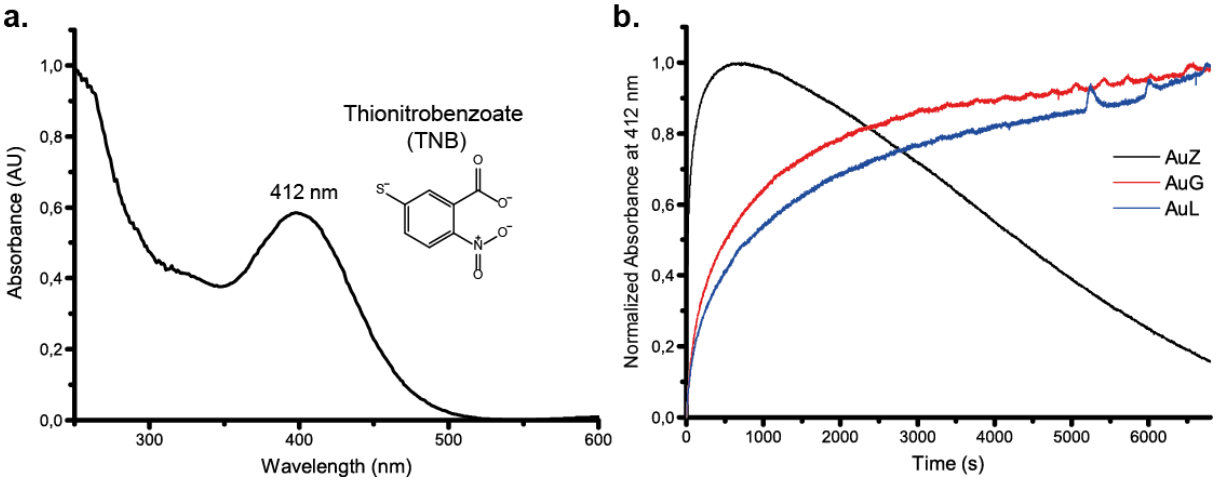

Figure 25. UV-Vis spectrum of the AuNP thiolate ligand TNB (a) and kinetics of thiolate-for-thiolate exchange on the surface of AuZ, AuG and AuL during reaction with peptide Cap (b). (a) The UV-Vis spectrum of TNB displays its maximum absorbance at 412 nm. Structure of TNB depicted next to the absorption peak. (b) The normalized absorbance at 412 nm as a function of time, representing the release of TNB, corresponds to the progress of the thiolate exchange on the surface of AuZ (black line), AuG (red line) and AuL (blue line).

From the absorption maxima at 412 nm of the three thiolate-for-thiolate exchange reactions (not normalized spectra, depicted in Figure 64, Supporting Information), and the knowledge of the extinction coefficient of TNB at 412 nm (ε = 13600 M^{-1} cm^{-1}),[191] it can be deduced that 79 nmol TNB were released during the reaction of AuZ, 57 nmol during the reaction of AuG and 75 nmol during the reaction of AuL.

Altogether, the comparison of the thiolate-for-thiolate exchange kinetics of the three differently sized AuNPs demonstrates that the full surface coverage of the larger AuNPs takes much longer than the one of the 1.4 nm AuZ and in case it is desired to fully passivate/functionalize AuG and AuL, the reaction should be carried out longer than 2 h (e.g. 4 h – overnight). It needs to be

noted that the increasing absorbance at 412 nm only reflects the release of TNB, because TAB does not significantly absorb at 412 nm. Yet, an NMR study previously performed in our laboratory demonstrated that TNB gets exchanged to a higher extent than TAB (evaluated for AuZ),[155] likely due to the electron withdrawing nitro group of TNB making the thiolate ligand a much better leaving group than TAB, thereby indicating that the TNB release is representative for the kinetic profile of the thiolate-for-thiolate exchange.

Taken together, in this first investigation we demonstrated that it is possible to produce AuNPs with a mixed TNB-/ TAB-surface coating that are larger than the 1.4 nm AuZ, initially developed in our laboratory, by changing the synthesis conditions, such as the type of solvent and thiol/Au ratio used throughout the synthesis. The three organothiolate-protected AuNPs (1.4 nm AuZ, 2.4 nm AuG and 2.6 nm AuL) could be modified with thiolated molecules *via* thiolate-for-thiolate exchange and the modification of AuZ and AuG could be conveniently tracked by SDS-PAGE thanks to the negative charge of the nanoparticles and their ability to migrate into SDS gels. Unfortunately, the 2.6 nm AuNP did not migrate sufficiently far into SDS gels to be discernable from functionalized/passivated AuL, which is a result of the AuNP's high MW. An examination of the thiolate exchange kinetics of the three AuNPs revealed that the reactivity of the nanoparticles towards thiolates is inversely proportional to the AuNPs size and that a full surface coverage for AuZ can be achieved within 10 min, whereas a complete modification of the surface of AuG and AuL requires more than 2 h.

3.4 Transduction of Gold nanoparticles into living cells

For exploring the biocompatibility and behavior of the AuNPs of various sizes and coatings inside cells we attempted to electroporate the three differently sized AuNPs coated with cysteine, glutathione, peptide Cap and thiolated high and low MW PEG (300 Da and 2000 Da) into living HeLa as illustrated in Figure 26 (a). After the electroporation of the AuNPs, the cells were further cultivated for 16 h, before being fixed with high grade glutaraldehyde. The AuNPs were subsequently revealed using a silver staining protocol adapted for bright-field optical microscopy imaging (non-electroporated cells (control) in Figure 26 (b) and electroporated cells in Figure 26 (c)).

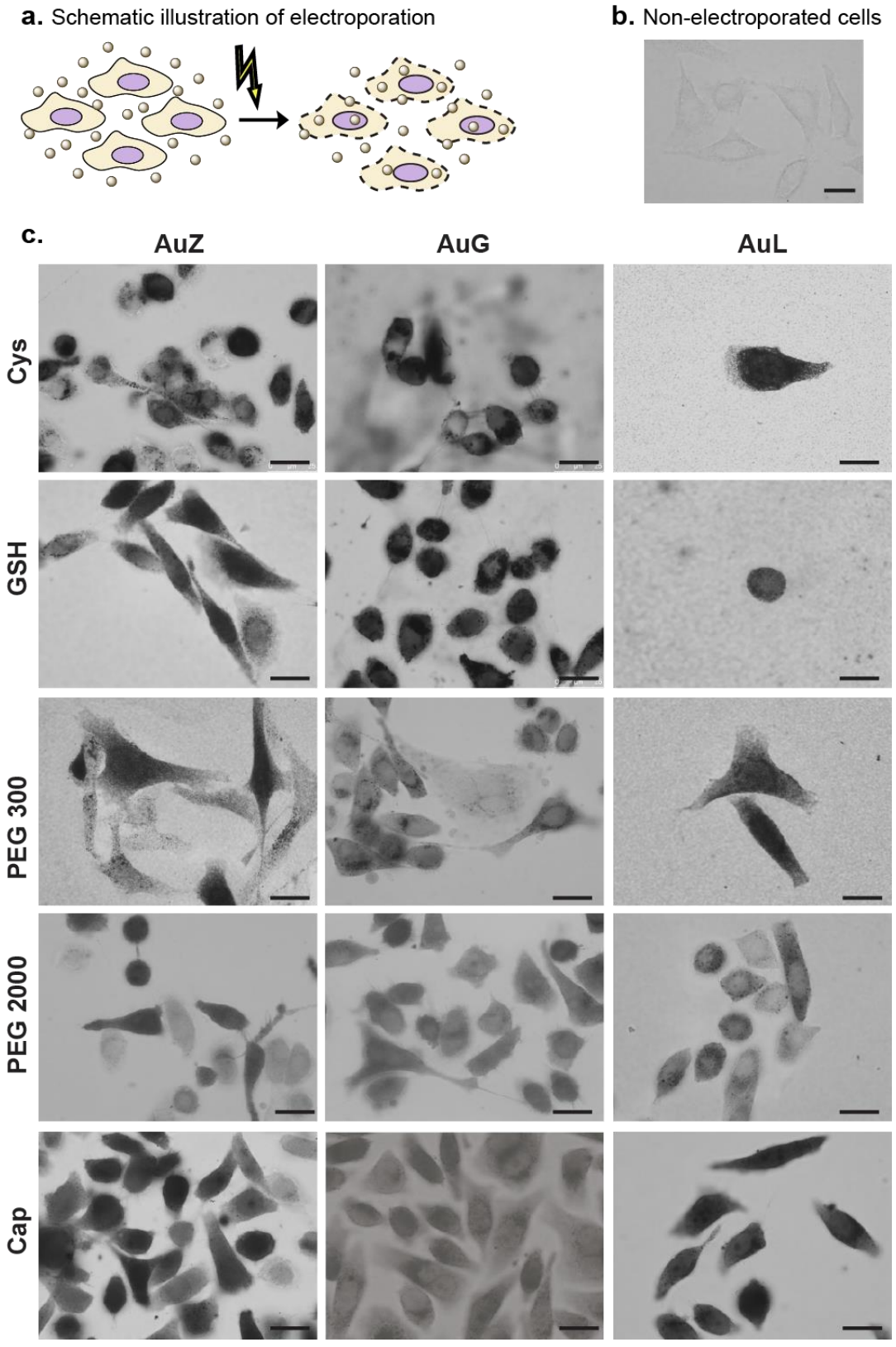

Figure 26. Electroporation of passivated AuNPs into HeLa cells. (a) Schematic illustration of electroporation; (b) Bright-field microscopy images of HeLa control cells (non-electroporated); (c) Bright-field microscopy images of HeLa cells electroporated with AuZ (left column), AuG (middle column) and AuL (right column) passivated with five different thiol-containing ligands: cysteine (Cys), glutathione (GSH), 300 Da polyethylene glycol (PEG 300), 2000 Da polyethylene glycol (PEG 2000) and peptide Cap (Cap). Silver enhancement of AuNPs allowed the detection of the nanoparticles by light microscopy (black staining). Scale bars in (b) and (c): 20 µm.

The results from the recorded light microscopy images firstly showed that all nanoparticles were efficiently delivered into the cells. As previously reported, the passivated 1.4 nm AuZ particles diffuse inside the cytosol and into the nucleus, but only certain surface coatings did not promote unspecific binding to cellular components and displayed a homogeneous distribution inside the cells. Passivation of AuZ with peptide Cap and PEG(2000) convincingly demonstrated to promote free diffusion of the electroporated AuNPs inside the living cells. In contrast, AuZ coated with cysteine, glutathione and PEG(300) were seen to accumulate in the perinuclear region, suggesting that these particles associated with components of the cell membrane and were subsequently internalized by endocytosis.

The behavior of the 2.4 nm AuG inside living cells was even more dependent on the surface coating, than it was the case for AuZ. For AuG, important endocytic accumulation was seen for the cysteine-, glutathione-, PEG(300)-, and Cap-coated particles. However, only few of the 2.4 nm AuNPs passivated with PEG(2000) were found in the endosomal/lysosomal compartments, but were mainly homogeneously distributed throughout the cytosol, suggesting that the high MW PEG provides sufficient stealth properties and furtiveness to the 2.4 nm particles. Despite the increased size of AuG and the passivation with PEG(2000), leading to an increased hydrodynamic diameter, some of the particles were detected inside nuclei. Unsurprisingly, the observed nuclear accumulation of AuG-PEG(2000) was lower than the one of AuZ-PEG(2000), which is in agreement with the fact that the passive passage though the nuclear pores is less effective for larger particles.

In case of the 2.6 nm AuL, the analysis of the recorded bright-field light microscopy images was complicated, since the AuNPs in combination with the electric pulses led to significant cell death. The few surviving cells clearly suffered, as can be seen from their roundish shape, small size and the accumulation of material into the nucleus. Nevertheless, it was evident that AuL passivated with the different thiolated ligands were to a large extent localized inside endosomes, suggesting that these particles bind to cellular components involved in tropism to endosomal/lysosomal compartments. Although not readily apparent, the passivation with PEG(2000) seemed to result in the most homogeneous distribution of the nanoparticles inside cells, thus following the same trend that was observed for AuG. Moreover, the nuclear accumulation of AuL was drastically impeded, in particular when the AuNP was coated with PEG(2000), indicating that 2.6 nm AuNPs are unable to passively pass through the nuclear pores.

Altogether, the obtained data reveal that electroporation enables the entry of AuNPs of various sizes into living cells and that the size and coating of the particles influence their subcellular localization. Homogenous cytosolic distribution was clearly size dependent. The smaller 1.4 nm AuNPs were seen to distribute more homogenously throughout the cell, than the larger 2.4 nm and 2.6 nm AuNPs. For the smallest particle, peptide Cap has proven effective for minimizing unspecific associations with cellular components and to ensure the particle's diffusion throughout the cell, including the nucleus. In case of the 2.4 nm AuG, peptide Cap did not provide enough stealth properties to the nanoparticle and was not able to prevent unspecific associations with cellular components and peculiar accumulation. In fact, only PEG(2000) ensured cytosolic diffusion of AuG, albeit at the cost of increasing the nanoparticle's (hydrodynamic) diameter.[192] Accordingly, the same trend is valid for AuL, but unfortunately the 2.6 nm AuNP appeared to be toxic when electroporated into HeLa cells. Based on these results we concluded that only the 1.4 nm AuZ and the 2.4 nm AuG are suitable for applications in live cells and that peptide Cap should be privileged for the passivation of AuZ and PEG(2000) for the passivation of AuG. The reason for preferring AuZ-Cap over AuZ-PEG(2000) is that peptide Cap does not increase the hydrodynamic diameter of the nanoparticle as drastic as PEG(2000), while providing the same inertness to the small-sized AuNP.

Next, we examined the behavior of the AuNPs functionalized with bioactive NLS peptides. Based on the above-described results, we chose to passivate the NLS-functionalized AuZ with peptide Cap and the NLS-functionalized AuG and AuL with PEG(2000). The synthesis and characterization of the modified AuNPs (AuZ-NLS-Cap, AuG-NLS-PEG and AuL-NLS-PEG) were performed as previously described (see Figure 21 and Figure 23) and then the AuNPs were delivered into HeLa cells by electroporation. After an overnight incubation the cells were fixed, silver stained and imaged, as done before (Figure 27).

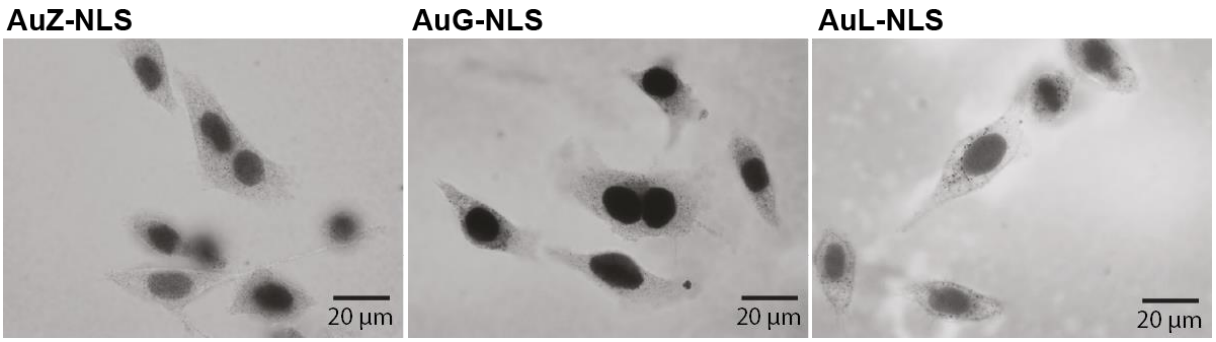

Figure 27. Bright-field light microscopy images of HeLa cells after electroporation with NLS functionalized AuNPs (AuZ-NLS-Cap, AuG-NLS-PEG and AuL-NLS-PEG). AuNPs were revealed by silver staining (black coloration inside the nucleus). Scale bar: 20 µm.

The obtained data show a remarkable nuclear accumulation of all three NLS-functionalized AuNPs, and in case of the largest 2.6 nm AuNP this observation stands in sharp contrast to the subcellular localization of the corresponding PEGylated particle (Figure 26). The recorded pattern hence demonstrates that the AuNPs are efficiently shuttled into the nucleus *via* the attached NLS. Moreover, the nuclear transport of the AuNPs indicates that the NLS peptide is neither structurally altered, nor shielded through the linkage to the AuNPs, as the nuclear transport machinery was able to bind to the NLS and shuttle the functionalized nanoparticles through the nuclear pore. By comparing the intensity of the nuclear silver staining of the three differently sized AuNPs it can be seen that the staining of the cells electroporated with AuL-NLS is less intense compared to AuG-NLS, suggesting that the concentration of AuL-NLS inside the nucleus is lower, than the one of AuG-NLS. This observation is consistent with the previous transduction of the passivated AuNPs, which revealed that the bulkiness of the 2.6 nm AuNPs limits their diffusion through the transient pores in the cell membrane created by the electric pulses of the electroporation. The nuclear silver staining intensity of AuG-NLS (2.4 nm) is more intense, than the one of AuZ-NLS (1.4 nm) as well, but since larger AuNPs provide a larger surface area onto which silver ions can be deposited during the staining process, it cannot be concluded that the higher intensity of AuG-NLS is correlated with a higher AuNP concentration, but likely results from the difference in size between AuZ and AuG. For proving the outlined interpretation about the concentration of the NLS-functionalized AuNPs inside the cellular nucleus after electroporation, TEM should be performed in future experiments. Finally, it needs to be pointed out that the electroporation of the NLS-grafted AuNPs, regardless of their size, did not promote high cytotoxicity.

In conclusion, the NLS-functionalized AuNPs were efficiently transported into the nucleus, suggesting that the AuNPs can be equipped with bioactive ligands *via* Au-S coordination, which remains stable inside the cytosol of living cells and does not impact the integrity of the NLS peptide. In agreement with the former transduction experiment, a high amount of NLS-modified AuZ and AuG could be delivered into the cell, while AuL was detectable in the cellular nuclei at lower concentrations.

Altogether, we developed synthetic procedures permitting the generation of three novel TNB-/TAB-protected AuNPs having a diameter of 1.4 nm (AuZ), 2.4 nm (AuG) and 2.6 nm (AuL). These particles were characterized by SDS-PAGE, HAADF-STEM, UV-Vis spectroscopy and mass spectrometry, indicating that the three AuNPs have a discrete size distribution and likely

are composed of 102 Au atoms and 44 ligands in case of AuZ, 420 Au atoms and 130 ligands in case of AuG and 480 Au atoms and 150 ligands in case of AuL. We demonstrated that all three AuNPs react smoothly with thiol-containing molecules via thiolate-for-thiolate exchange and that the reaction advancement can be conveniently tracked by SDS-PAGE, in particular for the smaller AuZ and AuG. We were able to graft several passivation agents onto the three AuNPs and to evaluate their behavior inside living cells after electroporation. A size- and surface coating-dependent behavior was observed. First, the homogenous staining mediated by diffusing AuNPs within the cytosol of living cells appears reversibly proportional to the AuNP size. Second, the nature of the surface has a dramatic impact on the intracellular behavior of the AuNPs. Cysteine, glutathione or low MW PEG(300) coordinated to the AuNP surface favored accumulation of the particles in vesicular compartments. In contrast, high MW PEG(2000) showed to clearly improve the homogenous distribution pattern of all three AuNPs, likely as a consequence of its ability to shield the AuNPs from interacting with cellular constituents, resulting in less restricted trafficking throughout the cytoplasm. The Cap peptide also proved useful for protecting the 1.4 nm AuZ from associating with cellular components, but for the larger particles (AuG and AuL) the passivation with high PEG(2000) was indispensable. This observation clearly points out that the AuNP surface chemistry gains increasing importance for minimizing unwanted associations with cellular components with increasing AuNP size. Consequently, the passivation agent needs to be carefully chosen for each type of AuNP and for generating probes based on AuNPs > 2 nm whose selective binding should only be dictated by the attached targeting biomolecule (e.g. antibody) PEG(2000) should be definitely privileged. Finally, we demonstrated that AuNPs that were functionalized with an NLS peptide and passivated with either Cap, or PEG(2000) could be electroporated into living cells, where they were efficiently shuttled into the cellular nuclei. This finding proves that mixed surface modifications can be carried out and that the newly formed Au-S bonds are stable enough to sustain sequential reactions, as well as elevated concentrations of reduced glutathione inside the cytosol of living cells.[193]

4 Discussion

4.1 Synthesis of TNB-/ TAB-protected AuNPs

For generating precise EM probes, the preparation of monodisperse and characterizable AuNPs that can be readily functionalized is of high importance. AuNPs prepared according to the Brust-Schiffrin method[145,146] and its modifications[194] usually yield polydisperse AuNPs of small sizes and methods were developed to narrow the size distribution of the nanoparticles, such as etching, annealing and size-focusing. Occasionally AuNPs containing nonpolar ligand shells were obtained with atomically precise formulas by employing these purification methodologies, but for water-soluble AuNPs the purification procedures have unfortunately not proven successful. As a consequence, researchers started to screen synthesis parameters and thiolated ligands to directly produce monodisperse and water-soluble thiolate-protected AuNPs. Kornberg and colleagues reported the direct synthesis of water–soluble AuNPs and described the *p*-MBA-protected AuNPs $Au_{144}(p\text{-MBA})_{60}$[182] and $Au_{102}(p\text{-MBA})_{44}$[147] which could be functionalized with biomolecules in water by a S_N2-like mechanism.[165] Based on these results, our laboratory developed a similar type of AuNPs counting ca. 102 Au atoms surrounded by a mixed monolayer of TNB and TAB.[155] This water-soluble AuNP having a diameter of 1.4 nm was obtained through the reduction of $HAuCl_4$ with $NaBH_4$ in the presence of DTNB. In order to further exploit this type of synthesis and to generate monodisperse TNB-/ TAB-protected AuNPs with larger particle diameter, providing an increased electron contrast, we systematically varied the reaction conditions, such as water-miscible solvent concentration and thiol/Au ratio, as several studies suggested that these parameters majorly impact the nanoparticles' size.[152,182,183]

4.1.1 Influence of type and concentration of co-solvent mixtures

The screening of different organic solvents mixed with water was assayed while all other synthesis parameters (concentration of Au, thiolate ligand, $NaBH_4$, temperature, pH and reaction time) were kept constant. The obtained result revealed that a mixture of acetonitrile/water (80/20) led to the generation of AuNPs with reduced electrophoretic mobility (larger nanoparticle diameter) compared to the one of AuZ, as well as a narrow size distribution. This AuNP for which a diameter of 2.4 nm was determined, was named AuG. Interestingly, the same type of AuNP could be produced by changing the cosolvent to 2-propanol/water (80/20), suggesting that the concentration of the organic solvent is of higher importance than its nature.

The decision to pursue using 80% acetonitrile in water over 80% 2-propanol in water for the production of AuG was arbitrary, as both solvents led to AuNPs of the same size and no differences were observed regarding the reproducibility of the nanoparticles. The finding that an 80% acetonitrile/water mixture promotes the production of monodisperse AuNPs being larger than the magic-sized gold cluster $Au_{144}SR_{60}$ (having a particle diameter of ca. 2 nm) is in agreement with a study published by Wong *et al*. during which the authors analyzed the effect of 13 water miscible solvents on the dispersity of AuNPs stabilized with *p*-MBA, thiomalic acid and glutathione.[152] Although Wong and colleagues observed a general cosolvent-dependent trend for the generation of monodisperse AuNPs being independent of the thiolate ligands used throughout the synthesis, the production of monodisperse AuNPs > 2 nm using an 80% acetonitrile/water mixture was only observed for *p*-MBA-protected AuNPs. Wong *et al.* moreover analyzed the impact of different concentrations of 2-propanol on the AuNPs' polydispersity, but unlike our observation, the authors did not obtain monodisperse AuNPs of 2.4 nm in 80% 2-propanol/water. Instead, the authors observed that the use of solvents with lower surface polarity that are able to chelate metals, such as diglyme, 1,2-dimethoxyethane, 1,4-dioxane and tetrahydrofuran, as well as alcohols with long hydrophobic chains, such as 1-butanole and 2-propanol (<50% in water) lead to the production of AuNPs with a discrete size distribution, independent of the type of protecting ligand (*p*-MBA, thiomalic acid and glutathione). In our hands, none of these solvents[152] yielded monodisperse TNB-/ TAB-protected AuNPs, indicating that the type of stabilizing ligand present in the reaction mixture in some cases plays a major role in the construction of the final AuNP. Altogether, the collected data underscore the point that the type and composition of co-solvents play a critical but not the only role in the formation of AuNPs and that different synthesis parameters need to be tuned to obtain AuNPs of various sizes.

4.1.2 Influence of Au:thiol ratio

A modification of the DTNB/$HAuCl_4$ ratio from 1.5 (used for the synthesis of AuZ) to 2 – 7 revealed that the DTNB/$HAuCl_4$ ratio of 4 performed in acetonitrile/water (80/20) led to the production of highly monodisperse AuNPs having a lower electrophoretic mobility (larger size) than AuG. This AuNP product that was further characterized to have a diameter of 2.6 nm was named AuL. At first glance, the generation of AuL (being larger than AuG and AuZ) at a DTNB/$HAuCl_4$ ratio of 4 was unexpected. For comparison with the literature it needs to be taken into account that DTNB undergoes hydrolytic disulfide cleavage under basic conditions

(DTNB was dissolved in 0.3 M NaOH prior to the reaction, pH ~13), due to which a DTNB/$HAuCl_4$ ratio of 4 corresponds to an thiol/Au ratio (TNB/$HAuCl_4$) of 8. The fact that a higher amount of thiolate ligands in the reaction mixture led to the production of larger AuNPs is in disagreement with early reports on the influence of the thiolate/Au ratio on the AuNP size, claiming that increasing thiolate/Au ratios cause a decrease in nanoparticle size.[183,195] This assumption, which was widely adopted for a long time, is explained by the monolayer-thiol-protected AuNP model, based on which an increasing ratio of thiolate/Au results in a higher amount of Au-S interface, thus requiring a larger surface/volume ratio, which is met by smaller AuNPs.[196] However, in 2008 Jiang *et al.* published a study, which suggested that the Au core of AuNPs is stabilized by a shell of Au(I)-S-motifs ("staple" motifs) and not as thus far assessed by a thiolate monolayer.[197] Inspired by this report Chen and coworkers hypothesized that the conventional monolayer-thiol-protected AuNP model might not be the only explanation for the dependence of the AuNP size on the thiol/Au ratio, but that the Au(I)-thiolate complex precursor plays a major role as well.[184] To test their hypothesis the authors prepared AuNPs from $HAuCl_4$ and *m*-MBA using thiol/Au ratios ranging from 1/8 to 8. In contrast to previous reports, Chen *et al.* did not observe a steady decrease in AuNP size with increasing amounts of thiolates, but observed a U-shaped trend with decreasing size when the thiol/Au ratio was varied from 1/8 to 1 and increasing size when the thiol/Au ratio was varied from 1 to 8.[184] Interestingly, the AuNP produced with a thiol/Au ratio of 8 had a size of 2.4 nm, which is close to the size of AuL (2.6 nm) synthesized using a TNB/Au ratio of 8 as well. To explain this U-shaped trend Chen and colleagues analyzed the MW of the Au(I)-thiolate complex precursors by electrospray ionization mass spectrometry (ESI-MS) and assessed that at very low thiol/Au ratios most thiolates are oxidized and Au atoms are mainly in the form of chloride or hydroxide complexes. At high thiol/Au ratios long Au(I)-thiolate complexes are formed and at even higher thiol/Au ratios short Au(I)-thiolate complexes are formed. Since small AuNPs have a higher curvature than larger particles, the authors concluded that small AuNPs can be only stabilized by long Au(I)-thiolate complexes, whereas larger AuNPs are better stabilized by short Au(I)-thiolate complexes. The observation of this U-shaped trend, as well as the explanation deduced from the MW of Au(I)-thiolate complex precursors fits with the relation of the AuNP size and thiol/Au ratio of the 2.4 nm AuG (DTNB/ $HAuCl_4$ = 1.5 ➔ TNB/ $HAuCl_4$= 3) and the 2.6 nm AuL (DTNB/ $HAuCl_4$ = 4 ➔ TNB/$HAuCl_4$ = 8), which reinforces the validity of the model described by Chen *et al.*[184]

Besides the described reaction conditions enabling the generation of AuL, all other synthesis attempts using different thiol/$HAuCl_4$ ratios, which were performed in 80% acetonitrile/water,

as well as 47% methanol/water, did not yield particles with a sufficient degree of monodispersity. In particular, it needs to be noted that the use of DTNB/$HAuCl_4$ ratios being higher than 4 (thiol/$HAuCl_4$ = 8) did not permit the precipitation of particles, which is somewhat contradictory with the U-shape model described by Chen *et al.*, according to which the AuNP size increases with increasing amounts of thiolates. However, apart from one publication made by Ackerson *et al.*[149] who attempted the synthesis of thiolate-protected AuNPs by using a ratio of *p*-MBA/ $HAuCl_4$ of 10 and did not succeed in producing monodisperse AuNPs under these conditions, there are no reports in the literature about the use of thiol/Au ratios being larger than 8, which might be the due to the impossibility of generating AuNPs in the presence of such high amounts of thiolate.

Altogether, we showed that two novel TNB-/ TAB-protected AuNPs having a diameter of 2.4 nm (AuG) and 2.6 nm (AuL) can be obtained by varying the solvent composition, as well as DTNB/$HAuCl_4$ ratio. The production of these two nanoparticles having different particle diameters than AuZ underscores the versatility of the screening of synthesis parameters for generating synthetically elusive water soluble AuNPs. The characterization of the two new AuNPs by SDS-PAGE, HAADF-STEM, MS and UV-Vis spectroscopy were coherent and demonstrated that the produced AuNPs have discrete size distribution, which makes them, together with their increased size, highly attractive for the generation of EM probes for high resolution immunolabeling not relying on silver enhancement.

4.2 Reactions with passive and bioactive thiolated molecules

One vital aspect of organothiolate-protected AuNPs is that their surface coating can be readily modified by thiolate-for-thiolate exchange.[148,156] To identify a surface coating preventing the AuNPs from aggregation and unspecific binding to cellular components, the three differently sized AuNPs were reacted with different thiolated molecules, such as cysteine, glutathione, PEG(300), as well as with the peptide Cap of the sequence [CALNNG] and PEG(2000). The pentapeptide of the sequence [CALNN] has been reported to stabilize AuNPs from aggregation,[186] whereas high MW PEG(2000) is widely used to shield surfaces from interacting with others components.[192] Substitution of TNB/TAB with the above mentioned thiolates on the AuNP surface readily occurred in aqueous solutions at neutral pH and the exchange reactions were easily monitored, either by SDS-PAGE analysis, or by measuring the release of the colored TNB. This possibility to follow the functionalization/passivation of the AuNPs by

a rapid and simple analysis method is of high advantage and not possible for larger AuNPs that do not migrate into SDS gels, such as 4.5 nm citrate-capped AuNPs.[155]

Important to note, we were able to assess the number of thiolated molecules that can be coordinated to the 1.4 nm AuZ and 2.4 nm AuG, thanks to their ability to migrate sufficiently far into SDS gels. The surface of AuZ was saturated with 10 thiolated peptides, whereas approximately 35 peptides could be grafted onto AuG. For AuL it was impossible to track the surface modification by SDS-PAGE and needed to be verified by the release of colored TNB, but based on its particle diameter (2.6 nm) it can be reasoned that more than 35 thiolated ligands can be linked to the AuNP's surface. Since all three AuNPs offer various coordination sites, the modification of the nanoparticles with a single thiolated molecule is not straightforward, unless the incoming molecule is so large that it consumes the whole surface of the AuNP (which is not the case for short peptides). Consequently, the reaction of thiolated molecules with the TNB-/ TAB-protected AuNPs usually yields heterogeneous populations of surface-modified AuNPs (i.e. not all AuNPs are coordinated by the same number of incoming thiolate ligands), unless the surfaces of the AuNPs are fully covered. Furthermore, it is noteworthy that the surface of the TNB-/ TAB-protected AuNPs can be modified sequentially allowing to produce particles with mixed surface coatings, as has been demonstrated with the functionalization of the three AuNPs with NLS peptides and subsequent passivation with either Cap or PEG(2000). Importantly, the incoming thiolate ligands that are reacted with the AuNPs in an initial stage are not exchanged when a second thiolate ligand is added, but the remaining TNB-/ TAB-ligands on the particle surface exchange with the second incoming ligand until the surface is saturated.

In order to examine whether the kinetics of the thiolate-for-thiolate exchanges at the AuNP surface are dependent on the AuNP core size, the release of the TNB ligand upon reaction with peptide Cap was followed by measuring the absorbance at 412 nm (absorption maximum of TNB). The collected data show that the reaction dynamics decrease with increasing AuNP size (i.e. ligand exchange on the surface of 1.4 nm AuZ is much faster than the one of 2.4 nm AuG and 2.6 nm AuL). Hence, it was assessed the complete passivation/functionalization of the surface of AuG and AuL needs to be carried out for a much longer time period, than the modification of AuZ. Thus far, only few studies have investigated the effect of the AuNP core size on the reactivity of the surface ligands,[198,199] but there are several characteristics of the surface of AuNPs that support the observed size-dependence of the thiolate-for-thiolate exchange kinetics. The surface of AuNPs, which is composed of Au(I) is not uniform, because

the inner metallic core is crystalline. As a consequence, the AuNP surface possesses different ligand binding sites, which are classified in edges, vertexes and terraces.[199] Since these different ligand binding sites differ in electron density and steric accessibility, the equilibrium thermodynamics and ligand exchange kinetics vary among them. Concerning the ligand exchange kinetics, edge and vertex sites have a higher reactivity than terrace sites.[200] Given the fact that smaller AuNPs have more edge and vertex sites on their surface than larger AuNPs, which are enriched in terraces, it appears logical that the thiolate-for-thiolate exchange is faster for the 1.4 nm AuZ, than for the ones of the larger AuG and AuL. Moreover, an ^{1}H NMR study, aimed at investigating the ligand exchange kinetics of alkane thiolate-coated AuNPs, found that the initial ligand exchange rate is rapid but slows down over time.[198] Based on this report, Guo *et al.* investigated the ligand exchange kinetics of thiolate-protected AuNPs having an atomic composition of $Au_{38}(SR)_{24}$ and $Au_{140}(SR)_{53}$ in order to analyze whether the nanoparticle core size impacts the reaction dynamics.[199] The results of the study demonstrated that the ligand exchange dynamics of the two nanoparticles are very similar during early exchanges, but clearly differ in the later ligand exchanges. In case of Au_{38} the dynamics slowed down modestly, whereas a drastic slow-down was observed for Au_{140}.[199] For AuZ being composed of 102 Au atoms, thus close to Au_{140}, the rapid increase in released TNB was followed by a rapid saturation as well, which is in agreement with the observations from Guo *et al*. One explanation for the rapid increase, as well as saturation of the TNB level observed for AuZ might be that the TNB ligands, whose release was followed, are exclusively localized on edges and vertexes, while the TAB ligands are present on terraces. In case of AuG and AuL an initial rapid increase in TNB release can be noted as well, but in contrast to AuZ this increase changes to a slow but steady increase of released TNB, which might again be explained by the higher ratio of terrace sites to edge and vertex sites in AuNPs of larger particle diameter. Certainly, it needs to be taken in mind that we did not follow the release of TAB and that the picture of the kinetics is consequently incomplete. Yet, an NMR study performed in our laboratory before my arrival showed that TNB is released faster and to a higher extent than TAB, suggesting that the release of TNB is representative for the thiolate-for-thiolate exchange kinetics.[155] Altogether, the ligand exchange on the surface of thiolate-protected AuNPs is a complex process and further investigations would be necessary to draw a more explicit conclusion on the causes determining the kinetic profiles of the TNB-/ TAB-protected AuNPs which clearly showed that the thiolate-for-thiolate exchange is influenced by the AuNP core size.

4.3 AuNP delivery into living cells

For studying the fate of the differently passivated AuNPs inside living cells, as well as to assess whether the AuNPs could serve as probes in an *in cellulo* set up AuZ, AuG and AuL were delivered into HeLa cells by electroporation using a protocol developed by Sibler *et al.* for antibody delivery.[181] All nanoparticles were detected inside the cells after transduction, but the distribution pattern of the AuNPs within the cells after 24h incubation was clearly size- and surface coating-dependent.

The nature of the surface coating clearly produced the most drastic effect on the AuNP trafficking inside the HeLa cells. On the one hand, the passivation with cysteine, glutathione and low MW PEG(300) led for all three AuNPs to an accumulation inside endocytic vesicles in the perinuclear region, suggesting that these particles associate with cellular membranes or constituents that promoting endocytosis. On the other hand, the passivation with high MW PEG(2000) proved to prevent the nanoparticles from unspecific binding to cellular components and to promote free diffusion throughout the cytosol. Interestingly, peptide Cap, which has been designed to stabilize AuNPs from aggregation,[186] only offers the same furtive effect as PEG(2000) and the resulting homogenous particle distribution inside the cells in case of the 1.4 nm AuZ and not for the larger 2.4 nm and 2.6 nm AuNPs. From these observations, it can be hence concluded that the stabilizing properties of Cap might only be sufficient for very small AuNPs when exposed to the crowded environment of living cells and not for AuNPs displaying plasmonic properties. In 2008, Nativo *et al.* reported a similar observation by conducting an electron microscopic study on the cellular uptake of 16 nm AuNPs synthesized by citrate reduction.[201] The authors observed that AuNPs passivated with high MW PEG did not bind to the surface of living cells, whereas AuNPs coated with the pentapeptide CALNN bound to the cell membrane and were consequently endocytosed to almost the same extent as the unmodified citrate -stabilized AuNPs. Rotello and coworkers claimed that thiolated ligands coordinated to 2 nm AuNPs can be released inside the cytosol by undergoing thiolate exchange with reduced glutathione,[193] but the collected data presented in this thesis do not support this theory for the TNB-/ TAB-protected AuNPs, since all three AuNPs linked to an NLS peptide *via* Au-S coordination were selectively shuttled into the nucleus after electroporation, demonstrating that the Au-S link is stable inside the cytosol containing high levels of reduced glutathione for at least 24 h. Furthermore, the nuclear accumulation of the NLS-functionalized AuNPs proves that the presence of the AuNPs does not impair the recognition of the NLS motif by the nuclear transport machinery. Finally, we did not observe significant changes in the cell morphology

after the transduction of the NLS-functionalized AuNPs, which is in sharp contrast with a previous study from Sun *et al.*, who delivered 13 nm, 30 nm and 60 nm AuNPs grafted with NLS peptides into living cells and observed a strong modification of the cell morphology, pointing out that the shuttling of the nanomaterials into the nucleus interfered with essential cellular mechanisms.[202]

The reduced ability of the larger AuNPs (notably the 2.6 nm AuL) to enter into Hela cells by using electroporation is likely linked to a hampered passage through the transient pores of the cell membrane that are created by the electric pulses. By employing other delivery methods, such as the use of cell penetrating peptides, AuNPs of larger size (5.5 nm and 8.2 nm) have been transduced into cells, as reported by Oh *et al.*, but a significant portion of the nanoparticles remained sequestered within endolysosomal compartments and could not escape into the cytosol.[203] Orlov and colleagues published the delivery of antibodies and Fab fragments conjugated to ultrasmall 0.8 nm AuNPs using a cationic lipid-based approach, which permitted the internalized conjugates to escape the endosomal pathway.[127] If however AuNPs of 6 nm were linked to the antibody, the conjugate was seen to remain in endocytic vesicles at the periphery of the cell membrane. Compared to methods permitting cell entry *via* endo- or pinocytosis, electroporation offers the advantage that the transduced material directly accesses the cytosol, thus avoiding endosomal entrapment. In this context microinjection would represent another potent possibility for the delivery of AuNPs, as it has the additional benefit that the delivered material cannot interact with the cell membrane and consequently no undesired endocytic uptake can take place.[204] However, microinjection is impractical for the transduction of a large number of cells and unlike electroporation does not allow the delivery of nanomaterials in a high throughput manner. As hinted before, the electroporation of AuZ, AuG and AuL could not completely avoid the entrapment of AuNPs inside endosomal compartments but was clearly influenced by the type of surface coating.

Apart from the delivery efficiency, a size-dependent behavior was noted for the nuclear accumulation of the nanoparticles, which was observed for AuZ, to a lower extent for AuG, but not for AuL (unless equipped with an NLS peptide). While there are many studies on the cellular uptake of AuNPs,[201–203,205] there are only few data available treating the distribution of AuNPs inside living cells (i.e. free diffusion throughout the cytosol, entry into the nucleus, adsorption to membrane complexes),[155] but as the nuclear pore complex limits the passive diffusion into the nucleus to molecules <60 kDa, it is unsurprising to observe a size-dependent nuclear diffusion/exclusion of the AuNPs.

5 Conclusion

In this chapter important results concerning the synthesis and behaviors of organothiolate-protected AuNPs were obtained. First, we set up synthetic procedures for generating water-soluble and monodispersed AuNPs containing a mixed surface layer of TNB and TAB. The variation of the co-solvent, as well as thiol/$HAuCl_4$ ratio allowed us to produce monodispersed TNB-/ TAB-protected AuNPs of 2.4 nm (AuG) and 2.6 nm (AuL). These two AuNPs, as well as the 1.4 nm AuZ recently developed in our laboratory showed to react smoothly with thiol-containing molecules *via* thiolate-for-thiolate exchange, which was conveniently tracked by SDS-PAGE. The analysis of the thiolate-exchange kinetics of three AuNPs revealed that the reactivity of the surface thiolate ligands decreases with increasing AuNP diameter. This size-dependent kinetic profile of the thiolate-exchange at the surface of AuNPs, which has been scarcely studied in the literature, might result from the fact that smaller AuNPs contain a higher proportion of reactive edge and vertex sites, compared to larger AuNPs, which on the other side possess a higher proportion of less reactive terrace sites. After passivating the three AuNPs with different thiolated molecules, we examined the fate of the nanoparticles inside living cells by using electroporation for the cellular delivery. The collected data revealed that all AuNPs could be transduced into living cells, but that the efficiency of transduction was clearly size-dependent (i.e. the smaller the AuNPs, the higher the delivery efficiency). Moreover, it was noted that the smallest 1.4 nm AuZ had the highest mobility inside the cells, regarding notably the diffusion into the nucleus. The 2.4 nm AuG was to some extent able to diffuse into the nucleus as well, but the 2.6 nm AuL was almost completely excluded. Apart from the size dependence, it was observed that the surface coating majorly impacts the behavior of the nanoparticles inside the cells. PEG with a MW of 2000 Da showed to drastically improve the diffusion ability of all three AuNPs, as well as to prevent unspecific biding to the cellular membrane and subsequent endocytic uptake. Interestingly, the passivation with peptide Cap, which is well-known for its stabilizing ability, only promoted free diffusion inside the cells in case of the 1.4 nm AuZ, suggesting that an increase in AuNP size, increases the challenge of counteracting nanoparticle aggregation and unspecific binding to cellular components. Ultimately, we demonstrated that all three AuNPs functionalized with NLS peptides are efficiently shuttled into the nucleus after being electroporated into the cells, which clearly proves that the Au-S bond is stable inside the cytosol for at least 24 h, despite the elevated concentrations of reduced glutathione. Based on the accumulated results we decided to focus on the 2.4 nm AuG passivated with 2000 Da PEG for the generation of novel EM probes, due to its beneficial combination of increased size, thus

increased opacity to electrons, and ability to freely diffuse throughout the crowded cytosol of living cells.

Chapter 2

Conjugation of gold nanoparticles to antibodies and biological evaluation

For generating precise and reproducible EM probes, site selective conjugation strategies for linking the electron opaque gold nanoparticles to targeting moieties are indispensable. In this chapter we describe a new approach for site-selectively linking the 2.4 nm thionitrobenzoate-, thioaminobenzoate-protected gold nanoparticle to the hinge are of antibodies *via* Au-S coordination. The generated conjugates were characterized for their antigen specificity and affinity and tested for their ability to probe nuclear targets in live cells – an essential criterion for EM probes being applicable for cryogenic work-flows.

Before presenting the gathered results, the structure and function of antibodies are introduced, which is followed by a summary on elaborated chemical modifications of antibodies, with an emphasis on site-selective conjugation strategies. Subsequently, established methods for linking antibodies to gold nanoparticles are reviewed.

1 Introduction

1.1 Structure and function of antibodies

Antibodies, also known as immunoglobulins, are multi-domain proteins that are characterized by high specificity and affinity binding to macromolecular domains (antigens) and are key elements of the adaptive immunity in vertebrates.[206] Our knowledge about the three-dimensional structure of immunoglobulins, dates back to the beginning of the 1970's when first crystallographic studies of antibodies were performed.[207] Human immunoglobulins are Y-shaped proteins that consist of two heavy and two light chains and have a molecular weight of approximately 150 kDa.[207] Under natural conditions heavy and light chains assemble into two identical heterodimers, building together an intact antibody. The assembly is stabilized by interchain disulfide bonds of cysteine residues between the heavy and light chains, as well as between the two heavy chains (schematic illustration of human IgG1 as typical antibody molecule in Figure 28 (a)). Human light chains comprise two classes: kappa (κ) and lambda (λ), while human heavy chains occur in 5 different isotypes: IgA, IgD, IgE, IgG and IgM. Both light chain classes are composed of one constant domain (CL) and one variable domain (VL) and the only difference between the two types is the elbow angle which describes the orientational and conformational flexibility of the light chains. The heavy chain isotypes IgA, IgD and IgG consist of three constant domains (CH1, CH2, CH3) and one variable domain (VH). The IgE and IgM are composed of 4 constant domains (CH1, CH2, CH3, CH4), as well as one variable domain. Moreover, IgA and IgM isotypes contain J-chains enabling the formation of dimers and pentamers (schematic illustration of different antibody isotypes in Figure 28(b)). Among these five isotypes, IgG being the most abundant immunoglobulin comprises four subclasses (IgG1, IgG2, IgG3 and IgG4), which differ in amino acid sequence in the constant domain. Regardless of the antibody's isotype or subclass, immunoglobulins share a similar structure and functional parts – they consisting of one Fc domain (Fragment crystallizable) and two fragment antigen binding (Fab) domains.[207] The two Fab domains are connected to the Fc part *via* the hinge region, which affords some degree of conformational flexibility for the Fab domains (ribbon representation of an intact antibody pointing out the hinge area depicted in Figure 28(c)). Each Fab is composed of VL and CL from the light chain and VH and CH1 from the heavy chain, whereby VL and VH form the antigen-binding site. On the other side, the Fc part consists of CH2 and CH3 and fulfills the effector function of the antibody by binding to receptors of immune cells, as well as components of the complement system, thus inducing an immune response. The finding that antibodies are composed of three

functional components was made in the 1950's, when IgG was for the first time digested with papain and three proteolytic products of approximately 50 kDa were obtained.[208,209] In the course of characterization, it was found that one of the fragments is able to compete with the intact antibody for antigen binding (Fab), while the other fragment has no antigen binding ability, but can be readily crystallized (Fc).

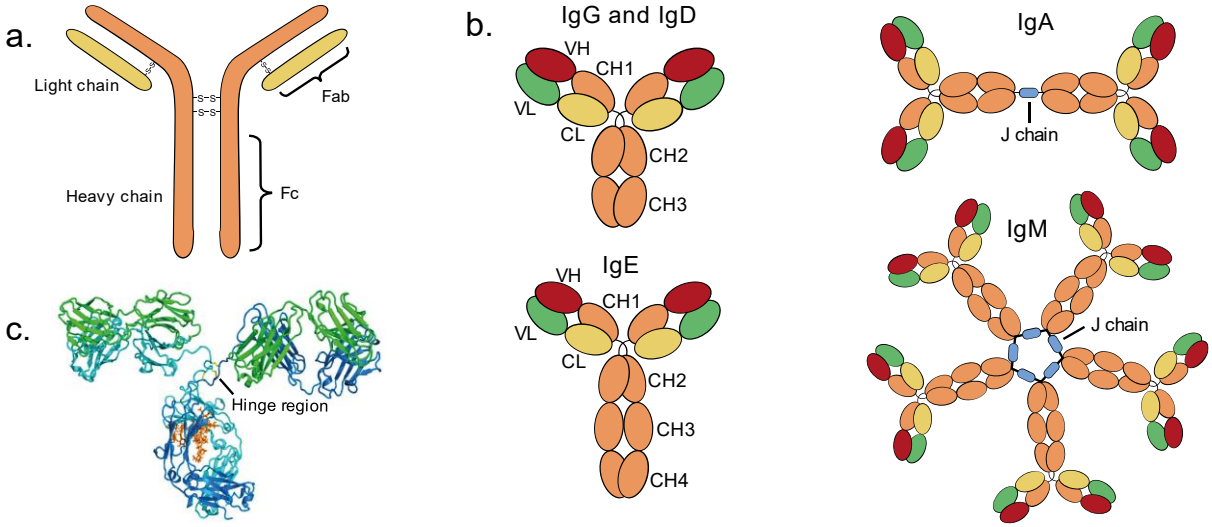

Figure 28. Schematic illustration of (a) antibody structure, (b) different antibody isotypes and (c) ribbon representation of intact immunoglobulin. (a) Antibody sketch to demonstrate the interactions of heavy chains and light chains, as well as disulfide bonds in intact immunoglobulin molecule. Heavy chains in orange and light chains in yellow connected by disulfide bonds (structure corresponding to IgG1, displaying two disulfides at the hinge area); (b) Different immunoglobulin isotypes comprising monomeric IgG and IgD consisting of four heavy chain and two light chain immunoglobulin domains, monomeric IgE consisting of five heavy chain and two light chain immunoglobulin domains, dimeric IgA having the same constant and variable domain structure as IgG and IgD, pentameric IgM having the same constant and variable domain composition as IgE. Antibody moieties in IgA and IgM are connected via the joining (J) chain; (c) Ribbon representation of intact immunoglobulin (mouse IgG2A isotype), structure obtained from Protein Data Bank (PDB)[207]

All antibody domains (such as CL, CH1, etc.) are composed of ca. 110 amino acids and form an "immunoglobulin fold".[207] For the constant domains, the immunoglobulin fold is made of two tightly packed β-sheets, of which one consists of four anti-parallel β-strands and the other one consists of three anti-parallel β-strands. The two β-sheets are held together by an intra-domain disulfide bond, as well as through non-covalent interactions between amino acid side chain residues. In general, the immunoglobulin fold of the constant domains is compact due to the short connection loops between β-strands. Variable immunoglobulin domains display a similar fold as the constant domains, with small alterations in the number of β-strands per β-sheet, as well as in the compactness. The two β-sheets forming the sandwich structure are composed of four and five anti-parallel β-strands respectively and due to longer connecting loops the immunoglobulin fold is less compact than the fold of the constant domains (immunoglobulin fold of constant and variable domains illustrated in Figure 29). Within the

Fab domain the variable VL and VH moieties contain hypervariable loops, referred to as complementarity-determining regions (CDRs), which dictate the antibody's antigen binding ability. Each VL and VH possesses three CDRs (CDR-L1, CDR-L2, CDR-L3 and CDR-H1, CDR-H2, CDR-H3) which form the Fab antigen binding site composed of six CDRs. The sequence and number of amino acids within the CDRs can vary significantly. Especially CDR-H3 offers high sequence variability and is one origin of the diversity in antibody-antigen interactions/recognition. Besides, the six CDRs can adopt different conformations, such as small and deep binding pockets for haptens,[210] groove-shaped depressions between VH and VL for peptides[211] and extended large recognition sites for larger proteins.[212]

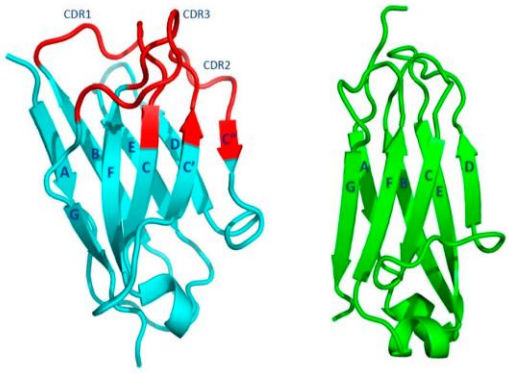

Figure 29. Ribbon structure of immunoglobulin fold of variable domains (left) and constant domains (right). The variable domain's complementarity determining regions (CDRs) are colored in red. Due to large connecting loops in variable domains and short connecting loops in constant domains, the immunoglobulin fold of constant domains is much more compact than the variable counterpart

As earlier mentioned, the Fc part of antibodies is composed of two or three constant immunoglobulin domains. In case of IgG1 the CH3 domains are tightly packed, whereas the CH2 domains do not directly interact with each other.[207] The space between the CH2 domains is filled with two carbohydrate chains being attached to each domain, that are interconnected *via* hydrogen bonds. Due to this indirect link, the two CH2 domains have a high degree of flexibility, which is of high importance for the interaction with Fc receptors of immune cells, as well as elements of the complement system. The connection between Fab and Fc domain, more precisely between CH1 and CH2 is accomplished by a polypeptide region within the heavy chain, which is called the hinge area.[207] The hinge area is divided into three parts: upper hinge, core hinge and lower hinge. While the upper (N-terminal) hinge enables the movement and rotation of Fabs, the core hinge possesses several cysteines that form interchain disulfides and stably connect the two heavy chains. The lower (C-terminal) hinge allows the movement of the Fc relative to Fab domains and in some cases amino acids of the lower hinge are involved in the binding to Fc receptors. There are significant differences in the hinge regions of IgG

subtypes, involving the length, amino acid composition, as well as number of disulfide bonds, altogether contributing to the stability of antibodies and their sensitivity to proteases.

To sum up, an extensive knowledge about the structure-function relationships of antibodies was acquired during the last five decades since the first publications of antibody crystal structures in the beginning of the 1970's. This knowledge in combination with the unique antigen binding ability of antibodies evoked the development of various applications in the field of biomedicine, including targeted anti-cancer therapy and diagnostic imaging. Moreover, antibodies became indispensable tools for *in vitro* assays daily used in research, such as western blots and immunofluorescence. For many of these applications antibodies need to be functionalized and as a consequence, various modification strategies have been developed during recent years.

1.2 Chemical Functionalization of antibodies

1.2.1 Non-selective modifications of amino acid residues

The first antibody modifications that have been performed, and are still widely used for *in vitro* applications, are based on the reaction of accessibly amino acid residues present in the antibody backbone with chemical reagents. The most commonly targeted amino acids are lysines and cysteines, due to their reactivity towards electrophiles, as well as their abundance at solvent accessible sites.[213] The ε-amino group of lysine residues is generally alkylated or acylated, *via* reaction with N-hydroxysuccinimide (NHS) esters, sulfonyl chlorides, isocyanates and isothiocyanates (Figure 30 illustrates common lysine modifications). It needs to be noted that NHS functionalities, although widely used, may cross-react with serine, threonine, tyrosine and cysteine, thereby forming less stable conjugates. In case of antibody drug conjugates, this cross-reactivity is particularly problematic, as the labile bonds resulting from side reactions might lead to premature drug release. Since antibodies contain up to 80 lysines, the modification of lysines leads to non-homogeneous populations of functionalized antibodies with modifications at different sites and different payload-to-antibody ratios (PARs). Moreover, modified lysines being in the proximity of the antigen binding site might impact the target recognition. These features are problematic for batch to batch reproducibility.

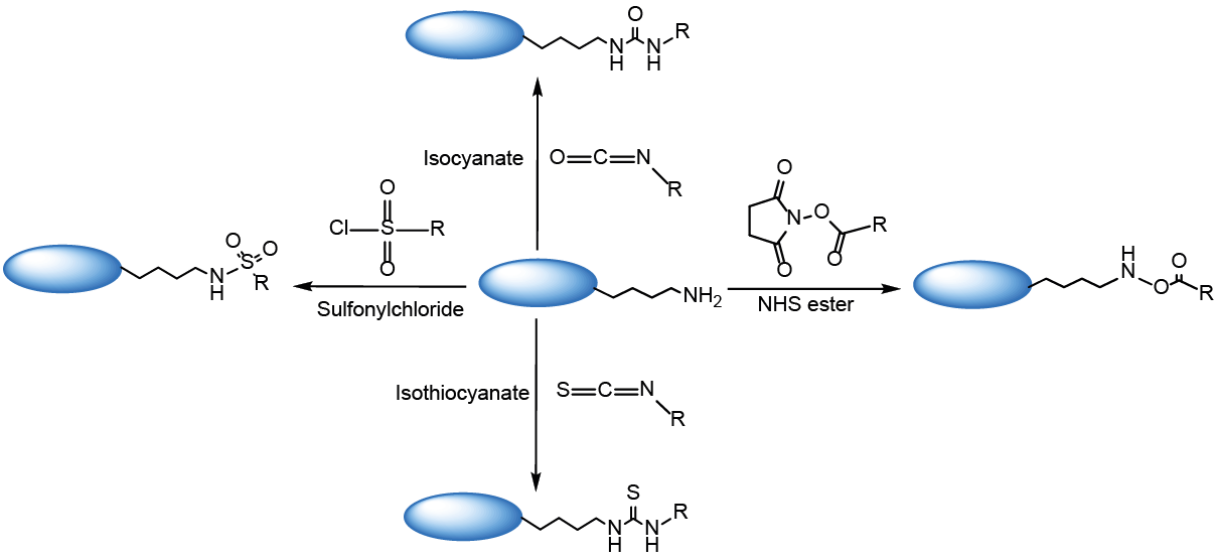

Figure 30. Non-selective functionalization strategies of antibodies by modifying the ε-amino group of lysine residues with N-hydroxysuccinimide (NHS) esters, sulfonylchlorides, isocyanates and isothiocyanates.

Cysteines are much less abundant in immunoglobulins and consequently their chemical modification results in less heterogeneous populations. Depending on antibody isotype and subclass antibodies have different number of interchain disulfides (varying between 4 and 13 disulfide bonds) that can be reduced and targeted for conjugation. The functionalization of cysteines can occur by disulfide exchange, as well as by reactions with electrophiles, such as maleimide or iodoacetamide groups (functionalization of reduced cysteine residues shown in Figure 31). Maleimides are pre-dominantly utilized for the conjugation to cysteines, due to the rapid reaction which can take place under physiological conditions. Yet, if the functionalization site is easily accessible, the modified cysteine is prone to maleimide exchange with albumin, glutathione or other thiol-containing molecules. This unwanted exchange reaction does not occur, if the conjugated maleimide moiety undergoes succinimide ring hydrolysis (illustrated in Figure 31). Based on this knowledge Lyon *et al.* developed self-hydrolyzing maleimides to generate antibody conjugates with improved stability.[214] These self-hydrolyzing maleimides contain a basic group next to the maleimide, which catalyzes the succinimide ring opening, thus forming a stable thioether bond. As the accessibility of interchain disulfides varies, the selective reduction of more solvent exposed cysteines can allow to better control the site of conjugation.[213] For instance, Billah and colleagues reported the site-specific attachment of antibodies to self-assembled monolayer modified gold electrodes by selectively reducing the antibody at the hinge area using 2-mercaptoethylamine, followed by reaction with a maleimide containing linker that allowed the conjugation to the gold electrode.[215] Sun *et al.* also explored the susceptibility of different disulfides in antibodies towards reduction and found that the reduction using dithiothreitol or tris(2-carboxyethyl)phosphine privileged the functionalization

of thiols forming the heavy-light chain connections. Moreover, the authors observed that a partial re-oxidation using DTNB led to antibody conjugates that are mainly functionalized at the hinge region.[216]

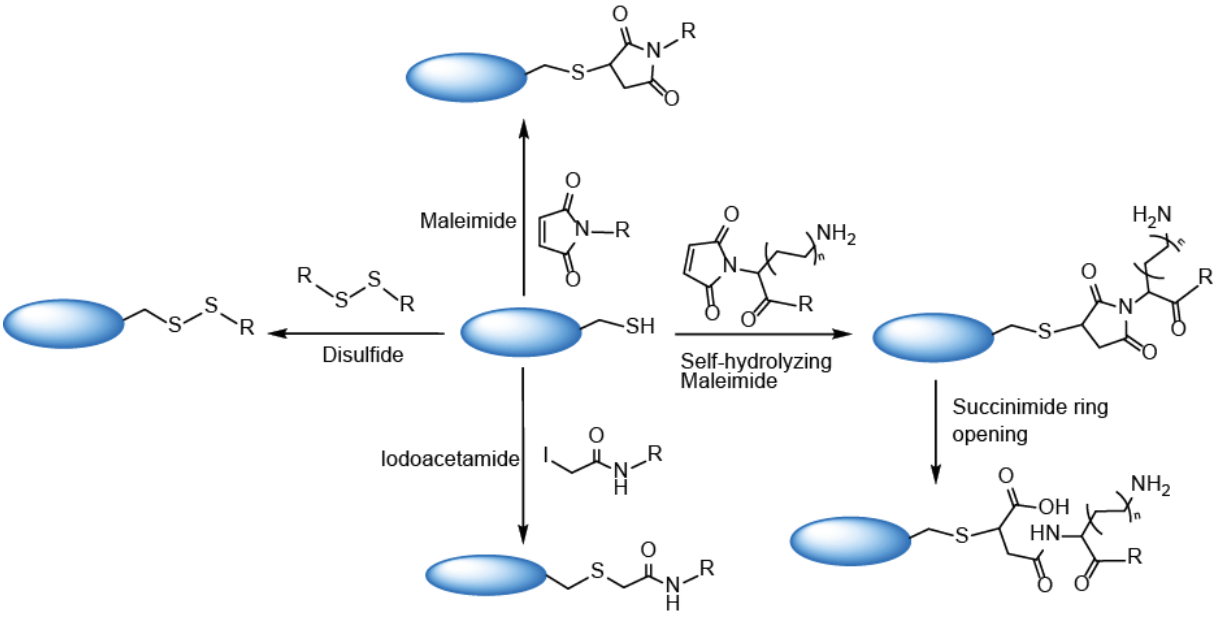

Figure 31. Conjugation strategies for functionalizing antibodies *via* cysteine thiols using iodoacetamides, disulfides, maleimides and self-hydrolyzing maleimides. The succinimide ring opening stabilizes the conjugation product.

1.2.2 Site-selective conjugation strategies

To further improve the uniformity of antibody conjugates, various site-selective conjugation strategies have been developed in recent years. One strategy that has proven valuable for improving the PAR is the incorporation of additional cysteines into the antibody backbone by genetic engineering. Stimmel *et al.* mutated a serine in the immunoglobulin domain CH3 to a cysteine and described the controlled reduction and site-selective modification with a chelator for generating an antibody-radionuclide conjugate.[217] In 2012, Shen *et al.* demonstrated that cysteines that are only partially accessible and surrounded by positively charged groups easily undergo succinimide ring opening, while highly solvent-exposed cysteines are prone to maleimide exchange.[218] So apart from controlling the PAR, cysteine engineering offers the advantage that one can choose a region in the immunoglobulin for the insertion of the additional cysteine that favors the stability of maleimide-thiol bonds by promoting succinimide ring hydrolysis. Despite all these advantages, engineered cysteines can be problematic, as the incorporated reactive thiol groups possibly form intermolecular disulfide bonds, which occasionally results in aggregation.

The incorporation of selenocysteine into the antibody structure is another approach for producing uniform antibody conjugates. Thanks to the nucleophilicity of the selenol group maleimides and iodoacetamides react preferentially with the SeH moiety, even in the presence of thiols. Diselenides, which is the selenium equivalent of disulfides, have a much weaker bond energy than disulfides (172 kJ/mol for Se-Se and 240 kJ/mol for S-S) and consequently eventual intermolecular diselenide bonds formed between selenocysteines introduced into the antibody backbone usually do not need to be reduced prior to their functionalization.[213] This is a huge advantage, since antibody reduction always poses a risk for altering the structure and consequently function of the immunoglobulin.

Unnatural amino acids have also proven particularly useful for the site-selective and controlled functionalization of antibodies, as they permit the introduction of chemical entities that do not occur in the native antibody, hence allowing for orthogonal reactions. For instance, Axup *et al.* reported the production of homogeneous antibody drug conjugates by incorporating *p*-acteylphenylalanine into the anti-Her2 antibody for the conjugation to the drug auristatin.[219] Auristatin was modified with an alkoxy-amine group, which could react with *p*-acteylphenylalanine *via* oxime ligation (orthogonal oxime ligation illustrated in Figure 32 (a)). In the following year the same group presented the incorporation of two different unnatural amino acids (*p*-acteylphenylalanine and azido-lysine) into the anti-HER2 antibody and demonstrated the site-selective modification with a drug and a fluorophore.[220] *p*-acteylphenylalanine was again functionalized with an alkoxy-derivatized drug, while azidolysine was conjugated to a fluorescent dye bearing a cyclooctyne moiety *via* strain-promoted azide-alkyne cycloaddition (also referred to as copper free click reaction, reaction scheme in Figure 32(b)).

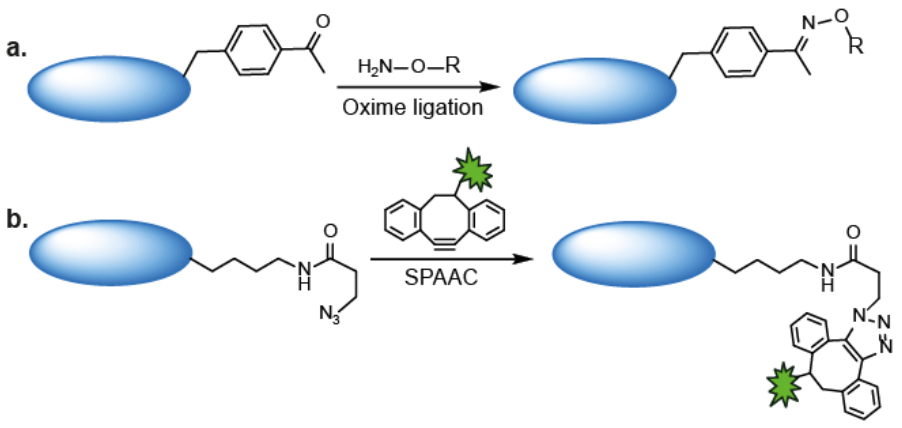

Figure 32. Orthogonal reactions with unnatural amino acids p-acetylphenylalanine and azidolysine. (a) alkoxy amine reacts with the keto group of p-acetylphenylalanine via oxime ligation. (b) Cycloocytne-functionalized fluorescent dye and azide moiety of azidolysine undergo strain promoted azide alkyne cycloaddition.

A totally different strategy for generating uniform antibody conjugates with a defined PAR is the functionalization *via* tags that are recognized by enzymes. A well-known example is the aldehyde-tag approach, in which a peptide sequence including a cysteine (LCxPxR) is cloned into the antibody sequence, and upon treatment with formyl-glycine generating enzyme the aforementioned cysteine is transformed into a formyl-glycine, which selectively reacts with amine oxy or hydrazide groups, thus forming oximes and hydrazones, respectively.[213] The sortase-mediated transpeptidation is another tag approach that is widely recognized. Sortatse A is a bacterial transpeptidase from *Staphylococcus aureus*, which catalyzes the ligation between the amino acid sequence LPxTG and a polyglycine motif. Several groups employed this approach for the functionalization of antibodies and demonstrated its versatility for generating uniform populations of conjugates.[221,222] Moreover, there is the glutaminase strategy, which is based on the enzymatic acyl transfer between γ-caboxyamide of glutamine and various primary amines under loss of ammonia. Initial attempts to produce antibody conjugates with defined PAR were not successful and it remained unclear to which sites the payloads were attached.[223] Jeger *et al*. however discovered that the modification by transglutamination of human IgGs can only occur at glutamine residue 295 situated next to the antibody glycosylation site (asparagine 297) and demonstrated that uniform antibody conjugates containing exactly 2 molecules per antibody can be obtained if asparagine 297 is de glycosylated prior to the transglutamination.[224]

For equipping antibodies with new properties, researchers sometimes address the functionalization of the antibody's carbohydrate structure, as well as the N-terminus.[213] In principle the carbohydrate structure of antibodies is a suitable site for attachment, as it is far from the antigen binding site, but due to variations in the glycosylation pattern between antibodies, the obtained antibody conjugates are often heterogeneous. For selectively functionalizing the N-terminus of antibodies *via* acylation, the difference in pKa of the α-amino group and ε-amino group of lysines is exploited.[225] The advantage of this approach is the applicability for in principle any antibody, but as the yield strongly depends on the physicochemical properties of the N-terminal amino acid, yields vary from 0 – 70%.[213]

Taken together a vast number of antibody conjugation strategies has been developed over the last years, with particular emphasis on site-selective approaches leading to homogenous antibody conjugates with defined PARs. While non-selective conjugation techniques are simple to perform and sufficient for many *in vitro* applications, medical applications usually require defined antibody conjugates, as the pharmacokinetic profile can significantly vary between antibody conjugates with different PARs and sites of attachment. Although not for the same

reason, the requirements regarding PAR and site of attachment, apply to immunogold probes as well, as only a controlled conjugation allows to directly relate the observed signal to the actual object.

1.3 Conjugation of antibodies to gold nanoparticles

Since AuNPs have been extensively employed for imaging, as well as sensing applications, which demands equipping the nanoparticles with targeting properties, researchers devoted time and efforts to develop conjugation strategies permitting the linkage of antibodies to the surface of AuNPs.[226] Generally speaking, there are three main approaches for immobilizing antibodies on AuNPs: (i) adsorption, (ii) covalent linkage and (iii) conjugation *via* adaptor molecules.[227] When functionalizing AuNPs with antibodies several issues need to be considered, such as the number of antibodies per AuNP, the orientation of the antibody, as well as the stability of the conjugate, and based on the requirements for the final AuNP-antibody conjugate or its application, the adapted conjugation strategy needs to be chosen.

The adsorption of antibodies on AuNPs is a non-covalent immobilization based on physical and ionic interactions. AuNPs contain a negatively charged surface coating and consequently antibodies containing a high number of basic amino acids (lysine and arginine) are stronger bound to the nanoparticle surfaces, than antibodies comprising a lower number of these amino acids. The process of adsorption is simple and quick to perform but suffers from several drawbacks. Firstly, the antibodies are randomly oriented on the AuNP surface, which eventually makes the antigen binding sites inaccessible to the target, or affects the structure of the antibody, thus impairing its binding ability. Secondly, ionic binding is strongly influenced by the pH and electrolyte concentration, rendering the conjugate instable to solvent variations. Thirdly, the conjugation *via* adsorption results in batch to batch variations.[226] For many *in vitro* applications, these issues are irrelevant, as pH and salt concentration can be easily controlled and in many cases the antibodies' targeting ability is fortunately not significantly impaired.[226] AuNP-based biosensors are often generated by the adsorption strategy[228–230] and immunogold EM probes allowing the labeling of selected proteins inside cells or tissue sections are classically generated by adsorbing antibodies on AuNPs as well.[101]

The covalent conjugation of antibodies to AuNPs is less straightforward but allows the generation of more stable and reproducible conjugates. The reagent that is most often employed for covalent conjugations is the water-soluble N-(3-Dimethylaminopropyl)-N'-

ethylcarbodiimide (EDC), but maleimide, click chemistry partners and NHS esters described in the previous section are used as well. For covalently linking antibodies to the surface of AuNPs, either the AuNP, or the antibody, or both of them need to be modified with bifunctional linkers permitting the formation of a covalent bond. In case of carbodiimide-promoted coupling a common approach is to first modify citrate capped AuNPs with mercaptoundecanoic acid (MUA). The thiol group of MUA allows the coordination of the carboxyl group to the AuNP's surface and hence, the subsequent carbodiimide-mediated coupling with amine-containing domains, or the reaction with NHS for equipping the gold surface with activated NHS esters, making the AuNP more reactive towards the primary amines of antibodies (carbodiimide coupling reaction is illustrated in Figure 33).[231] Since antibodies possess both primary amines and carboxyl groups, it is important to always remove excess EDC/NHS after the activation of the AuNP's carboxyl group, prior to the addition of the antibody. In case this is not performed, remaining EDC/NHS risk to activate the carboxyl moieties of aspartate and glutamate residues of the antibody, thereby promoting self-polymerization of the antibody.[226] AuNP-antibody conjugates generated by carbodiimide coupling display a higher stability than conjugates produced by the adsorption method and furthermore, the number of antibodies per particle can be controlled to a certain extent, as the MUA/AuNP ratio can be varied. However, the conjugated antibodies are randomly oriented on the AuNP surface, since antibodies contain about 30 surface exposed lysine residues.

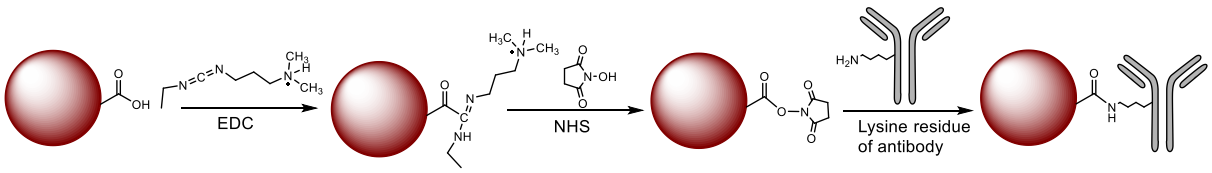

Figure 33. Conjugation of antibody to AuNP *via* carbodiimide coupling. Activation of carboxyl group on AuNP with EDC and NHS, followed by reaction with ε-amine of lysine from antibody resulting in the formation of an amide bond.

In order to equip AuNPs with antibodies being all oriented in the same manner, more sophisticated covalent conjugation approaches have been developed. García-Fernández *et al.* reported the functionalization of 17 nm AuNPs with the antibody Cetuximab and described a well-defined orientation of the antibody molecules on the nanoparticle surface.[232] In this approach the carbohydrate molecules attached to the antibody's constant region were firstly oxidized to introduce aldehyde moieties into the antibody and then these aldehydes were reacted with a bifunctional linker containing a hydrazide group (forming a hydrazone with the aldehyde) and a dithiol entity that enables the coordination to the AuNP. Mustafaoglu and coworkers presented another strategy enabling the oriented conjugation of antibodies to AuNPs

via the UV-NBS method.[233] The UV-NBS method relies on the linkage of indole-3-butyric acid to the nucleotide binding site (NBS) of antibodies.[234] The NBS is conserved in antibodies and has a high affinity for indole-3-butyric acid, which upon UV irradiation can be linked to the NBS (schematic illustration in Figure 34(a)). Mustafaoglu *et al.* mixed antibodies targeting the prostate specific antigen (PSA) with a bifunctional linker containing on the one hand indole-3-butyric acid, on the other hand 1,2-dithiolane (from thioctic acid). After UV exposure the functionalized antibody could be linked to the AuNP *via* Au-S coordination thanks to the 1,2-dithiolane. The generated conjugate showed enhanced detection ability for PSA compared to conjugates obtained by adsorption or carbodiimide chemistry. The copper(I)-catalyzed 1,3 dipolar cycloaddition (click chemistry) was also employed for covalently conjugating antibodies to AuNPs in a controlled and correctly oriented manner. Finetti *et al.* generated AuNPs coated with a synthetic polymer into which alkyne moieties have been introduced. In parallel the authors functionalized an anti-mouse IgG with an azide group, thereby permitting the linkage to the AuNP through triazole formation (shown in Figure 34(b)) .[235]

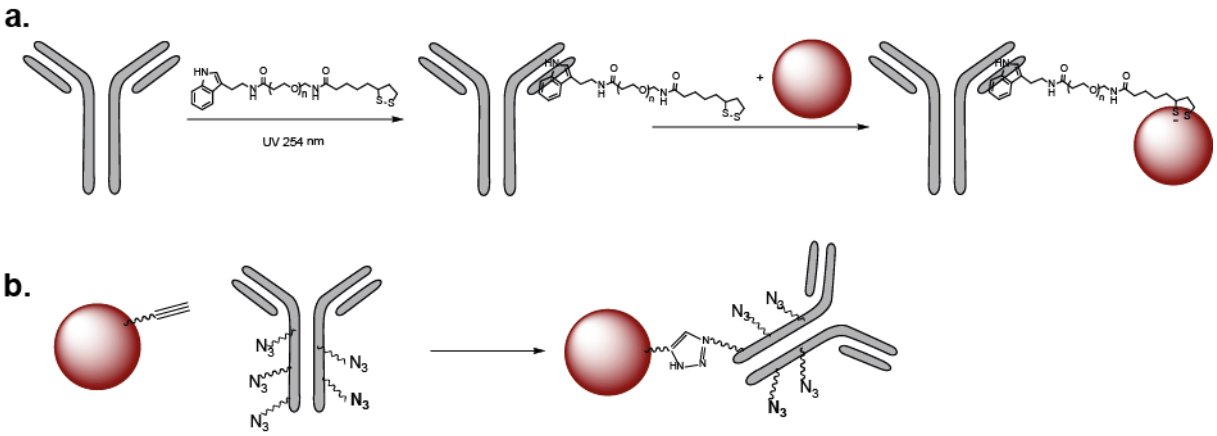

Figure 34. Conjugation of antibody to AuNP *via* (a) UV-NBS method and (b) copper(I)-catalyzed 1,3 dipolar cycloaddition. (a) Bifunctional linker (containing indole-3-butyric acid and thioctic acid) is conjugated *via* the indole-3-butyric acid group to the nucleotide binding site of the antibody under UV exposure (254 nm). Functionalized antibody is hence coordinated to the AuNP *via* thioctic acid moiety. (b) AuNP functionalized with alkyne moiety reacts with azide bearing antibody *via* copper(I)-catalyzed 1,3 dipolar cycloaddition resulting in the formation of a triazole bond.

In 1992 Hainfeld and Furuya reported the conjugation of a 1.4 nm phosphine-protected AuNP containing one maleimide functionality to a rabbit anti-human red blood cell IgG for immunolabeling purpose.[105] The authors reduced the antibody selectively at the hinge region using mercaptoethylamine and reacted the reduced thiols with the maleimide functionality present on the AuNP.

The strategy of using adaptor molecules for the conjugation of antibodies to AuNPs is another way of ensuring the uniform attachment of antibodies. The interaction between biotin and avidin is most commonly exploited for the linkage of antibodies to AuNPs.[226] Biotin is a small molecule that can be easily linked to antibodies, whereas avidin is a large protein that can be readily adsorbed to the surface of AuNPs. Due to the positive net charge of avidin the adaptor molecule is strongly bound to the negatively charged AuNP surface, thus forming a stable base for the biotinylated antibody. Hsieh *et al.* explored another interaction for the conjugation of antibodies to AuNPs – the interaction between protein A and the Fc part of antibodies.[228] Similar to the biotin/avidin strategy, protein A was simply adsorbed to the AuNPs, which permitted the binding of the immunoglobulins in a homogeneously oriented manner.

Altogether three main methods are employed to conjugate antibodies to AuNPs, including adsorption, covalent linkage and conjugation *via* adaptor molecules. Each approach has its advantages and pitfalls and it is of uttermost importance to choose the right strategy for each particular application. Moreover, it should be mentioned that for optimizing the conjugation strategy it is essential to have a reliable method allowing to characterize the antibody-coverage of the AuNP.

In the work presented in the following we aimed at conjugating the 2.4 nm TNB-, TAB-protected AuNPs to the hinge area of antibodies *via* direct Au-S coordination, thereby producing conjugates consisting of one particle per antibody. This type of direct Au-S conjugation has been reported for single chain variable fragments (scFv) by Levi-Kalsiman *et al.* using Au_{102}(*p*-MBA)$_{44}$, but thus far never for intact antibodies. The site-selective attachment at the hinge region offers the advantage that the overall size of the conjugate is not significantly larger than the size of the native antibody and that the distance between the electron-opaque AuNP and the target is known, which might allow to exactly pinpoint the targeted antigens by high-resolution EM. After having established this site-selective conjugation and evaluated the bioconjugates' antigen binding abilities, we investigated whether the produced probes permit the labeling of targets in live cells.

2 Materials and Methods

2.1 Antibodies

Antibodies Cetuximab (Cmab) and Bevacizumab (Bmab) were a gift from Centre de lutte contre le Cancer Paul Strauss (France) and originally bought from Roche and Merck KGaA, respectively. The initial buffer solution of Cmab and Bmab was changed to PBS using illustra NAP-10 column (GE Healthcare). The antibody 7G5 targeting the non-phosphorylated C-terminal domain of the largest subunit of RNA polymerase II was produced in house, raised in mouse.

2.2 Synthesis of AuNP-antibody conjugates

Initially, the reduction conditions necessary to reduce the antibodies 7G5, Cetuximab and Bevacizumab at the hinge area were determined for each antibody separately by incubating 4 µL of a 2 mg/mL antibody solution in PBS with 3 µL of a Tris(2-carboxyethyl)phosphine-HCl (TCEP) solution, pH 7.4 for 1.5 h at 37°C (0.1 – 4 mM final TCEP concentration). The reduction of the antibodies was subsequently analyzed on non-reducing 10% SDS gels. Having determined the appropriate TCEP concentration for each antibody, 2 mg/mL antibody solutions in PBS (225 µl, 0.45 mg, 2.9 nmol) were mixed with 90 µL of TCEP (concentration indicated in results section for each antibody) for 1.5 h at 37 °C. Then, AuNPs of 2.4 nm at a concentration of 42 µM (73 µl, 3.06 nmol) were added to the reduced antibodies (297 µl, 0.42 mg, 2.8 nmol) in 0.1M HEPES buffer, pH 7.5 at 25 °C and the reaction was let to proceed overnight. The next day the AuNP-antibody conjugates were passivated with a 1 mM solution of peptide Cap [CALNNG] or alpha-methoxy-omega-mercapto poly(ethylene glycol) (123 µl, 123 nmol or 40 molar eq. of AuNP-antibody conjugate) for 4 h at 25 °C in 0.1M HEPES buffer, pH 7.5. The released TNB-/ TAB-ligands and excess thiolated molecules were removed by ultrafiltration using Amicon 100 K ultracentrifugal devices, if not stated otherwise.

2.3 Cell culture

All cell lines were grown in a humified incubator at 37°C, supplied with 5%CO_2. Human cancerous HeLa cells (ATCC CCL2) and non-cancerous human foreskin fibroblast cells (HFF-1, ATCC SCRC-1041) were maintained in Dulbecco's modified eagle medium containing 2 mM L-glutamine, 10 mM HEPES buffer, pH 7.0, 10% heat-inactivated fetal bovine serum

(FBS) and 50 µg/mL gentamycin. The human U87 glioblastoma cell line (U87 MG, ATCC HTB-14), the EGFR(+) U87 cell line (gift from Professor Furnari)[236] and the human fibrosarcoma cell line (HT-1080, ATCC CCL-121) were grown in Eagle's minimum essential medium containing 10% fetal bovine serum, 1% sodium pyruvate and 1% nonessential amino acids. For co-culturing the EGFR(+) U87 glioblastoma cell line and the non-cancerous HFF cell line, cells were grown in Opti-MEM cell culture medium containing 10% FCS. For immunofluorescence and immunocytochemistry experiments (revelation of AuNP domain by silver enhancement for optical microscopy) cells were seeded into 24-well plates at a density of 25000 cells/well and were let to adhere on glass coverslips overnight.

2.4 Immunolabeling of fixed cells

HeLa cells were seeded on glass-coverslips in 24-well plates the day before the experiment at a density of $5*10^4$ cells/mL. Cells were fixed with 4% PFA in PBS (20 min), aldehydes were quenched with 50 mM glycine in PBS (20 min) and cells were permeabilized with 0.2% triton in PBS (5 min). Between each of these steps, cells were washed with PBS (3 times). Then, cells were incubated with 10% BSA in PBS (1 h) and washed with 0.2% acetylated BSA, BSA-c, (2 times 5 min). The AuNP-IgG conjugates were diluted in 0.2% BSA-c containing 10% FCS and 10 mg/mL heparin. Cells were soaked in the conjugate and antibody solutions (5 nM) for 1 h, before being washed again with 0.2% BSA-c (2 times 5 min). Next, the presence of the conjugate/antibody was revealed by immunofluorescence, as well as gold-induced silver staining. For immunofluorescence, the cells were soaked in 10% FCS in PBS containing goat anti-Mouse IgG (H+L) Antibody, Alexa Fluor 488 (diluted 1:3000) for 1 h, washed with PBS (3 times) and finally the coverslips were mounted using DAPI Fluoremount-G (SouthernBiotech). The silver staining procedure permitting the revelation of the AuNP domain was performed following a modified protocol from the Danscher method, as described in Groysbeck *et al.* 2019,[156] attached to the thesis in the appendix.

2.5 Electroporation of AuNP-antibody conjugate

Electroporation was performed as described in Material and Methods section of Chapter 1 using 10 pmol of the GFP-targeting AuNP-antibody conjugates and AuNP solutions as control.

SDS-PAGE analysis, Western Blot, preparation of cellular specimen for AuNP-antibody conjugate detection (immunofluorescence and AuNP-induced silver staining), downregulation of EGFR expression in U87 MG cells, EGFR binding assay, assay of EGFR-mediated endocytosis and MTT test were performed as described in Groysbeck *et al.* 2019 attached to the thesis in the appendix.[156]

3 Results

3.1 Site-selective conjugation of gold nanoparticles to antibodies

Inspired by the work of Levi-Kalisman *et al.*, who reported the direct conjugation of an Au_{102}(*p*-MBA)$_{44}$ nanoparticle to thiolated DNA, as well as an scFv containing an N-terminal cysteine *via* Au-S coordination,[147] we evaluated the ability of the TNB-/ TAB-protected AuNPs to react with reduced sulfhydryl groups at the hinge area of antibodies, with the aim of producing a conjugate consisting of one AuNP per antibody. Besides the control over the stoichiometric AuNP:antibody ratio, the attachment of the AuNP at the hinge region offers the advantage that the distance between the contrasting domain and the target is known. Although it is well-known that the selective reduction of antibodies at the hinge area does not perturb the non-covalent interactions between the two heavy chains within the Fc region, due to which the antibody maintains its quaternary structure, we assumed that the TNB- /TAB-stabilized AuNPs are small enough to reach the hinge are and to react with the reduced sulfhydryls *via*-thiolate-for-thiolate exchange. As models, we selected the therapeutic antibodies Cetuximab (Cmab) targeting the epidermal growth factor receptor (EGFR) and Bevacizumab (Bmab) targeting the vascular endothelial growth factor (VEGF), as well as an in house made antibody raised in mouse, named 7G5, targeting RNA polymerase II. For the site-selective conjugation to the three antibodies, we chose to use the 2.4 nm AuNP AuG, for the following reasons. First, AuNPs > 2 nm have been reported to be directly detectable by HAADF-STEM when embedded in cell sections, permitting to avoid silver staining.[108] Second, AuG was able to freely diffuse inside living cells after electroporation, as well as to passively diffuse into the nucleus, which was not the case for the 2.6 nm AuNP (AuL).

At an initial stage, the reaction conditions for selectively reducing the three antibodies at the hinge area were evaluated. We therefore mixed the antibodies with the thiol-free and weakly nucleophilic reducing agent TCEP at different concentrations (ranging from 0.1 mM to 4 mM TCEP final concentration) and incubated the mixture for 90 min at 37°C. Afterwards, the reduced antibodies were analyzed by SDS-PAGE under non-reducing conditions, thus showing the intact antibody at 150 kDa and the antibody with reduced hinge disulfides at 75 kDa. The SDS gels of the test reductions (depicted in Figure 35) revealed that Cmab was completely reduced with a final TCEP concentration of 2 mM, Bmab with a final TCEP concentration of 0.1 mM and 7G5 with a final TCEP concentration of 1 mM. The observation that the three antibodies required different concentrations of TCEP for achieving a full reduction of the hinge disulfide bonds was surprising, since all three antibodies belong to the IgG1 subclass, thus

contain 2 disulfides at the hinge area. By comparing the amino acid sequences of the two therapeutic antibodies Cmab and Bmab (available on drugbank.ca) the observed proneness to reduction becomes even more puzzling, since the amino acid sequence at the hinge area, as well as approximately 100 amino acids on the N-terminal and the C-terminal site match exactly between the two antibodies (heavy chains of human IgG1 antibody). Yet, it could be presumed that differences in the glycosylation pattern, which strongly depend on the way of antibody production and sometimes vary from batch to batch, might be the reason why the three IgG1 antibodies required different concentrations of TCEP to achieve a complete reduction of the hinge disulfides.

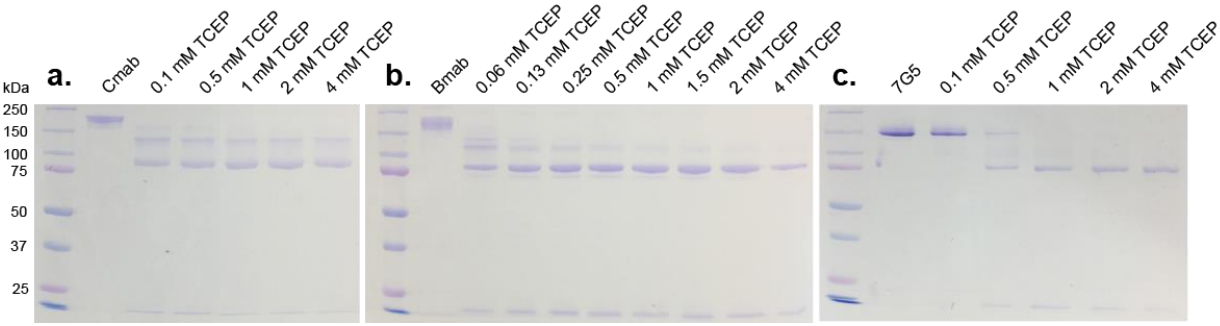

Figure 35. SDS-PAGE analysis (10% gels) for evaluating the ideal TCEP concentration for selectively reducing the antibodies Cmab (a), Bmab (b) and 7G5 (c) at the hinge area. The TCEP concentrations were varied from 0.1 mM to 4 mM as indicated above the lanes showing the reduced antibodies. In case of Bmab the concentration of TCEP was increased using smaller increments, since it was observed that the antibody is more susceptible to reduction, than Cmab, or 7G5.

Next, the reduced antibodies were reacted with AuG using a slight excess of the AuNP (AuG/IgG of 1.2) to ensure that no unlabeled antibodies remain in the reaction mixture. Thanks to the ability of the AuNPs to migrate into SDS gels, the conjugation progress could be monitored by SDS-PAGE. For protein detection SDS gels were stained with Coomassie blue and for enhancing the slightly brown color of the AuNP-antibody conjugates (caused by the presence of AuG), the gels were moreover stained with silver ions. After the thiol-specific reaction of the reduced antibodies with AuG, the nanoparticles were passivated with peptide Cap in order to exchange all remaining reactive TNB-/ TAB-ligands and to cover the AuNPs with an inert peptide layer. The reason for choosing peptide Cap for the passivation of AuG over 2000 Da PEG, which has proven highly suitable for the surface coating of the 2.4 nm AuNP, was the aim to keep the hydrodynamic diameter of the nanoparticle as small as possible at an initial stage. The SDS-PAGE analysis of three conjugation reactions (Figure 36 (a) conjugation to Cmab, (b) conjugation to Bmab and (c) conjugation to 7G5) revealed that the thiolate exchange on the AuNP surface with the hinge sulfhydryls of the reduced antibodies

proceeded smoothly, which was reasoned from the occurrence of a brown colored band at 150 kDa and no remaining band at 75 kDa, corresponding to the reduced antibodies, in the lane of Au-Cmab (Figure 36 (a)), Au-Bmab (Figure 36 (b)) and Au-7G5 (Figure 36 (c)), which are the final reaction products of the conjugation of AuG to Cmab, Bmab and 7G5, respectively, after passivation with peptide Cap. It needs to be mentioned that the brown bands at 150 kDa assigned to the AuNP-IgG conjugation products only occurred when the antibodies were reduced at the hinge area and not if AuG was added to intact antibodies (see Figure 65, Supporting Information), demonstrating that AuG indeed binds to the hinge thiols in the expected manner and not by adsorbing to the antibody. Besides the band at 150 kDa in the lane of Au-Cmab, Au-Bmab and Au7G5, a second brown band at approximately 250 kDa is visible, which might result from a dimerization of the IgGs. It needs to be noted that in case of Au-Cmab the proportion of the band at 250 kDa was less than 10%, whereas the proportion in the lane of Au-Bmab and Au-7G5 was higher, roughly estimated to about 20%. Based on the results from the SDS-PAGE analyses and the knowledge about the stoichiometric ratio used for the conjugation reactions, we assumed that the major apparent band at 150 kDa corresponds to a 1:1 AuNP-IgG conjugate, while the additional band at 250 kDa might either result from the formation of a AuNP-$(IgG)_2$ conjugate, or an aggregate of two 1:1 AuNP-IgGs. The point that the electrophoretic mobility of the AuG-antibody conjugates (Au-Cmab, Au-Bmab and Au-7G5) was almost the same as the one of the unconjugated antibodies appears puzzling at first glance. Yet, the fact that AuG, having a MW of 80 kDa, does not migrate like an 80 kDa protein on SDS gels can be readily explained by the negative charge of the nanoparticle, as well as by the high volumetric mass density of gold (19.3 g/mL). In all three cases a small amount of unreacted AuG was present in the AuNP-IgG conjugation products (brown band with high electrophoretic mobility in the lane of Au-Cmab, Au-Bmab and Au-7G5), which likely results from the slight excess of AuG that was used for the conjugation reactions.

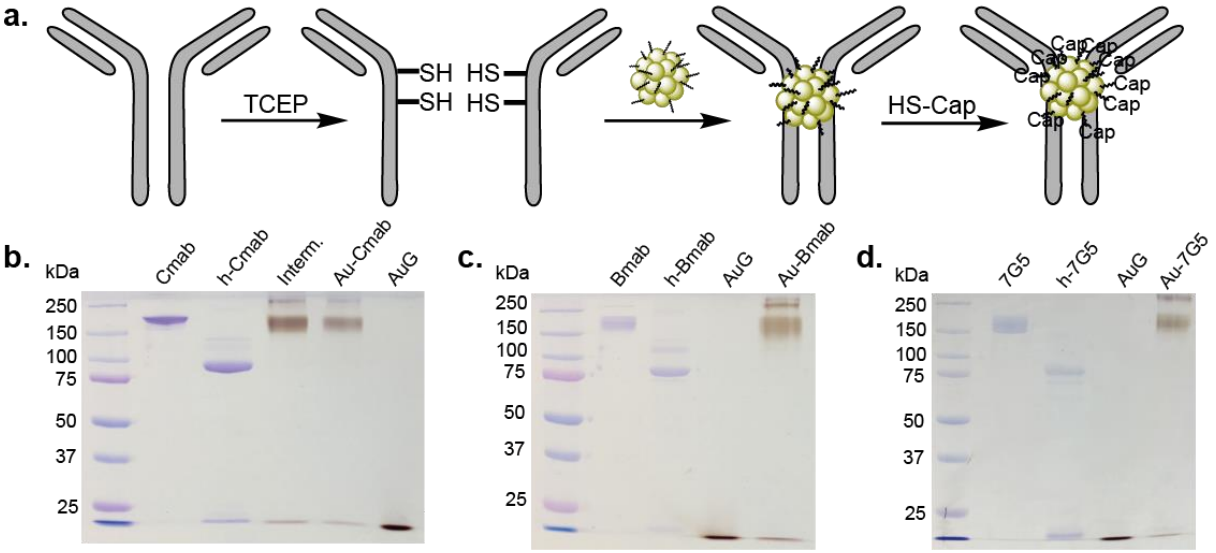

Figure 36. Schematic illustration of AuG-antibody conjugation strategy in (a) and SDS-PAGE analyses of the conjugate formation on 10% SDS gels under non-reducing conditions in (b – d). (a) Site-selective conjugation strategy. 1st step: Reduction of the antibody's hinge disulfides, 2nd step: Thiolate-for-thiolate exchange of reduced antibody's hinge thiols with AuG ligands, 3rd step: Passivation of AuG with peptide Cap; (b) Au-Cmab formation. Order on the gel from left to right: Cetuximan (Cmab), selectively reduced Cetuximab (h-Cmab), AuG-Cetuximab before passivation (Interm.), AuG-Cetuximab conjugate after passivation with Cap (Au-Cmab), gold nanoparticle AuG; (c) Au-Bmab formation. Order on the gel from left to right: Bevacizumab (Bmab), selectively reduced Bevacizumab (h-Bmab), gold nanoparticle AuG (AuG), AuG-Bevacizumab conjugate after passivation with Cap; (d) Au-7G5 formation. Order on the gel from left to right: Antibody 7G5 (7G5), selectively reduced 7G5 (h-7G5), gold nanoparticle AuG, AuG-7G5 conjugate after passivation with Cap (Au-7G5).

Finally, the exchanged TNB-/ TAB-ligands, as well as excess passivation agent (peptide Cap) were removed from the conjugates using ultracentrifugal devices having a cut-off at 100 kDa. At the present stage, the as-prepared AuNP-IgG conjugates (Au-Cmab, Au-Bmab and Au-7G5) were not further purified, since the un-reacted ANPs present in the conjugation products were expected to do not interfere during antigen targeting.

3.2 Characterization of binding ability of AuNP-IgG conjugates

To examine whether the attachment of the 2.4 nm AuNP AuG at the hinge area has an impact on the biological activity of the antibodies, we evaluated the ability of the conjugates to bind to their antigens, compared to the unconjugated antibodies. As mentioned earlier, Cmab targets the EGFR, an extracellular receptor overexpressed on many cancer cells, Bmab targets the VEGF, a signal protein secreted by cells to promote the formation of blood vessels, and 7G5 targets the RNA polymerase II, transcribing DNA into mRNA, being localized inside the nucleus. Since the VEGF is a secreted protein and thus neither localized on the cell surface (as it is the case for EGFR), nor inside the cell (as it is the case for 7G5), the binding ability of Au-

Bmab was not evaluated, but instead the conjugate served as a control during the characterization of Au-Cmab and Au-7G5. In the interest of simplification, we first tested the targeting ability of Au-Cmab, since the EGFR is localized on the cell surface and the binding to the receptor does not require the conjugate to be delivered into (living) cells.

3.2.1 Biological characterization of Au-Cmab

The biological evaluation of the Au-Cmab conjugate was described in detail in the scientific article "Synthesis and biological evaluation of 2.4 nm thiolate-protected gold nanoparticles conjugated to Cetuximab for targeting glioblastoma cancer cells via the EGFR", which was published in the journal *Nanotechnology* (Groysbeck *et al*. 2019)[156] and is included in the appendix of this thesis. A summary of the biological characterization of Au-Cmab will be recapped in the following paragraph.

For evaluating the capability of Au-Cmab to selectively bind the EGFR, a U87 glioblastoma cell line overexpressing the EGFR (hereafter referred to as EGFR(+) U87) was used. As a control, the EGFR expression of U87 wild type cells was knocked down using siRNA-mediated gene silencing (cells hereafter referred to as EGFR(-) U87). In a first experiment living EGFR(+) and EGFR(-) U87 cells were incubated with Cmab, Au-Cmab and Au-Bmab for 30 min and after three washes with PBS, the cells were fixed, permeabilized and the localization of the conjugates was detected by revealing the gold, as well as antibody domain, using gold-induced silver enhancement and immunofluorescence (IF), respectively (Figure 37). The data showed that only Cmab and Au-Cmab bound to the surface of EGFR(+) U87 cells, indicating that the antigen binding ability of Cmab was not perturbed by appending the 2.4 nm AuG at the hinge area of the antibody. It needs to be noted that the EGFR(+)/EGFR(-) U87 cells incubated with Au-Bmab showed some silver staining in endosomes as well, suggesting that the AuNP domain has a slight tendency of binding to cell surfaces, thus promoting endocytic uptake. Yet, the silver staining pattern of the cells that were incubated with Au-Bmab was not seen on the corresponding IF images. This inconsistency might either result from the higher sensitivity of the silver staining, compared to IF, or the endocytosed material observed in the silver stained images of the Au-Bmab treated cells resulted from the small amount of unreacted AuNPs which were not removed from the conjugation products, due to their low quantity.

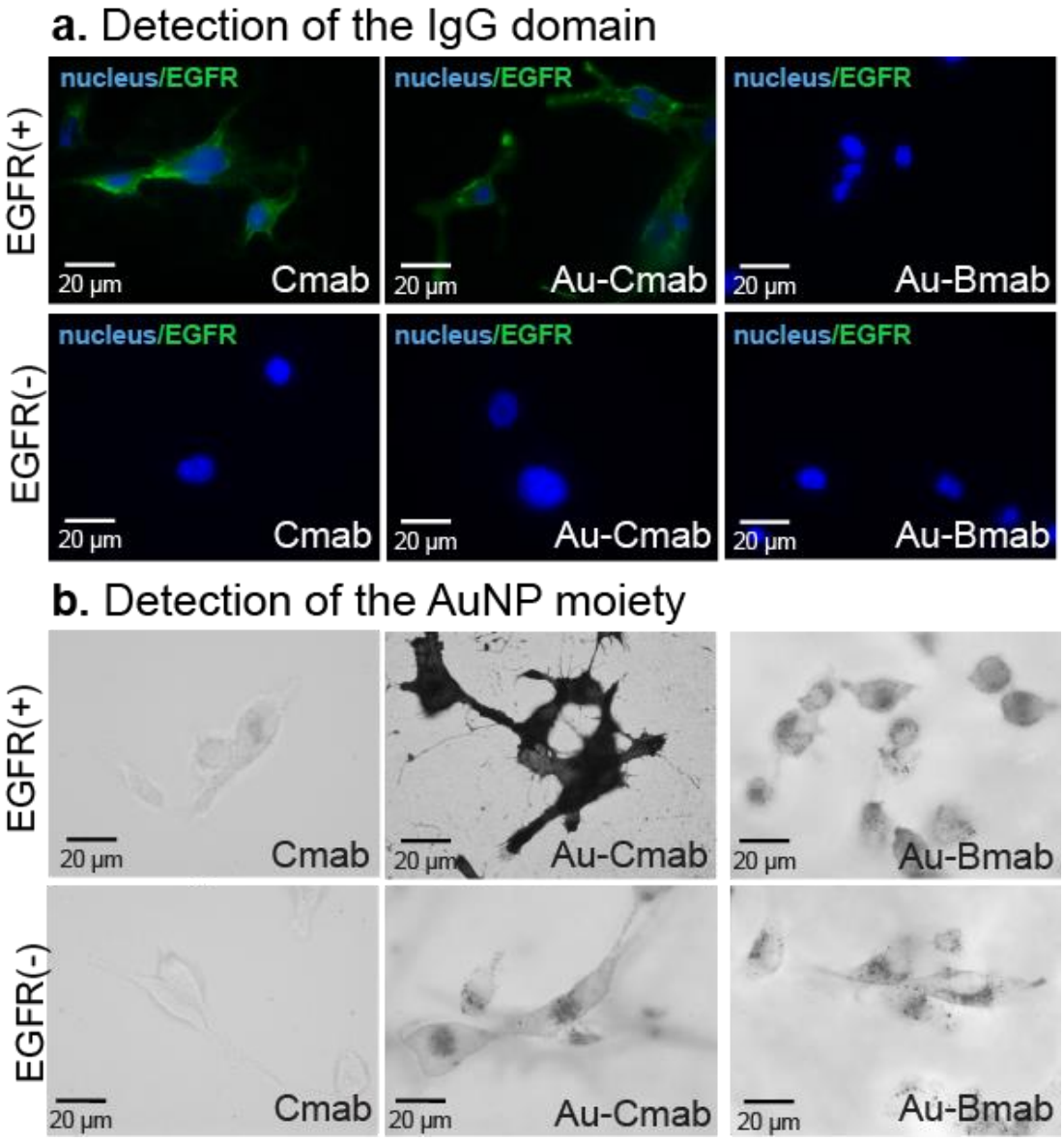

Figure 37. Evaluation of EGFR targeting ability of Cmab, Au-Cmab and Au-Bmab using living EGFR(+) U87 cells and EGFR(-) U87 cells as control. (a) The antibody/conjugates were revealed by detecting the IgG domain *via* secondary IF; (b) The localization of the conjugates was assessed by detecting the AuNP domain *via* silver staining. Scale bar: 20 µm.

To assess whether Au-Cmab has an altered affinity towards EGFR, compared to the unconjugated Cmab, the binding study described before was repeated using concentrations varying from 0.67 pM to 167 nM. The binding of the antibody and the conjugate was revealed by IF and an on/off fluorescence detection threshold as a function of the concentration was identified. The results from this rough quantitative analysis demonstrated that the detection of surface-bound EGFR requires 10 times more of Au-Cmab, compared to Cmab, implying that the site-selective conjugation of AuG was not completely traceless.

Next, we tested the ability of Au-Cmab to internalize into EGFR(+) U87 cells, as well as to inhibit EGFR autophosphorylation, which are both characteristic effects of the therapeutic

antibody. The obtained data showed that the Au-Cmab conjugate is internalized by EGFR-overexpressing cells and efficiently blocks the autophosphorylation of EGFR, which demonstrates that the biological activity of Cmab, going beyond the binding to its target, was not impaired by the linkage to AuG. However, slight differences between Cmab and Au-Cmab were noted in both experiments, which emphasizes the above-made deduction that the attachment of the 2.4 nm AuNP at the hinge area of Cmab may not be completely innocuous. Finally, we demonstrated that Au-Cmab is able to distinguish between EGFR(+) U87 cells and EGFR(-) non-cancerous HFF cells being co-cultured, thus confirming the selectivity of Au-Cmab towards EGFR.

3.2.2 Evaluation of the targeting ability of Au-7G5 to RNA polymerase II

The characterization of the AuNP-IgG conjugate Au-7G5 for its ability to target RNA polymerase II (RNAP II) was more sophisticated, than the biological evaluation of Au-Cmab, since RNAP II is localized inside the nucleus and therefore requires passage of Au-7G5 across the plasma membrane, diffusion inside the cytosol and entry into the nucleus for biding to RNAP II. As a first step, prior to tackling the targeting of the multiprotein complex inside living cells, we tested the RNAP II specific binding ability of Au-7G5 on fixed and permeabilized cells.

To evaluate the binding ability of Au-7G5 to RNAP II using fixed cells, HeLa cells adhered to glass-coverslips were fixed with 4% PFA and the plasma membranes were permeabilized with Triton X-100®. The cells were then soaked in solutions containing the Au-7G5 conjugate, as well as the 7G5 antibody as control (final antibody concentrations of 5 nM). After 1 h of incubation, excess antibodies were removed by several washes. The bound conjugates were then detected making use of either the AuNP domain (gold-induced silver staining) or the antibody moiety (secondary IF) as described for the binding study of Au-Cmab. Figure 38 shows the fluorescence and bright-field microscopy images of the immunolabeled HeLa cells.

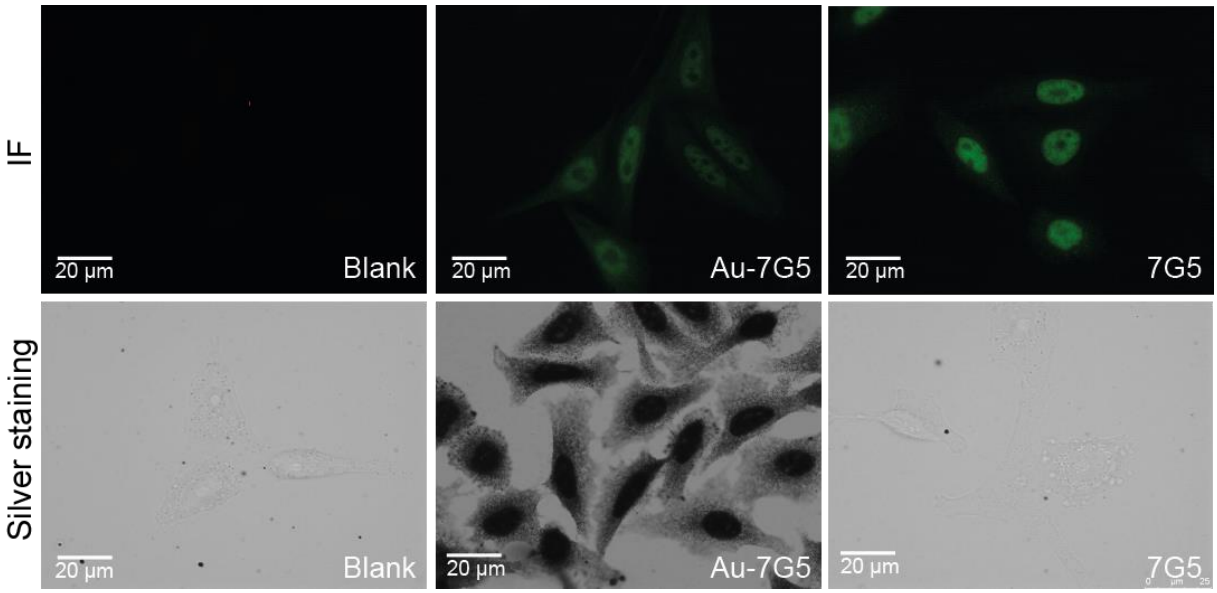

Figure 38. Evaluation of the ability of the Au-7G5 conjugate to bind nuclear RNAP II in fixed and permeabilized HeLa cells. The IgG- and AuNP domains of the Au-7G5 conjugate and non-functionalized 7G5 were detected with an anti-mouse IgG-Alexa488 by IF (green fluorescence in top row) and silver staining (bottom row). Scale bar: 20 µm.

The data clearly demonstrate that the Au-7G5 binds to the nuclear RNAP II in a similar fashion than 7G5 and an overlap between the IF and the silver staining pattern can be observed. Yet, the silver staining did not provide the same sharpness than the fluorescent labeling methods and the nucleoli were stained in the silver stained image (Au-7G5), although RNAP II is excluded from the nucleoli. Moreover, a significant background labeling of the cytoplasm was detected for the cells that were incubated with Au-7G5, clearly visible on the silver stained images, but also detectable on the secondary IF images. Although silver staining is prone to autonucleation, the observed degree of background labeling led us believe that the AuNP domain of the conjugate promoted weak, unspecific association to cellular components. We hypothesized that the observed unspecific binding of Au-7G5 might be driven by the surface of the AuNP, since we already observed during the electroporation of the AuNPs that the stabilizing properties of peptide Cap are ideal for the 1.4 nm AuZ, but not for the 2.4 nm AuG. In case of Au-Cmab, which was passivated with peptide Cap as well, we did not observe a significant degree of unspecific labeling, but in this case the target was an extracellular receptor and during the EGFR binding study the cell plasma membranes were intact (living) and hence the conjugate could not interact with the various components of the cells' interior. Besides the specificity issue, it was noted that Au-7G5 started to precipitate after several days, which is another indication that the conjugate was not sufficiently stabilized. To test this hypothesis that the insufficient inertness of AuG passivated with peptide Cap was responsible for the unspecific binding and unsatisfactory colloidal stability of Au-7G5, we re-synthesized the Au-7G5 conjugate and

passivated the AuNP domain with thiolated-PEG of MW 2000 Da. Moreover, the novel conjugate was purified by gel filtration in order to separate the conjugate from any excess AuNPs, or aggregated species (see next paragraph).

3.2.3 Impact of PEGylation on the RNAP II targeting ability of Au-7G5

During the preparation of several conjugates, precipitation occurred occasionally. We found out that raising the pH of the reaction buffer from 7.5 to 7.7 efficiently counteracts this issue, presumably because the deprotonation of the AuNP surface ligands (TNB and TAB) promotes electrostatic repulsions and consequently prevents particle aggregation. Moreover, we added EDTA to the reaction buffer and performed a gel filtration after the conjugation of AuG to 7G5 to separate the conjugate from excess AuG before proceeding with the passivation with PEG. The SDS-PAGE analysis of Au-7G5-PEG (depicted in Figure 39) showed that the 7G5 antibody fully reacted with AuG (no remaining protein band at 75 kDa, corresponding to reduced 7G5, in the lane of Au-7G5) and that excess AuG could be effectively removed from the conjugate (no remaining AuNP band with high electrophoretic mobility, corresponding to AuG, in the lane of Au-7G5). The coverage of the AuNP domain of Au-7G5 with PEG(2000) resulted in a clearly visible shift on the SDS gel, from which it was assessed that AuG was fully passivated, since no band having the same electrophoretic mobility as Au-7G5 was detectable in the lane of Au-7G5-PEG. Unlike Au-7G5 passivated with peptide Cap, the generated Au-7G5-PEG conjugate was stable at 4°C for months.

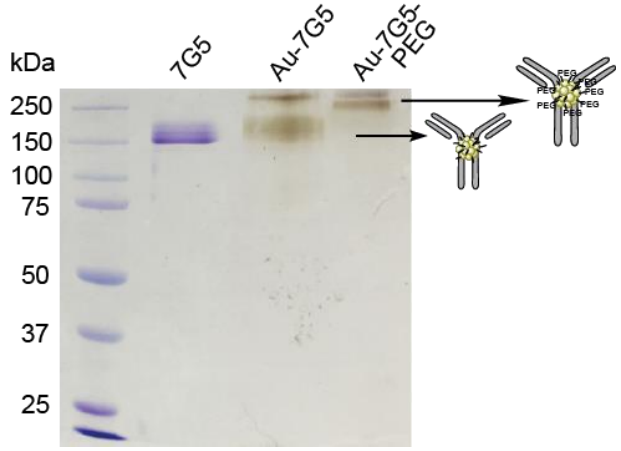

Figure 39. SDS-PAGE analysis of Au-7G5-PEG formation on a 10% SDS gel using non-reducing conditions. Order on the gel from left to right: anti-RNAP II antibody 7G5, purified conjugation product of AuG and antibody 7G5 (Au-7G5), conjugation product Au-7G5 after passivation with PEG (Au-7G5-PEG).

Next, we analyzed the ability of the newly synthesized conjugate Au-7G5-PEG to bind to RNAP II on fixed and permeabilized HeLa cells, as described in the previous section. The

fluorescence and optical microscopy images of the immunolabeled cells (Figure 40) demonstrate that Au-7G5-PEG specifically binds to RNAP II with less apparent background than Au-7G5 passivated with Cap (Figure 35). Remarkably, the corresponding silver stained image displays the same nuclear labeling pattern (i.e. nuclear staining with nucleoli excluded) as the fluorescent labeling method. Hence, the obtained data confirm the assumption that the unspecific interactions of Au-7G5 passivated with peptide Cap were caused by the insufficient stabilization of the peptide-coated nanoparticle and not by a deterioration of the antigen binding ability of 7G5 due to structural alterations at the antigen binding site caused by the conjugation at the hinge area.

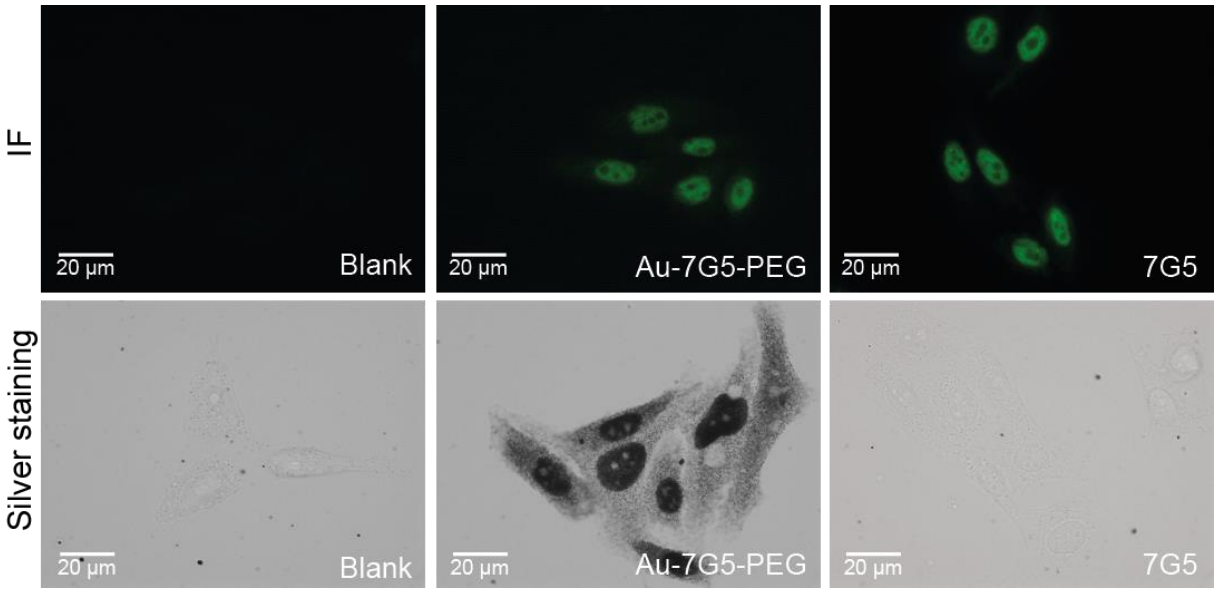

Figure 40. Binding study for evaluating the ability of Au-7G5-PEG for targeting nuclear RNAP II on fixed and permeabilized HeLa cells. The conjugates/antibodies were revealed by secondary IF, as well as silver staining. Scale bar: 20 µm

Based on these results we next tackled the delivery of Au-7G5-PEG into living cells in order to examine whether the produced conjugate is able to bind to its nuclear target in a native context, which is the prerequisite for an EM probe being applicable in a cryogenic workflow.

3.2.4 Delivery of Au-7G5-PEG into live cells

Since we already assessed that AuG passivated with 2000 Da PEG can be efficiently delivered into HeLa cells using an electroporation protocol that was initially designed for antibody delivery,[181] we chose to use the same electroporation procedure for the transduction of Au-7G5-PEG. In principle, the nuclear pore complex limits the passive diffusion into the nucleus to molecules having a MW below 60 kDa. Therefore, 150 kDa antibodies and consequently

antibody conjugates should remain in the cytosol if they succeeded in entering the cells. Yet, it was noticed in our laboratory that 7G5 when transduced into the cytosol of living cells by electroporation is able to accumulate into the nucleus.[181] It was hypothesized that this antibody is piggybacked by de novo synthesized RNAP II, which needs to travel from the ribosomes (cytoplasm) into the nucleus. Hence, we presumed that the electroporated Au-7G5-PEG might be transported into the nucleus by the same piggyback mechanism as 7G5 (schematic illustration of the expected piggyback process after transduction of Au-7G5-PEG depicted in Figure 41).

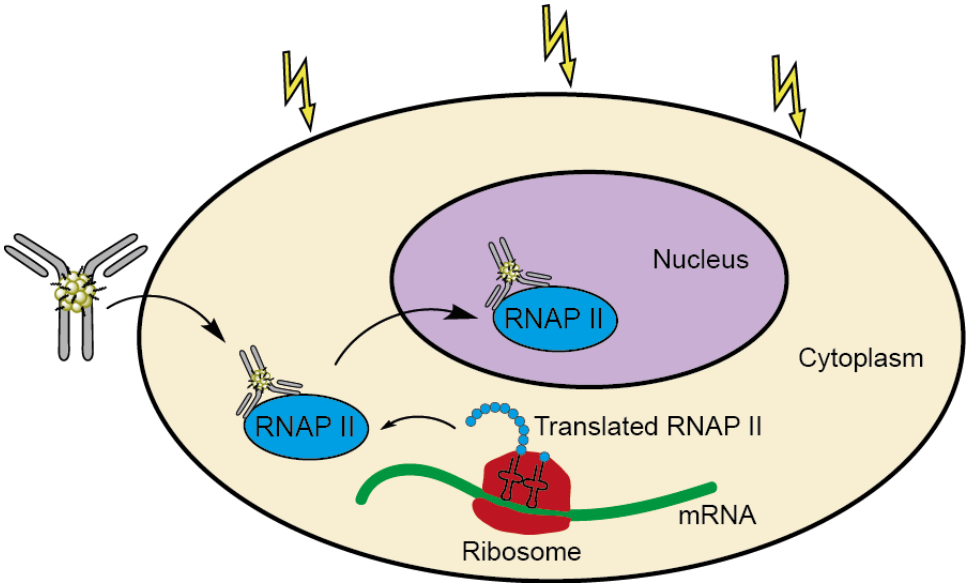

Figure 41. Illustration of the piggybacking process allowing cytosolic (electroporated) Au-7G5-PEG to enter into the nucleus of living cells. Au-7G5-PEGs diffuse into the cytoplasm through transient wholes of the cellular membrane created by the electric pulse and bind to newly translated RNAP II in the cytoplasm. It is the RNAP II that carries the bound Au-7G5-PEG conjugate when it passes through the nuclear pore.

To test the validity of the outlined hypothesis Au-7G5-PEG, as well as different control compounds were electroporated into HeLa cells and their localization was analyzed the next day. In short, the Au-7G5-PEG conjugate (10 pmol), the unconjugated antibody 7G5 (33 pmol, serving as positive control), the Au-Bmab-PEG conjugate (10 pmol, serving as negative control) and AuG passivated with PEG (10 pmol) were added to freshly trypsinized HeLa cells in PBS (final volume of 10 µL). Electric pulses were then applied and the cells were diluted into cell culture medium (0.5 mL) and were let to adhere on glass coverslips for 24 h at 37°C. Afterwards, the electroporated cells were fixed and permeabilized and the localization of the electroporated conjugates, antibody and AuNPs inside the cells was revealed by secondary IF using an Alexa488-mouse antibody, as well as silver staining (fluorescence and bright-field optical microscopy images displayed in Figure 42). Both the 7G5 antibody and the Au-7G5-

PEG conjugate were localized inside the nucleus and showed a pattern that matches with the one we observed during the binding study using fixed and permeabilized cells (staining of the nucleus, nucleoli excluded), suggesting that the RNAP II-targeting antibody, as well as conjugate were transported into the nucleus by the described piggybacking mechanism. The electroporated AuG passivated with PEG was homogeneously distributed throughout the cells including the nuclei and the Au-Bmab conjugate was seen to enter into the cytosol but to be completely excluded from the nucleus, which is in accordance with the fact that 150 kDa antibodies cannot freely enter into the nucleus of live cells. As mentioned in the beginning of the results section of this chapter, Bmab targets the VEGF, which is a secreted protein, and is therefore expected to do not interact with any intracellular components. Together, the obtained data emphasize that the nuclear silver staining/fluorescence pattern observed for the cells electroporated with Au-7G5-PEG is caused by the conjugate's specific binding to de novo synthesized RNAP II and the subsequent shuttling of the conjugate-antigen complex into the nucleus, and not by any artefacts related to the AuNP moiety. Moreover, the absence of any signal in the cytoplasm points out that (i) Au-7G5-PEG is essentially pure and does not contain any unreacted AuG and (ii) the PEGylation of the conjugate efficiently prevents unspecific interactions with cellular components, even in a living and dynamic context. Finally, it needs to be noted that we did not observe any toxicity caused by the transduction of Au-7G5-PEG, even when the electroporated cells were cultivated for a prolonged time-period (48 h).

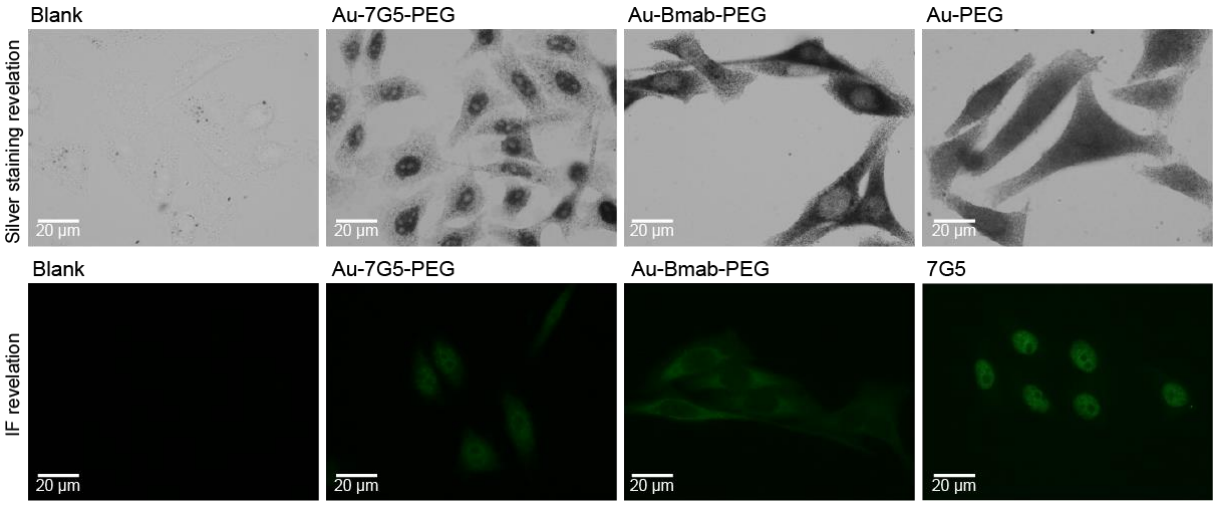

Figure 42. Bright-field and fluorescence microscopy images of HeLa cells electroporated with Au-7G5-PEG, Au-Bmab-PEG, PEGylated AuG (Au-PEG) and 7G5. The localization of the electroporated species inside the cells was revealed by silver staining, as well as IF. Blank corresponds to non-electroporated cells. Scale bar: 20 µm.

Overall, the gathered results demonstrate that the PEGylation of the Au-7G5 conjugate is crucial for reducing unspecific interactions of the conjugate with cellular components and as a result allows a highly specific labeling of RNAP II on fixed and permeabilized cells.

Furthermore, Au-7G5-PEG appears to diffuse into the cytosol of living cells through transient pores that are created by electric pulses. Once inside the cytosol, Au-7G5-PEG binds to its target RNAP II and enters into the nucleus most likely *via* the same piggybacking mechanism that was proposed for 7G5. This opportunity to label a nuclear protein with electron dense AuNPs without the use of chemical fixatives, or detergents opens new possibilities for cryo-EM and high-resolution imaging of the labeled proteins in quasi native conditions.

Taken together, we set up a procedure for linking a 2.4 nm organothiolate-protected AuNP (AuG) to the hinge are of selectively reduced antibodies via thiolate-for-thiolate exchange. The conjugation reaction was performed for three different antibodies (Cmab targeting the EGFR, Bmab targeting the VEGF and 7G5 targeting the RNAP II) and in all three cases a 1:1 AuNP:IgG conjugate was obtained as the main product, demonstrating the feasibility of the site-selective conjugation strategy. By evaluating the ability of Au-Cmab and Au-7G5 to specifically bind to their targets, which was performed using living, as well as fixed cells, we assessed that the direct attachment of AuG at the hinge area did not perturb the antigen-binding ability of the two antibodies. Nevertheless, it needs to be noted that in case of Au-Cmab, which was characterized most detailed, we did observe slight variations in the behavior of the antibody and the conjugate, suggesting that the attachment of a 2.4 nm AuNP at the hinge region of antibodies is not completely innocuous. The evaluation of the EGFR binding ability of Au-Cmab using living EGFR-overexpressing glioblastoma cells proceeded smoothly, although the conjugate was not purified from an insignificant quantity of unreacted AuG present in the conjugation product. In case of Au-7G5 targeting the nuclear multi-complex protein RNAP II, not only the binding to the antigen needed to be considered, but also the association with the cytoskeleton, passage though the plasma membrane and the nuclear envelop. When we first examined the ability of Au-7G5 to bind to RNAP II within fixed and permeabilized cells, we observed a significant degree of background labeling. We attributed the observed unspecific associations with components of the cytoplasm and the nucleus to the insufficient stabilization of AuG, which was passivated with peptide Cap. The occurrence of these undesired unspecific associations was solved by PEGylating the AuNP domain of the Au-7G5 conjugate and by adapting the synthetic protocol. Moreover, the addition of a final gel filtration chromatography proved useful. More interestingly, the behavior of Au-7G5-PEG inside living cells fulfilled our hope. The obtained data revealed that the transduced conjugate traffics inside living cells like the native 7G5, in terms of diffusion inside the cytosol, binding

to newly translated RNAP II and subsequent piggybacking into the nucleus, where the conjugate finally remains bound to its target. These data confirm the applicability of the generated AuNP-IgG conjugates as probes for the live cell labeling of extracellular, as well as nuclear proteins, and thus opens possibilities for undergoing studies to obtain high-resolution gold-labeled images by cryo-EM.

4 Discussion

4.1 Direct Au-S AuNP-antibody conjugation strategy

AuNP-antibody conjugates with defined structure and stoichiometry are indispensable tools for subcellular mapping in high-resolution EM. Thus far only few reported or commercially available immunolabeling agents meet these requirements, such as conjugates made of Undecagold (0.8 nm) or Nanogold (1.4 nm) provided by *Nanoprobes*, which consist of AuNPs that are too small to be directly detected by EM when embedded in biological specimens, hence requiring silver amplification. Due to this gap, we developed a procedure permitting the site-selective conjugation of a 2.4 nm AuNP (AuG), providing increased opacity to electrons, to the hinge area of different antibodies *via* direct Au-S coordination. The thiolate-specific reaction could be conveniently tracked by SDS-PAGE from which it was assessed that the reaction went to completion by forming an AuNP-antibody conjugate with a 1:1 stoichiometry as the main product.

The direct gold-thiol conjugation of small-sized, thiolate-protected AuNPs was already described for small proteins,[148,237–239] peptides,[186] oligonucleotides[240] and bioactive small molecules,[241] but so far never for intact antibodies. For instance, in 2006 Ackerson *et al.* reported the linkage of an engineered scFv containing a surface exposed cysteine to a glutathione-coated AuNP of 1.5 nm *via* direct Au-S coordination.[148] In an initial attempt, the authors attempted the Au-S conjugation by simply mixing the glutathione-coated AuNP with the scFv, but the obtained yields were very low, which is in accordance with our data that suggest that passivated AuNPs are unreactive towards other thiolated molecules, even if the thiolates are present in high excess. Next, Ackerson and colleagues studied the influence of the AuNP charge state on the reactivity towards thiolated proteins.[148] Therefore, the glutathione-coated AuNPs were oxidized with potassium permanganate ($KMNO_4$) and it was found that the reaction rate increased significantly. Moreover, it was shown that, as the reaction can be activated by oxidation, the reaction can be quenched by reducing the AuNP using tiopronin. Yet, the reaction of the glutathione-stabilized cluster with the thiolated scFv never reached completion and therefore left room for improvement. In 2010, the laboratory of Ackerson investigated the use of an $Au_{144}MBA_{66}$ gold cluster for the linkage to an scFv containing an exposed cysteine *via* Au-S coordination.[182] As opposed to the reaction with the glutathione-coated cluster, the formation of a conjugate was possible without the activation of the AuNP by oxidation, but the bioconjugation did not reach completion, despite the use of a 5-fold excess of the gold cluster, which can be seen from the SDS-PAGE gel showing intense bands

corresponding to the remaining protein, as well as Au_{144} particle.[182] In our case, the AuNP-antibody conjugation proceeded readily with requirement of little excess of AuNP. Several reasons may explain this difference in reactivity between the AuNP-bioconjugation reported by Ackerson in 2010 and our data. One explanation might be that TNB (partially coating the surface of AuG) is simply a better leaving group than MBA, due to the electron withdrawing nitro group of TNB, which therefore gets exchanged with incoming thiols more easily. Another possible reason might be that the zwitterionic nature of the TAB ligand, present on the surface of AuG as well, enhances the colloidal stability of the AuNP and consequently facilitates accessing the cysteine side chain of the protein to be labeled and the subsequent thiolate-for-thiolate exchange.

Compared to the widely used protocol for preparing AuNP-antibody conjugates *via* adsorption,[91,97] the site-selective attachment of AuG at the antibody hinge area yields more accurate EM probes, since the distance between the nanoparticle and the paratope is fixed. This characteristic is particularly useful for the localization of cellular proteins by high-resolution EM, as the fixed distance de facto improves the spatial resolution of the recorded image. Another interesting feature of the antibody conjugation with the TNB-/ TAB-protected AuNP is that the reaction progress can be easily monitored by SDS-PAGE. Besides assessing the stoichiometry of the produced conjugate, the characterization by SDS-PAGE allows detecting batch-to-batch variations. For many of the reported AuNP-antibody conjugation strategies employed to make EM probes the composition of the conjugate is usually described as average number of antibodies per nanoparticle and the quality of the batch is only assessed when it is tested on EM specimens.[102] Hence, the possibility to characterize AuNP-antibody conjugates in terms of their reproducibility using a simple method is a clear advancement and to the best of our knowledge, has not been described before.

4.2 Antigen binding ability of AuNP-antibody conjugates

The ability of the generated AuNP-antibody conjugates Au-Cmab and Au-7G5 to bind to their respective antigens EGFR and RNAP II, was evaluated using fixed, as well as living cells. Since the third conjugate Au-Bmab targets the VEGF, an excreted signal protein, we were not able to study its binding ability using a cell line model, and consequently we did not evaluate its antigen binding ability, but instead used it as a control during the characterization of Au-Cmab and Au-7G5.

Au-Cmab selectively bound to EGFR of living cells in a similar, but not completely identical manner as the unconjugated Cmab. On the one hand, these results clearly demonstrated that the conjugation of the 2.4 nm AuG to the hinge region of the antibody did not destroy the antibody's specificity towards its target. On the other hand, as we observed a decreased apparent binding affinity and slight variations between the fate of Cmab and Au-Cmab when incubated with living cells, we concluded that the presence of the AuNP, even when conjugated to the hinge region, was not completely traceless. The mentioned differences, as well as similarities between Au-Cmab and the unconjugated therapeutic antibody in terms of their biological function are discussed in detail in Groysbeck *et al.*[156] attached to this thesis.

For evaluating the specific binding of Au-7G5 to RNAP II, we first performed an immunocytochemistry experiment using fixed and permeabilized cells, before addressing the more challenging *in cellulo* labeling. Au-7G5 primarily labeled the nucleus of fixed HeLa cells in a manner similar to the native 7G5 antibody, but also led to some background staining of the cytoplasm and the nucleoli, which was not observed for the unconjugated 7G5. Since the biological characterization of Au-Cmab demonstrated that the conjugation of the 2.4 nm AuNP to the antibody's hinge area did not majorly alter the function and activity of the antibody, we hypothesized that the unspecific binding of Au-7G5 might be due to the fact that the Cap-coating does not provide the AuNP with sufficient stealth properties.

Peptide Cap, initially used for the coating of Au-7G5, is derived from the pentapeptide CALNN, which is well-known for its ability to stabilize AuNPs and was designed for this purpose by Lévy *et al.*[186] The remarkable stabilization properties of this short peptide results from the formation of a dense peptide layer around the nanoparticle due to intermolecular hydrophobic interactions between the alanine (A) and leucine (L) side chains, as well as due to the hydrophilicity of the peptide thanks to the uncharged, but polar amide groups of the two asparagine (N) residues. While there are several studies on the stabilizing properties of CALNN under physiological conditions,[186] as well as studies investigating the biodistribution of CALNN-coated AuNPs that have been intravenously injected in animals,[242–244] there are no reports in the literature about the interactions of CALNN-stabilized AuNPs with fixed cells. Yet, some of the studies evaluating the AuNP blood circulation and biodistribution underline the presumption that the CALNN-coating does not prevent unspecific interactions of AuNPs with proteins as effectively as high MW PEG.[242] For instance, Morais *et al.*, who wanted to examine the effect of the AuNP surface coating on the biodistribution of AuNPs in rats, reported that the biodistribution of CALNN-coated AuNPs was almost the same as the one of citrate-

capped AuNPs 24 h after injection and that the blood circulation time was even decreased for CALNN-coated particles.[242]

We therefore passivated the AuNP domain of Au-7G5 with a PEG layer and we observed that the unspecific associations were drastically reduced without hampering the specificity of 7G5 for its target RNAP II. In principle, the fact that the PEG-coating reduced unspecific interactions between the nanoparticle and the cellular constituents was expected, as it is well-established that the water-soluble polymer stabilizes nanoparticles and prevents protein adsorption.[190,245] However, it appeared puzzling that the background labeling observed for Au-7G5 (passivated with Cap) was not noted to the same extent in case of Au-Cmab, which was stabilized by Cap as well. There is one main difference between the experimental set ups which might explain this inconsistency. The binding study for evaluating the EGFR-targeting ability of Au-Cmab was performed with living (intact) cells, while the ability of Au-7G5 to specifically bind to RNAP II was tested using fixed and permeabilized cells. Hence, it can be presumed that the unspecific binding that was observed for Au-7G5 passivated with Cap might result from the fact that the Cap-coated AuG associates with the cytoskeleton and other intracellular components of fixed and permeabilized cells.

Apart from the presumption that the Cap-coating did not provide sufficient stealth properties to the AuNP domain of Au-7G5, another possibility for explaining the observed background labeling of Au-7G5 might be that the negatively charged Cap-layer led to electrostatic interactions with amino acid residues close to the AuNP attachment site and therefore caused structural alterations of the 7G5 antibody and a subsequent decrease in binding specificity, as supported by a study published by Aubin-Tam *et al.*[238] The laboratory of Aubin-Tam investigated the effect of the ligand charge of a 1.5 nm AuNP on the structure of covalently and site-specifically labeled Cytochrome c. By comparing the effect of three different ligand types: PEG (neutral), bis-(*p*-sulfonatopehnyl)phenylphosphine (negative) and aminoethanethiol (positive), the authors found that only the neutral PEG ligand permitted maintaining the native protein structure.[238] With regards to our study it needs to be mentioned that Cytochrome c consists of 104 amino acids, whereas the heavy chain of IgG antibodies consists of approximately 450 amino acids, with the hinge region being in the middle of the 450 residues. Yet, at the same time the size of AuG (2.4 nm) is larger than the one of the AuNP used in the study of Aubin-Tam *et al.* (1.5 nm) and therefore AuG might produce more pronounced structural changes to attached biomolecules.

4.3 In cellulo labeling of RNAP II

To explore whether Au-7G5-PEG is applicable for the labeling of the nuclear antigen RNAP II in living cells, we transduced the conjugate into HeLa cells using an electroporation protocol and revealed the localization of the transduced species after 24 h. Unlike Au-Bmab-PEG, which was again used as a control and was found to exclusively localize inside the cytosol, excluded from the nucleus, Au-7G5-PEG was detected inside the nucleus similarly to the native 7G5. This observation suggests that both the unconjugated 7G5 antibody and the Au-7G5-PEG conjugate undergo the same piggyback mechanism after binding to de novo translated RNAP II.

The *in cellulo* targeting of nuclear RNAP II through electroporation of non-functionalized, as well as fluorescently labeled anti-RNAP II antibodies, has been reported previously and it is well-accepted that the nuclear import of the antibody molecules proceeds *via* a piggyback mechanism.[181,246] The transduction of fluorescently labeled anti-RNAP II antibody into human osteosarcoma cells, which was reported by Conic *et al.*, permitted the live cell imaging of the transcription factor using confocal microscopy, as well as its visualization by super-resolution microscopy (3D structure illuminated microscopy).[246] In 2015, Orlov *et al.* reported the cellular delivery of anti-RNAP II antibodies linked to 0.8 nm AuNPs using cationic lipids with the aim to uncover the ultracellular context of RNAP II by EM.[127] The anti-RNAP II-AuNP conjugate was, analogous to the present study and the above-mentioned reports, localized inside the nucleus after the lipid-mediated delivery as jugged by TEM. The delivered anti-RNAP II-AuNP was furthermore imaged by FIB/SEM, which allowed the mapping of the RNAP II distribution within the entire nuclear volume. Since the 0.8 nm AuNPs, which were randomly adsorbed to the antibody, are too small to be directly detected by EM when embedded in the cellular ultrastructure, the AuNPs needed to be silver enhanced (resulting in a particle size of ca. 20 nm). This requirement for particle enlargement unfortunately necessitated chemical fixation of the cellular specimens and did not allow for non-denaturating cryo-fixation. Orlov and coworkers also conjugated the anti-RNAP II antibody to 6 nm colloidal gold particles and attempted the lipid-based cellular delivery, but the 6 nm AuNP-conjugate did not reach the nucleus and remained entrapped in cytosolic vesicles close to the cell membrane.[127] This finding is in agreement with our observations presented in the first chapter of this thesis that the delivery efficiency for AuNPs decreases with increasing nanoparticle size. With regards to the study of Orlov *et al.*, the successful cellular delivery and nuclear translocation of Au-7G5-PEG might have been possible thanks to the site-specific attachment of the 2.4 nm AuNP at the hinge area

of the antibody, which theoretically does not lead to a drastic size increase, whereas the adsorption of antibodies to 6 nm AuNPs imperatively results in conjugates consisting of several antibodies per nanoparticle.

In 2012, the laboratory of Richard Leapman demonstrated that 2 nm AuNPs coated with glutathione and the cell-penetrating peptide TAT can be directly detected by dark-field STEM after internalization in living HeLa cells.[108] Based on this report, as well as the recent advances in EM image resolution, we believe that the Au-7G5-PEG conjugate could prove highly useful as novel probe for the *in cellulo* labeling of nuclear RNAP II by cryo-EM. As the 2.4 nm AuNPs will likely not need a silver amplification step, the cells transduced with Au-7G5-PEG could be cryo-fixed and imaged by cryo-EM, eventually yielding images with discernable AuNPs bound to RNAP II *via* the 7G5 moiety. Such precise indexation of the RNAP II within the cellular nucleus may ensure the structural resolution of the transcription machinery within its native context.

5 Conclusion

In conclusion, we set up a site-specific conjugation protocol that allows appending a 2.4 nm organothiolate-protected AuNP at the hinge area of monoclonal antibodies using direct Au-S coordination. The site-specific conjugation was performed with three different antibodies (Cmab, Bmab and 7G5) and in all cases we obtained a main product consisting of a conjugate having a 1:1 AuNP:IgG stoichiometry, suggesting that the approach is generally applicable. While the direct Au-S conjugation of small-sized, thiolate-protected AuNPs to small proteins has been described before,[147,148,176] we report for the first time an efficient protocol for a site-specific thiolate-for-thiolate exchange reaction with antibodies. The conjugation progress could be readily monitored by SDS PAGE and as opposed to previously reported thiolate exchange reactions between AuNPs and other thiolated biomolecules, the AuNP-IgG conjugations described in this thesis went to completion. The ability of Au-Cmab and Au-7G5 to selectively bind to extracellular EGFR and to nuclear RNAP II was assayed and the binding studies revealed that the attachment of AuG at the hinge area did not majorly perturb the function of the antibodies. Yet, the biological characterization of Au-Cmab indicated that the behavior of the conjugate was slightly different compared to the one of the unconjugated antibody, with regards to apparent binding affinity, as well as intracellular fate after incubation with living EGFR-overexpressing cells, which points out that the conjugation of the 2.4 nm AuNP to the antibody's hinge region was not completely innocuous. Interestingly, only Au-7G5 passivated with high MW PEG specifically bound to RNAP II, whereas the Cap-coated counterpart associated with intracellular components of fixed cells in an unspecific manner. Lastly, we delivered Au-7G5-PEG into living cells by electroporation and observed a nuclear accumulation of the conjugate after 24 h. The labeling pattern matched with the nuclear distribution of RNAP II, which suggests that the electroporated Au-7G5-PEG bound to de novo synthesized RNAP II in the cytoplasm and was then transported into the nucleus by a piggyback mechanism, as it has been reported for the native 7G5 antibody. These qualitative results clearly demonstrate that we can generate and deliver EM probes (in the form of AuNP-IgG conjugates) into live cells *via* electroporation and that these probes diffuse and selectively bind to their targets inside the crowded environment of the cells' cytosol. This novel system, which might be further characterized in terms of delivery efficiency (i.e. number of EM probes delivered inside cells), can now be applied for cryo-EM, eventually allowing for the first time the labeling of cellular proteins with discrete AuNP probes under non-denaturating conditions. Alternatively, the presented AuNP-antibody conjugates, notably Au-Cmab targeting the EGFR,

overexpressed on many cancer types, might hold promises for targeted anti-cancer therapy, since AuNPs can be prepared from β-emitting radioactive gold-189,[62] allow for radiosensitization[247] and can be readily conjugated to drugs.[248] Figure 43 illustrates the potential imaging and therapeutic applications of the generated AuNP-antibody conjugates.

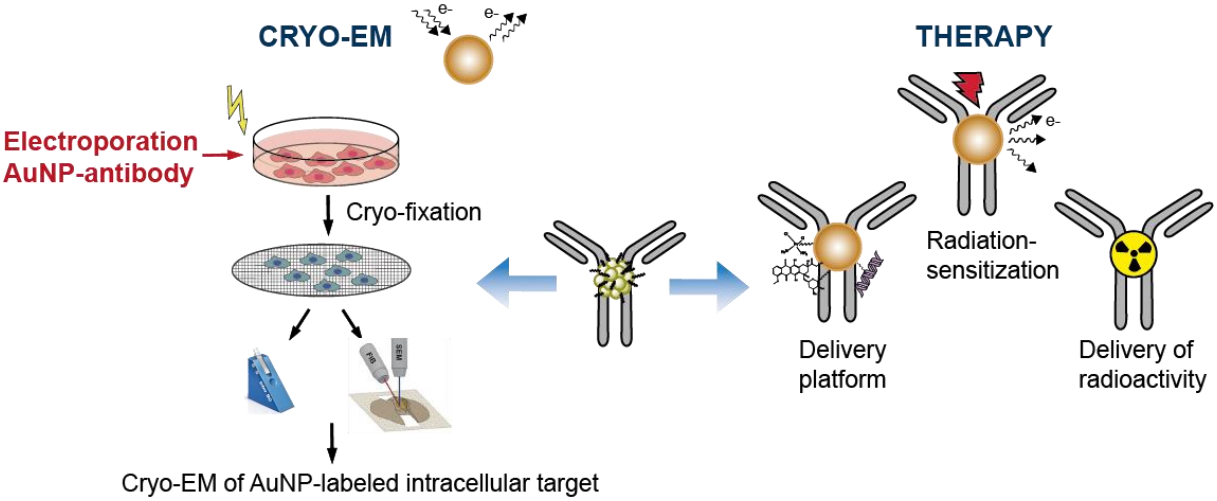

Figure 43. Schematic illustration of potential application of the novel AuNP-antibody conjugates described in this chapter. On the left: Use of AuNP-antibody conjugates as probes for cryo-EM imaging of intracellular proteins. AuNP-antibody conjugates are transduced into living cells by electroporation, cryo-fixed, thinned under cryogenic conditions and subsequently imaged by cryo-EM. On the right: Use of AuNP-antibody conjugates as targeted therapy tools (delivery platforms, radiation enhancers and radioactive compounds).

Chapter 3

Conjugation to nanobodies and application as electron microscopy probe

For generating electron microscopy probes offering improved diffusion and labeling efficiency, we aimed for making probes of smaller overall size, than the gold nanoparticle-antibody conjugates presented in the previous chapter, by site-selectively linking nanobodies to the thionitrobenzoate-/ thioaminobenzoate-stabilized gold nanoparticles. In this chapter we present two different conjugation approaches for meeting this goal. One strategy was to directly link the gold nanoparticle to the nanobody *via* Au-S coordination, involving genetic engineering of the nanobody in order to add a surface exposed cysteine to the binder. The second strategy was based on the use of complementarily associating peptides as linker between the nanobody and the gold nanoparticles. The generated probes were characterized for their target-specific binding ability, employed for immunocytochemistry experiments imaged by light, as well as electron microscopy and finally delivered into live cells *via* electroporation to evaluate whether the conjugates are compatible with a workflow permitting immunogold labeling for cryo-electron microscopy.

Before presenting our studies, the structural features and properties of nanobodies are introduced and their versatility for cellular biology is highlighted. Afterwards, the use of nanobodies for super-resolution microscopy is discussed.

1 Introduction

1.1 Structure, properties and production of VHHs (nanobodies)

VHHs represent the variable domain of heavy-chain antibodies occurring in the Camelidae family and are the smallest available monomolecular antigen-binding fragments counting a total of ca. 115 amino acids (for comparison antibodies are comprised of ca. 1330 amino acids as sum of 12 immunoglobulin domains).[249] When VHHs are recombinantly expressed, these single-domain antibodies are referred to as nanobodies. The existence of heavy-chain antibodies in the sera of Camelidae was first reported in 1993 by Hamers-Casterman and colleagues.[250] Only two years later a similar class of heavy-chain antibodies was discovered in sharks, named nurse shark antigen receptor (NAR).[251] While conventional antibodies are comprised of two heavy and two light chains, heavy-chain antibodies lack the light chain, as well as the first constant domain CH1 (Figure 44(a) illustrates the structure of heavy-chain antibodies compared to the structure of common IgG). As a result, heavy-chain antibodies have a more compact architecture and a reduced molecular weight of 90 kDa (MW of IgG = 150 kDa). Moreover, the antigen binding domain (the VHH) has a MW of only 12 – 15 kDa. The crystal structure of a VHH has been first solved in 1996,[252] which revealed that the general architecture of VHHs consists of nine β-strands, which moreover arrange into two β-sheets consisting of four and five β-strands, respectively. These two β-sheets form a β-sandwich structure (4 x 2.5 nm in size) *via* connecting loops and two conserved cysteines forming an intramolecular disulfide bond (crystal structure of a nanobody depicted in Figure 44(b)).

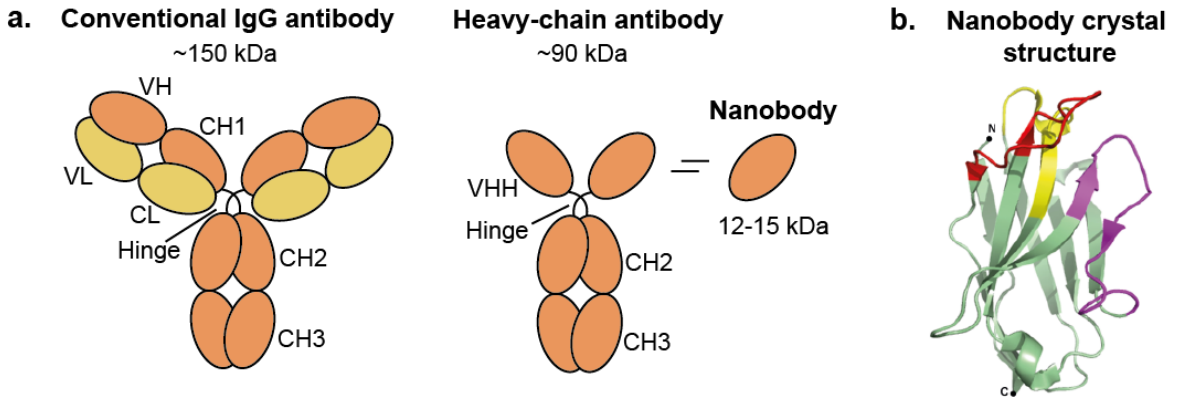

Figure 44. Schematic illustration of conventional IgG and heavy-chain antibody in (a) and nanobody crystal structure showing VHH fold in (b). (a) Heavy chains of IgG and heavy-chain antibodies in orange and light chains present in conventional antibody in yellow. To note, heavy-chain antibody does not contain CH1, only VHH, hinge, CH2 and CH3. (b) Crystal structure of anti-gelsolin nanobody showing the β-sandwich structure of nanobodies with the three CDRs in color (CDR1 yellow, CDR2 magenta, CDR3 red). X-ray crystal structure obtained from Beghein and Gettemans *et al* 2017.[253]

Three hypervariable loops form the antigen-binding site and are therefore called complementarity determining regions (CDR1, CDR2, CDR3). In Figure 44 (b), the hypervariable loops are colored in yellow, magenta and red. The lower number of CDRs (three versus six for IgG) theoretically limits the adaptation of the VHH to a target, but the hypervariable loops in VHHs are longer, than in the VH of conventional immunoglobulins, and therefore allow for more sequence variation. The paratope of VHHs has a convex shape, which makes VHHs particularly suited for the binding to cavities. Nevertheless, the paratopes of VHHs are not restricted to the interaction with cavities, but can adopt various structures, allowing likewise the binding to flat surfaces and protruding linear peptides.[249]

Nanobodies are usually generated by immunizing a member of the Camelidae family such as camels, llamas, alpacas or vicugna.[249] Subsequently, the peripheral lymphocytes of the immunized animal are isolated and the variable domain gene repertoire is extracted. The extracted and amplified genes are then cloned into phagemids, thus allowing the selection of monoclonal nanobodies by phage display. Besides phage display, other selection techniques can be applied, involving bacterial display, yeast display or 2 hybrid selection.[249] Once a nanobody has been successfully selected the small binder protein can be expressed in microorganisms, mammalian cell lines or plants at high levels.[249] Since nanobodies have a high content of hydrophilic amino acids, the small binders are water soluble, thus facilitating their manipulation for biological applications. Nanobodies can be stored at 4°C for several months and even longer at -20°C without losing their antigen-binding ability. Furthermore, nanobodies are resistant to high pressure, low pH and heat. Besides, some nanobodies can be equipped with fluorescent-, epitope- or affinity-tags, without compromising their stability and affinity.[253] The fact that nanobodies can be genetically engineered makes them extremely versatile for cellular biology and has led to the development of various nanobody-based tools.

1.2 Nanobodies for high-resolution imaging

1.2.1 Super-resolution microscopy

The small size, monomolecular nature and affinity lying in the nanomolar range make nanobodies ideal candidates for super-resolution microscopy imaging probes.[254] Traditionally, the detection of selected proteins inside cells or tissue sections *via* fluorescence microscopy is performed by immunolabeling involving the use of primary antibodies targeting the structure of interest and secondary antibodies bearing fluorescent labels for detection. Due to the large

size of antibodies (12 – 15 nm), this indirect labeling approach results in a displacement of the fluorescent label from the target of ca. 24 – 30 nm (also referred to as linkage error).[254] For classical fluorescence microscopy, whose resolution is limited by the diffraction of light (200 – 300 nm) a linkage error of 30 nm is negligible. However, for novel super-resolution methodologies reaching resolutions up to 20 nm, a signal displacement of such dimension is getting an important inaccuracy.[255] Nanobodies, having a size of only 4 x 2.5 nm, conjugated to bright fluorescent dyes thus represent an appropriate alternative for super-resolution imaging.[255]

In 2012, Ries and colleagues reported for the first time the use nanobodies for super-resolution imaging, more precisely for photoactivated localization microscopy (PALM) and stochastic optical reconstruction microscopy (STORM).[256] The authors used fluorescently labeled anti-GFP and anti-RFP (red fluorescent protein) nanobodies for the labeling of microtubules, yeast cells and living neurons tagged with fluorescent proteins. Interestingly, Ries *et al.* observed that nanobodies are able to penetrate into fixed and permeabilized yeast cells having intact cell walls. In 2015, Platonova and coworkers also employed GFP- and RFP-targeting nanobodies coupled to bright organic dyes for super-resolution microscopy and single-particle tracking.[257] The authors employed the nanobody probes for several GFP-/RFP-tagged proteins, including the nuclear pore protein Nup43-eGFP, for which a clear difference in epitope accessibility was observed between nanobody and antibody labeling, leading to an increased labeling density and resolution for the nanobody labeled cells (Figure 45).[257]

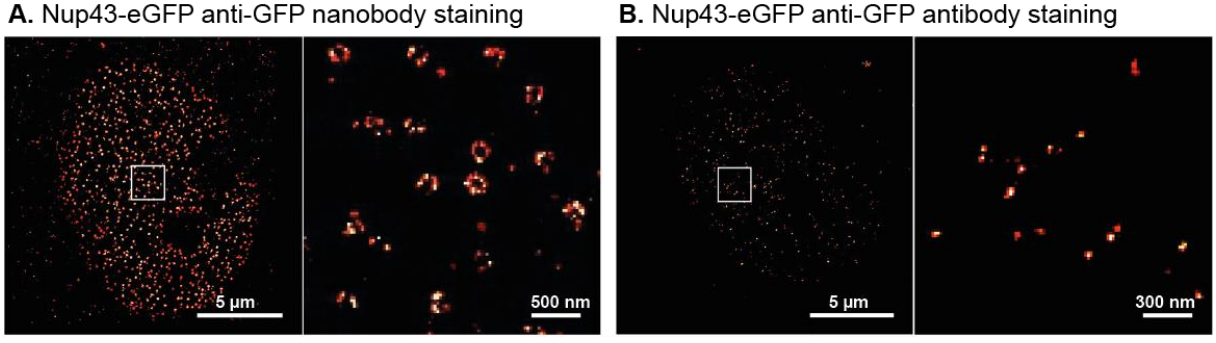

Figure 45. Difference in epitope accessibility of nuclear pore complex components between nanobodies (A) and antibodies (B). Images show nucleus of U2OS cells stably expressing Nup43-eGFP. Image obtained from Platonova *et al.* 2015.[257]

Mikhaylova and colleagues developed a nanobody directed against tubulin and employed the fluorescently labeled binder for super-resolution imaging of microtubules.[258] This imaging approach ensured optical resolution of individual microtubules of microtubule bundles that were generated with a known spacing of 50 – 70 nm. Resolving individual microtubules of such

spacing was not possible using conventional antibody labeling, as the indirect labeling increased the diameter of microtubules and blended neighboring microtubules into one structure. In 2018, Klein *et al.* presented nanobody-mediated labeling of selected proteins in live cells.[259] The researchers simultaneously transduced a GFP-targeting nanobody and an anti-lamin nanobody conjugated to two different fluorophores (sCy3 and sCy5) by microfluidic cell squeezing. The described strategy allowed for live cell visualization of high, as well as low abundant endogenous proteins with low background signal.

Another important contribution in the field of nanobody-aided super-resolution imaging was made by Pleiner *et al.* who reported a thorough study on the site-selective functionalization of nanobodies *via* engineered cysteines.[254] Pleiner developed a nanobody directed against the nuclear pore complex and generated six mutants bearing cysteines at alternative solvent-exposed sites. In order to selectively label the engineered cysteines and not the native cysteines forming the conserved disulfide bond, the labeling with maleimide modified fluorophores was carried out at 0°C. The study revealed that cysteines at all six alternative sites could be quantitatively labeled and that the binding to the nuclear pore complex was neither impaired by the mutations, nor by the labeling. Traditionally, nanobodies have been functionalized non-selectively *via* the ε-amino group of lysines using NHS esters. As for antibodies, this non-selective conjugation approach often impacted the specificity and affinity of the nanobody negatively.[254] To get around this issue researchers introduced C-terminal oligo-lysine stretches, to divert the conjugation from the native lysine residues.[257] Another strategy for circumventing conjugation-induced structural alterations is the labeling *via* Sortase A.[260] This however is restricted to the N- or C-terminus of the nanobody and accordingly functionalized fluorophores are not readily available. Hence at the present stage, cysteine engineering and careful modification, as it was described by Pleiner et al.,[254] can be considered as the most promising approach for generating site-selectively labeled nanobodies without compromising affinity and specificity.[254]

1.2.2 Electron microscopy

Thanks to the technical advances of the last decades, EM allows nowadays the imaging of cellular proteins with nanometer resolution. Analogous to immunofluorescence, the classical immunolabeling for EM, involving primary and secondary antibodies or alternatively protein A coupled to electron dense AuNPs, does not appear appropriate anymore and there is a need for new labeling tools leading to a decreased signal displacement.

The use of nanobodies for immunogold labeling of cellular proteins for EM was first reported by Kijanka *et al*.[261] The authors developed a nanobody directed against HER2 and employed it for the labeling of HER2-positive breast cancer cells in a pre-embedding, as well as post-embedding approach. As the anti-HER2 nanobody was not directly linked to an AuNP or any other electron dense marker, the immunolabeling required two further incubation steps using an anti-VHH antibody and protein A-immunogold (15 nm AuNPs). Given this fact the displacement of the contrasting AuNP from the targeted HER2 receptor was comparable to classical immunogold labeling and the gain in resolution unfortunately negligible. In 2015, Ariotti and colleagues developed a nanobody based tool for immuno-EM, which relies on the genetic engineering of a GFP-targeting nanobody to a modified soybean ascorbate peroxidase (APEX) tag.[262] APEX is a 28 kDa peroxidase which converts 3,3'-diaminobenzidine (DAB) in the presence of H_2O_2 into an osmiophilic brownish polymer.[263] This produced polymer is detectable by light microscopy and can be further converted into an electron dense product through treatment with OsO_4.[264] In contrast to horseradish peroxidase (HRP), APEX does not contain disulfide bonds and Ca^{2+} binding sites, and consequently remains active inside the cytosol.[263] This is a huge advantage of APEX compared to HRP, as it permits to use the tag for extracellular, as well as intracellular targets, whereas HRP can only be applied for the labeling of extracellular epitopes. Thus, upon transfection of the anti-GFP nanobody-APEX construct into cells expressing GFP-tagged proteins, the expressed nanobody-APEX is recruited to the GFP fusion proteins, where an electron dense signal can be produced. In contrast to the labeling procedure presented by Kijanka, the protocol developed by Ariotti *et al.* does not require any secondary antibody incubation and therefore clearly improves the spatial resolution (according to the authors to approximately 10 nm). Three years after the publication of this approach, Ariotti and colleagues reported the dual labeling using GFP-, and mcherry-targeting nanobody-APEX constructs and demonstrated that the expressed fusion constructs are degraded by the proteasome when unbound to their antigen.[265] The proteasomal degradation of the nanobody-APEX fusions when unbound to their targets allows to not only image high, but also less abundant proteins and leads to a high signal-to-noise ratio. De Beer *et al.* developed another nanobody-based approach for CLEM by generating a fusion construct between a nanobody, an APEX tag and a fluorescent protein.[266] The generated fusion protein is referred to as FLIPPER-body, standing for Fluorescent Indicator and Peroxidase for Precipitation with EM Resolution (schematic illustration of FLIPPER-body compared to traditional indirect antibody-immunogold labeling depicted in Figure 46). As opposed to the approach of Ariotti *et al.*, FLIPPER-bodies are expressed in bacteria, purified and used in a classical immunolabeling

setting using fixed cells. Fluorescence microscopy is performed at wet, fixed samples and only afterwards the cells are treated with DAB/H_2O_2, post-fixed with OsO_4 and processed for electron microscopy, allowing to finally correlate the fluorescence and EM images.

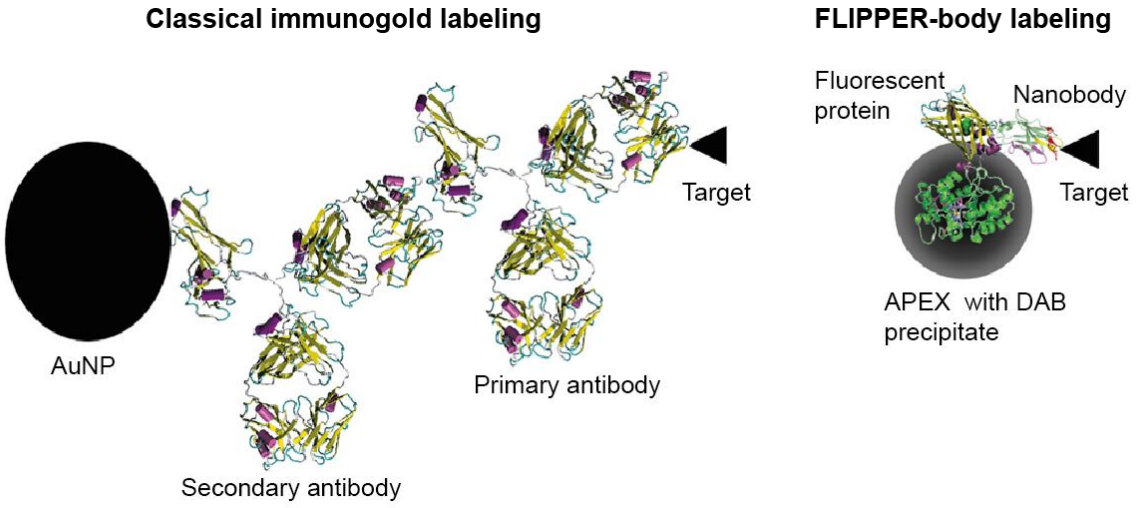

Figure 46. FLIPPER-body labeling compared to traditional indirect antibody-gold labeling. Image reproduced from de Beer *et al.* 2018.[266]

Very recently, Jiang *et al.* reported the development of genetically encoded tags permitting the in situ synthesis of AuNPs having diameters of 3 – 6 nm being visible by EM.[267] The authors moreover fused this novel tag to the anti-GFP nanobody for generating an EM probe outperforming previous immunolabeling approaches in terms of spatial resolution. The concept published by Jiang *et al.* is based on the use of cysteine-rich tags, which form an Au(I)-thiolate polymer upon addition of $HAuCl_4$, which can be further reduced to Au(0) by $NaBH_4$, thus promoting the growth of nanoparticles,[267] as it is described for the classical Brust-Schiffrin method.[146] It is important to specify that the immunolabeling using the tagged nanobody, as well as the in situ AuNP synthesis were not performed in living cells. Instead, the cells were fixed by high pressure freezing, freeze substituted and finally rehydrated and permeabilized to permit the penetration of the tagged nanobody and the AuNP synthesis. Although very original, the described strategy raises issues regarding denaturation of the samples' ultrastructure. First, the cells need to be permeabilized with Triton X-100, which compromises the cellular ultrastructure. Second, the rehydration of the cells and temperatures above 0°C, necessary for performing the in situ AuNP synthesis, downgrades the ultrastructure of the cells once more.

Altogether, novel strategies for immuno-EM have been developed that rely on the use of nanobodies and clearly improve the spatial resolution compared to standard immunogold labeling techniques. So far, these approaches are based on the genetic engineering of

nanobodies with peptide tags permitting the formation of an electron dense product. The majority of the publications in this field describes the use of genetically encoded peroxidase tags and as the immunolabeling procedure is straightforward and the modules of these nanobody-APEX constructs can be readily switched using standard molecular cloning tools, researchers lately started to employ these tools to study cellular processes (Buser 2018, Abdellatif 2019).[268,269] Nevertheless, it is noteworthy that the electron dense DAB reaction product can diffuse away from the targeted structure, thus eventually resulting in inaccurate (false) information about the target location.[270] If instead AuNPs are conjugated to the binder molecules this phenomenon should not occur, as the electron dense material is directly linked to the binder. The cysteine-rich tag fused to the anti-GFP nanobody described by Jiang *et al.* meets this requirement,[267] but at the current stage the process is restricted to cell fixation and harsh permeabilization and does not permit the antigen binding under native conditions. In order to propose an alternative nanobody-based immuno-EM tool that (i) yields a discrete electron dense signal at the target site that is not prone to drifting away and (ii) can be employed in living cells, we set up procedures for conjugating the small-sized TNB-/ TAB-protected AuNPs to nanobodies in a controlled manner and evaluated their applicability for classical immuno-EM, as well as *in cellulo* labeling.

Since electron contrast is a function of AuNP size, we chose again to use the 2.4 nm TNB-/ TAB-protected AuNP in the first stage for making a new nanobody-based EM probe. The anti-GFP nanobody whose crystal structure in complex with GFP has been published[271] and which has already been employed for super-resolution microscopy,[254,256–258] as well as APEX-based immuno-EM,[262,266] was selected as a model system for the conjugation to the 2.4 nm AuNP, due to the popularity of GFP in research and presumed availability of cell lines expressing GFP-tagged proteins. To generate a probe that is as precise and small as possible, thus resulting in a decreased linkage error, while at the same time permitting improved diffusion inside fixed as well as living cells, two different conjugation strategies were tested and the binding abilities of the produced conjugates evaluated. The different approaches involved the direct linkage of the nanobody to the AuNP *via* Au-S coordination to minimize the signal displacement to a maximum and the use of complementarily associating peptides serving as adaptor and linker molecules promoting a non-covalent conjugation.

2 Materials and Methods

2.1 Materials

The donkey anti-goat IgG (H+L) antibody, Alexa Fluor Plus 594 was ordered from Invitrogen and the affinity pure goat anti-Alpaca IgG, VHH domain antibody was purchased from Jackson ImmunoResearch. BSA was bought from Euromedex and BSA-c (10% solution) used for immunocytochemistry was purchased from Aurion. DNA transfection reagent jetOPTIMUS was obtained from Polyplus-transfection and Ni NTA agarose beads for his6-affinity purification was purchased from Qiagen.

2.2 Genetic engineering of anti-GFP nanobody constructs

The DNA sequence of the anti-GFP nanobody obtained from the publication of Kubala *et al.*[271] was purchased from Integrated DNA Technologies (DNA and amino acid sequences plotted in Figure 66 (a), Supporting Information). The serine 7 of the anti-GFP nanobody sequence was mutated to a cysteine to generate anti-GFP nanobody S7C (hereafter referred to as C7nabo) by genetic engineering using the PCR methodology and primers of sequences: 5'-GGAGAT ATACCA TGGGGT CCCAGG TTCAGC TGGTTG AATGTG GTGGTG-3' and 5'CACTAG TTGCGG CCGCTG AGGAGA CGGT-3'. The amplified DNA fragment was digested with NcoI and NotI restriction enzymes and inserted into a pETOM vector encoding a c-myc sequence and a his6 tag.[272] Next, the anti-GFP nanobody DNA sequence was fused to a peptide tag E3,[273] which allows for complementary association. The generation of the nanobody-E3 construct (hereafter referred to as *nd*-nabo) was performed by PCR amplification of the anti-GFP nanobody DNA sequence using oligonucleotides: forward CGTCAG CCATGG GGTCCC AGGTTCAGC and reversed CCACAG GAATTC ACAATG GTGATG ATGGTG ATGTGCG. The DNA fragment was finally inserted into a pETOM vector containing the *nd* tag DNA sequence[273] using NcoI and SpeI restriction sites (DNA and amino acid sequences plotted in Figure 66 (b), Supporting Information).

2.3 Expression and purification of anti-GFP nanobody variants

The C7nabo and *nd*-nabo recombinant proteins were expressed in *E. coli* BL21(DE3)pLys after induction with 1 mM IPTG in 100 mL LB medium. Cells were lysed by ultrasonication and subsequently the his-tagged proteins were purified by immobilized metal affinity

chromatography using a HisTrap HP column (1 mL) charged with $NiSO_4$. The fractions eluted with excess imidazole contained the his-tagged proteins, which were further purified by gel filtration on a HiLoad Superdex 75 pg preparative column operating at a flow rate of 0.4 mL/min. Protein fractions in PBS were then analyzed by SDS-PAGE, pooled and concentrated using Amicon Ultra 4 mL centrifugal devices (MWCO 3 kDa).

2.4 Synthesis of AuNP-nanobody conjugates

2.4.1 Direct Au-S conjugation approach

To ensure that the cysteine at position 7 of the engineered C7nabo is in its reduced form a 40 µM solution of C7nabo (75 µL, 3 nmol) was mixed with 0.4 mM TCEP (25 µL, 10 nmol) and incubated for 15 minutes at 25°C in 0.1 M HEPES, pH 7.5. Then, a 42 µM solution of the 2.4 nm AuNPs (250 µL, 10.5 nmol) was added to the reduced nanobody solution (88 µL 30 µM, 2.64 nmol) leading to a molecular ratio of AuNP/nanobody of 4.The thiolate exchange was allowed to proceed overnight at 25°C, which was followed by a 3 h passivation reaction with a 1 mM solution of peptide Cap of the sequence [CALNNG], or a 1 mM solution of alpha-methoxy-omega-mercapto poly(ethylene glycol) 2000 Da (818 µL, 818 nmol) at 25°C. The released TNB-/ TAB-ligands and excess thiolated molecules were then separated from the AuNPs by ultrafiltration using Amicon 30 K ultracentrifugal devices (5 washes with PBS). The crude AuNP-nanobody conjugates, hereafter referred to as AuC-C7nabo (when passivated with Cap) and AuP-C7nabo (when passivated with PEG), were then purified using Ni-NTA agarose beads (100 µL beads, equilibrated in PBS) by mixing the crude with the beads under mild agitation for 1.5 h in PBS. Afterwards, the beads were washed with PBS (3 times 1 mL), with 15 mM imidazole in PBS (2 times 1 mL) and finally AuC-C7nabo and AuP-C7nabo were eluted with 500 µL 200 mM imidazole in PBS. The eluates were concentrated to a volume of 100 µL using Amicon 30 K ultracentrifugal devices.

2.4.2 Non-covalent conjugation approach

A 42 µM AuNP solution (70 µL, 3 nmol) was reacted with the complementary associating peptide K3 of the sequence [CALNNGEYFTLQIRGRERFEMIRKLNKALELKDAQA] (176 µL 1 mM, 18 nmol of the peptide) for 3 h at 25°C in 0.1 M HEPES pH 7.5. For exchanging the remaining reactive TNB-/ TAB-ligands on the AuNP surface, the AuNPs were then passivated with 1 mM alpha-methoxy-omega-mercapto poly(ethylene glycol) 2000 Da

(276 µL, 276 nmol) for 2 h at 25°C in 0.1 M HEPES pH 7.5. The functionalized AuNPs were separated from released TNB-/ TAB-ligands and excess thiolated molecules *via* ultrafiltration (30 kDa) to yield the purified AuNP-K3-PEG, hereafter referred to as AuP-*bi*; in 0.1 M HEPES, pH 7.5 (concentration of Au-*bi* determined to be 25 µM). Then, AuP-*bi* was mixed with an equal volume of 25 µM *nd*-nabo in 0.1 M HEPES pH 7.5 at 25°C for 1h to obtain the (non-covalent) conjugation product AuP-*bind*-nabo.

2.5 Enzyme-Linked Immunosorbent Assay (ELISA)

The wells of an immunosorbent plate (Thermo Scientific) were coated with GFP (1 µg/mL in PBS, produced in house) by an overnight incubation at 4°C. For blocking remaining adsorbing surfaces, the wells were incubated with 3% (w/v) BSA in PBS (200 µL per well) for 1 h. Then, the AuNP-nanobody conjugate solutions were added into the wells for 1 h at different concentrations (100 µL per well). For revealing the nanobody domain a goat anti-VHH Alpaca IgG (2.5 µg/mL) was added into the wells for 1 h (100 µL per well), followed by an anti-goat-HRP antibody (1:1000 dilution, 100 µL per well, 1 h). Between each incubation, the wells were washed three times with PBS containing 0.1% NP40 and three times with PBS. The colorimetric output was generated by adding a developing reagent (100 µL of 10 mg/mL 3,3',5,5'-tetramethylbenzidine (TMB) in0.1 M sodium acetate pH 6, containing 0.007% hydrogen peroxide) into the wells. The revelation reaction was stopped with 1 M sulfuric acid (50 µL per well) and the signal was quantified with an ELISA plate reader (BioRad 550) at 450 nm.

Alternatively, the binding of the AuNP-nanobody conjugates was evaluated by revealing the AuNP moiety. The binding of the AuNP-nanobody conjugates to GFP-coated immunosorbent plates was performed as described before, but instead of revealing the nanobody domain with antibodies, the bound AuNPs were silver-enhanced in the dark for 15 min using a published silver developing solution.[274] The silver enhancement reaction was stopped by washing the wells with H_2O (3 times).

2.6 Cell culture

The human cancerous cell lines HeLa, HeLa H2B-GFP, HCC-1954 and MDA-MB-231 were grown in a humidified atmosphere at 37°C supplied with 5% CO_2. HeLa and HeLa H2B-GFP cells were maintained in Dulbecco's modified eagle medium containing 2 mM L-glutamine,

10 mM HEPES buffer, pH 7.0, 10% heat-inactivated fetal bovine serum (FBS) and 50 µg/mL gentamycin. HCC-1954 and MDA-MB-231 were cultivated in Roswell Park Memorial Institute (RPMI) 1640 medium supplemented with penicillin and streptomycin. For immunocytochemistry, immunofluorescence and pre-embedding immuno-EM experiments, cells were seeded into 24-well plates at a density of 25000 cells/well and were let to adhere on glass coverslips overnight.

2.7 Transfection experiments

Transfection of HeLa cells with GFP-fusion protein encoding plasmids (eGFP-β-galactosidase, eGFP-β-galactosidase-NLS and eGFP-con1) were performed using the transfection agent jetOPTIMUS (Polyplus-Transfection). The day before the transfection experiment, cells were seeded into 24-well plates at density of 50000 cells/well. For one well 0.5 µg DNA were diluted in 50 µL of jetOPTIMUS buffer and 0.5 µL jetOPTIMUS reagent was added. This mixture was incubated at room temperature for 10 min and then added dropwise to the cells by dilution into the cell culture medium. Cells were fixed after 24 h to analyze transgenic expression.

2.8 Immunolabeling for optical microscopy

2.8.1 Immunocytochemistry

Cells adhered on glass coverslips were fixed with 4% PFA in PBS for 20 min at 20°C. Fixed cells were then washed with PBS (3 x 0.5 mL, 5 min), PBS containing 50 mM glycine (0.5 mL, 20 min) and the cell plasma membranes were permeabilized with 0.05% Triton X-100 in PBS (0.5 mL, 5 min). Afterwards, cells were soaked in PBS containing 10% (w/v) BSA for 1h, washed with 0.2% acetylated BSA (BSA-c) in PBS (2 x 0.5 mL, 5 min) and incubated with the AuNP-nanobody conjugates (6 nM in 0.2% BSA-c containing 10% FCS, 0.5 mL) for 1 h. Following the conjugate incubation, cells were again washed with 0.2% BSA-c (2 x0.5 mL, 5 min) and subsequently with 80 mM citrate buffer pH 6.2 (3 x 0.5 mL, 5 min). Finally, AuNPs were enlarged using a silver staining protocol modified from the Danscher method[275] as described in Groysbeck *et al.* 2019,[156] included in the appendix of the thesis. Immunolabeled and silver stained cells were imaged by bright-field microscopy on a Leica DM5500 microscope (Leica Microsystems, Wetzlar, Germany).

For detecting DNA-bound PCNA in con1-GFP transfected cells, soluble proteins, unbound to the cytoskeleton or chromatin, were removed from the cells by treating the cells with a

cytoskeleton buffer (300 mM sucrose, 10 mM HEPES, 1 mM EGTA, 3 mM $MgCl_2$, 0.2% triton X-100, 100 mM NaCl and protease inhibitor) for 3 min on ice prior to fixation.

2.8.2 Immunofluorescence

For revealing the binding of the GFP-targeting AuNP-nanobody conjugates to GFP-expressing cells by detecting the nanobody moiety, the cells were incubated with goat anti-Alpaca IgG, VHH domain antibody (2.5 µg/mL) and donkey anti-goat IgG (H+L) antibody, Alexa Fluor Plus 594 (1:10000 dilution) after the two BSA-c washes following the conjugate incubation (thus replacing the silver enhancement step). Antibody incubations were each performed for 1 h and finally coverslips were mounted using DAPI Fluoromount-G (SouthernBiotech). Immunofluorescence images were recorded on a Leica DM5500 microscope (Leica Microsystems, Wetzlar, Germany).

2.9 Pre-embedding immunolabeling and sample preparation for electron microscopy

Coverslip-adhered cells were fixed with 4% PFA in PBS for 20 min at 20°C. Then, cells were washed with PBS (3 x 0.5 mL, 5 min), PBS containing 50 mM glycine (0.5 mL, 20 min) and the cell plasma membranes were permeabilized with 0.05% Triton X-100 in PBS (0.5 mL, 5 min). Thereafter, cells were soaked in PBS containing 10% (w/v) BSA for 1h, washed with 0.2% acetylated BSA (BSA-c) in PBS (2 x 0.5 mL, 5 min) and incubated with the Au-*bind*-nabo conjugate (12 nM in 0.2% BSA-c containing 10% FCS) overnight at 4°C. On the following day cells were washed with PBS (5 x 0.5 mL, 8 min) and post-fixed with 1% glutaraldehyde in PBS (15 min). Next, cells were washed with PBS (3 times), with H_2O (5 times) and the AuNPs were enlarged using R-Gent SE-EM Silver Enhancement Reagent (Aurion, 80 min of development). After the silver enhancement, cells were washed with H_2O (5 times) and post-fixed with 0.5% osmium tetroxide (15 min). Then, the cellular samples were again washed with H_2O, dehydrated with increasing concentrations of ethanol and flat embedded in Epon. The resin-embedded specimens were sectioned into 60 nm thick slices that were deposited onto copper 200 mesh grids (Electron Microscopy Sciences). For observation of cellular specimens by HAADF-STEM the silver enhancement step was omitted.

2.10 Cellular specimen observation by electron microscopy

2.10.1 Conventional TEM

Images of cellular specimens were recorded on a Hitachi H7500 transmission electron microscope (Hitachi High Technologies Corporation) equipped with an AMT Hamatsu digital camera (Hamatsu Photonics).

2.10.2 HAADF-STEM and EDX analysis

Cellular samples were imaged using a Cs-corrected JEOL JEM-2100F scanning transmission electron microscope operating at 200 keV. Energy dispersive x-ray (EDX) analysis was performed on the same instrument equipped with an EDX detector.

2.11 Electroporation

Electroporation was performed as described in Material and Methods section of Chapter 1 using 60 pmol of the GFP-targeting AuNP-nanobody conjugates and AuNP solutions as control.

3 Results

3.1 Bioconjugation to nanobodies

For generating AuNP-based immunolabeling agents displaying a minimal recognition (antigen binding) domain and an improved spatial resolution of the targeting system, compared to the AuNP-antibody conjugates presented in the previous chapter, we explored the conjugation of the 2.4 nm AuG to a nanobody targeting the green fluorescent protein (GFP). We chose the anti-GFP nanobody (GFP-nabo) because GFP is ubiquitously used in research and a huge number of GFP-tagged fusion proteins are reported in the literature. We also obtained a HeLa cell line expressing the nuclear protein H2B fused to GFP, thus facilitating the characterization of the conjugation product. Besides, the association of the GFP-nabo with GFP has been structurally determined and the dissociation constant lies in the nanomolar range (K_d = 0.23 nM).[276] For linking the GFP-nabo to AuG we pursued two different strategies. The first approach was based on creating a direct Au-S bond between a thiol-modified GFP-nabo and the TNB-/ TAB-protected AuNP (covalent strategy), resulting in "zero distance" between AuG and the GFP-nabo. The second approach involved the use of complementarily associating peptides tags that were linked/fused to the AuNP/nanobody domain, hence permitting a non-covalent selective association of the two building blocks (non-covalent strategy). The reason for tackling these two strategies was to investigate (i) whether the conjugation approaches are applicable to nanobodies and small-sized AuNPs and (ii) whether the different approaches lead to differences in the biological function of the bioconjugate.

3.1.1 Direct Au-S (covalent) conjugation strategy

Pleiner *et al.* reported the cysteine engineering of an anti-Nup nanobody by mutating six alternative surface exposed amino acids to cysteines to allow the quantitative labeling with maleimide-functionalized fluorophores. Neither the mutations, nor the labeling majorly impaired the antigen binding ability of the nanobody. Among the six mutations the serine at position 7, being in close proximity to the nanobody's paratope, was mutated to a cysteine and a cysteine was added to the C-terminus of the protein, being the farthest away from the antigen binding site. Based on the study from Pleiner *et al.* and the mentioned difference in distance to the nanobody's paratope, we performed a point mutation of the serine7 to a cysteine in the GFP-nabo (yielding C7nabo), and inserted an additional cysteine at the C-terminus of the nanobody (yielding CtCnabo). Besides, a his6 tag for affinity purification, as well as a myc epitope tag

allowing cellular localization by IF was added to the sequence of C7nabo and CtCnabo. The two nanobody constructs were expressed in *E. coli* (cytoplasmic expression) and the fusion proteins were purified by immobilized metal affinity chromatography (IMAC) and gel filtration. Next, we evaluated their apparent affinity for GFP by performing an indirect ELISA using purified GFP as the antigen and an anti-nanobody antibody, as well as an anti-species antibody linked to horse radish peroxidase, as chromogenic signal amplifier. The ELISA tests revealed that the nanobody variants bind to GFP and that their apparent binding affinities are almost identical (IC_{50} of C7nabo: 0.8654 ± 0.335 nM and IC_{50} of CtCnabo: 0.7848 ± 0.247 nM, see ELISA and amino acid sequences of C7nabo and CtCnabo in Figure 47).

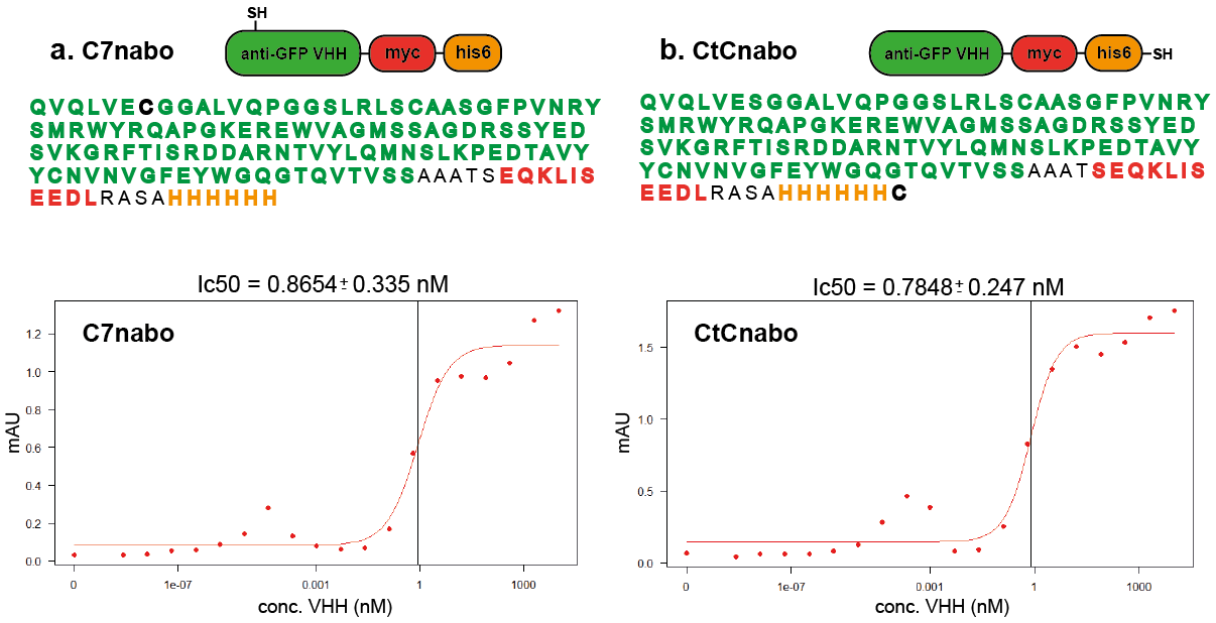

Figure 47. Amino acid sequence and ELISA of GFP-targeting C7nabo and CtCnabo. (a) Amino acid sequence of C7nabo showing the sequence of the VHH domain in green, the sequence of the myc tag in red, the his6 tag in orange and the cysteine at position 7 in black (color code according to sketch). The ELISA revealed an apparent binding affinity of 0.87 nM for C7nabo; (b) Amino acid sequence of CtCnabo showing the different domains in the same color code as for C7nabo and the cysteine (in black) at the C-terminus. The ELISA revealed an apparent binding affinity of 0.78 nM for CtCnabo.

While the apparent affinity for GFP was very similar between the two GFP-nabo mutants, we noticed that the C7nabo was easier to handle than the CtCnabo, as we assessed a difference in proteolytic stability. SDS-PAGE analysis showed that after only three weeks of storage at 4°C the 15 kDa CtCnabo was cleaved in peptidic fragments, whereas the C7nabo was still intact (Figure 67, Supporting Information). Based on the cleavage products we hypothesized that a highly sensitive proteolytic site is located between the VHH domain and the myc tag, which gets hydrolyzed even with small amounts of protease contamination in case of CtCnabo. Since the engineered thiol group in CtCnabo is at the C-terminus of the fusion protein and a hydrolysis between the VHH domain and the myc tag separates the additional cysteine from the VHH

moiety, the desired thiolate-for thiolate exchange reaction between CtCnabo and AuG cannot occur if CtCnabo is degraded. Due to this issue, we decided to only pursue with C7nabo for the direct Au-S conjugation to AuG.

To identify the reactivity of C7nabo towards AuG, as well as to assess how many nanobody molecules can be linked to the surface of AuG *via* direct Au-S coordination, we reacted AuG with increasing amounts of C7nabo. To ensure that the cysteine at position 7 is in its reduced form and can react with the AuG, C7nabo (40 µM) was pre-treated with TCEP (0.1 mM final concentration). A low TCEP concentration was used to favor the reduction of eventual intermolecular disulfide bonds between cysteine7 residues while keeping the naturally occurring intramolecular disulfides intact. Following a 15 min reduction, AuG was mixed with different amounts of reduced C7nabo (1 – 30 eq. C7nabo based on AuG). The reactions were allowed to proceed overnight and the conjugation products were subsequently analyzed by SDS-PAGE (schematic illustration of conjugation strategy in Figure 48 (a) and SDS-PAGE analysis of test conjugations in Figure 48 (b)).

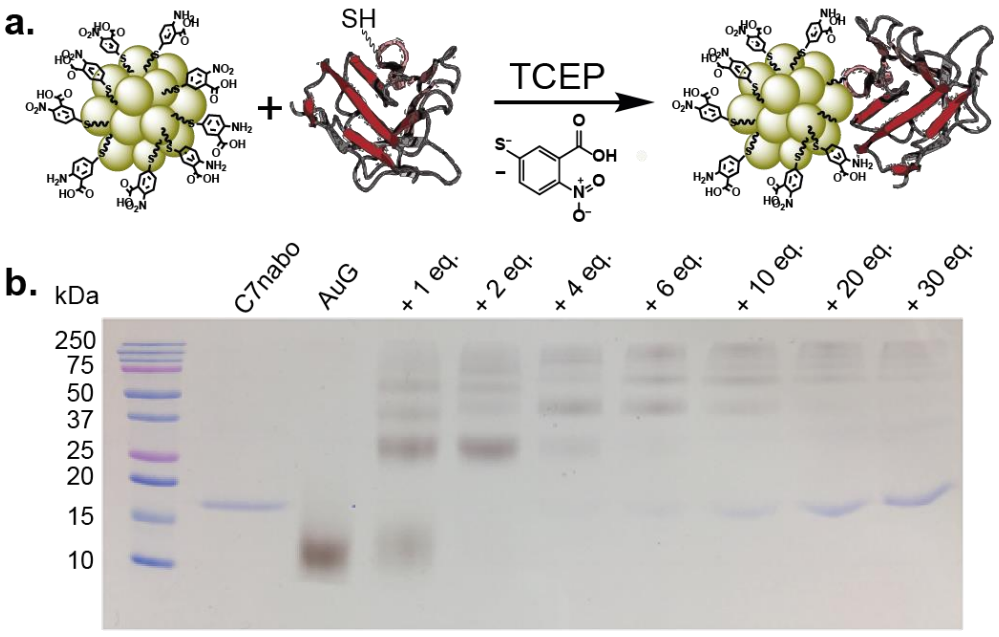

Figure 48. Schematic illustration of direct Au-S conjugation of C7naboo to TNB-/ TAB-protected AuG in (a) and SDS-PAGE analysis of the reactions of AuG with increasing amounts of C7nabo in (b). AuG was reacted with 1 eq., 2 eq., 4 eq., 6 eq., 10 eq., 20 eq., and 30 eq., of C7nabo. AuNP-containing species appeared as brown bands on the gel (no silver staining) and protein bands were revealed by Coomassie blue staining.

The SDS-gel showed that C7nabo reacts with AuG in a similar manner as thiolated peptides, such as the thiolated NLS peptide (ca. 2000 Da) presented in Chapter 1. As previously observed for the reaction with the NLS peptide, the thiolate-for-thiolate exchange always yields a mixture of conjugates consisting of different amounts of protein per particle. By counting the AuNP

bands that appear upon reaction with C7nabo, having a lower electrophoretic mobility than AuG, it can be deduced that up to five nanobody molecules can be linked to the surface of AuG.

Since we aimed at generating an EM probe being as precise and small as possible, we ideally wanted to produce a conjugate being composed of one GFP-nabo molecule per AuNP. In order to favor the formation of such a 1:1 AuNP-nanobody conjugate, we performed the described thiolate exchange using excess of AuG. By varying the ratio of AuG/C7nabo from 1 – 10 we assessed that all ratios yield at least two conjugate bands, very likely representing Au-$(C7nabo)_1$ and Au-$(C7nabo)_2$ (SDS-PAGE analysis of test reactions in Figure 68, Supporting Information). Considering that AuG bears approximately 130 ligands on its surface, thus offers 130 possible reaction sites for the thiolated GFP-nabo, it is not surprising that a conjugate mixture was obtained and in fact a mixture of only two conjugate species represents a rather low polydispersity. Due to the small difference in size of Au-$(C7nabo)_1$ and Au-$(C7nabo)_2$, whose separation would likely be accompanied by high product losses, we decided to produce a conjugate consisting of a mixture of Au-$(C7nabo)_1$ and Au-$(C7nabo)_2$ and to purify this mixture from unreacted AuG. The AuG/C7nabo ratio of 4 was identified as the most suitable ratio in terms of product yield and we therefore proceeded with this condition for the scale up. Figure 49 (a) shows the SDS-PAGE analysis of the direct Au-S conjugation of C7nabo to AuG. As mentioned before, the two AuNP bands with retarded electrophoretic mobility in the lane of Au-C7nabo were assigned to Au-$(C7nabo)_1$ and Au-$(C7nabo)_2$ (see sketches next to lane of Au-C7nabo). Then, the remaining reactive TNB-/ TAB-ligands present on the AuNP surface were exchanged with peptide Cap. The reason for using Cap for the passivation of the conjugate, instead of furtive PEG was to be able to easily follow the reaction progress by SDS-PAGE, as PEG shields charge and blurries electrophoretic analysis. As we wanted to finally separate the passivated Au-C7nabo from unreacted (passivated) AuG, it was of uttermost importance to be able to discern the products from the educts – at least at the stage of implementation. The crude Cap-coated conjugate, named "AuC-C7nabo" was thereafter purified using Ni-NTA agarose beads, making use of the his6-tag that was fused to the C7nabo. The purification of AuC-C7nabo was tracked by SDS-PAGE (Figure 49 (b)), which revealed that unreacted (passivated) AuG did not bind to the beads and was entirely removed by washing the beads with PBS (see the UB, W1 and W2 fractions in Figure 49 (b)). The third PBS wash fraction (W3) and further two wash factions containing 15 mM imidazole did not contain any proteins or AuNPs and finally, two retarded bands, assigned to the conjugate species AuC-$(C7nabo)_1$ and AuC-$(C7nabo)_2$, were eluted from the beads with 200 mM imidazole (encircled in red in Figure 49 (b)).

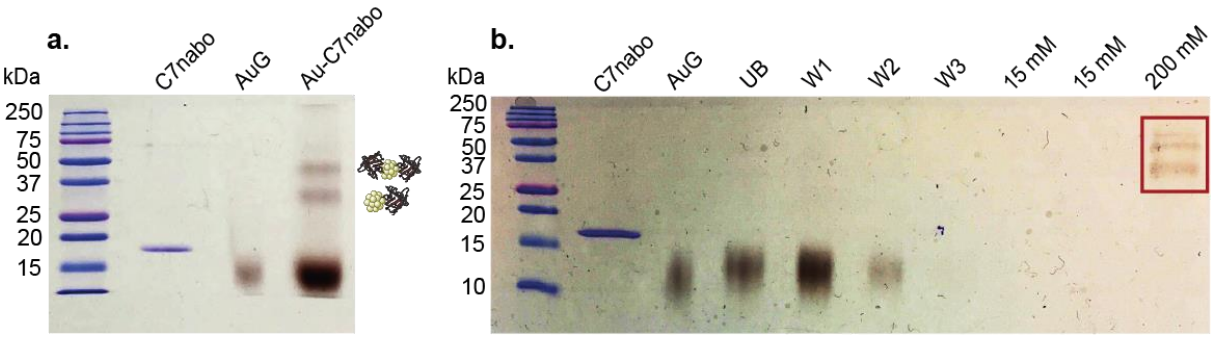

Figure 49. SDS-PAGE analyses of AuC-C7nabo formation. (a) Crude reaction product of AuG and C7nabo using AuG/C7nabo ratio of 4; (b) Ni NTA affinity purification of AuC-$(C7nabo)_1$ and AuC-$(C7nabo)_2$ from unreacted AuG. Order on the gel from left to right: C7nabo, AuG, fraction unbound to Ni NTA beads (UB), PBS wash fraction 1 (W1), PBS wash fraction 2 (W2), PBS wash fraction 3 (W3), first wash with 15 mM imidazole (15 mM), second wash with 15 mM imidazole (15 mM) and elution of AuC-C7nabo conjugate with 200 mM imidazole (200 mM).

After having established this purification procedure, we also prepared Au-C7nabo coated with 2000 Da PEG (named "AuP-C7nabo") and purified the conjugate accordingly to the described procedure. (SDS-PAGE analysis of purification of AuP-C7nabo in Figure 69, Supporting Information). Although the passivation with PEG disturbed the electrophoretic mobility in a way that did not permit to distinguish between PEGylated AuG and the Au-$(C7nabo)_1$-PEG and Au-$(C7nabo)_2$-PEG products, the Au-C7nabo-PEG purification profile was similar to the one of the Cap-coated conjugate. The binding and the imidazole-promoted elution of the brown AuNP-conjugate solution to/from the blue Ni-NTA beads were observed in both cases.

3.1.2 Non-covalent conjugation strategy

For the non-covalent linkage between the GFP-nabo and the 2.4 nm AuG, we aimed at equipping the AuNP and the nanobody domain with peptide tags that are able to assemble with each other in a selective and highly stable manner. It was demonstrated that point mutations in the p53 tetramerization domain[277] can transform the homo tetramer into a hetero tetramer (dimer of dimers) with high selectivity and affinity.[278] These peptide dimers, named K3 and E3 were chosen due to their low molecular weights (ca. 5 kDa), as well as their high affinity for each other permitting K3-E3 association in biological fluids – even inside living cells.[273] In this manuscript the peptide tag K3, which was linked to the AuNP, is hereafter referred to as "*bi"* and the E3 tag which was fused to the GFP-nabo is hereafter named "*nd"*.

To equip the GFP-nabo with the *nd* tag, the *nd* sequence was cloned to the C-terminus of the GFP-nabo and the fusion protein was produced in *E.coli*, hereafter referred to as *nd*-nabo. Due to the dimerization of the *nd*-tag, the produced *nd*-nabo immediately associates into dimers in solution forming (*nd*-nabo$_2$). A schematic illustration of the(*nd*-nabo$_2$) homodimer, as well as the SDS-PAGE analysis of IMAC-purified protein fractions and the chromatogram of *nd*-nabo after gel filtration are depicted in Figure 50. Note, that the 23 kDa *nd*-nabo fusion protein has a reduced electrophoretic mobility (migrating at ca. 30 kDa), which is due to the *nd* motif consisting of a β-strand followed by an α-helix.[273]

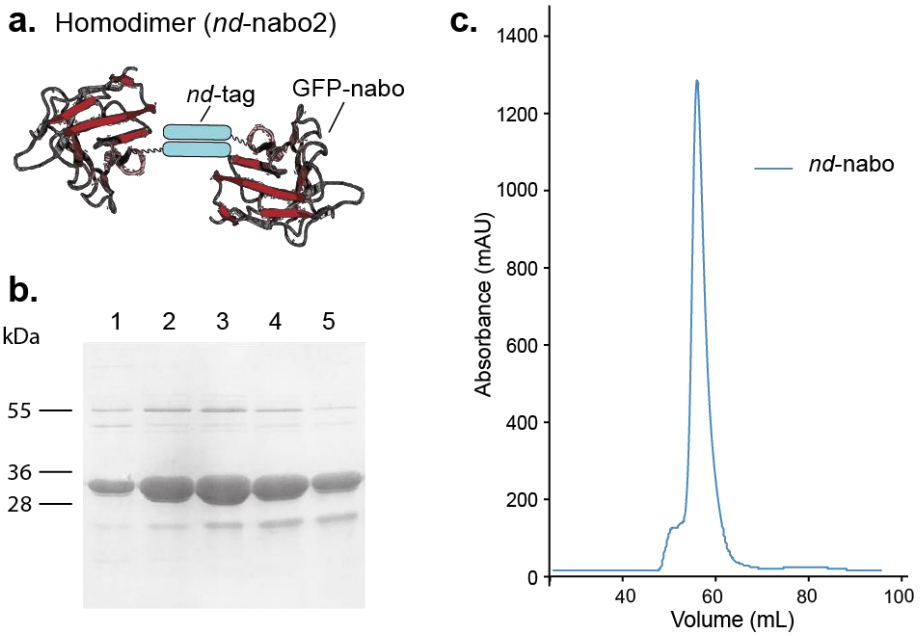

Figure 50. Schematic illustration of the (*nd*-nabo$_2$) homodimer and purification of *nd*-nabo by IMAC and gel filtration. (a) Ribbon diagram of GFP-nabo (in red), fused to *nd*-tag (in blue), which mediates the homodimerization of the nanobody fusion protein; (b) reducing SDS-PAGE analysis of *nd*-nabo fractions from IMAC showing the tagged GFP-nabo at 30 kDa (actual MW of *nd*-nabo is 23 kDa, but *nd*-motif retards the electrophoretic migration); (c) Chromatogram of *nd*-nabo purified by gel filtration.

For tagging the AuG particle, a synthetic peptide containing the sequence of the *bi* tag, as well as the sequence of the 6 amino acid peptide Cap at the N-terminus [CALNNG EYFTLQIRGRERFEMIRKLNKALELKDAQA] was purchased (sequence of *bi* tag underlined). Since the amino acid sequence of the *bi* tag does not contain any cysteines, the synthetic peptide, containing only one cysteine at the C-terminus (part of Cap) is ideally suited for the attachment to AuG *via* Au-S coordination. To evaluate the reactivity of the synthetic peptide *bi* with AuG, the AuNP was mixed with the peptide at *bi*/AuG ratios ranging from 0 to 12. It needs to be noted that once peptide *bi* is solubilized in water, it immediately self-assembles into *bi* dimers and consequently, the ratios of *bi*/AuG ranging from 0 to 12 represent (*bi*$_2$)/AuG ratios ranging from 0 to 6. The thiolate-exchange reactions were allowed to proceed

overnight and subsequently analyzed by SDS-PAGE. A schematic illustration of the thiolate-for-thiolate exchange reaction of the *bi* dimer with AuG and the corresponding analysis by SDS-PAGE are depicted in Figure 51 (a) and (b). The analysis of the products showed that a (bi_2)/AuNP ratio of 3 resulted in the formation of three distinctive AuNP species (encircled in red in Figure 51 (b)), most likely corresponding to Au-(bi_2), Au-(bi_2)$_2$ and Au-(bi_2)$_3$, and left no unreacted AuNPs. When using less than 3 equivalents of (bi_2) a significant amount of AuG remained unreacted and when the (bi_2)/AuNP ratio was increased to higher values than 3, the amounts of (bi_2) on the AuNP surface further increased. In order to do not complicate the conjugation to *nd*-nabo by increasing the number of *bi* on the surface of AuG and to avoid a purification step for separation from unreacted AuG, we selected the (bi_2)/AuNP ratio of 3 for the functionalization of AuG (hereafter simply referred to as "Au-*bi*") .

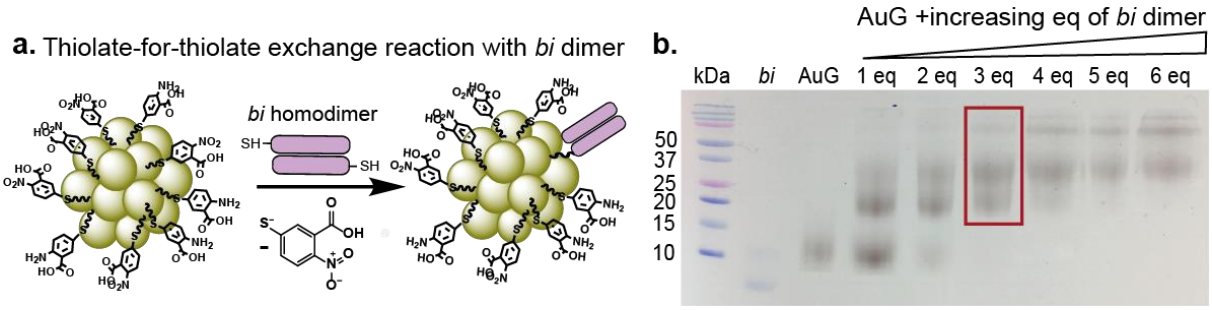

Figure 51. Schematic illustration of the functionalization of AuG with bi peptide dimer via thiolate for thiolate exchange in (a) and SDS-PAGE analysis of AuG reacted with increasing amounts of bi peptide in (b). The use of 3 eq. *bi* dimer [(bi_2)/AuNP ratio of 3], yielding three Au-*bi* species, while leaving no unreacted AuG, is encircled in red.

Having identified the reaction conditions for generating Au-*bi*, the tagged nanoparticle was prepared at a larger scale, thus permitting the non-covalent conjugation to *nd*-nabo (schematic representation of the conjugation approach depicted in Figure 52 (a)). As a next step, Au-*bi* was passivated with peptide Cap, as well as with PEG. The addition of Cap caused irreversible precipitation of the nanoparticles in aqueous solutions, whereas the PEGylated *bi*-tagged gold particles (named "AuP-*bi*") did not appear to precipitate and could be analyzed by SDS-PAGE (Figure 52 (b)). The generated AuP-*bi* was subsequently tested for the non-covalent conjugation to *nd*-nabo. Therefore, AuP-*bi* was titrated with increasing amounts of *nd*-nabo for 1 h at RT and afterwards the assembled products were analyzed by native PAGE (Figure 52 (c)). The band corresponding to *nd*-nabo is visible with an apparent and expected molecular weight of 40 kDa (dimerization of the *nd*-tag, lane 1). AuP-*bi* (lane 2) barely migrated into the polyacrylamide gel, which is likely due to charge shielding caused by PEG. Consequently, the non-covalent association of *nd*-nabo and *bi*-tagged AuG did not result in an electrophoretic

mobility shift. However, the association of *nd*-nabo and AuP-*bi* could be assessed by monitoring an increased Coomassie blue staining of the non-migrating AuP-*bi* upon addition of increasing amounts of *nd*-nabo. At the initial stoichiometric *nd*-nabo/AuP-*bi* ratios of 0.5 and 1 (lanes 3 and 4), no free *nd*-nabo is visible on the gel. However, unassociated *nd*-nabo started to appear with *nd*-nabo/AuP-*bi* ratios of 2 and above (lanes 5 and 6), indicating that on average only one *nd*-nabo can be bound to AuP-*bi* (yielding AuP-*bind*-$(nabo)_1$). Based on this titration assay, the AuP-*bind*-nabo conjugate was generated by mixing equimolar amounts of AuP-*bi* and *nd*-nabo together.

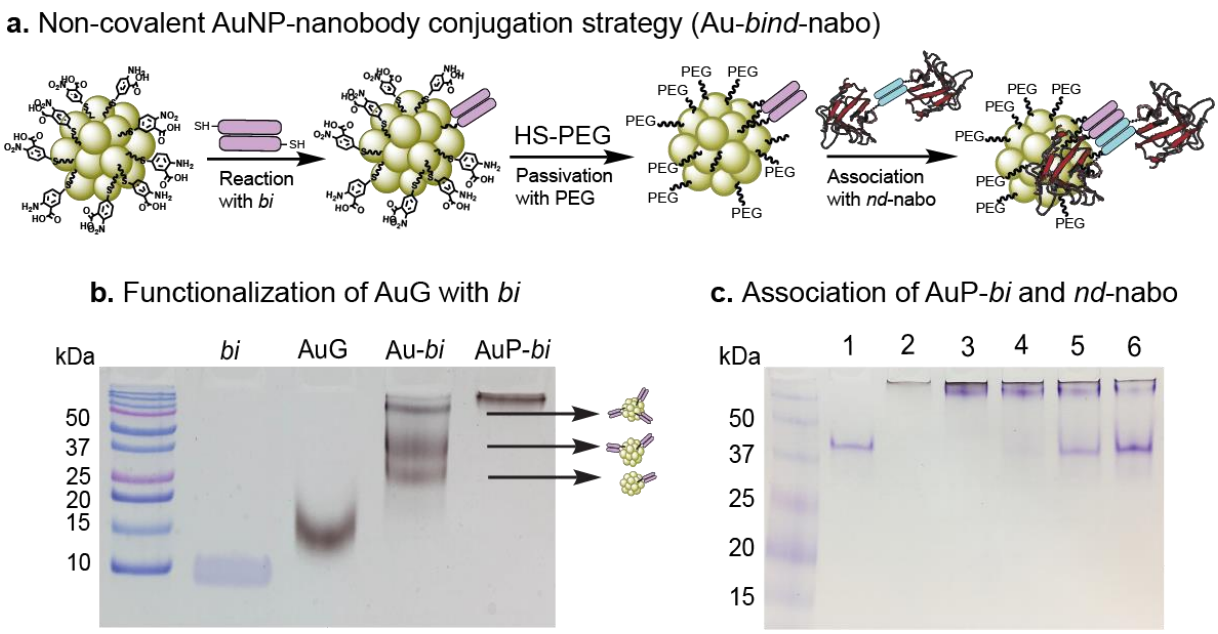

Figure 52. Non-covalent conjugation strategy for linking GFP-nabo to AuG mediated by *bi*/*nd* tags. (a) Schematic representation of the conjugation approach: Functionalization of AuG with peptide *bi* in first step, passivation with thiolated PEG in the second step and association with (*nd*-$nabo_2$) in the third step; (b) SDS-PAGE analysis of functionalization of AuG with peptide *bi* (yielding Au-*bi*) and passivation with PEG (yielding AuP-*bi*); (c) Native gradient PAGE of self-assembly between AuP-*bi* and *nd*-nabo (1= *nd*-nabo, 2 = AuP-*bi*, 3 = 1 eq. *nd*-nabo + 2 eq. AuP-*bi*, 4 = 1 eq. *nd*-nabo + 1 eq. AuP-*bi*, 5 = 2 eq. *nd*-nabo + 1 eq AuP-*bi*. 6 = 4 eq. *nd*-nabo + 1 eq. AuP-*bi*).

The finding that on average only one *nd*-nabo can be linked to AuP-*bi* was puzzling, since *nd*-nabo is known to self-assemble into the homodimer (*nd*-$nabo_2$), which upon addition to (bi_2) peptide forms a heterotetramer (bi_2)(*nd*-$nabo_2$). Based on this knowledge it was expect that the Au-(bi_2) species forms a conjugation product consisting of 2 nabos per particle, Au$(bi_2)_2$ a conjugate with 4 nanobodies per particle and Au-$(bi_2)_3$ a conjugate with 6 nanobodies per particle. Yet, the dimerization/tetramerization of *bi*-*nd* tags on the surface of nanoparticles has not been studied before and the presence of the passive PEG-layer, or potential inter-particle crosslinks mediated by the *bi* dimer might influence the peptide tag assembly.

3.2 Evaluation of GFP-binding ability

In order to test the ability of the generated covalent and non-covalent AuNP-nanobody conjugates to bind to GFP-fused proteins, we firstly performed an immunocytochemistry experiment using a stably transformed HeLa cell line that expresses the nuclear histone protein H2B fused to GFP. The wild type HeLa cell line devoid of GFP was used as a control. Both cell lines were cultivated on glass coverslips before being fixed, permeabilized and incubated with the conjugates. Since the passivation of Au-*bi* with peptide Cap promoted the particle's aggregation and it was therefore not possible to produce the corresponding non-covalent conjugate, we only compared the binding ability of the covalent conjugates (AuC-C7nabo and AuP-C7nabo) to the one of the PEGylated non-covalent conjugate (AuP-*bind*-nabo). The fixed and permeabilized cells were incubated with the three conjugates for 1 h at a concentration of 6 nM and after several washes the AuNP moiety was revealed by gold-induced silver enhancement up to a stain visible by optical microscopy (Figure 53).

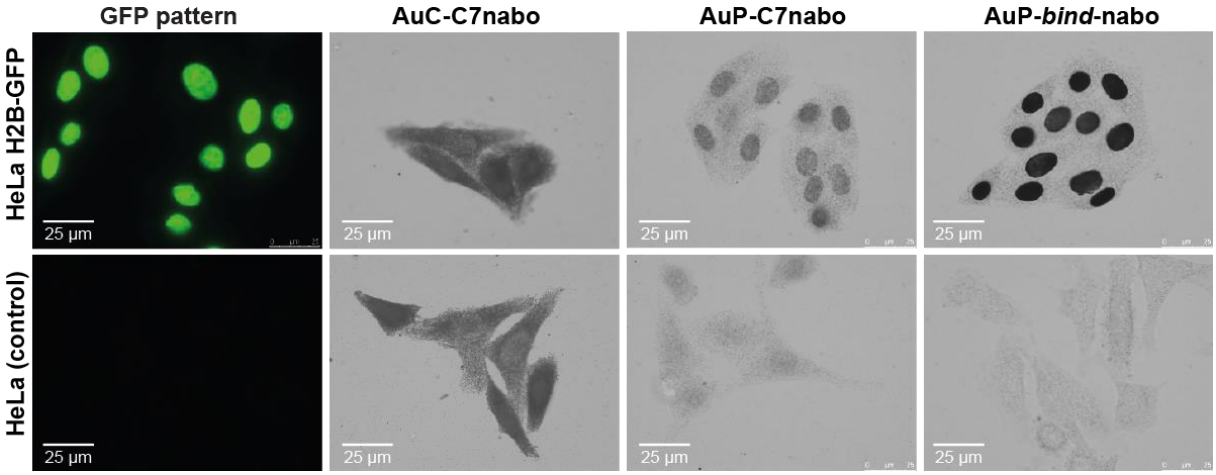

Figure 53. Optical microscopy images of HeLa H2B-GFP cells (top row) and HeLa cells devoid of GFP expression (bottom row) incubated with the covalent conjugates AuC-C7nabo and AuP-C7nabo and the non-covalent conjugate AuP-*bind*-nabo. AuNPs were revealed by silver staining. Scale bar: 25 µm.

The incubation with AuC-C7nabo caused a strong staining of the nucleus, as well as the cytoplasm of H2B-GFP expressing- and control cells, which demonstrates that the conjugate is unfortunately not able to bind to GFP specifically, but strongly interact with cellular components in an unspecific manner. Although some degree of background labeling was already observed for the Cap-coated AuNP-antibody conjugate Au-7G5 targeting RNAP II, the extent of unspecificity observed for AuC-C7nabo was not comparable and clearly showed that further biding studies with this conjugate are pointless. The immunolabeling using AuP-C7nabo produced the expected nuclear staining in HeLa H2B-GFP cells, but at the same time the conjugate also caused some labeling of the nucleus of wild type Hela cells, suggesting that this

probe has some specificity issues as well. In contrast, the AuP-*bind*-nabo conjugate yielded a strong nuclear staining for HeLa H2B-GFP cells and almost no background staining of the nuclei of the wild type HeLa cells, which implies that the non-covalent AuP-*bind*-nabo is more performant as GFP-targeting probe than the C7nabo conjugates generated by direct Au-S conjugation.

Based on the obtained data, we next wanted to compare the apparent binding efficiency for GFP of the PEGylated, covalent conjugate AuP-C7nabo and the PEGylated, non-covalent conjugate AuP-*bind*-nabo (AuC-C7nabo was not used in further experiments). We therefore performed an indirect ELISA using purified GFP as the antigen and an anti-VHH antibody, as well as an anti-species antibody linked to horse radish peroxidase, as chromogenic signal amplifier. The apparent binding efficiency for AuP-*bind*-nabo was determined at 1.74 +/- 0.12 nM (Figure 54 (a)), which corresponds to the expected nanomolar range of the GFP-nabo.[276] As opposed to this, the apparent binding affinity for the covalent AuP-C7nabo conjugate could not be determined, because we did not obtain signal variations of sufficient magnitude (Figure 54 (b)). To exclude that this lack of signal was not simply caused by the fact that the anti-VHH antibody was unable to bind to the C7nabo due to the shielding by the PEGylated particle, a second ELISA was carried out, during which the AuNP moiety was revealed *via* gold-induced silver staining, according to a published protocol from Moeremans *et al.*[274] Yet, the second ELISA revealed the same binding profiles, as the previous one, in which the nanobody moiety was revealed (Figure 54 (c) and (d)). Altogether, the data obtained from the ELISA lead to the conclusion that only AuP-*bind*-nabo has the potential for probing GFP, whereas the covalent AuP-C7nabo conjugate cannot be employed for this purpose, since the affinity of C7nabo for GFP was obviously lost through the conjugation to the AuNP. This observed loss in GFP binding ability is unfortunate but might be explained by a modification of the nanobody's 3D structure caused by the direct contact between the C7nabo and the surface of AuG.

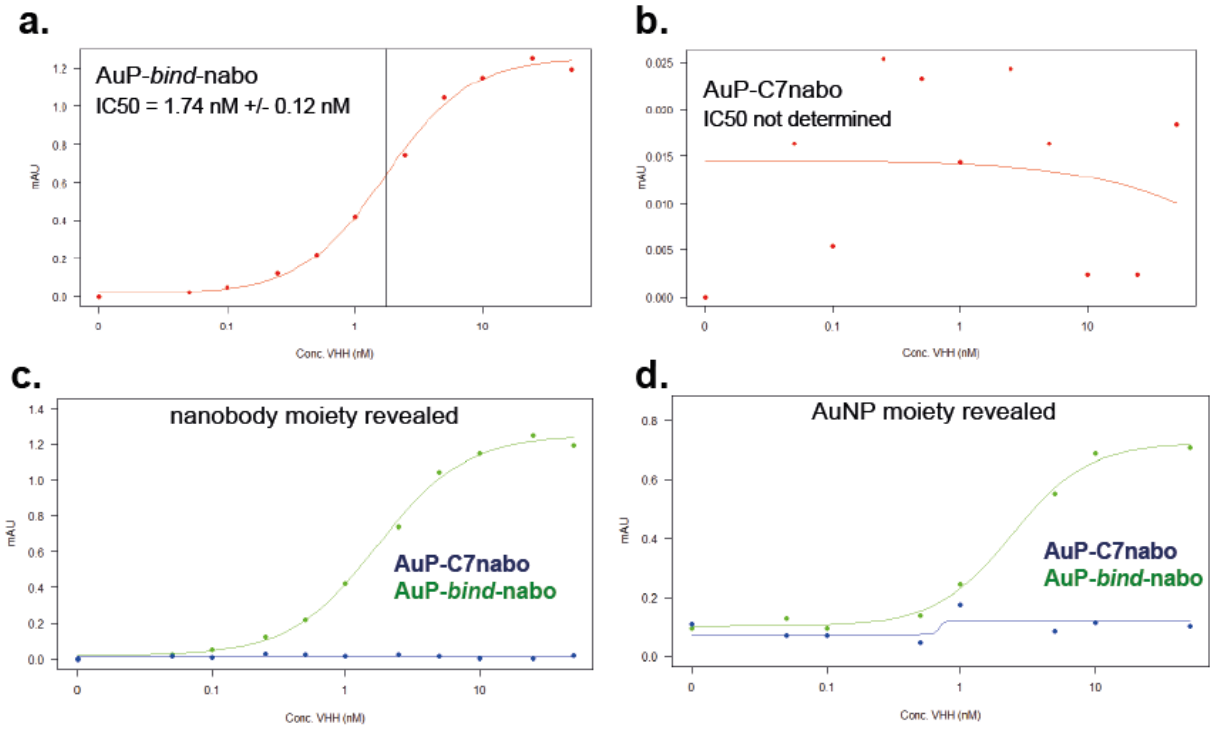

Figure 54. Determination of apparent binding affinity of AuNP-nanobody conjugates by indirect ELISA (immobilized purified GFP at 1 µg/mL). (a) The apparent binding efficiency for AuP-*bind*-nabo was determined to be 1.74 nM +/- 0.12 nM; (b) No apparent binding efficiency could be determined for AuP-C7nabo; (c) Comparison of the covalent and non-covalent conjugate by revealing the nanobody domain; (d) Comparison of the covalent and non-covalent conjugate by revealing the AuNP moiety.

3.2.1 Applicability of AuP-*bind*-nabo for probing other GFP-tagged proteins

The usefulness of the non-covalent AuP-*bind*-nabo conjugate for probing the localization of GFP-fused proteins was next verified using different GFP-tagged proteins that were transiently expressed in HeLa cells. 24 h after transfection the cells were fixed, permeabilized and incubated with AuP-*bind*-nabo, as it was described for the binding to H2B-GFP. The localization of the conjugate was again revealed by gold-induced silver enhancement. The fusion protein β-galactosidase-GFP having a molecular weight of over 520 kDa localizes only in the cytosolic compartment of the cell. Yet, when an NLS is fused to β-galactosidase-GFP, the protein is translocated into the nucleus, resulting in a nuclear green fluorescence signal. When AuP-*bind*-nabo was used to detect the localization of β-galactosidase-GFP and β-galactosidase-GFP-NLS, the expected cytosolic and nuclear labeling patterns were observed (Figure 55). As another example, we probed the proliferating cell nuclear antigen (PCNA) using the con1-GFP fusion protein which has a high affinity for PCNA (affinity constant of con1 for PCNA = 10^7 M^{-1}).[279] PCNA is a sliding platform that binds to DNA to mediate protein interactions with the DNA strand.[280] The soluble form of PCNA is homogeneously distributed

inside the nucleus, whereas DNA-bound PCNA molecules form foci. For visualizing the mixture of DNA-bound and homogeneous PCNA, the cells were fixed 24 h after transfection with con1-GFP, as it was performed during the previous experiments. For exclusively observing DNA-bound PCNA, unbound PCNA and con1-GFP were washed away from the cell interior by plasma membrane permeabilization with a cytoskeleton buffer[281] prior to the fixation. Again, for the classical specimen preparation, meant to label the soluble, as well as DNA-bound form of PCNA, a homogenous nuclear staining was observed. Yet when the specimens were treated with the cytoskeleton buffer, discrete foci were detected (Figure 55).

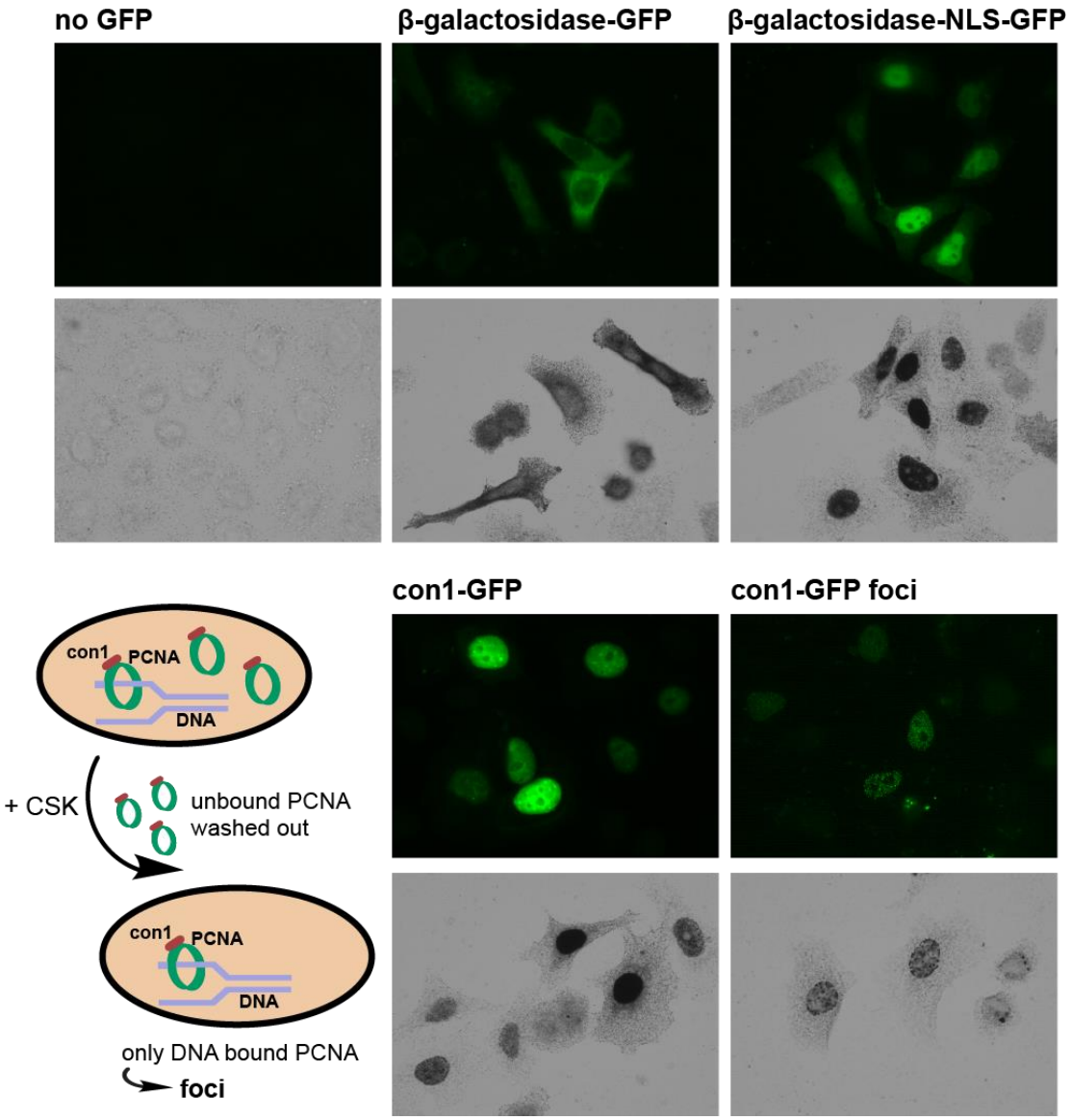

Figure 55. Immunolabeling of different GFP-fused proteins with AuP-*bind*-nabo. HeLa cells were transiently transfected with the following GFP fusion constructs: β-galactosidase-GFP, β-galactosidase-NLS-GFP and con1-GFP. 24 h after transfection cells were fixed, permeabilized and incubated with AuP-*bind*-nabo. The localization of the probe was revealed by gold-induced silver staining. con1-GFP (PCNA) foci were detected by treating the cells with a cytoskeleton buffer prior to fixation.

Taken together, AuP-*bind*-nabo was able to bind to all of the tested transiently expressed GFP-tagged proteins (β-galactosidase-GFP, β-galactosidase-GFP-NLS and con1-GFP), thus confirming the potential of the AuP-*bind*-nabo conjugate as a probe for the localization of different GFP-fused proteins inside cells.

3.2.2 Pre-embedding immunolabeling of H2B-GFP for EM observation

After having assessed that AuP-*bind*-nabo is well suited for the targeting of various GFP-fused proteins and has an apparent affinity for GFP lying in the nanomolar range, its suitability for classical immuno-EM using fixed cells remained to be clarified, before proceeding with the more challenging *in cellulo* labeling. We decided to perform pre-embedding immunolabeling, over post-embedding for a twofold reason. First, pre-embedding immuno-EM is technically simple and requires only minimum EM equipment. Second, pre-embedding immunolabeling does not require glutaraldehyde fixation prior to the antibody incubations and it was assessed that the GFP-nabo does not bind to GFP-fused proteins when cells are fixed with glutaraldehyde.

To test the applicability of AuP-*bind*-nabo for pre-embedding immuno-EM, we used the stable cell line HeLa H2B-GFP and HeLa cells as a control. The labeling of the fixed and permeabilized cells was performed accordingly to the immunocytochemistry experiment for optical microscopy described earlier with the only alteration that the incubation with the AuP-*bind*-nabo conjugate was performed at 4°C overnight. After a post-fixation step AuNPs were silver enhanced and membranes were stained with osmium tetroxide. The AuNPs were enlarged by silver enhancement, because the samples were imaged with a standard TEM in the first place, whose resolution is limited to the visualization of AuNPs > 5 nm when embedded in cellular sections. The TEM observation of the cell sections revealed that HeLa H2B-GFP cells were labeled exclusively inside the nucleus (no particles detectable in the cytoplasm), while labeling was completely absent in HeLa cells (Figure 56). These results are in agreement with the former binding studies, which showed that AuP-*bind*-nabo binds to H2B-GFP specifically. It can be noted that the labeling density in HeLa H2B-GFP cells is higher at the periphery of the nucleus, compared to the density in the center. This observation was surprising, because neither the GFP fluorescence, nor the immunolabeling performed for optical microscopy during which the AuNP domain was revealed by silver staining showed this pattern. However, it needs to be considered that entire cells were imaged during the optical microscopy observation and cell sections during the current EM study. Hence, the higher abundance of H2B-GFP at the nuclear

periphery might eventually only be detectable when thin slices of cells are imaged. Another possible reason might be related to the diffusion properties of the AuP-*bind*-nabo probe and a higher accessibility to certain sites within the nucleus (discussed in more detail in the discussion part of this chapter). Finally, it needs to be noted that the cellular ultrastructure of the imaged cells is compromised, showing a particular denaturation of the cytosol, which is cause by the permeabilization using Triton X-100. Prior to performing the pre-embedding immunolabeling, we tested different permeabilization methods, including various concentrations of saponin (classically used for pre-embedding EM studies), but the mild permeabilization did not permit the penetration of the AuP-*bind*-nabo probe into the nucleus, which restricted us to the use of Triton X-100.

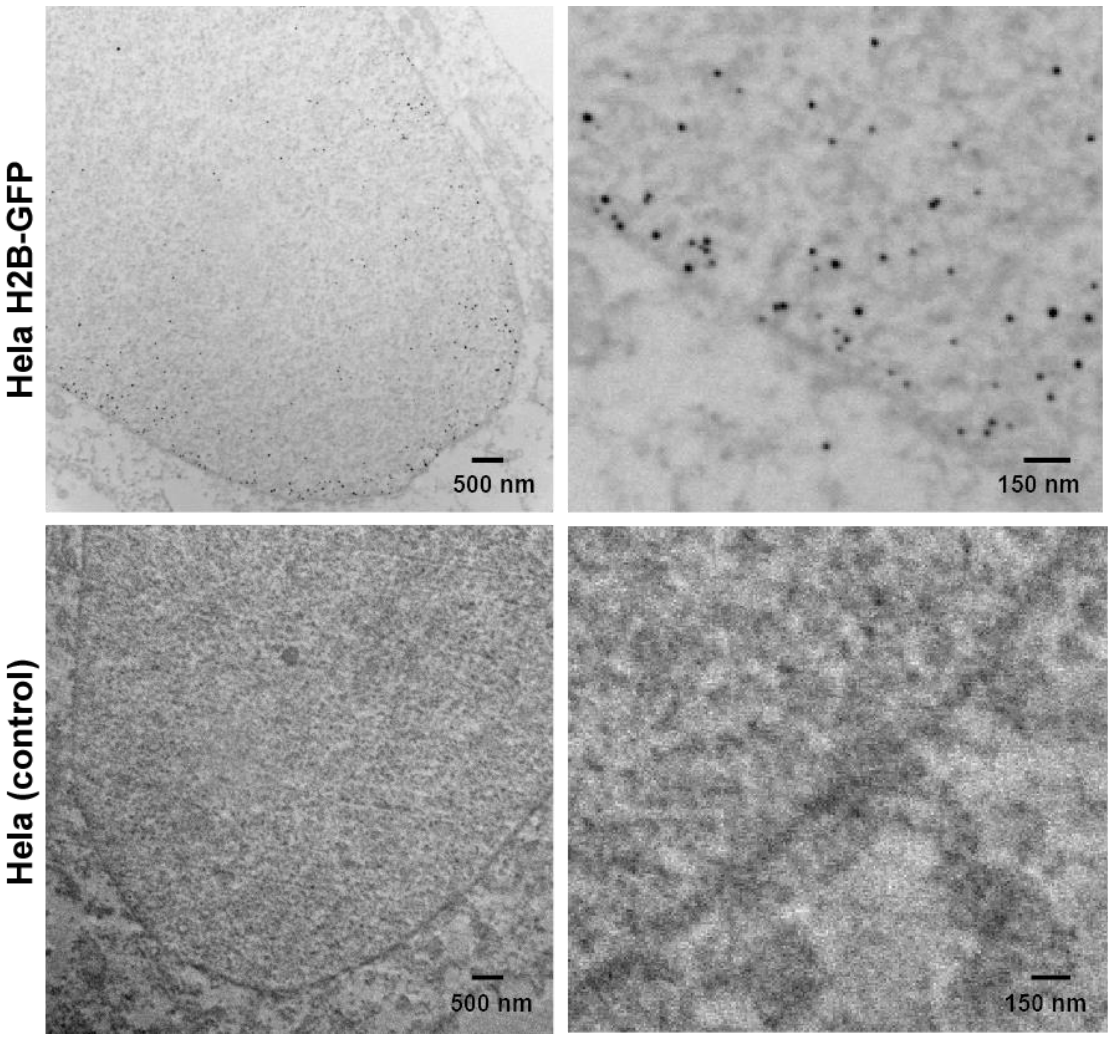

Figure 56. Transmission electron micrograph of immunolabeled histone protein H2B-GFP using AuP-*bind*-nabo in a pre-embedding approach. Top row: HeLa cells expressing the GFP-tagged histone H2B. Bottom row: HeLa cells devoid of GFP expression as control. After immunolabeling and post-fixation, AuNPs were silver enhanced and membranes stained with OsO_4. HeLa H2B-GFP cells were exclusively labeled inside the nucleus (preferentially at the nuclear periphery), no labeling was observed for HeLa cells. Images on the right show magnification of images on the left. Scale bar (images on the left): 500 nm. Scale bar (magnified images on the right): 150 nm.

Altogether, the specificity of AuP-*bind*-nabo for GFP was once more confirmed and it was demonstrated that the conjugate can be applied as probe for pre-embedding immuno-EM. Since the immunolabeling using AuP-*bind*-nabo does not involve several incubations with antibodies and antibody-AuNP conjugates, but only a single labeling step, the novel nanobody probe represents an attractive alternative to conventional immunogold labeling agents with regards to working time requirement. Nevertheless, it needs to be stated that the requirement for Triton X-100 permeabilization is a weakness of the AuP-*bind*-nabo probe and raises questions about the conjugate's diffusion profile.

3.2.3 Direct visualization by HAADF-STEM

HAADF-STEM enables the imaging of hard materials at atomic resolution. In recent years, the laboratory of Richard D. Leapman has for the first time reported the direct visualization of 2 nm AuNPs, coated with glutathione and the cell penetrating peptide TAT, inside cell sections by HAADF-STEM, without the use of silver enhancement and heavy metal staining.[108] The authors were not able to observe single particles, but small aggregates consisting of estimated 2 – 10 AuNPs. To find out whether the 2.4 nm AuNPs of the AuP-*bind*-nabo probe can be directly visualized when embedded in cell sections by HAADF-STEM as well, we repeated the pre-embedding immunolabeling of H2B-GFP by omitting the silver enhancement step. The cell sections were subsequently analyzed by HAADF-STEM. As control, we imaged the silver stained samples from the previous experiment as well. The recorded HAADF-STEM images of the silver enhanced H2B-GFP cells clearly showed the AuNPs inside the nucleus, according to the former results showing a preferential labeling at the nuclear periphery (Figure 57 (a)). The visualization of the AuNPs in the cell sections that were not silver stained was more challenging (images depicted in Figure 57 (b)). While it was possible to detect aggregates of AuNPs having a diameter of 50 – 100 nm at the nuclear periphery, as well as in the cytosol, most likely representing a labeling artefact (red arrows on left image Figure 57 (b)), we were not able to detect induvial particles or small aggregates as it was described by Leapman *et al.*[108] When going to higher magnification at regions within the cellular nucleus that were brighter and hence expected to correspond to small aggregates of AuNPs, the bright structures became very diffuse and it was not possible to detect any discrete particles, making it hard to believe that the observed structures are AuNPs (Figure 57 (b) image on the right). Yet, when an EDX spectrum of the imaged area was recorded (Figure 58), it was assessed that the imaged region clearly contains gold.

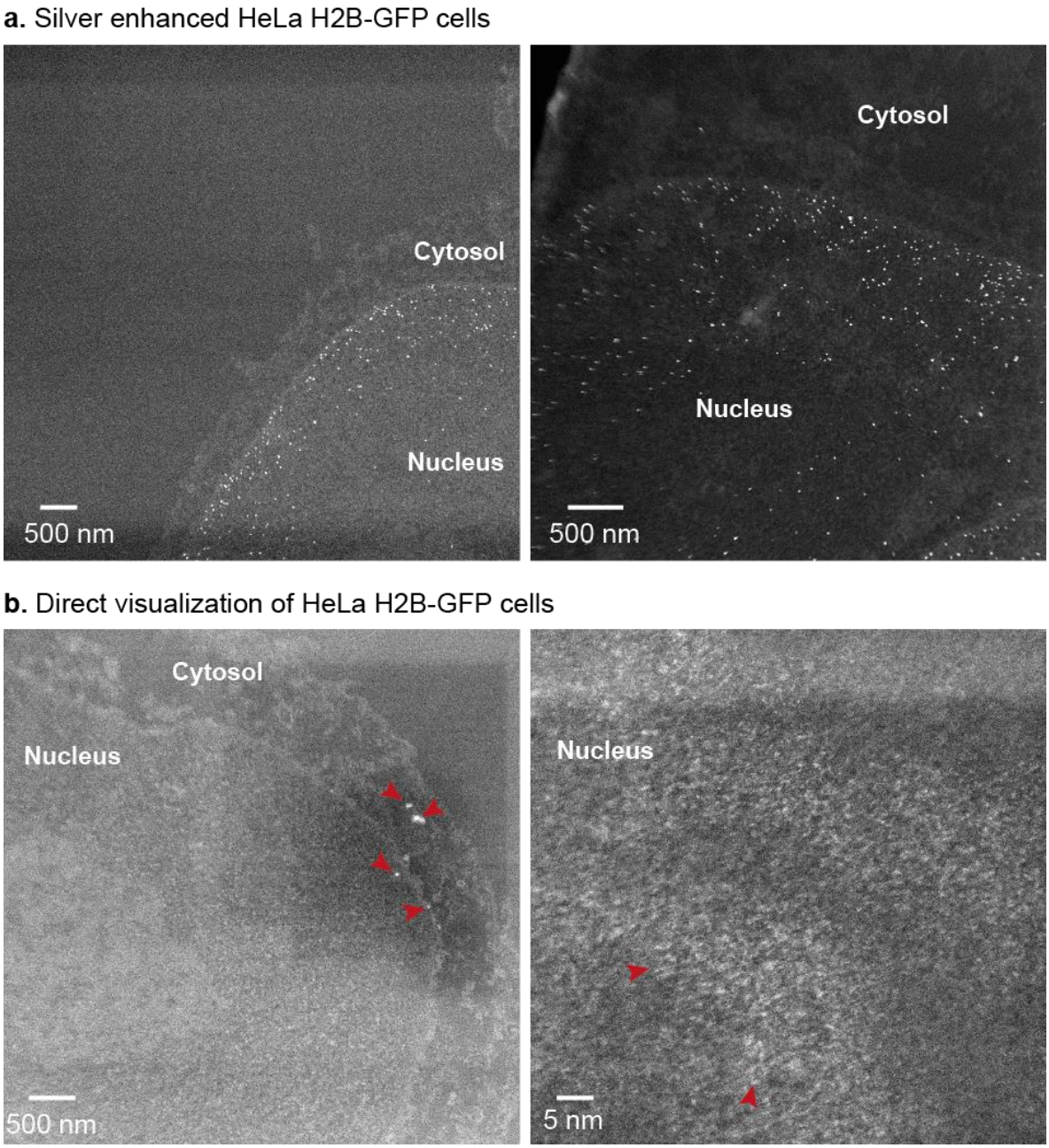

Figure 57. HAADF-STEM observation of HeLa H2B-GFP cells immunolabeled with AuP-*bind*-nabo. (a) Cells were silver stained allowing to clearly see the AuNPs at lower magnification (scale bar: 500 nm); (b) AuNPs were not silver enhanced and only large aggregates of AuNP can be detected at lower magnification (red arrows in image on the left, scale bar: 500 nm). At higher magnification (image on the right, scale bar: 5 nm) regions with high contrast are detectable (arrows), but no discrete particles can be seen. Cellular samples imaged by Dr. Dris Ihiawakrim (IPCMS- Plateforme Microscopie électronique).

These observations were puzzling, as it was expected that the 2.4 nm AuNPs provide enough contrast to be clearly discernable from the cellular constituents, but it needs to be noted that the electron beam operating at 200 keV, intended to visualize hard materials, is very strong and easily destroys biological material, especially at high magnification. For instance, the crosslinking of organic molecules, that are adsorbed to the biological specimen, through the electron beam (phenomenon called contamination),[282] which resulted in a visual cloud over the

imaged sample, clearly impaired the observation of the specimen. Hence, it can be concluded that further investigations in future studies will be necessary for making a clear deduction on whether the gold domain of Au-*bind*-nabo can be directly detected by EM when embedded in the cellular ultrastructure.

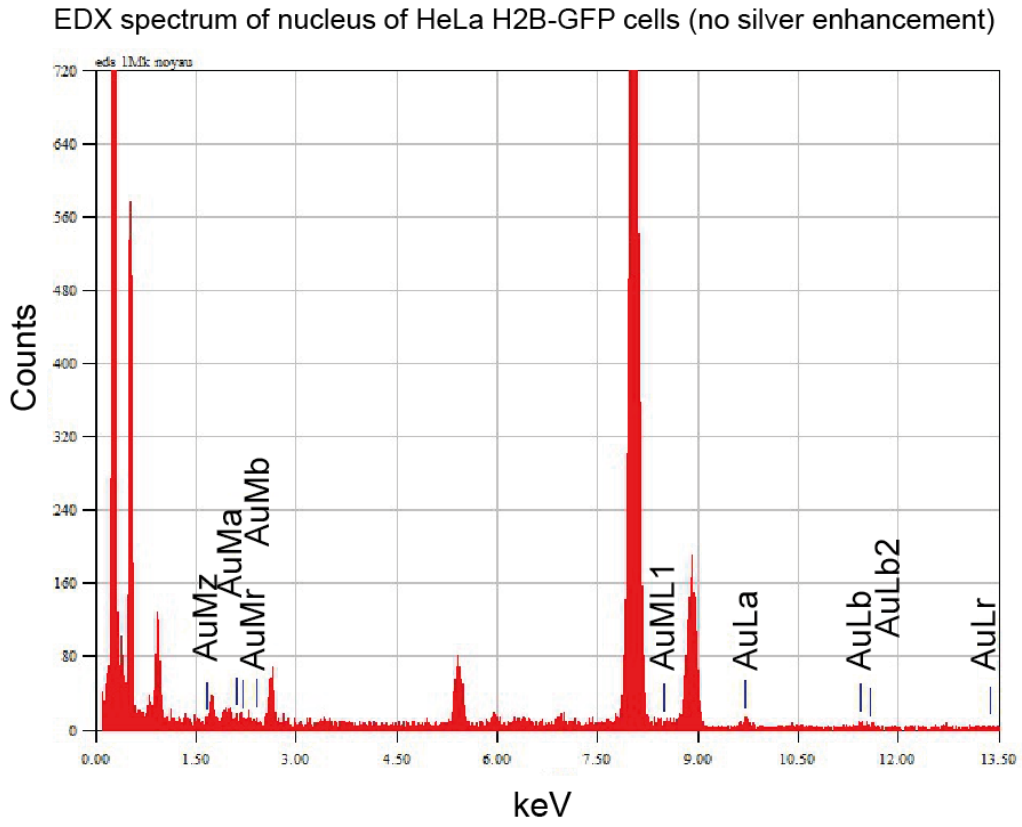

Figure 58. EDX spectrum of nucleus of HeLa H2B-GFP cells not subjected to silver enhancement. The spectrum shows that the imaged region contains gold (respective peaks labeled in the spectrum) The intense peak at 0.277 keV is attributed to carbon and the intense peaks at 0.93 keV, 8.04 keV and 8.9 keV are attributed to copper, both resulting from the EM grids. EDX spectrum recorded by Dr. Dris Ihiawakrim (IPCMS- Plateforme Microscopie électronique)

3.3 AuP-*bind*-nabo for antigen labeling in living cells

3.3.1 Labeling of extracellular targets

Before addressing the cellular delivery of the non-covalent conjugate in order to permit the labeling of intracellular proteins in their native conditions, we wished to examine whether the probe is capable of binding to extracellular receptors specifically, or whether the conjugate associates to the surface of living cells and gets internalized in an non-specific manner. We therefore conjugated a nanobody targeting the HER2/neu (human epidermal growth factor receptor 2) to the 2.4 nm AuNP with the help of *bi*/*nd* tags and tested the binding ability of the conjugate (named HER-AuP-*bind*-nabo) to HER2 overexpressing breast cancer cells

(HCC1954 cell line). The triple-negative breast cancer cell line MDA-MB-231 was used as control. Briefly, cells adhered to glass coverslips were incubated with the HER2/neu-targeting nanobody (HER-nabo), the HER-AuP-*bind*-nabo conjugate and the GFP-targeting AuP-*bind*-nabo conjugate serving as control (for clarification called GFP-AuP-*bind*-nabo) at a concentration of 200 nM for 30 min at 37°C. Then, the cells were washed with PBS, fixed and permeabilized and the nanobody/conjugates were revealed by gold-induced silver staining, as well as secondary IF (Figure 59).

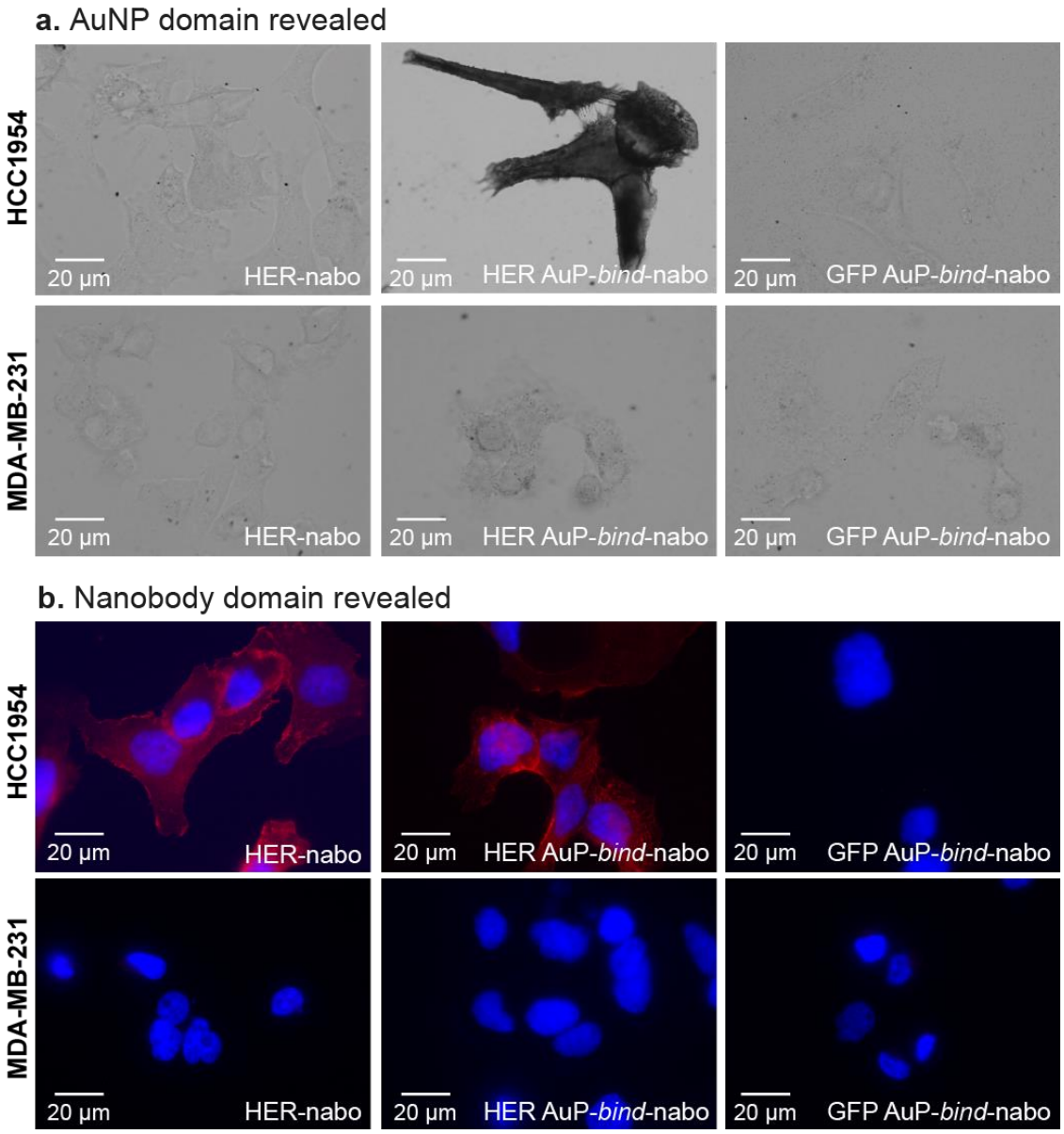

Figure 59. Evaluation of HER2/neu targeting ability of HER-AuP-*bind*-nabo using living HCC1954 cells (overexpressing HER2/neu) and MDA-MB-231 cells (devoid of HER2/neu expression) as control. The unconjugated anti-Her2/neu nanobody (HER-nabo) served as positive control and the GFP-AuP-*bind*-nabo served as negative control. The AuNP and nanobody domains were revealed by silver staining and secondary IF. Scale bar: 20 µm.

The bright-field and fluorescence microscopy observation demonstrated that only HER-nabo and the HER-AuP-*bind*-nabo conjugate bind to HER2/neu expressing HCC1954 cells. Neither, the silver stained, nor the IF images showed any labeling of the triple negative MDA-MB-231 cells for the HER2/neu-targeting nanobody or conjugate. Likewise, the GFP-AuP-*bind*-nabo conjugate did not bind to any of the HER2/neu-expressing or non-expressing cells. Interestingly, even the images of the silver stained cells incubated with GFP-AuP-*bind*-nabo do not show any background labeling, while during the EGFR binding study (Au-Cmab characterization, Chapter 2, Figure 37), the control conjugate Au-Bmab always produced some minor background staining. Since Au-Bmab was passivated with peptide Cap and the two AuP-*bind*-nabo conjugates were coated with PEG, it can be presumed that the hydrophilic polymer was again responsible for avoiding any non-specific interactions.

Taken together, the data revealed that the two AuP-*bind*-nabo conjugates targeting HER2/neu and GFP do not unspecifically bind to the surface of living cells and the HER-AuP-*bind*-nabo probe proved to selectively target living, HER2/neu overexpressing breast cancer cells.

3.3.2 Labeling of intracellular targets

Next, the *in cellulo* probing ability of the anti-GFP AuP-*bind*-nabo conjugate was studied for intracellular targets. As a model, we used the stable HeLa cell line expressing the histone H2B fused to GFP, thus requiring the conjugate to diffuse or to be transported by a piggyback mechanism into the nucleus for allowing the selective labeling of the target. According to the previous experiments, wild type HeLa cells were used as control. For the cellular delivery we employed the same electroporation protocol that permitted the transduction of the passivated AuNPs and AuNP-antibody conjugates into HeLa cells. Prior to transducing the conjugates, we verified that the anti-GFP *nd*-nabo can be electroporated into HeLa H2B-GFP cells, as well as wild type HeLa cells and analyzed the localization of the GFP-nabo 15 h after electroporation by IF (Figure 70, Supporting Information). When transduced into HeLa H2B-GFP cells the *nd*-nabo was detected inside the nucleus and the IF pattern perfectly matched with the GFP expression, demonstrating that the nanobody bound to GFP-tagged H2B. In the control cells (wild type HeLa), the GFP-targeting *nd*-nabo was detected inside the entire cellular volume, showing that the nanobody diffuses into the nucleus, but does not unspecifically interact with any cellular compartments. After completion of this initial test, we addressed the cellular delivery of GFP-AuP-*bind*-nabo. In short, GFP-AuP-*bind*-nabo and AuP-*bi* (serving as a control) were electroporated into the cells at a concentration of 6 µM and after 15 h of

incubation at 37°C, the cells were processed for gold-induced silver staining and imaging by bright-field optical microscopy. The reason for analyzing the cells 15 h after the transduction was that we assessed that the unconjugated nanobody freely diffuses into the nucleus and we wanted to know whether this applies for the conjugate as well. The microscopy observation of the electroporated cells (Figure 60) revealed that the AuP-*bind*-nabo conjugate, as well as the *bi*-tagged AuNP (AuP-*bi*) were successfully delivered into HeLa H2B-GFP and HeLa wild type cells, but that neither AuP-*bind*-nabo, nor AuP-*bi* can enter into the nucleus by diffusion. This observation was surprising and the fact that even the *bi*-functionalized, PEGylated AuNP was excluded from the nucleus was particularly puzzling, since the PEGylated 2.4 nm AuNP was able to diffuse into the nucleus of HeLa cells after transduction (as demonstrated in Chapter 1, Figure 27). However, it was already assessed during the pre-embedding immunolabeling that the AuP-*bind*-nabo probe does not display the beneficial diffusion properties that were expected for the small-sized conjugate.

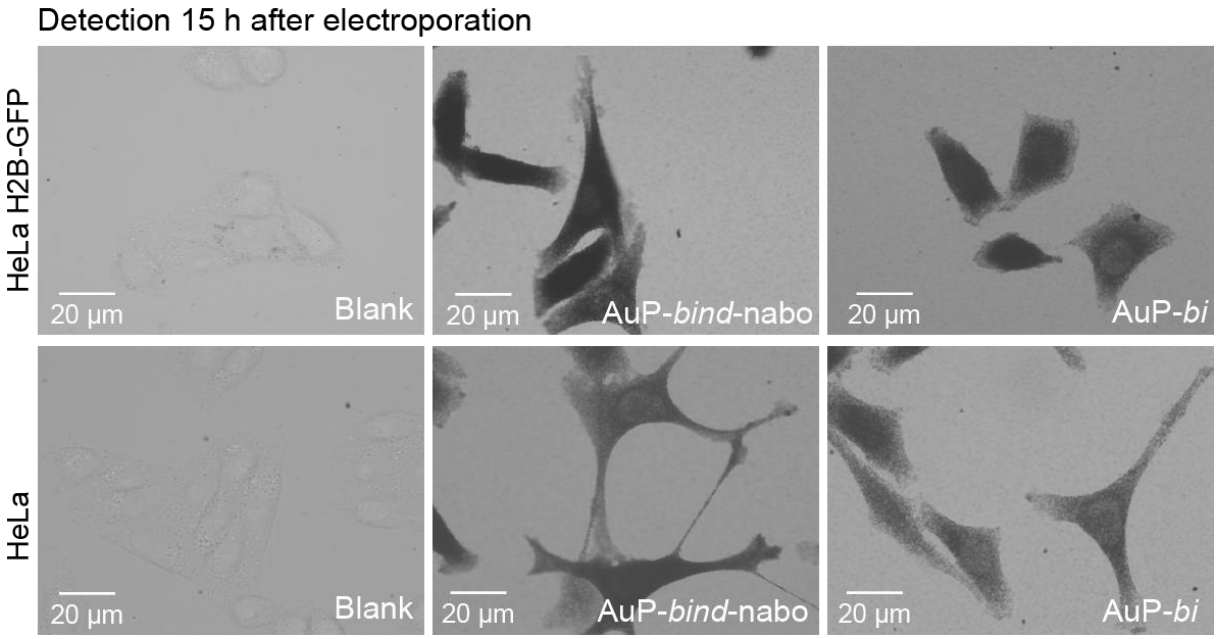

Figure 60. Cellular delivery of AuP-*bind*-nabo for labeling the histone protein H2B fused to GFP. The AuP-*bind*-nabo probe and AuP-*bi* (control) were electroporated into HeLa H2B-GFP cells and HeLa cells, which were further cultivated for 15 h and then fixed and silver stained for bright-field light microscopy observation. Blank represents cells that were not electroporated. Scale bar: 20 µm.

We next investigated whether cell division impacts the distribution (nuclear accumulation) of electroporated AuP-*bind*-nabo. Since HeLa cells divide approximately every 18 h, a cultivation of the electroporated cells for more than 18 h before analysis implies that every cell underwent division at least once. Therefore, we repeated the electroporation of the AuP-*bind*-nabo conjugate and the AuP-*bi* particle and incubated the cells for 24 h at 37°C before processing

them for silver enhancement and observation by optical microscopy (Figure 61). The recorded images showed that the prolonged cultivation time-period resulted in a readily apparent accumulation of AuP-*bind*-nabo in the nucleus of Hela H2B-GFP cells, but also in a nuclear accumulation of the conjugate in few HeLa wild type cells, which was unexpected. Even more surprisingly, AuP-*bi* was found exclusively inside the nucleus of HeLa He2B-GFP cells as well, whereas the distribution in HeLa cells was relatively homogenous for the *bi*-tagged particle.

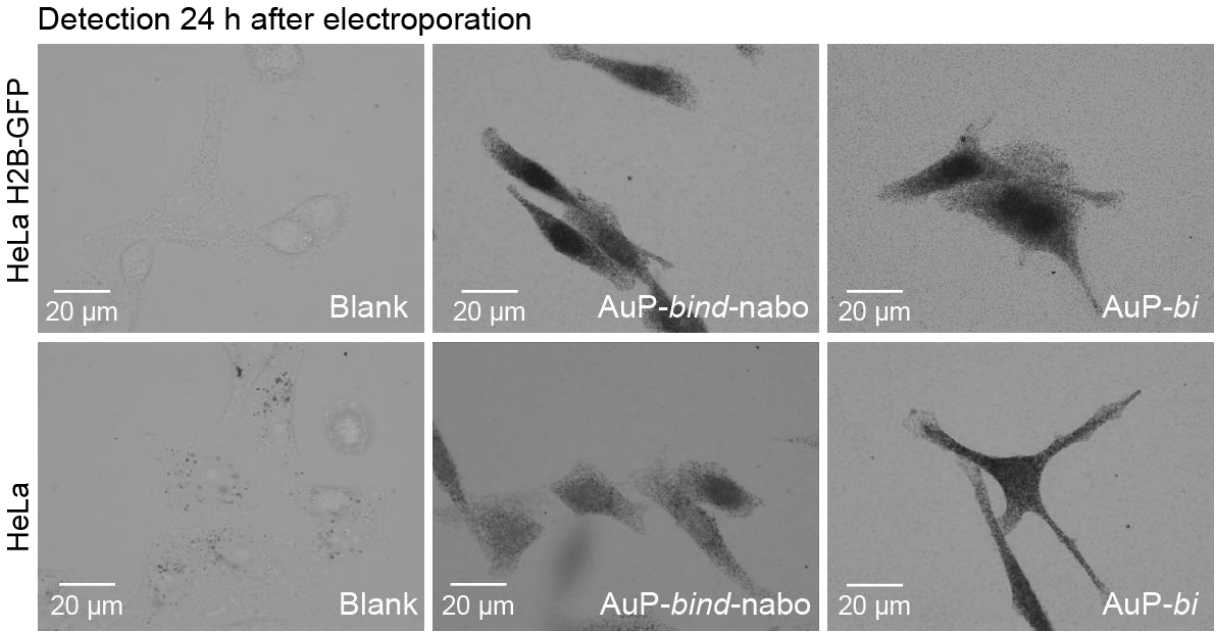

Figure 61. Electroporation of AuP-*bind*-nabo AuP-*bi* (control) into HeLa H2B-GFP and HeLa cells to assess the impact of cultivating the cells for 24h after transduction on the distribution of the GFP-targeting probe within live cells. After electroporation HeLa cells were incubated for 24 h at 37°C, before fixation and silver staining for bright-field light microscopy observation. Blank represents cells that were not electroporated. Scale bar: 20 µm.

Hence, the obtained data revealed that Hela H2B-GFP cells tend to accumulate electroporated AuNPs into their nuclei, if the cells are cultivating for 24 h after the transduction, independent of the presence of a targeting domain on the AuNP surface. Interestingly, the described fate of AuP-*bind*-nabo and AuP-*bi* was not observed in wild type HeLa cells, suggesting that there are differences in certain cellular processes between the two cell lines, likely including a shorter cell cycle for HeLa H2B-GFP cells. Based on these results it was difficult to draw a conclusion on the ability of the AuP-*bind*-nabo conjugate to target GFP-fused proteins inside living cells.

In order to shed more light on the diffusion and trafficking abilities of the probe, especially through the nuclear pores, we synthesized the GFP-targeting AuP-*bind*-nabo conjugate using the 1.4 nm AuNP AuZ, instead of the 2.4 nm AuG. The generation of the AuP-*bind*-nabo conjugate using AuZ, hereafter referred to as AuZ-*bind*-nabo, was performed analogous to the conjugation using AuG with the only alteration that a (bi_2)/AuZ ratio of 2 was used (already

this ratio, yielding a mixture of 2 Au-*bi* species, led no unreacted AuZ particles). The characterization of the AuZ-*bind*-nabo conjugate formation by SDS-PAGE and native PAGE can be found in Figure 71, Supporting Information, which demonstrates that the synthesis proceeded smoothly. Besides the GFP-targeting AuZ-*bind*-nabo, we synthesized the HER2/neu-targeting AuZ-*bind*-nabo (as a control conjugate) and the *bi*-tagged and PEGylated AuZ (AuZ-P-*bi*). Both conjugates (for clarification hereafter referred to as GFP-AuZ-*bind*-nabo and HER-AuZ-*bind*-nabo), as well as AuZ-P-*bi* were transduced into HeLa H2B-GFP cells by electroporation. After 15 h, the cells were fixed and the gold particles were revealed as described in the former experiments. The light microscopy observation of the electroporated cells (Figure 62) showed that all particles localize at least to some extent in the nucleus, indicating that the AuZ-conjugates, as well as AuZ-P-*bi* passively diffuse through the nuclear pores. For GFP-AuZ-*bind*-nabo a clear nuclear accumulation was observed, whereas AuZ-P-*bi* and the control conjugate HER-AuZ-*bind*-nabo were distributed throughout the entire cellular volume.

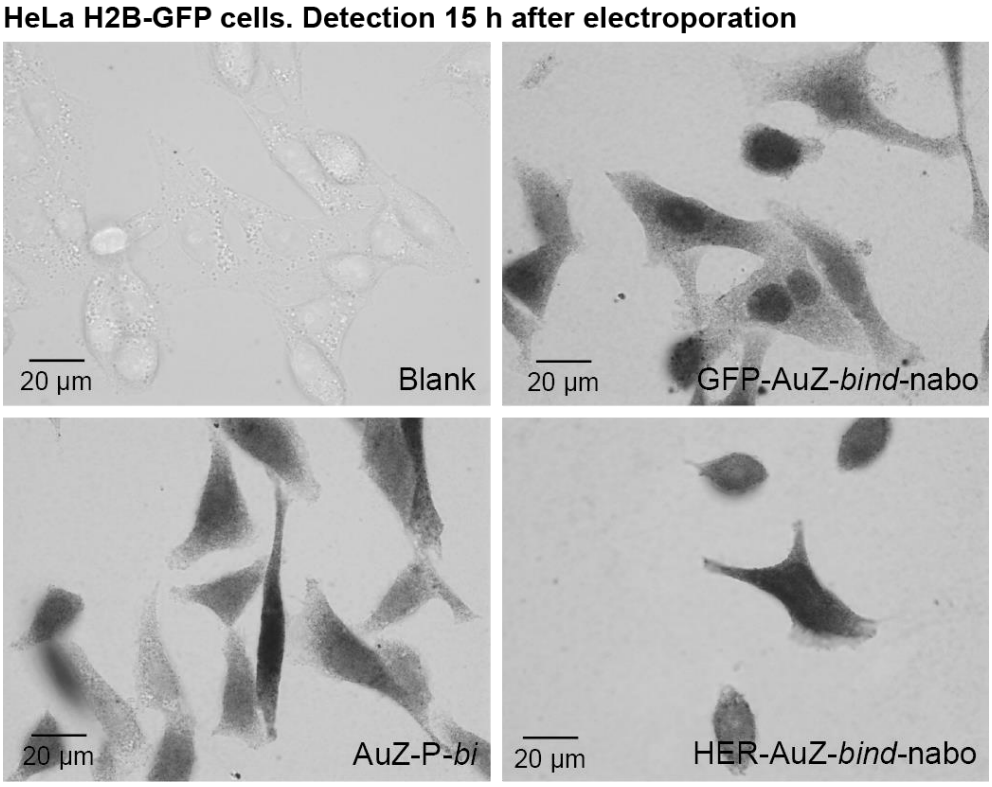

Figure 62. Transduction of GFP-AuZ-*bind*-nabo, HER-AuZ-*bind*-nabo and AuZ-P-*bi* (synthesized from 1.4 nm AuNP AuZ) into HeLa H2B-GFP cells. The transduced cells were cultivated for 15 h and then processed for silver staining and light microscopy observation. Blank represents cells that were not electroporated. Scale bar: 20 µm.

It needs to be noted that the transduction of HER-AuZ-*bind*-nabo caused a diminished cell survival in comparison to the transduction of the GFP-targeting conjugate and the *bi*-tagged

AuZ particles (approximately 50% cell survival for HER-AuZ-*bind*-nabo relative to approximately 90% cell survival for GFP-AuZ-*bind*-nabo and AuZ-P-*bi*). Yet, despite the observed difference in cell survival, the results clearly indicated that H2B-GFP can be probed with GFP-AuZ-*bind*-nabo inside living cells.

For undermining the conclusion that the small sized GFP-AuZ-*bind*-nabo conjugate is capable of labeling the GFP-tagged histone H2B inside the crowded environment of living cells, we again electroporated GFP-AuZ-*bind*-nabo and HER-AuZ-*bind*-nabo into HeLa H2B-GFP cells and detected the conjugates by gold induced silver staining and secondary IF in parallel. Importantly, we performed only one electroporation for each of the two conjugates and subsequently split the transduced cells for enabling the revelation by silver staining and secondary IF in parallel (bright-field and fluorescence microscopy images depicted in Figure 63).

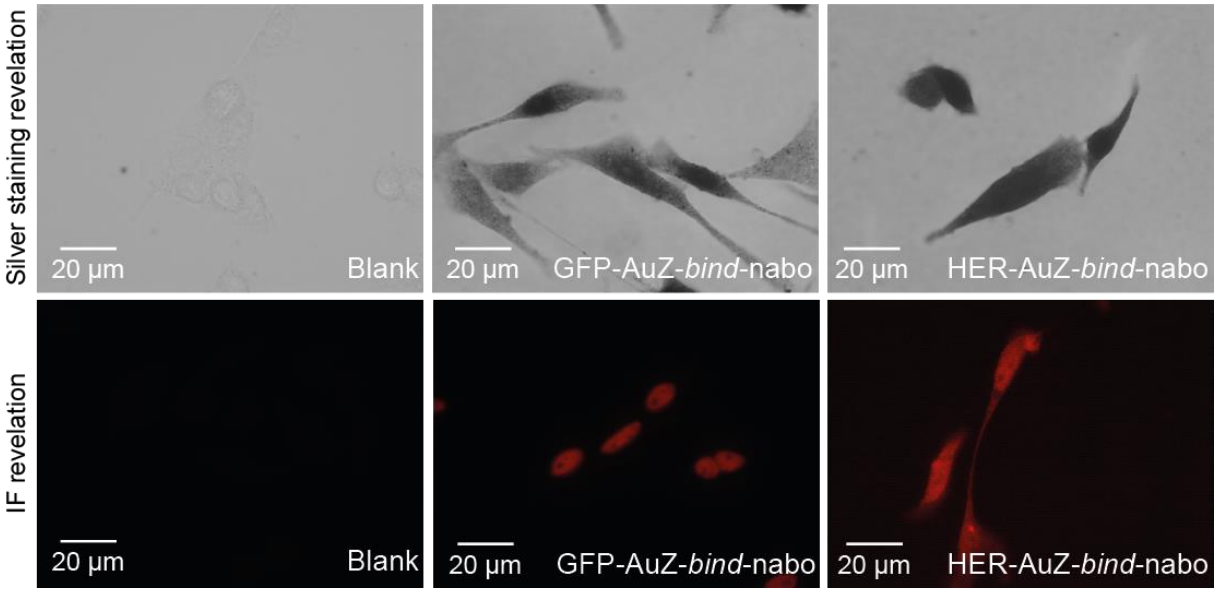

Figure 63. Electroporation of GFP-AuZ-*bind*-nabo and HER-AuZ-*bind*-nabo into HeLa H2B-GFP cells followed by revelation of the conjugates by silver staining and IF in parallel. After the electroporation, the cells were cultivated for 15 h before being analyzed. Blank represents cells that were not electroporated. Scale bar: 20 µm.

Overall, the silver staining and the fluorescence pattern of the cells electroporated with GFP-AuZ-*bind*-nabo and HER-AuZ-*bind*-nabo matched with each other (i.e. nuclear stain for GFP-AuZ-*bind*-nabo and homogenous stain of the entire cell for HER-AuZ-*bind*-nabo), which underlines the above-made conclusion that GFP-AuZ-*bind*-nabo successfully labels GFP-tagged H2B inside living cells.

In summary, we have developed two conjugation strategies for linking the GFP-nabo to the 2.4 nm TNB-/ TAB-protected AuNP AuG. The first approach was based on a direct linkage between the GFP-nabo and AuG mediated by thiolate-for-thiolate exchanges between the AuNP's thiolate ligands and a surface exposed cysteine that was introduced into the sequence of the GFP-nabo by genetic engineering (direct Au-S covalent conjugation approach). The second strategy was to equip the AuNP and the GFP-nabo with complementary associating peptides bi and nd, permitting a non-covalent selective association between the two building blocks (non-covalent approach). The conjugates from both conjugation approaches (Au-C7nabo and Au-bind-nabo) were prepared with a PEG- and a Cap-surface coating, but first experiments showed that the passivation with PEG is indispensable for preventing nanoparticle aggregation and unspecific interactions with cellular components. We compared the binding ability of the two PEGylated conjugates AuP-C7nabo and AuP-bind-nabo for their ability to target GFP by ELISA and immunocytochemistry experiments and it became apparent that only AuP-bind-nabo is able to specifically bind to GFP with an affinity comparable to the unconjugated GFP-nabo. After verifying by optical microscopy that AuP-bind-nabo binds to a multitude of GFP-tagged proteins in vitro using fixed and permeabilized cells that were transfected with GFP-fusion constructs, we evaluated the usefulness of AuP-bind-nabo as probe for immuno-EM in a pre-embedding setting. As model the stable HeLa cell line expressing the histone protein H2B fused to GFP was selected. At an initial stage, the cell sections were silver stained for imaging using a standard transmission electron microscope. The results showed, in agreement with the former binding test, that AuP-bind-nabo selectively labels nuclear H2B-GFP and that the conjugate is hence applicable for classical pre-embedding immuno-EM. Of note, the use of the AuP-bind-nabo probe provides the advantage that only one labeling step is necessary throughout the entire procedure, as opposed to classical immunogold labeling that includes several time-consuming antibody and antibody-AuNP conjugate incubations. Yet, there were indications that the conjugate has issues regarding diffusion. Next, we observed the immunolabeled cell sections that were not silver enhanced by HAADF-STEM to assess whether the 2.4 nm AuNPs can be directly visualized without silver enhancement. At the present stage, we were not able to see individual AuNPs, but only aggregates of AuNPs. However, it needs to be stated that the electron beam of HAADF-STEM apparatuses is very strong and easily destroys the organic specimens, which does not permit going to maximum magnification. Finally, we tested the applicability of AuP-bind-nabo for probing GFP-tagged proteins inside living cells. As a proof of principle, we first tested the binding ability of this type of conjugate to extracellular receptors of living cells. Therefore, we

conjugated the HER2/neu-targeting nanobody to the 2.4 nm AuG via non-covalent association of bi- and nd-tags and tested its specificity for Her2/neu using breast cancer cells. After having assessed that the conjugate does not unspecifically interact with the living breast cancer cells, but only binds to its target, we addressed the cellular delivery of the GFP-targeting AuP-bind-nabo conjugate into HeLa H2B-GFP cells using electroporation. We observed that the anti-GFP AuP-bind-nabo does not passively diffuse into the cellular nucleus, suggesting that the size of AuP-bind-nabo might not be as small as expected, or that the particles are interconnected. The rupture of the nuclear envelop during cell division after the transduction (obtained by incubating HeLa cells for >24h) led to un-conclusive results, indicating the conjugate was unfortunately not useful for in cellulo labeling of nuclear H2B-GFP. We therefore synthesized the AuP-bind-nabo conjugate using the 1.4 nm AuNP AuZ (yielding AuZ-bind-nabo). This small-sized conjugate proved to passively diffuse into the nucleus of H2B-GFP expressing HeLa cells and to selectively bind to the GFP-tagged histone protein.

Altogether, the gathered results clearly demonstrate that the AuNP-nanobody conjugates generated via non-covalent bi:nd association can be used for probing various GFP-tagged proteins and the 1.4 nm AuNP-nanobody conjugate even allows the labeling of nuclear targets in living cells, thanks to its ability to passively diffuse through the nuclear pores after transduction. For the moment we could not prove the direct detectability of the 2.4 nm AuNP moiety of AuP-bind-nabo embedded in cell sections by HAADF-STEM – an issue that needs to be solved in future studies. Moreover, the fate of the 1.4 nm AuZ-bind-nabo inside living cells should be investigated in more details, as the transduction of the probes into live cells opens novel ways of approaching the cellular physiology and dynamics and therefore the equilibrium (distinction) between bound and unbound probes needs to be considered.

4 Discussion

4.1 Different bioconjugation strategies for generating AuNP-nanobody probes

Since their discovery in 1993,[250] nanobodies have been employed for numerous biological applications, as their properties and recombinant nature offer multiple advantages over conventional antibodies.[254,257,283,284] For EM probes and the labeling of selected cellular proteins for high-resolution EM imaging, nanobodies provide several benefits. Firstly, the minimal size of nanobodies improves the diffusion ability of the probe and the targeting of hidden epitopes is in principle easier than with larger antibodies and antibody fragments. Secondly, the distance between the targeted structure and the contrast agent should be smaller, thanks again to the small size of nanobodies. Thirdly, nanobodies are recombinant proteins, which allows genetic engineering, as well as their preparation in large scale. This point is furthermore important regarding reliability. In order to generate a potentially optimal EM probe, fulfilling the outlined characteristics, we set up two conjugation strategies for a site-selective linkage of the well-characterized GFP-nabo[271] to the TNB-/ TAB-protected AuNPs. In the first strategy, the GFP-nabo was conjugated to the 2.4 nm AuG *via* a direct thiolate-for-thiolate exchange between the TNB-/ TAB-ligands of AuG and a surface exposed cysteine that was introduced into the amino acid sequence of the GFP-nabo by genetic engineering. The second non-covalent approach was based on the use of complementarily associating peptide dimers (*bi* and *nd*) that were linked/fused to the AuNP and nanobody domain, respectively. Our data indicate that both direct and indirect (non-covalent) conjugations were successful and that products could be purified and conveniently monitored by SDS-PAGE. However, the direct conjugation promoted somehow structural modifications of the GFP-nabo, leading to a severe diminished binding affinity to GFP. In contrast, the indirect (non-covalent) conjugation using *bi* and *nd* dimers did not compromise the apparent binding affinity of the nanobody.

Leduc *et al.* reported the conjugation of the GFP-nabo to a 5 nm AuNP functionalized with mercaptoundecanoic acid by employing carbodiimide-coupling chemistry for photothermal imaging.[285] In comparison to this study our conjugation approaches provide the advantage that the reaction/association products can be accurately characterized by SDS-PAGE allowing to differentiate the conjugates from unreacted species and in case of the covalent conjugation, it even enabled counting the number of nanobody molecules per AuNP. Leduc and colleagues claimed to have generated a monovalent AuNP-nanobody conjugate, but the authors did not

provide any data to prove that the produced conjugates consist of one nanobody per particle and only referred to the use of excess AuNPs.[285] Moreover, the SDS-PAGE analyses described in this thesis enabled assessing the reproducibility of the conjugation reactions and to assess batch-to-batch variations, as it was already described for the AuNP-antibody conjugation products in Chapter 2.

For the covalent conjugation strategy, the SDS gels revealed that the direct thiolate-for-thiolate exchange yielded a mixture consisting of conjugates with one GFP-nabo per AuNP and conjugates with two GFP-nabos per AuNP. So, although AuG was used in excess, it was not possible to produce a monovalent probe *via* direct Au-S coordination. Yet, when taking into account that the surface coating of AuG consists of approximately 130 ligands, thus offers 130 possible reaction sites for the thiolated GFP-nabo, it is not surprising that a conjugate mixture was obtained and in fact a mixture of only two conjugate species represents a comparatively low polydispersity. Certainly, one possibility to obtain a monovalent probe following this conjugation strategy would be to separate the two conjugate species by purification, but as the size difference of the two species is relatively low, the purification would likely be challenging and accompanied by high product losses. Due to these considerations, as well as the fact that each further step in which the conjugate is kept under non-physiological conditions, increases the risk of impairing the biological function of the nanobody, it was decided to not separate the two conjugate species, but to use the conjugate mixture straight away.

In case of the non-covalent conjugation strategy it was less obvious to determine the number of nanobodies linked to the AuNP. The functionalization of AuG with peptide *bi* clearly yielded three AuNP species (Au-(bi_2), Au-(bi_2)$_2$ and Au-(bi_2)$_3$), which were further PEGylated (yielding AuP-*bi*). Next, the *bi*-tagged particles were titrated with increasing amounts of *nd*-nabo and the assembled products were analyzed by native PAGE. However, as the PEGylation of Au-*bi* almost abolished the electrophoretic mobility of the nanoparticle, the number of *nd*-nabo molecules per AuNP could not be simply counted on the gel, as it was possible for the covalent conjugation. Instead, the association of AuP-*bi* with *nd*-nabo was assessed from the Coomassie blue coloration of proteins, which is absent on unconjugated AuP-*bi*, but appears once the particles assemble with *nd*-nabo. Thus, the number of nanobodies that can be linked to the AuNPs was indirectly determined by steadily increasing the amount of *nd*-nabo added to AuP-*bi* and by determining the *nd*-nabo/AuP-*bi* ratio at which free *nd*-nabo was detectable by PAGE. Surprisingly, the analysis by native PAGE revealed that a *nd*-nabo/AuP-*bi* ratio above 1 resulted in the presence of excess nabo in the reaction mixture, suggesting that on average only one nabo

molecule is linked to the AuNP (AuP-*bind*-(nabo)$_1$). This finding was puzzling, as *nd*-nabo is known to self-assemble into a homodimer (*nd*-nabo$_2$), which upon addition to *bi* dimer forms a heterotetramer (*bi*$_2$)(*nd*-nabo$_2$) and consequently, AuP-*bi* (consisting of Au-(*bi*$_2$), Au-(*bi*$_2$)$_2$ and Au-(*bi*$_2$)$_3$) should be able to capture more *nd*-nabo molecules, than what was observed. Yet, it needs to be noted that the non-covalent *bi*:*nd* association was not studied on the surface of AuNPs before and it in unknown whether the PEGylation limits the accessibility on the AuNP surface, or even shields the *bi* peptide from *nd*-nabo. Another possibility might be that crosslinks between the nanoparticles (mediated by the dimerization of peptide *bi* present on different AuNPs) are responsible for the limited accessibility on the AuNP surface. Hence, the indirect determination of the stoichiometric composition of Au-*bind*-nabo entails uncertainties.

The passivation of Au-*bi* with the peptide Cap would have probably enabled counting the number of associated *nd*-nabo molecules using SDS-PAGE analysis. Unluckily, the addition of Cap caused an irreversible aggregation of the nanoparticles and it was not possible to proceed with the conjugation. The passivation with PEG did not produce aggregation, very likely due to steric repulsions between the polymer chains. The fact that the passivation of Au-C7nabo using peptide Cap did not lead to an irreversible aggregation of the particles as it was observed for Au-*bi*, supports the hypothesis that the *bi* dimer somehow causes interparticle interactions, most likely *via bi* homodimerization, which eventually also influences the assembly with *nd*-nabo.

4.2 Impact of conjugation approach on GFP-targeting ability

The binding to GFP was only tested for the non-aggregated conjugates Cap-coated AuC-C7nabo, PEGylated AuP-C7nabo (direct linkage) and the PEGylated AuP-*bind*-nabo (indirect non-covalent linkage). An initial immunocytochemistry experiment demonstrated that AuC-C7nabo strongly bound to fixed and permeabilized cells in an unspecific manner, independent of GFP expression, confirming that peptide Cap does not provide enough stealth properties to the 2.4 nm AuNP and that the nanoparticle requires the passivation with PEG 2000 Da. While this initial binding test already indicated that the covalent AuP-C7nabo has specificity issues as well, the subsequently performed ELISA clearly demonstrated that solely the non-covalent conjugate AuP-*bind*-nabo binds to GFP with an affinity comparable to the one of the unconjugated GFP-nabo. These data, revealing that only the non-covalent conjugate is functional, consequently raised the question which parameters of the two conjugation strategies were responsible for perturbing and maintaining the nanobody's antigen binding ability. On the

one hand, it can be presumed that the direct thiolate-for-thiolate exchange and the resulting close proximity between the bulky AuNP and the GFP-nabo impacted the structure of the binder and thus caused a loss in its antigen binding ability. On the other hand, it can be assumed that defined orientation of the GFP-nabo in AuP-*bind*-nabo mediated by the *bi:nd* assembly, which is not given in AuP-C7nabo, was responsible for maintaining the nanobody's functionality.

The direct conjugation of AuG to antibodies *via* Au-S coordination described in the previous Chapter 2 did not cause a destruction of the antigen binding ability. However, antibodies have a MW that is 10 times higher than the one of nanobodies and the Fab located between the antibody's paratope and the hinge thiols (to which the AuNP was conjugated) was presumably of enough bulkiness to cope with the structural alterations induced by the AuNP. In contrast, in case of C7nabo the coordination to the AuNP was probably too deleterious, since the nanobody does not provide sufficient bulkiness (spacing) between the site of attachment and the antigen binding site. In fact, there are several reports in the literature describing that the functionalization of nanobodies by random labeling of lysine residues with fluorophores containing a N-hydroxysuccinimide (NHS) group can drastically reduce the nanobody's binding ability,[283] supporting the above-made presumption. Yet, the direct conjugation of C7nabo to AuG described in the present chapter was not performed *via* lysine residues, but *via* a genetically engineered cysteine at position 7, which has been successfully labeled with fluorophores in a nanobody targeting the nuclear pore complex, as described by Pleiner *et al*.[254] Nonetheless, it needs to be kept in mind that AuG is sterically demanding and therefore more prone to inducing structural alteration in biomolecules upon conjugation, than organic fluorophores. Besides, it should be taken into consideration that the GFP-nabo contains two additional native cysteines, which form an intramolecular disulfide bond. Since the GFP-nabo was reduced with low concentrations of TCEP prior to the conjugation to AuG to ensure that the cysteines at position 7 do not form intermolecular disulfides, it cannot be precluded that the native cysteines coordinated to the AuNP surface. However, it is in principle very unlikely that the native cysteines were involved in the conjugation, since it is known from the crystal structure of the GFP-nabo that the nanobody retains its structure even if the intramolecular disulfides are reduced and that the native cysteine residues thus remain unexposed to solvents.[271]

Levi-Kalisman *et al.* reported the conjugation of a 1.3 nm thiolate-protected AuNP to an scFv targeting RNAP II *via* direct-thiolate-for-thiolate exchange.[147] As the size of scFvs (ca. 25 kDa) is almost in the same order as the size of nanobodies, the bioconjugation described by Levi-

Kalisman is more relevant to the nanobody conjugation presented in this thesis, than the conjugation of AuNPs to antibodies, or the functionalization of nanobodies with fluorophores. The AuNP-scFv conjugate was seen to bind to RNAP II in solution by TEM observation, but the authors did not compare the apparent binding affinity of the AuNP-scFv to the unmodified scFv. It is therefore unknown whether the direct linkage of the 1.3 nm AuNP resulted in structural changes of the scFv to the same extent, as the direct conjugation of the 2.4 nm AuG to C7nabo described in this thesis. In general, it can be stated that the conjugation of small-sized biomolecules to AuNPs *via* thiolate-for-thiolate exchange and the impact on the structure and function of the small biomolecules has not been widely studied and is thus far poorly understood, which raises the need for more systematic studies. One obvious follow-up experiment to the study described in this chapter would be to solve the issue of proteolytic cleavage of CtCnabo (GFP-nabo containing an additional cysteine at the C-terminus) and to test whether the Au-S coordination to AuG produces better outcomes, which would appear logical, as the C-terminal cysteine is farther away from the nanobody's paratope, than the cysteine at position 7.

With regards to the orientation of the nanobody on the AuNP surface, a study from van der Heide supports the assumption that the GFP binding ability of AuP-*bind*-nabo was maintained (in part) due to a specific orientation of the nanobody on the AuNP surface.[286] Van der Heide and colleagues compared different strategies for functionalizing 16 nm AuNPs with anti-cocaine antibodies. The first approach involved carbodiimide chemistry, which resulted in random orientation of the attached antibodies and impaired binding affinity. In the second approach the chimeric protein A/G fusion protein was used as the intermediate between the AuNP and the antibody and it was demonstrated that this conjugate had the highest binding affinity, because it favors proper orientation of the attached antibodies.[286] Hence, the investigation points out that a controlled and favorable orientation of the targeting moiety is crucial for antigen-binding, suggesting that the defined orientation of the nanobody domain in AuP-*bind*-nabo most likely positively contributed to maintaining the high affinity and specificity for GFP.

4.3 Suitability as probe for pre-embedding immuno-EM

The applicability of AuP-*bind*-nabo as EM probe was evaluated in a pre-embedding approach using HeLa H2B-GFP cells. In agreement with the data from the optical microscopy observation, only H2B-GFP expressing cells were labeled and no biding to HeLa cells was

observed. The fact that the AuNP labeling was denser at the nuclear periphery compared to the center of the nucleus was puzzling, as this pattern did neither correspond to the observed H2B-GFP fluorescence, nor to the silver staining pattern of the immunolabeled cells imaged by optical microscopy. Due to the fact that entire cells were imaged during the optical microscopy studies and cells section during the EM experiment, we first hypothesized that the higher density of H2B-GFP at the nuclear periphery might indeed be the case and only be noticeable when cell sections are analyzed. However, various reports from the literature providing confocal microscopy images of H2B demonstrate that this histone protein (with or without GFP fusion) is enriched at the nuclear periphery, but also in the nucleolar periphery.[287–289] Hence, it can be concluded that the dense labeling of AuP-*bind*-nabo at the nuclear periphery corresponds in part to the actual protein distribution, but the lack of staining at the nucleolar periphery is an open question and may result from a hampered diffusion ability of the conjugate. The inconsistency between the EM and optical microscopy images of the H2B-GFP-expressing cells that were immunolabeled with AuP-*bind*-nabo was thus attributed to the high sensitivity of the silver developer permitting the visualization of the AuNPs by optical microscopy, which likely produced a strong stain at the center of the nucleus caused by only a few particles present in this region. Overall, the results clearly demonstrated that AuP-*bind*-nabo can be applied for immuno-EM using a pre-embedding approach, during which the procedure can be reduced to a single labeling step, providing an advantage over conventional immunogold labeling, but that the conjugate has issues regarding penetration and diffusion.

The discussed limitations of AuP-*bind*-nabo with regards to penetration throughout the meshwork of fixed cells was furthermore noted, when it was assessed that cell permeabilization using Triton X-100 is required for allowing the probe to reach the cellular nucleus. Unfortunately, permeabilization with Triton X-100 drastically compromises the cellular ultrastructure and the requirement for such harsh conditions will likely prevent the AuP-*bind*-nabo probe from being routinely used for the labeling of intracellular proteins. While conventional immunolabeling agents consisting of 5 – 15 nm AuNPs coupled to antibodies cannot diffuse through cellular membranes after mild permeabilization neither (i.e. low concentrations of saponin),[92] Fab fragments of IgG conjugated to 1.4 nm AuNPs, first described by Hainfeld and Furuya,[105] are able to penetrate through the cellular membrane after mild permeabilization. Hence, with regards to the existing Fab-conjugates, the AuP-*bind*-nabo probe described in here does not provide a progress in terms of image quality. Based on the fact that nanobodies have a MW corresponding to one third of the one of Fab fragments and that the 2.4 nm particle AuG was shown to passively diffuse into the nucleus of living cells, it appears

surprising that the penetration through the cell membrane of fixed cells permeabilized with saponin is impossible for AuP-*bind*-nabo and raises questions about the stoichiometric composition of the conjugate. As discussed earlier, the titration experiments revealed that on average one GFP-nabo molecule was linked to the *bi*-tagged and PEGylated AuNPs, but based on the assessed diffusion issues, the assumption regarding the composition of AuP-*bind*-nabo should be regarded critically. Besides, it should be necessarily clarified in future experiments, whether the *bi*-tagged AuNPs are crosslinked by homodimerization between *bi* tags present on different AuNPs, since this could be a reason explaining the observed diffusion problems.

One possibility to preclude concerns regarding multimerization of the developed nanobody-targeting system would be to exchange the *bi* and *nd* tag with other tags, such as the recently described versatile interacting peptides (VIP).[290] VIPs are ca. 5 kDa peptides forming alpha-helices (CoilE and CoilR) which together form an alpha-helical coiled coil, without involving homo- or tetramerization. As neither CoilE, nor CoilR contain cysteines, one peptide could be fused to the nanobody domain and the other one could be generated by solid phase peptide synthesis with an additional N-, or C-terminal cysteine permitting the Au-S coordination to the AuNP.

4.4 Direct visualization of Au-*bind*-nabo in the cellular nucleus

Based on the studies conducted in the laboratory of Leapman *et al.*, who reported the direct visualization of intracellular AuNPs of ca. 2 nm coated with glutathione and the cell penetrating peptide TAT,[108] we attempted to find out whether the 2.4 nm AuNP of the AuP-*bind*-nabo probe can be directly visualized inside the nucleus of cells as well. Therefore, the immunolabeled HeLa H2B-GFP cells were not silver enhanced and after resin embedment and sectioning directly imaged by HAADF-STEM. Unfortunately, at the current stage it was not possible to detect individual particles, or small aggregates of few (<10) AuNPs. Instead, we observed large aggregates having diameters of 50 – 100 nm, but as these aggregates were partly seen in the cytoplasm, they likely represent labeling artefacts. When it was attempted to go to higher magnification in order to zoom into these aggregates of particles, the AuNPs were suddenly not visible as distinct nanostructures anymore but looked very diffuse (no crystal planes of the AuNPs detectable), making it hard to imagine that the imaged structures are electron dense AuNPs. Yet, EDX spectra of the imaged regions confirmed that the investigated areas contain gold. At present, it is difficult to conclude, whether the 2.4 nm AuNPs of AuP-*bind*-nabo do not provide enough electron contrast to be directly visualized as isolated particles or small

aggregates inside the dense cellular nucleus, which would contradict the report from Leapman,[108] or whether the nature of the analysis was responsible for the ambiguous results. In fact, during previous experiments we observed that when a certain region of a sample is exposed to the strong electron beam of the HAADF-STEM apparatus for several seconds – minutes, the electron beam is able to liberate atoms of the imaged gold nanoparticles, as well as to merge particles. Due to this knowledge, as well as the frequent occurrence of contamination during the STEM observation, we believe that the high electron doses might have been responsible for the fact that we did not observe individual AuNPs or small aggregates. It would hence certainly be worth investing more time to acquire EM data and to get access to more recent EM apparatuses that are operating at lower electron dosages.

4.5 AuP-*bind*-nabo for in cellulo labeling

To finally investigate whether AuP-*bind*-nabo can be employed as probe for the labeling in live cells, as it was demonstrated for Au-7G5-PEG targeting the nuclear enzyme RNAP II, we delivered the nanobody probe into living cells by electroporation. As a model system, we used again the HeLa cell line stably expressing the histone H2B fused to GFP and HeLa cells devoid of GFP expression as control. For testing whether AuP-*bind*-nabo, as well as the *bi*-tagged particles AuP-*bi* can passively diffuse into the nucleus of cells, as it was confirmed for the unconjugated GFP-nabo, HeLa H2B-GFP and HeLa control cells were fixed, silver stained and analyzed by optical microscopy 15 h after the electroporation (instead of 24 h after the transduction, as performed for the AuNP-antibody conjugates). The microscopy observation showed that AuP-*bind*-nabo, as well as the *bi*-tagged particles (AuP-*bi*) were localized exclusively inside the cytoplasm in both cell lines, indicating (i) that AuP-*bind*-nabo and AuP-*bi* do not diffuse into the nucleus through the nuclear envelop and (ii) that AuP-*bind*-nabo does not get piggybacked into the nucleus by binding to de novo synthesized H2B-GFP. Next, we tested whether a prolonged cultivation of the electroporated cells (24 h prior to fixation), permitting each cell to go through cell division, influences the subcellular distribution of the electroporated AuNP-conjugates and AuNPs. Unfortunately, it turned out that under these conditions Hela H2B-GFP cells accumulate AuP-*bind*-nabo, as well as AuP-*bi* into their nuclei. We hypothesized that this nuclear accumulation was due to interactions between the AuNPs and certain nuclear components getting accessible to the nanoparticles during mitosis, which makes it challenging to draw any conclusions on the GFP-targeting ability of AuP-*bind*-nabo. Interestingly, the nuclear accumulation of AuP-*bind*-nabo and AuP-*bi* was observed to a

completely different extent in HeLa wild type cells (i.e. only few cells showed nuclear staining). Based on these results being difficult to interpret, we generated two new nanobody conjugates using the 1.4 nm AuNP AuZ – one targeting GFP, the other one targeting HER2/neu – and electroporated the small-sized probes into the HeLa H2B-GFP cell line to test whether the reduced size of the conjugate permits diffusion into the nucleus. The obtained data convincingly demonstrated that both conjugates passively diffuse into the nucleus and that the GFP-targeting AuZ-*bind*-nabo specifically binds to H2B-GFP. These observation first of all confirmed that the non-covalent *bi*:*nd* link, attached to the nanoparticle's surface *via* Au-S coordination, is stable inside living cells and furthermore that this type of conjugate is applicable for the *in cellulo* labeling of nuclear proteins. With regards to EM, it needs to be considered that the 2.4 nm AuG was not yet discernable from cellular constituents without silver enhancement and consequently, the 1.4 nm AuZ will be even more difficult to detect. So at the current stage, the *in cellulo* immunolabeling of H2B-GFP is possible using the AuZ-*bind*-nabo probe but it would need silver enhancement for EM observation.

Concerning the results from the pre-embedding immuno-EM study, the finding that AuP-*bind*-nabo (2.4 nm AuNP) does not passively diffuse into the nucleus was not surprising, because there were already evidences suggesting that AuP-*bind*-nabo does not display the advantageous diffusion properties that were expected for the nanobody probe. Yet, it was astonishing that the conjugate was not transported into the nucleus by binding to H2B-GFP using a piggyback mechanism, as we already demonstrated that the RNAP II-targeting conjugate consisting of a full-size IgG antibody and the 2.4 nm AuG can be efficiently transduced into living cells, where it is subsequently piggybacked into the nucleus through binding to newly translated RNAP II. Recent results from our laboratory showed that the transduction of an anti-GFP antibody (unconjugated) into Hela H2B-GFP cells does not lead to the labeling of nuclear H2B-GFP neither, which led us to the presumption that the binding to de novo synthesized H2B-GFP might be hindered for some reason and that the piggybacking of the antibody/AuP-*bind*-nabo probe can therefore not occcur. Despite the small size of the histone core proteins (H2A, H2B, H3, H4), histones do not passively diffuse into the nucleus, but are transported by importins, which is likely due to the strongly regulated nucleosome assembly and histone exchange.[291] In 2019, Padavannil resolved the crystal structure of the nuclear import receptor Importin-9 wrapped around its cargo, the H2A-H2B dimer.[292] It was demonstrated that the superhelical Importin-9 does not primarily interact with the disordered N-terminal tails of H2A and H2B, containing many basic amino acids, somewhat resembling classical NLS motifs, but buries a large surface of the H2A-H2B complex (1352 A^2 corresponding to 26% of the H2A-H2B

surface, being much higher than the surface coverage of other well-characterized H2A-H2B chaperons, such as Nap1 and Swr1).[292] Based on this finding, we suggest that the binding of AuP-*bind*-nabo to H2B-GFP might be blocked by the association of the H2A-H2B complex with Importin-9. Moreover, we hypothesize that the small-sized AuZ-*bind*-nabo capable of diffusing into the nucleus is able to specifically bind to H2B-GFP, precisely because Importin-9 is not bound to the H2A-H2B complex anymore once the dimer is assembled into a nucleosome.

While there are various publications available on the folding and nuclear import of the histone protein H2B,[291,293,294] there is only one article published by Ariotti *et al.*, reporting the piggybacking of a probe bound to mcherry fused to H2B, which is in disagreement with our above-described hypothesis.[265] In 2018, Ariotti and colleagues reported the immunolabeling of the fusion protein H2B-mcherry by co-expressing H2B-mcherry with an anti-mcherry-nanobody-APEX construct, followed by DAB oxidation and OsO_4 treatment. Although previously described that the expressed nanobody-APEX fusion protein (ca. 45 kDa) is homogeneously distributed throughout the cytoplasm and does not diffuse into the nucleus in the absence of any antigen, the authors observed a dense labeling of H2B-mcherry using the nanobody-APEX, suggesting that the in situ generated probe was piggybacked into the nucleus. These results certainly contradict our hypothesis, but it needs to be considered that the authors did not specify the mode of binding and it might be possible that the entry of the nanobody-APEX fusion protein into the nucleus was facilitated by cell division. Furthermore, it is unknown whether the fusion of mcherry to H2B from the study of Ariotti *et al.* and the fusion of GFP to H2B described in this thesis were performed in the same manner, or whether there are differences in position (N-terminal vs. C-terminal), or length of spacer between the protein of interest and the fluorescent proteins, which could explain the observed differences.

5 Conclusion

In conclusion, we developed two types of conjugates consisting of the well-characterized GFP-nabo and the 2.4 nm TNB-/ TAB-protected AuG and evaluated their potential as EM probes. The first conjugation approach was based on the direct Au-S coordination of a genetically engineered cysteine present at position 7 of the nanobody's sequence to the AuNP surface. The aim of this strategy was to produce a conjugate in which the electron contrasting AuNP is as close as possible to the GFP-nabo's paratope to maximally improve the linkage error. The second conjugation approach was to equip the AuNP and nanobody domain with complementarily associating *bi* and *nd* peptide tags, which form a strong and selective non-covalent bond. The generated conjugates could be characterized by SDS-PAGE, from which it was assessed that the conjugation reactions/associations are reproducible. While there were uncertainties about the stoichiometric composition of the non-covalent conjugate, AuP-*bind*-nabo, the SDS-PAGE analysis of the conjugate produced by direct Au-S conjugation, Au-C7nabo, revealed that the product consists of a mixture of conjugates containing one and two nanobodies per AuNP, which represents a rather homogeneous population when considering that AuG bears approximately 130 exchangeable TNB-/ TAB ligands. As evidenced by different *in vitro* binding studies, only the non-covalent AuP-*bind*-nabo conjugate proved to specifically bind to GFP with an affinity comparable to the unconjugated GFP-nabo. The fact that no specific binding to GFP was observed for AuP-C7nabo was unfortunate and we attributed the loss of function to changes in the nanobody's 3D structure that probably occurred during the direct Au-S conjugation to the AuNP, since bulky AuNPs certainly have different steric effects than small organic fluorescent molecules. Moreover, we presumed that the defined orientation of the nanobody domain in AuP-*bind*-nabo positively contributed to the conjugate's binding ability to GFP. Next, it was demonstrated that AuP-*bind*-nabo can be used as EM probe for pre-embedding immunolabeling of the histone protein H2B fused to GFP. Although we did not observe any background labeling, it turned out that AuP-*bind*-nabo is still improvable. First, the conjugate required harsh cell membrane permeabilization using Triton X-100 to get into the nuclei. Second, the conjugate primarily stained H2B-GFP present at the nuclear periphery, but almost no H2B-GFP present at the nucleolar periphery, located more towards the center of the nucleus. At the present stage, we were unable to directly detect the 2.4 nm AuNPs inside the immunolabeled cells by HAADF-STEM as individual particles or small aggregates. However, as the electron beam of the STEM apparatus constantly caused contamination and we have previously observed that the beam is capable of liberating gold atoms of AuNPs, as well as to

merge particles, we are optimistic that the direct visualization of the 2.4 nm AuNPs inside cell sections will be possible by improving the careful experimentation and balance between the strong electron beam and the delicate biological specimen. Finally, the suitability of the 2.4 nm AuP-*bind*-nabo probe to label proteins inside living cells was evaluated by electroporating the conjugate into H2B-GFP-expressing HeLa cells. Initial experiments demonstrated that the probe does not passively diffuse into the nucleus, which underlines the previous observation that AuP-*bind*-nabo does not display the advantageous diffusion properties that were expected for the nanobody conjugate. Moreover, it was assessed that the conjugate is not delivered into the nucleus by a piggyback mechanism. Regarding the diffusion of the AuP-*bind*-nabo probe, we need to consider that multimerization (in particular interparticle crosslinks) might play a role and that peptide tags forming a heterodimer without involving multimerization, such as the recently described VIPs (CoiE and CoilR) may be more suited and should be investigated for this system in future studies. The fact that the AuP-*bind*-nabo probe did not enter into the nucleus by binding to de novo synthesized H2B-GFP was unfortunate and surprising, as nuclear transport mediated by piggybacking was observed for the AuNP-antibody conjugate (Au-7G5-PEG) targeting RNAP II. Yet, we can speculate that Importin-9 (a protein involved in the nuclear import machinery) wraps around the histone heterodimer and may cover a large surface area of the H2A-H2B complex, including the GFP binding site, thereby precluding the binding of the probe. To get more insight into the intracellular trafficking of the nanobody probe, we finally conjugated the 1.4 nm AuNP (AuZ) to the GFP-nabo by employing the non-covalent approach, yielding AuZ-*bind*-nabo, and electroporated the small-sized probe into HeLa H2B-GFP cells. The 1.4 nm AuZ-*bind*-nabo passively diffused into the nucleus and appeared to specifically bind to H2B-GFP. This finding convincingly demonstrated that the non-covalent conjugate is stable and functional inside living cells, which emphasizes the quality of the conjugation approach.

The content of this chapter is currently under assessment for publication in a scientific journal.

General conclusion and perspectives

The aim of this project was to develop innovative probes for EM of cellular specimens to label selected proteins within their native context (living cells) with an increased spatial resolution, compared to classical immunogold labeling agents that appear outdated with regards to the technical advances of electron microscopes and non-denaturing cryo-fixation. To meet this goal, we set up procedures for the chemical synthesis of water soluble and monodispersed thiolate-protected AuNPs, that are (i) large enough to be directly visualized within the cellular ultrastructure by high-resolution EM, and (ii) small enough for allowing diffusion inside the crowded environment of living cells. We succeeded in producing series of AuNPs of different sizes and established that the 2.4 nm AuG was presently the most suitable particle in terms of balance between intracellular trafficking and opacity towards electrons, thus detectability by EM. Importantly, only the coordination of PEG 2000 Da to the AuNP surface enabled a homogeneous distribution of the 2.4 nm AuG inside live cells, confirming that among the tested passivation agents, only PEG 2000 Da effectively protects the gold surface from interacting with cellular components. Then, site-selective conjugation strategies were established in order to link targeting biomolecules, such as antibodies and nanobodies, to the 2.4 nm AuNP in a defined manner.

For site-selectively conjugating AuG to antibodies, we developed a synthetic protocol for linking the AuNP to the hinge area of antibodies, resulting in conjugates with a 1:1 AuNP/antibody stoichiometry as the main product. This conjugation strategy was employed for three different antibodies, suggesting that the approach is generally applicable. The conjugates proved to specifically bind to their antigens, but there were evidences that the site-selective conjugation at hinge area was not completely innocuous. Moreover, we demonstrated that the AuNP-antibody conjugates can be applied for the labeling of proteins in living cells through delivery by electroporation.

The conjugation to nanobodies was intended to further improve the spatial resolution and the diffusion properties of the generated probes. To site-selectively link AuG to nanobodies, two conjugation approaches were pursued. The first approach, aimed at minimizing the linkage error as much as possible, was based on the direct thiolate-for-thiolate exchange between the TNB-/TAB-ligands of AuG and a cysteine that was introduced into the sequence of the nanobody by genetic engineering. In the second strategy, the AuNP and the nanobody were equipped with complementarily associating peptide tags which allow for a selective and non-covalent association of the two building blocks. A detailed characterization of the two types of

conjugates revealed that solely the non-covalent conjugate is functional and at the current stage the *in cellulo* labeling of nuclear proteins was only achieved with the non-covalent nanobody probe prepared from 1.4 AuNPs. Unfortunately, the 2.4 nm analog proved to have issues regarding diffusion and further investigations are needed to optimize the link.

The main objective of this work – the generation of small AuNP-based probes permitting the labeling of selected proteins inside living cells – was achieved and we are now ready to go one step further to test whether the generated probes prove useful for cryo-EM and allow the visualization of single intracellular proteins in close-to-native conditions. It needs to be noted that a thorough characterization of the quality of the EM probes, the possibility to prepare the probes in large scale and securing that the probes "work" in 100% of the cases, which has been carried out during this project, is of uttermost importance before tackling the employment for cryo-EM, since the sample preparations are laborious, require a lot of material (large cell pellets need to be fixed by high pressure freezing) and classical artefacts (water crystallization, wrinkled cells) may complicate the interpretation of the data.

At the current stage the generated antibody conjugates seem more promising for cryo-EM studies, than the nanobody conjugates, since we achieved the labeling of nuclear proteins inside living cells using antibody conjugates comprising the 2.4 nm AuNPs, whereas only the nanobody conjugates made from 1.4 nm AuNPs proved useful for *in cellulo* targeting, and the probability of directly detecting AuNPs within thin cryosections is proportional to the size of the particles. Based on the promising results of the RNAP II-targeting AuNP-antibody conjugate, collaborations with the group of P. Schultz, O. Ersen and S. Ory were established to investigate whether the *in cellulo* labeling of the nuclear enzyme RNAP II with the novel AuNP-antibody probe can be imaged by TEM and then cryo-FIB/TEM.

With regards to today's resolution of electron microscopes adapted for biological specimens, the AuNP-nanobody conjugate synthesized from the 1.4 nm AuNP, which passively diffuses into the nucleus after cellular delivery, does not seem to fulfill the requirements for cryo-EM studies. However, it needs to be stated that we have not yet tried whether the 1.4 nm AuNP can be directly detected in ultrathin cryosections and the steady progress in the development of EM detectors and sample preparation procedures might allow the use of the small-sized nanobody probe in the future. This possibility would be even more advantageous than the above-discussed antibody conjugate, due to the ability of the 1.4 nm AuNP-nanobody probe to diffuse through

the entire cellular volume, as well as the fact that smaller AuNPs expose less surface to biological fluids, which minimizes the risk of unspecific association.

Finally, the defined and small-sized AuNP-bioconjugates described in this thesis might prove useful for other fields than high-resolution EM, such as therapy and diagnostics. Notably, the EGFR-targeting AuNP-antibody conjugate Au-Cmab could be investigated for innovative therapeutic approaches to treat EGFR-overexpressing tumors, such as radiosensitization of cancerous cells, or delivery of radioactive gold isotopes to diseased tissue.

References

(1) Kumari, Y.; Kaur, G.; Kumar, R.; Singh, S. K.; Gulati, M.; Khursheed, R.; Clarisse, A.; Gowthamarajan, K.; Karri, V. V. S. N. R.; Mahalingam, R.; Ghosh, D.; Awasthi, A.; Kumar, R.; Yadav, A. K.; Kapoor, B.; Singh, P. K.; Dua, K.; Porwal, O. Gold Nanoparticles: New Routes across Old Boundaries. *Adv. Colloid Interface Sci.* **2019**, *274*, 102037. https://doi.org/10.1016/j.cis.2019.102037.

(2) Miao, Z.; Gao, Z.; Chen, R.; Yu, X.; Su, Z.; Wei, G. Surface-Bioengineered Gold Nanoparticles for Biomedical Applications. *Curr. Med. Chem.* **2018**, *25* (16), 1920–1944. https://doi.org/10.2174/0929867325666180117111404.

(3) Monopoli, M. P.; Åberg, C.; Salvati, A.; Dawson, K. A. Biomolecular Coronas Provide the Biological Identity of Nanosized Materials. *Nat. Nanotechnol.* **2012**, *7* (12), 779–786. https://doi.org/10.1038/nnano.2012.207.

(4) Ma, Y.; Hong, J.; Ding, Y. Biological Behavior Regulation of Gold Nanoparticles via the Protein Corona. *Adv. Healthc. Mater.* **2020**, *9* (6), 1901448. https://doi.org/10.1002/adhm.201901448.

(5) Saha, K.; Rahimi, M.; Yazdani, M.; Kim, S. T.; Moyano, D. F.; Hou, S.; Das, R.; Mout, R.; Rezaee, F.; Mahmoudi, M.; Rotello, V. M. Regulation of Macrophage Recognition through the Interplay of Nanoparticle Surface Functionality and Protein Corona. *ACS Nano* **2016**, *10* (4), 4421–4430. https://doi.org/10.1021/acsnano.6b00053.

(6) Tsoli, M.; Kuhn, H.; Brandau, H.; Schmid, G. Cellular Uptake and Toxicity of Au55 Clusters. *Small* **2005**, No. 8, 4.

(7) Pan, Y.; Neuss, S.; Leifert, A.; Fischler, M.; Wen, F.; Simon, U.; Schmid, G.; Brandau, W.; Jahnen-Dechent, W. Size-Dependent Cytotoxicity of Gold Nanoparticles. *Small* **2007**, *3* (11), 1941–1949. https://doi.org/10.1002/smll.200700378.

(8) Soenen, S. J.; Manshian, B.; Montenegro, J. M.; Amin, F.; Meermann, B.; Thiron, T.; Cornelissen, M.; Vanhaecke, F.; Doak, S.; Parak, W. J.; De Smedt, S.; Braeckmans, K. Cytotoxic Effects of Gold Nanoparticles: A Multiparametric Study. *ACS Nano* **2012**, *6* (7), 5767–5783. https://doi.org/10.1021/nn301714n.

(9) Nie, S. Probing Single Molecules and Single Nanoparticles by Surface-Enhanced Raman Scattering. *Science* **1997**, *275* (5303), 1102–1106. https://doi.org/10.1126/science.275.5303.1102.

(10) Mie, G. Beiträge zur Optik trüber Medien, speziell kolloidaler Metallösungen. *Ann. Phys.* **1908**, *330* (3), 377–445. https://doi.org/10.1002/andp.19083300302.

(11) Tweney, R. D. Discovering Discovery: How Faraday Found the First Metallic Colloid. *Perspect. Sci.* **2006**, *14* (1), 97–121. https://doi.org/10.1162/posc.2006.14.1.97.

(12) Jain, P. K.; Lee, K. S.; El-Sayed, I. H.; El-Sayed, M. A. Calculated Absorption and Scattering Properties of Gold Nanoparticles of Different Size, Shape, and Composition: Applications in Biological Imaging and Biomedicine. *J. Phys. Chem. B* **2006**, *110* (14), 7238–7248. https://doi.org/10.1021/jp057170o.

(13) Milowska, K. Z.; Stolarczyk, J. K. Role of Ligand–Ligand vs. Core–Core Interactions in Gold Nanoclusters. *Phys. Chem. Chem. Phys.* **2016**, *18* (18), 12716–12724. https://doi.org/10.1039/C5CP06795B.

(14) Zuber, G.; Weiss, E.; Chiper, M. Biocompatible Gold Nanoclusters: Synthetic Strategies and Biomedical Prospects. *Nanotechnology* **2019**, *30* (35), 352001. https://doi.org/10.1088/1361-6528/ab2088.

(15) Dykman, L.; Khlebtsov, N. Gold Nanoparticles in Biomedical Applications: Recent Advances and Perspectives. *Chem Soc Rev* **2012**, *41* (6), 2256–2282. https://doi.org/10.1039/C1CS15166E.

(16) Ajdari, N.; Vyas, C.; Bogan, S. L.; Lwaleed, B. A.; Cousins, B. G. Gold Nanoparticle Interactions in Human Blood: A Model Evaluation. *Nanomedicine Nanotechnol. Biol. Med.* **2017**, *13* (4), 1531–1542. https://doi.org/10.1016/j.nano.2017.01.019.

(17) Jin, R. Atomically Precise Metal Nanoclusters: Stable Sizes and Optical Properties. *Nanoscale* **2015**, *7* (5), 1549–1565. https://doi.org/10.1039/c4nr05794e.
(18) Porret, E.; Le Guével, X.; Coll, J.-L. Gold Nanoclusters for Biomedical Applications: Toward in Vivo Studies. *J. Mater. Chem. B* **2020**, *8* (11), 2216–2232. https://doi.org/10.1039/C9TB02767J.
(19) Hötzer, B.; Medintz, I. L.; Hildebrandt, N. Fluorescence in Nanobiotechnology: Sophisticated Fluorophores for Novel Applications. *Small* **2012**, *8* (15), 2297–2326. https://doi.org/10.1002/smll.201200109.
(20) Wu, Z.; Jin, R. On the Ligand's Role in the Fluorescence of Gold Nanoclusters. *Nano Lett.* **2010**, *10* (7), 2568–2573. https://doi.org/10.1021/nl101225f.
(21) Louis, C.; Pluchery, O. *Gold Nanoparticles for Physics, Chemistry and Biology*; IMPERIAL COLLEGE PRESS, 2011. https://doi.org/10.1142/p815.
(22) Haruta, M.; Kobayashi, T.; Sano, H.; Yamada, N. Novel Gold Catalysts for the Oxidation of Carbon Monoxide at a Temperature Far Below 0°C. *Chem. Lett.* **1987**, *16* (2), 405–408.
(23) Hashmi, A. S. K.; Hutchings, G. J. Gold Catalysis. *Angew. Chem. Int. Ed Engl.* **2006**, *45* (47), 7896–7936. https://doi.org/10.1002/anie.200602454.
(24) Sardar, R.; Funston, A. M.; Mulvaney, P.; Murray, R. W. Gold Nanoparticles: Past, Present, and Future †. *Langmuir* **2009**, *25* (24), 13840–13851. https://doi.org/10.1021/la9019475.
(25) Thomas, K. G.; Kamat, P. V. Chromophore-Functionalized Gold Nanoparticles. *Acc. Chem. Res.* **2003**, *36* (12), 888–898. https://doi.org/10.1021/ar030030h.
(26) Sztandera, K.; Gorzkiewicz, M.; Klajnert-Maculewicz, B. Gold Nanoparticles in Cancer Treatment. *Mol. Pharm.* **2019**, *16* (1), 1–23. https://doi.org/10.1021/acs.molpharmaceut.8b00810.
(27) E. Abraham Peter B. Himmel, G. Management of Rheumatoid Arthritis: Rationale for the Use of Colloidal Metallic Gold. *J. Nutr. Environ. Med.* **1997**, *7* (4), 295–305. https://doi.org/10.1080/13590849762411.
(28) Ghosh, P.; Han, G.; De, M.; Kim, C.; Rotello, V. Gold Nanoparticles in Delivery Applications☆. *Adv. Drug Deliv. Rev.* **2008**, *60* (11), 1307–1315. https://doi.org/10.1016/j.addr.2008.03.016.
(29) Huang, X.; Jain, P. K.; El-Sayed, I. H.; El-Sayed, M. A. Plasmonic Photothermal Therapy (PPTT) Using Gold Nanoparticles. *Lasers Med. Sci.* **2008**, *23* (3), 217–228. https://doi.org/10.1007/s10103-007-0470-x.
(30) Hainfeld, J. F.; Slatkin, D. N.; Smilowitz, H. M. The Use of Gold Nanoparticles to Enhance Radiotherapy in Mice. *Phys. Med. Biol.* **2004**, *49* (18), N309–N315. https://doi.org/10.1088/0031-9155/49/18/N03.
(31) Anselmo, A. C.; Mitragotri, S. Nanoparticles in the Clinic: An Update. *Bioeng. Transl. Med.* **2019**, *4* (3). https://doi.org/10.1002/btm2.10143.
(32) Dreaden, E. C.; Mackey, M. A.; Huang, X.; Kang, B.; El-Sayed, M. A. Beating Cancer in Multiple Ways Using Nanogold. *Chem. Soc. Rev.* **2011**, *40* (7), 3391. https://doi.org/10.1039/c0cs00180e.
(33) Asadishad, B.; Vossoughi, M.; Alemzadeh, I. Folate-Receptor-Targeted Delivery of Doxorubicin Using Polyethylene Glycol-Functionalized Gold Nanoparticles. *Ind. Eng. Chem. Res.* **2010**, *49* (4), 1958–1963. https://doi.org/10.1021/ie9011479.
(34) Chen, Y.-H.; Tsai, C.-Y.; Huang, P.-Y.; Chang, M.-Y.; Cheng, P.-C.; Chou, C.-H.; Chen, D.-H.; Wang, C.-R.; Shiau, A.-L.; Wu, C.-L. Methotrexate Conjugated to Gold Nanoparticles Inhibits Tumor Growth in a Syngeneic Lung Tumor Model. *Mol. Pharm.* **2007**, *4* (5), 713–722. https://doi.org/10.1021/mp060132k.
(35) Agasti, S. S.; Chompoosor, A.; You, C.-C.; Ghosh, P.; Kim, C. K.; Rotello, V. M. Photoregulated Release of Caged Anticancer Drugs from Gold Nanoparticles. *J. Am. Chem. Soc.* **2009**, *131* (16), 5728–5729. https://doi.org/10.1021/ja900591t.
(36) Eghtedari, M.; Liopo, A. V.; Copland, J. A.; Oraevsky, A. A.; Motamedi, M. Engineering of Hetero-Functional Gold Nanorods for the in <i/> Vivo Molecular Targeting of Breast Cancer Cells. *Nano Lett.* **2009**, *9* (1), 287–291. https://doi.org/10.1021/nl802915q.

(37) Paciotti, G. F.; Kingston, D. G. I.; Tamarkin, L. Colloidal Gold Nanoparticles: A Novel Nanoparticle Platform for Developing Multifunctional Tumor-Targeted Drug Delivery Vectors. *Drug Dev. Res.* **2006**, *67* (1), 47–54. https://doi.org/10.1002/ddr.20066.

(38) Truong, N. P.; Whittaker, M. R.; Mak, C. W.; Davis, T. P. The Importance of Nanoparticle Shape in Cancer Drug Delivery. *Expert Opin. Drug Deliv.* **2015**, *12* (1), 129–142. https://doi.org/10.1517/17425247.2014.950564.

(39) Black, K. C. L.; Wang, Y.; Luehmann, H. P.; Cai, X.; Xing, W.; Pang, B.; Zhao, Y.; Cutler, C. S.; Wang, L. V.; Liu, Y.; Xia, Y. Radioactive ^{198}Au-Doped Nanostructures with Different Shapes for *In Vivo* Analyses of Their Biodistribution, Tumor Uptake, and Intratumoral Distribution. *ACS Nano* **2014**, *8* (5), 4385–4394. https://doi.org/10.1021/nn406258m.

(40) Hutter, E.; Boridy, S.; Labrecque, S.; Lalancette-Hébert, M.; Kriz, J.; Winnik, F. M.; Maysinger, D. Microglial Response to Gold Nanoparticles. *ACS Nano* **2010**, *4* (5), 2595–2606. https://doi.org/10.1021/nn901869f.

(41) Gu, H.; Ho, P. L.; Tong, E.; Wang, L.; Xu, B. Presenting Vancomycin on Nanoparticles to Enhance Antimicrobial Activities. *Nano Lett.* **2003**, *3* (9), 1261–1263. https://doi.org/10.1021/nl034396z.

(42) Noh, S. M.; Kim, W.-K.; Kim, S. J.; Kim, J. M.; Baek, K.-H.; Oh, Y.-K. Enhanced Cellular Delivery and Transfection Efficiency of Plasmid DNA Using Positively Charged Biocompatible Colloidal Gold Nanoparticles. *Biochim. Biophys. Acta BBA - Gen. Subj.* **2007**, *1770* (5), 747–752. https://doi.org/10.1016/j.bbagen.2007.01.012.

(43) Lee, J.-S.; Green, J. J.; Love, K. T.; Sunshine, J.; Langer, R.; Anderson, D. G. Gold, Poly(β-Amino Ester) Nanoparticles for Small Interfering RNA Delivery. *Nano Lett.* **2009**, *9* (6), 2402–2406. https://doi.org/10.1021/nl9009793.

(44) Hirsch, L. R.; Stafford, R. J.; Bankson, J. A.; Sershen, S. R.; Rivera, B.; Price, R. E.; Hazle, J. D.; Halas, N. J.; West, J. L. Nanoshell-Mediated near-Infrared Thermal Therapy of Tumors under Magnetic Resonance Guidance. *Proc. Natl. Acad. Sci.* **2003**, *100* (23), 13549–13554. https://doi.org/10.1073/pnas.2232479100.

(45) Zhou, F.; Xing, D.; Ou, Z.; Wu, B.; Resasco, D. E.; Chen, W. R. Cancer Photothermal Therapy in the Near-Infrared Region by Using Single-Walled Carbon Nanotubes. *J. Biomed. Opt.* **2009**, *14* (2), 021009. https://doi.org/10.1117/1.3078803.

(46) Pitsillides, C. M.; Joe, E. K.; Wei, X.; Anderson, R. R.; Lin, C. P. Selective Cell Targeting with Light-Absorbing Microparticles and Nanoparticles. *Biophys. J.* **2003**, *84* (6), 4023–4032. https://doi.org/10.1016/S0006-3495(03)75128-5.

(47) Riley, R. S.; Day, E. S. Gold Nanoparticle-Mediated Photothermal Therapy: Applications and Opportunities for Multimodal Cancer Treatment: Gold Nanoparticle-Mediated Photothermal Therapy. *Wiley Interdiscip. Rev. Nanomed. Nanobiotechnol.* **2017**, *9* (4), e1449. https://doi.org/10.1002/wnan.1449.

(48) Maeda, H. The Enhanced Permeability and Retention (EPR) Effect in Tumor Vasculature: The Key Role of Tumor-Selective Macromolecular Drug Targeting. *Adv. Enzyme Regul.* **2001**, *41* (1), 189–207. https://doi.org/10.1016/S0065-2571(00)00013-3.

(49) Larson, T. A.; Joshi, P. P.; Sokolov, K. Preventing Protein Adsorption and Macrophage Uptake of Gold Nanoparticles *via* a Hydrophobic Shield. *ACS Nano* **2012**, *6* (10), 9182–9190. https://doi.org/10.1021/nn3035155.

(50) Phillips, M. A.; Gran, M. L.; Peppas, N. A. Targeted Nanodelivery of Drugs and Diagnostics. *Nano Today* **2010**, *5* (2), 143–159. https://doi.org/10.1016/j.nantod.2010.03.003.

(51) Loo, C.; Lowery, A.; Halas, N.; West, J.; Drezek, R. Immunotargeted Nanoshells for Integrated Cancer Imaging and Therapy. *Nano Lett.* **2005**, *5* (4), 709–711. https://doi.org/10.1021/nl050127s.

(52) Sauvage, F.; Fraire, J. C.; Remaut, K.; Sebag, J.; Peynshaert, K.; Harrington, M.; Van de Velde, F. J.; Xiong, R.; Tassignon, M.-J.; Brans, T.; Braeckmans, K.; De Smedt, S. C. Photoablation of Human Vitreous Opacities by Light-Induced Vapor Nanobubbles. *ACS Nano* **2019**, *13* (7), 8401–8416. https://doi.org/10.1021/acsnano.9b04050.

(53) Her, S.; Jaffray, D. A.; Allen, C. Gold Nanoparticles for Applications in Cancer Radiotherapy: Mechanisms and Recent Advancements. *Adv. Drug Deliv. Rev.* **2017**, *109*, 84–101. https://doi.org/10.1016/j.addr.2015.12.012.

(54) Berrezoug, A.; A Dib, A. S.; Belbachir, A. H. Enhanced X-Ray Absorption by Using Gold Nanoparticles in a Biological Tissue. *Radioprotection* **2015**, *50* (4), 281–285. https://doi.org/10.1051/radiopro/2015019.

(55) McMahon, S. J.; Hyland, W. B.; Muir, M. F.; Coulter, J. A.; Jain, S.; Butterworth, K. T.; Schettino, G.; Dickson, G. R.; Hounsell, A. R.; O'Sullivan, J. M.; Prise, K. M.; Hirst, D. G.; Currell, F. J. Nanodosimetric Effects of Gold Nanoparticles in Megavoltage Radiation Therapy. *Radiother. Oncol.* **2011**, *100* (3), 412–416. https://doi.org/10.1016/j.radonc.2011.08.026.

(56) Shrestha, S.; Cooper, L. N.; Andreev, O. A.; Reshetnyak, Y. K.; Antosh, M. P. Gold Nanoparticles for Radiation Enhancement in Vivo. 15.

(57) Chang, M.-Y.; Shiau, A.-L.; Chen, Y.-H.; Chang, C.-J.; Chen, H. H.-W.; Wu, C.-L. Increased Apoptotic Potential and Dose-Enhancing Effect of Gold Nanoparticles in Combination with Single-Dose Clinical Electron Beams on Tumor-Bearing Mice. *Cancer Sci.* **2008**, *99* (7), 1479–1484. https://doi.org/10.1111/j.1349-7006.2008.00827.x.

(58) Chattopadhyay, N.; Cai, Z.; Kwon, Y. L.; Lechtman, E.; Pignol, J.-P.; Reilly, R. M. Molecularly Targeted Gold Nanoparticles Enhance the Radiation Response of Breast Cancer Cells and Tumor Xenografts to X-Radiation. *Breast Cancer Res. Treat.* **2013**, *137* (1), 81–91. https://doi.org/10.1007/s10549-012-2338-4.

(59) Jain, S.; Coulter, J. A.; Butterworth, K. T.; Hounsell, A. R.; McMahon, S. J.; Hyland, W. B.; Muir, M. F.; Dickson, G. R.; Prise, K. M.; Currell, F. J.; Hirst, D. G.; O'Sullivan, J. M. Gold Nanoparticle Cellular Uptake, Toxicity and Radiosensitisation in Hypoxic Conditions. *Radiother. Oncol.* **2014**, *110* (2), 342–347. https://doi.org/10.1016/j.radonc.2013.12.013.

(60) Joh, D. Y.; Sun, L.; Stangl, M.; Al Zaki, A.; Murty, S.; Santoiemma, P. P.; Davis, J. J.; Baumann, B. C.; Alonso-Basanta, M.; Bhang, D.; Kao, G. D.; Tsourkas, A.; Dorsey, J. F. Selective Targeting of Brain Tumors with Gold Nanoparticle-Induced Radiosensitization. *PLoS ONE* **2013**, *8* (4), e62425. https://doi.org/10.1371/journal.pone.0062425.

(61) Hainfeld, J. F.; Lin, L.; Slatkin, D. N.; Avraham Dilmanian, F.; Vadas, T. M.; Smilowitz, H. M. Gold Nanoparticle Hyperthermia Reduces Radiotherapy Dose. *Nanomedicine Nanotechnol. Biol. Med.* **2014**, *10* (8), 1609–1617. https://doi.org/10.1016/j.nano.2014.05.006.

(62) Chanda, N.; Kan, P.; Watkinson, L. D.; Shukla, R.; Zambre, A.; Carmack, T. L.; Engelbrecht, H.; Lever, J. R.; Katti, K.; Fent, G. M.; Casteel, S. W.; Smith, C. J.; Miller, W. H.; Jurisson, S.; Boote, E.; Robertson, J. D.; Cutler, C.; Dobrovolskaia, M.; Kannan, R.; Katti, K. V. Radioactive Gold Nanoparticles in Cancer Therapy: Therapeutic Efficacy Studies of GA-198AuNP Nanoconstruct in Prostate Tumor–Bearing Mice. *Nanomedicine Nanotechnol. Biol. Med.* **2010**, *6* (2), 201–209. https://doi.org/10.1016/j.nano.2009.11.001.

(63) Khan, M. K.; Minc, L. D.; Nigavekar, S. S.; Kariapper, M. S. T.; Nair, B. M.; Schipper, M.; Cook, A. C.; Lesniak, W. G.; Balogh, L. P. Fabrication of {198Au0} Radioactive Composite Nanodevices and Their Use for Nanobrachytherapy. *Nanomedicine Nanotechnol. Biol. Med.* **2008**, *4* (1), 57–69. https://doi.org/10.1016/j.nano.2007.11.005.

(64) Leuvering, J. H.; Thal, P. J.; van der Waart, M.; Schuurs, A. H. Sol Particle Immunoassay (SPIA). *J. Immunoassay* **1980**, *1* (1), 77–91. https://doi.org/10.1080/01971528008055777.

(65) Medley, C. D.; Smith, J. E.; Tang, Z.; Wu, Y.; Bamrungsap, S.; Tan, W. Gold Nanoparticle-Based Colorimetric Assay for the Direct Detection of Cancerous Cells. *Anal. Chem.* **2008**, *80* (4), 1067–1072. https://doi.org/10.1021/ac702037y.

(66) Wang, X.; Li, Y.; Wang, H.; Fu, Q.; Peng, J.; Wang, Y.; Du, J.; Zhou, Y.; Zhan, L. Gold Nanorod-Based Localized Surface Plasmon Resonance Biosensor for Sensitive Detection of Hepatitis B Virus in Buffer, Blood Serum and Plasma. *Biosens. Bioelectron.* **2010**, *26* (2), 404–410. https://doi.org/10.1016/j.bios.2010.07.121.

(67) Li, H.; Rothberg, L. J. DNA Sequence Detection Using Selective Fluorescence Quenching of Tagged Oligonucleotide Probes by Gold Nanoparticles. *Anal. Chem.* **2004**, *76* (18), 5414–5417. https://doi.org/10.1021/ac049173n.
(68) Shawky, S. M.; Bald, D.; Azzazy, H. M. E. Direct Detection of Unamplified Hepatitis C Virus RNA Using Unmodified Gold Nanoparticles. *Clin. Biochem.* **2010**, *43* (13–14), 1163–1168. https://doi.org/10.1016/j.clinbiochem.2010.07.001.
(69) Sato, K.; Hosokawa, K.; Maeda, M. Rapid Aggregation of Gold Nanoparticles Induced by Non-Cross-Linking DNA Hybridization. *J. Am. Chem. Soc.* **2003**, *125* (27), 8102–8103. https://doi.org/10.1021/ja034876s.
(70) Ambrosi, A.; Airò, F.; Merkoçi, A. Enhanced Gold Nanoparticle Based ELISA for a Breast Cancer Biomarker. *Anal. Chem.* **2010**, *82* (3), 1151–1156. https://doi.org/10.1021/ac902492c.
(71) Cho, J.-H.; Paek, S.-H. Semiquantitative, Bar Code Version of Immunochromatographic Assay System for Human Serum Albumin as Model Analyte. *Biotechnol. Bioeng.* **2001**, *75* (6), 725–732. https://doi.org/10.1002/bit.10094.
(72) Peruski, A. H.; Peruski, L. F. Immunological Methods for Detection and Identification of Infectious Disease and Biological Warfare Agents. *Clin. Diagn. Lab. Immunol.* **2003**, *10* (4), 506–513. https://doi.org/10.1128/CDLI.10.4.506-513.2003.
(73) Beck, O.; Kraft, M.; Moeller, M. R.; Smith, B. L.; Schneider, S.; Wennig, R. Frontline ® Immunochromatographic Device for On-Site Urine Testing of Amphetamines: Laboratory Validation Using Authentic Specimens. *Ann Clin Biochem* 6.
(74) Nusz, G. J.; Curry, A. C.; Marinakos, S. M.; Wax, A.; Chilkoti, A. Rational Selection of Gold Nanorod Geometry for Label-Free Plasmonic Biosensors. *ACS Nano* **2009**, *3* (4), 795–806. https://doi.org/10.1021/nn8006465.
(75) Brainina, K.; Kozitsina, A.; Beikin, J. Electrochemical Immunosensor for Forest-Spring Encephalitis Based on Protein A Labeled with Colloidal Gold. *Anal. Bioanal. Chem.* **2003**, *376* (4), 481–485. https://doi.org/10.1007/s00216-003-1912-3.
(76) Haes, A. J.; Chang, L.; Klein, W. L.; Van Duyne, R. P. Detection of a Biomarker for Alzheimer's Disease from Synthetic and Clinical Samples Using a Nanoscale Optical Biosensor. *J. Am. Chem. Soc.* **2005**, *127* (7), 2264–2271. https://doi.org/10.1021/ja044087q.
(77) Sharifi, M.; Attar, F.; Saboury, A. A.; Akhtari, K.; Hooshmand, N.; Hasan, A.; El-Sayed, M. A.; Falahati, M. Plasmonic Gold Nanoparticles: Optical Manipulation, Imaging, Drug Delivery and Therapy. *J. Controlled Release* **2019**, *311–312*, 170–189. https://doi.org/10.1016/j.jconrel.2019.08.032.
(78) Li, W.; Chen, X. Gold Nanoparticles for Photoacoustic Imaging. *Nanomed.* **2015**, *10* (2), 299–320. https://doi.org/10.2217/nnm.14.169.
(79) Wan, X.-Y.; Zheng, L.-L.; Gao, P.-F.; Yang, X.-X.; Li, C.-M.; Li, Y. F.; Huang, C. Z. Real-Time Light Scattering Tracking of Gold Nanoparticles- Bioconjugated Respiratory Syncytial Virus Infecting HEp-2 Cells. *Sci. Rep.* **2015**, *4* (1), 4529. https://doi.org/10.1038/srep04529.
(80) Klein, N. D.; Hurley, K. R.; Feng, Z. V.; Haynes, C. L. Dark Field Transmission Electron Microscopy as a Tool for Identifying Inorganic Nanoparticles in Biological Matrices. *Anal. Chem.* **2015**, *87* (8), 4356–4362. https://doi.org/10.1021/acs.analchem.5b00124.
(81) Boyer, D. Photothermal Imaging of Nanometer-Sized Metal Particles Among Scatterers. *Science* **2002**, *297* (5584), 1160–1163. https://doi.org/10.1126/science.1073765.
(82) Gobin, A. M.; Lee, M. H.; Halas, N. J.; James, W. D.; Drezek, R. A.; West, J. L. Near-Infrared Resonant Nanoshells for Combined Optical Imaging and Photothermal Cancer Therapy. *Nano Lett.* **2007**, *7* (7), 1929–1934. https://doi.org/10.1021/nl070610y.
(83) Kim, D.; Park, S.; Lee, J. H.; Jeong, Y. Y.; Jon, S. Antibiofouling Polymer-Coated Gold Nanoparticles as a Contrast Agent for in Vivo X-Ray Computed Tomography Imaging. *J. Am. Chem. Soc.* **2007**, *129* (24), 7661–7665. https://doi.org/10.1021/ja071471p.
(84) Mallidi, S.; Larson, T.; Aaron, J.; Sokolov, K.; Emelianov, S. Molecular Specific Optoacoustic Imaging with Plasmonic Nanoparticles. *Opt. Express* **2007**, *15* (11), 6583. https://doi.org/10.1364/OE.15.006583.

(85) Li, C.; Wang, L. V. Photoacoustic Tomography and Sensing in Biomedicine. *Phys. Med. Biol.* **2009**, *54* (19), R59-97. https://doi.org/10.1088/0031-9155/54/19/R01.
(86) Chen, J.; Irudayaraj, J. Quantitative Investigation of Compartmentalized Dynamics of ErbB2 Targeting Gold Nanorods in Live Cells by Single Molecule Spectroscopy. *ACS Nano* **2009**, *3* (12), 4071–4079. https://doi.org/10.1021/nn900743v.
(87) Mielańczyk, Ł.; Matysiak, N.; Klymenko, O.; Wojnicz, R. Transmission Electron Microscopy of Biological Samples. In *The Transmission Electron Microscope - Theory and Applications*; Maaz, K., Ed.; InTech, 2015. https://doi.org/10.5772/60680.
(88) Wagner, J.; Schaffer, M.; Fernández-Busnadiego, R. Cryo-Electron Tomography-the Cell Biology That Came in from the Cold. *FEBS Lett.* **2017**, *591* (17), 2520–2533. https://doi.org/10.1002/1873-3468.12757.
(89) Winey, M.; Meehl, J. B.; O'Toole, E. T.; Giddings, T. H. Conventional Transmission Electron Microscopy. *Mol. Biol. Cell* **2014**, *25* (3), 319–323. https://doi.org/10.1091/mbc.e12-12-0863.
(90) Zobel, C. R.; Beer, M. The Use of Heavy Metal Salts as Electron Stains. *Int. Rev. Cytol.* **1965**, *18*, 363–400. https://doi.org/10.1016/s0074-7696(08)60558-6.
(91) Roth, Jürgen. The Silver Anniversary of Gold- 25 Years of the Colloidal Gold Marker System for Immunocytochemistry and Histochemistry. *Histochem. Cell Biol.* **1996**, *106*, 1–8.
(92) Polishchuk, E. V.; Polishchuk, R. S. Pre-Embedding Labeling for Subcellular Detection of Molecules with Electron Microscopy. *Tissue Cell* **2019**, *57*, 103–110. https://doi.org/10.1016/j.tice.2018.11.002.
(93) Jones, J. C. R. Pre- and Post-Embedding Immunogold Labeling of Tissue Sections. In *High-Resolution Imaging of Cellular Proteins*; Schwartzbach, S. D., Skalli, O., Schikorski, T., Eds.; Methods in Molecular Biology; Springer New York: New York, NY, 2016; Vol. 1474, pp 291–307. https://doi.org/10.1007/978-1-4939-6352-2_19.
(94) Bendayan, M. Colloidal Gold Post-Embedding Immunocytochemistry. *Prog. Histochem. Cytochem.* **1995**, *29* (4), 1–159. https://doi.org/10.1016/s0079-6336(11)80027-6.
(95) Painter, R. G.; Tokuyasu, K. T.; Singer, S. J. Immunoferritin Localization of Intracellular Antigens: The Use of Ultracryotomy to Obtain Ultrathin Sections Suitable for Direct Immunoferritin Staining. *Proc. Natl. Acad. Sci.* **1973**, *70* (6), 1649–1653. https://doi.org/10.1073/pnas.70.6.1649.
(96) Möbius, W.; Posthuma, G. Sugar and Ice: Immunoelectron Microscopy Using Cryosections According to the Tokuyasu Method. *Tissue Cell* **2019**, *57*, 90–102. https://doi.org/10.1016/j.tice.2018.08.010.
(97) Faulk, W Page; Taylor, G Malcom. An Immunocolloid Method for the Electron Microscope. *Immunocytochemistry* **1971**, 1081–1083.
(98) Romano, E. L.; Stolinski, C.; Hughes-Jones, C. An Antiglobulin Reagent Laebled with Colloidal Gold for Use in Electron Microscopy. *Immunocytochemistry* **1974**, *11*, 521–522.
(99) Roth, J.; Bendayan, M.; Orci, L. Ultrastructural Localization of Intracellular Antigens by the Use of Protein A-Gold Complex. *J. Histochem. Cytochem.* **1978**, *26* (12), 1074–1081. https://doi.org/10.1177/26.12.366014.
(100) Baschong, W.; Lucocq, J. M.; Roth, J. "Thiocyanate Gold": Small (2–3 Nm) Colloidal Gold for Affinity Cytochemical Labeling in Electron Microscopy. *Histochemistry* **1985**, *83* (5), 409–411. https://doi.org/10.1007/BF00509201.
(101) Robinson, J. M.; Takizawa, T.; Vandre, D. D.; Burry, R. W. Ultrasmall Immunogold Particles: Important Probes for Immunocytochemistry. *Microsc Res Tech.* **1998**, *42* (1), 13–23.
(102) Baschong, W.; Wrigley, N. G. Small Colloidal Gold Conjugated to Fab Fragments or to Immunoglobulin g as High-Resolution Labels for Electron Microscopy: A Technical Overview. *J. Electron Microsc. Tech.* **1990**, *14* (4), 313–323. https://doi.org/10.1002/jemt.1060140405.
(103) De Valck, V.; Renmans, W.; Segers, E.; Leunissen, J.; De Waele, M. Light Microscopical Detection of Leukocyte Cell Surface Antigens with a One-Nanometer Gold Probe. *Histochemistry* **1991**, *95* (5), 483–490. https://doi.org/10.1007/bf00315744.

(104) Horisberger, M. Colloidal Gold and Its Application in Cell Biology. *Int. Rev. Cytol.* **1992**, *136*, 227–287. https://doi.org/10.1016/s0074-7696(08)62054-9.
(105) Hainfeld, J. E.; Furuya, F. R. A 1.4-Nm Gold Cluster Covalently Attached to Antibodies Improves Immunolabeling. *J Histochem Cytochem* **1992**, *40* (2), 177–184.
(106) Hainfeld, J. F. Gold Cluster-Labelled Antibodies. *Nature* **1988**, *333* (6170), 281–282. https://doi.org/10.1038/333281a0.
(107) Danscher, G. Histochemical Demonstration of Heavy Metals. A Revised Version of the Sulphide Silver Method Suitable for Both Light and Electronmicroscopy. *Histochemistry* **1981**, *71* (1), 1—16. https://doi.org/10.1007/bf00592566.
(108) Sousa, A. A.; Morgan, J. T.; Brown, P. H.; Adams, A.; Jayasekara, M. P. S.; Zhang, G.; Ackerson, C. J.; Kruhlak, M. J.; Leapman, R. D. Synthesis, Characterization, and Direct Intracellular Imaging of Ultrasmall and Uniform Glutathione-Coated Gold Nanoparticles. *Small* **2012**, *8* (14), 2277–2286. https://doi.org/10.1002/smll.201200071.
(109) Postupalenko, V.; Desplancq, D.; Orlov, I.; Arntz, Y.; Spehner, D.; Mely, Y.; Klaholz, B. P.; Schultz, P.; Weiss, E.; Zuber, G. Protein Delivery System Containing a Nickel-Immobilized Polymer for Multimerization of Affinity-Purified His-Tagged Proteins Enhances Cytosolic Transfer. *Angew. Chem. Int. Ed.* **2015**, *54* (36), 10583–10586. https://doi.org/10.1002/anie.201505437.
(110) Tao-Cheng, J.-H. Immunogold Labeling of Synaptic Vesicle Proteins in Developing Hippocampal Neurons. *Mol. Brain* **2020**, *13* (1), 9. https://doi.org/10.1186/s13041-020-0549-x.
(111) Steinman, R. M.; Silver, J. M.; Cohn, Z. A. Pinocytosis in Fibroblasts. *J. Cell Biol.* **1974**, *63* (3), 949–969. https://doi.org/10.1083/jcb.63.3.949.
(112) Tawde, S. S.; Sri Ram, J. Conjugation of Antibody to Ferritin by Means of p,P'-Difluoro-m,M'-Dinitrodiphenylsulphone. *Arch. Biochem. Biophys.* **1962**, *97* (2), 429–430. https://doi.org/10.1016/0003-9861(62)90102-9.
(113) Ram, J. S.; Tawde, S. S.; Pierce, B.; Midgley, A. R. PREPARATION OF ANTIBODYWERRITIN CONJUGATES FOR IMMUNO-ELECTRON MICROSCOPY. 3.
(114) Adrian, M.; Dubochet, J.; Lepault, J.; McDowall, A. W. Cryo-Electron Microscopy of Viruses. **1984**, 5.
(115) Dubochet, J.; Adrian, M.; Chang, J.-J.; Homo, J.-C.; Lepault, J.; McDowall, A. W.; Schultz, P. Cryo-Electron Microscopy of Vitrified Specimens. 100.
(116) Parton, R. G. Twenty Years of Traffic: A 2020 Vision of Cellular Electron Microscopy. *Traffic* **2020**, *21* (1), 156–161. https://doi.org/10.1111/tra.12684.
(117) Brüggeller, P.; Mayer, E. Complete Vitrification in Pure Liquid Water and Dilute Aqueous Solutions. *Nature* **1980**, *288* (5791), 569–571. https://doi.org/10.1038/288569a0.
(118) Koning, R. I.; Koster, A. J.; Sharp, T. H. Advances in Cryo-Electron Tomography for Biology and Medicine. *Ann. Anat. - Anat. Anz.* **2018**, *217*, 82–96. https://doi.org/10.1016/j.aanat.2018.02.004.
(119) Moor, H. Chapter 8 Theory and Practice of High Pressure Freezing. 2.
(120) Bonnard, D.; Le Rouzic, E.; Eiler, S.; Amadori, C.; Orlov, I.; Bruneau, J.-M.; Brias, J.; Barbion, J.; Chevreuil, F.; Spehner, D.; Chasset, S.; Ledoussal, B.; Moreau, F.; Saïb, A.; Klaholz, B. P.; Emiliani, S.; Ruff, M.; Zamborlini, A.; Benarous, R. Structure-Function Analyses Unravel Distinct Effects of Allosteric Inhibitors of HIV-1 Integrase on Viral Maturation and Integration. *J. Biol. Chem.* **2018**, *293* (16), 6172–6186. https://doi.org/10.1074/jbc.M117.816793.
(121) Papai, G.; Frechard, A.; Kolesnikova, O.; Crucifix, C.; Schultz, P.; Ben-Shem, A. Structure of SAGA and Mechanism of TBP Deposition on Gene Promoters. *Nature* **2020**, *577* (7792), 711–716. https://doi.org/10.1038/s41586-020-1944-2.
(122) Abdelkareem, M.; Saint-André, C.; Takacs, M.; Papai, G.; Crucifix, C.; Guo, X.; Ortiz, J.; Weixlbaumer, A. Structural Basis of Transcription: RNA Polymerase Backtracking and Its Reactivation. *Mol. Cell* **2019**, *75* (2), 298-309.e4. https://doi.org/10.1016/j.molcel.2019.04.029.

(123) Bykov, Y. S.; Schaffer, M.; Dodonova, S. O.; Albert, S.; Plitzko, J. M.; Baumeister, W.; Engel, B. D.; Briggs, J. A. The Structure of the COPI Coat Determined within the Cell. *eLife* **2017**, *6*, e32493. https://doi.org/10.7554/eLife.32493.

(124) Guo, Q.; Lehmer, C.; Martínez-Sánchez, A.; Rudack, T.; Beck, F.; Hartmann, H.; Pérez-Berlanga, M.; Frottin, F.; Hipp, M. S.; Hartl, F. U.; Edbauer, D.; Baumeister, W.; Fernández-Busnadiego, R. In Situ Structure of Neuronal C9orf72 Poly-GA Aggregates Reveals Proteasome Recruitment. *Cell* **2018**, *172* (4), 696-705.e12. https://doi.org/10.1016/j.cell.2017.12.030.

(125) Mahamid, J.; Pfeffer, S.; Schaffer, M.; Villa, E.; Danev, R.; Kuhn Cuellar, L.; Forster, F.; Hyman, A. A.; Plitzko, J. M.; Baumeister, W. Visualizing the Molecular Sociology at the HeLa Cell Nuclear Periphery. *Science* **2016**, *351* (6276), 969–972. https://doi.org/10.1126/science.aad8857.

(126) Eltsov, M.; Grewe, D.; Lemercier, N.; Frangakis, A.; Livolant, F.; Leforestier, A. Nucleosome Conformational Variability in Solution and in Interphase Nuclei Evidenced by Cryo-Electron Microscopy of Vitreous Sections. *Nucleic Acids Res.* **2018**, *46* (17), 9189–9200. https://doi.org/10.1093/nar/gky670.

(127) Orlov, I.; Schertel, A.; Zuber, G.; Klaholz, B.; Drillien, R.; Weiss, E.; Schultz, P.; Spehner, D. Live Cell Immunogold Labelling of RNA Polymerase II. *Sci. Rep.* **2015**, *5* (1), 8324. https://doi.org/10.1038/srep08324.

(128) Mahato, K.; Nagpal, S.; Shah, M. A.; Srivastava, A.; Maurya, P. K.; Roy, S.; Jaiswal, A.; Singh, R.; Chandra, P. Gold Nanoparticle Surface Engineering Strategies and Their Applications in Biomedicine and Diagnostics. *3 Biotech* **2019**, *9* (2), 57. https://doi.org/10.1007/s13205-019-1577-z.

(129) Zhao, P.; Li, N.; Astruc, D. State of the Art in Gold Nanoparticle Synthesis. *Coord. Chem. Rev.* **2013**, *257* (3–4), 638–665. https://doi.org/10.1016/j.ccr.2012.09.002.

(130) Hühn, J.; Carrillo-Carrion, C.; Soliman, M. G.; Pfeiffer, C.; Valdeperez, D.; Masood, A.; Chakraborty, I.; Zhu, L.; Gallego, M.; Yue, Z.; Carril, M.; Feliu, N.; Escudero, A.; Alkilany, A. M.; Pelaz, B.; del Pino, P.; Parak, W. J. Selected Standard Protocols for the Synthesis, Phase Transfer, and Characterization of Inorganic Colloidal Nanoparticles. *Chem. Mater.* **2017**, *29* (1), 399–461. https://doi.org/10.1021/acs.chemmater.6b04738.

(131) Kumar, S.; Gandhi, K. S.; Kumar, R. Modeling of Formation of Gold Nanoparticles by Citrate Method †. *Ind. Eng. Chem. Res.* **2007**, *46* (10), 3128–3136. https://doi.org/10.1021/ie060672j.

(132) Turkevich, J.; Stevenson, P. C.; Hillier, J. A Study of the Nucleation and Growth Processes in the Synthesis of Colloidal Gold. *Discuss. Faraday Soc.* **1951**, *11*, 55. https://doi.org/10.1039/df9511100055.

(133) Sharma, N.; Bhatt, G.; Kothiyal, P. Gold Nanoparticles Synthesis, Properties, and Forthcoming Applications : A Review. *Indian J. Pharm. Biol. Res.* **2015**, *3* (02). https://doi.org/10.30750/ijpbr.3.2.3.

(134) Frens, G. Controlled Nucleation for the Regulation of the Particle Size in Monodispersed Gold Suspensions. *Nat. Phys. Sci.* **1973**, *241* (20).

(135) Piella, J.; Bastús, N. G.; Puntes, V. Size-Controlled Synthesis of Sub-10-Nanometer Citrate-Stabilized Gold Nanoparticles and Related Optical Properties. *Chem. Mater.* **2016**, *28* (4), 1066–1075. https://doi.org/10.1021/acs.chemmater.5b04406.

(136) Schulz, F.; Homolka, T.; Bastús, N. G.; Puntes, V.; Weller, H.; Vossmeyer, T. Little Adjustments Significantly Improve the Turkevich Synthesis of Gold Nanoparticles. *Langmuir* **2014**, *30* (35), 10779–10784. https://doi.org/10.1021/la503209b.

(137) Bastús, N. G.; Comenge, J.; Puntes, V. Kinetically Controlled Seeded Growth Synthesis of Citrate-Stabilized Gold Nanoparticles of up to 200 Nm: Size Focusing versus Ostwald Ripening. *Langmuir* **2011**, *27* (17), 11098–11105. https://doi.org/10.1021/la201938u.

(138) Ji, X.; Song, X.; Li, J.; Bai, Y.; Yang, W.; Peng, X. Size Control of Gold Nanocrystals in Citrate Reduction: The Third Role of Citrate. *J. Am. Chem. Soc.* **2007**, *129* (45), 13939–13948. https://doi.org/10.1021/ja074447k.

(139) Kimling, J.; Maier, M.; Okenve, B.; Kotaidis, V.; Ballot, H.; Plech, A. Turkevich Method for Gold Nanoparticle Synthesis Revisited. *J. Phys. Chem. B* **2006**, *110* (32), 15700–15707. https://doi.org/10.1021/jp061667w.

(140) Schmid, G.; Pfeil, R.; Boese, R.; Bandermann, F.; Meyer, S.; Calis, Gijs. H. M.; van der Velden, J. W. A. Au55[P(C6H5)3]12Cl6 — Ein Goldcluster Ungewöhnlicher Größe. *Chem. Ber.* **1981**, *114* (11), 3634–3642. https://doi.org/10.1002/cber.19811141116.

(141) Schmid, G.; Klein, N.; Korste, L.; Kreibig, U.; Schönauer, D. Large Transition Metal Clusters—VI. Ligand Exchange Reactions on Au55(PPh3)12Cl6—the Formation of a Water Soluble Au55 Cluster. *Polyhedron* **1988**, *7* (8), 605–608. https://doi.org/10.1016/S0277-5387(00)80366-6.

(142) Weare, W. W.; Reed, S. M.; Warner, M. G.; Hutchison, J. E. Improved Synthesis of Small (DCORE ≈ 1.5 Nm) Phosphine-Stabilized Gold Nanoparticles. *J. Am. Chem. Soc.* **2000**, *122* (51), 12890–12891. https://doi.org/10.1021/ja002673n.

(143) Shem, P. M.; Sardar, R.; Shumaker-Parry, J. S. One-Step Synthesis of Phosphine-Stabilized Gold Nanoparticles Using the Mild Reducing Agent 9-BBN. *Langmuir* **2009**, *25* (23), 13279–13283. https://doi.org/10.1021/la903003n.

(144) Moores, A.; Goettmann, F.; Sanchez, C.; Le Floch, P. Phosphinine Stabilised Gold Nanoparticles; Synthesis and Immobilisation on Mesoporous Materials. *Chem. Commun.* **2004**, No. 24, 2842. https://doi.org/10.1039/b412553c.

(145) Brust, M.; Walker, M.; Bethell, D.; Schiffrin, D. J.; Whyman, R. Synthesis of Thiol-Derivatised Gold Nanoparticles in a Two-Phase Liquid–Liquid System. *J Chem Soc Chem Commun* **1994**, *0* (7), 801–802. https://doi.org/10.1039/C39940000801.

(146) Brust, M.; Fink, J.; Bethell, D.; Schiffrin, D. J.; Kiely, C. Synthesis and Reactions of Functionalised Gold Nanoparticles. *J. Chem. Soc. Chem. Commun.* **1995**, No. 16, 1655. https://doi.org/10.1039/c39950001655.

(147) Levi-Kalisman, Y.; Jadzinsky, P. D.; Kalisman, N.; Tsunoyama, H.; Tsukuda, T.; Bushnell, D. A.; Kornberg, R. D. Synthesis and Characterization of Au $_{102}$ (*p* -MBA) $_{44}$ Nanoparticles. *J. Am. Chem. Soc.* **2011**, *133* (9), 2976–2982. https://doi.org/10.1021/ja109131w.

(148) Ackerson, C. J.; Jadzinsky, P. D.; Jensen, G. J.; Kornberg, R. D. Rigid, Specific, and Discrete Gold Nanoparticle/Antibody Conjugates. *J. Am. Chem. Soc.* **2006**, *128* (8), 2635–2640. https://doi.org/10.1021/ja0555668.

(149) Ackerson, C. J.; Powell, R. D.; Hainfeld, J. F. Site-Specific Biomolecule Labeling with Gold Clusters. In *Methods in Enzymology*; Elsevier, 2010; Vol. 481, pp 195–230. https://doi.org/10.1016/S0076-6879(10)81009-2.

(150) Schaaff, T. G.; Whetten, R. L. Controlled Etching of Au:SR Cluster Compounds. *J. Phys. Chem. B* **1999**, *103* (44), 9394–9396. https://doi.org/10.1021/jp993229d.

(151) Qian, H.; Zhu, Y.; Jin, R. Size-Focusing Synthesis, Optical and Electrochemical Properties of Monodisperse Au $_{38}$ (SC $_{2}$ H $_{4}$ Ph) $_{24}$ Nanoclusters. *ACS Nano* **2009**, *3* (11), 3795–3803. https://doi.org/10.1021/nn901137h.

(152) Wong, O. A.; Compel, W. S.; Ackerson, C. J. Combinatorial Discovery of Cosolvent Systems for Production of Narrow Dispersion Thiolate-Protected Gold Nanoparticles. *ACS Comb. Sci.* **2015**, *17* (1), 11–18. https://doi.org/10.1021/co500072c.

(153) Kumar, S.; Jin, R. Water-Soluble Au25(Capt)18 Nanoclusters: Synthesis, Thermal Stability, and Optical Properties. *Nanoscale* **2012**, *4* (14), 4222. https://doi.org/10.1039/c2nr30833a.

(154) Ackerson, C. J.; Jadzinsky, P. D.; Kornberg, R. D. Thiolate Ligands for Synthesis of Water-Soluble Gold Clusters. *J. Am. Chem. Soc.* **2005**, *127* (18), 6550–6551. https://doi.org/10.1021/ja046114i.

(155) Desplancq, D.; Groysbeck, N.; Chiper, M.; Weiss, E.; Frisch, B.; Strub, J.-M.; Cianferani, S.; Zafeiratos, S.; Moeglin, E.; Holy, X.; Favier, A. L.; De Carlo, S.; Schultz, P.; Spehner, D.; Zuber, G. Cytosolic Diffusion and Peptide-Assisted Nuclear Shuttling of Peptide-Substituted Circa 102 Gold Atom Nanoclusters in Living Cells. *ACS Appl. Nano Mater.* **2018**, *1* (8), 4236–4246. https://doi.org/10.1021/acsanm.8b00988.

(156) Groysbeck, N.; Stoessel, A.; Donzeau, M.; da Silva, E. C.; Lehmann, M.; Strub, J.-M.; Cianferani, S.; Dembélé, K.; Zuber, G. Synthesis and Biological Evaluation of 2.4 Nm Thiolate-Protected Gold Nanoparticles Conjugated to Cetuximab for Targeting Glioblastoma Cancer Cells via the EGFR. *Nanotechnology* **2019**, *30* (18), 184005. https://doi.org/10.1088/1361-6528/aaff0a.

(157) Jadzinsky, P. D.; Calero, G.; Ackerson, C. J.; Bushnell, D. A.; Kornberg, R. D. Structure of a Thiol Monolayer-Protected Gold Nanoparticle at 1.1 A Resolution. *Science* **2007**, *318* (5849), 430–433. https://doi.org/10.1126/science.1148624.

(158) Jana, N. R.; Gearheart, L.; Murphy, C. J. Wet Chemical Synthesis of High Aspect Ratio Cylindrical Gold Nanorods. *J. Phys. Chem. B* **2001**, *105* (19), 4065–4067. https://doi.org/10.1021/jp0107964.

(159) Oldenburg, S. J.; Averitt, R. D.; Westcott, S. L.; Halas, N. J. Nanoengineering of Optical Resonances. *Chem. Phys. Lett.* **1998**, *288* (2–4), 243–247. https://doi.org/10.1016/S0009-2614(98)00277-2.

(160) Chen, J.; McLellan, J. M.; Siekkinen, A.; Xiong, Y.; Li, Z.-Y.; Xia, Y. Facile Synthesis of Gold−Silver Nanocages with Controllable Pores on the Surface. *J. Am. Chem. Soc.* **2006**, *128* (46), 14776–14777. https://doi.org/10.1021/ja066023g.

(161) Dumur, F.; Dumas, E.; Mayer, C. Functionalization of Gold Nanoparticles by Inorganic Entities. *Nanomaterials* **2020**, *10* (548).

(162) Leifert, A.; Pan-Bartnek, Y.; Simon, U.; Jahnen-Dechent, W. Molecularly Stabilised Ultrasmall Gold Nanoparticles: Synthesis, Characterization and Bioactivity. *Nanoscale* **2013**, *5* (14), 6224. https://doi.org/10.1039/c3nr00916e.

(163) Thanh, N. T. K.; Green, L. A. W. Functionalisation of Nanoparticles for Biomedical Applications. *Nano Today* **2010**, *5* (3), 213–230. https://doi.org/10.1016/j.nantod.2010.05.003.

(164) Mariscal, M. M.; Olmos-Asar, J. A.; Gutierrez-Wing, C.; Mayoral, A.; Yacaman, M. J. On the Atomic Structure of Thiol-Protected Gold Nanoparticles: A Combined Experimental and Theoretical Study. *Phys. Chem. Chem. Phys.* **2010**, *12* (37), 11785. https://doi.org/10.1039/c004229c.

(165) Heinecke, C. L.; Ni, T. W.; Malola, S.; Mäkinen, V.; Wong, O. A.; Häkkinen, H.; Ackerson, C. J. Structural and Theoretical Basis for Ligand Exchange on Thiolate Monolayer Protected Gold Nanoclusters. *J. Am. Chem. Soc.* **2012**, *134* (32), 13316–13322. https://doi.org/10.1021/ja3032339.

(166) Kassam, A.; Bremner, G.; Clark, B.; Ulibarri, G.; Lennox, R. B. Place Exchange Reactions of Alkyl Thiols on Gold Nanoparticles. *J. Am. Chem. Soc.* **2006**, *128* (11), 3476–3477. https://doi.org/10.1021/ja057091q.

(167) Donkers, R. L.; Song, Y.; Murray, R. W. Substituent Effects on the Exchange Dynamics of Ligands on 1.6 Nm Diameter Gold Nanoparticles. *Langmuir* **2004**, *20* (11), 4703–4707. https://doi.org/10.1021/la0497494.

(168) Pal, A. Preparation of Ultrafine Colloidal Gold Particles Using a Bioactive Molecule. *J. Nanoparticle Res.* **2004**, *6* (1), 27–34. https://doi.org/10.1023/B:NANO.0000023205.00731.6d.

(169) Unal Gulsuner, H.; Ceylan, H.; Guler, M. O.; Tekinay, A. B. Multi-Domain Short Peptide Molecules for in Situ Synthesis and Biofunctionalization of Gold Nanoparticles for Integrin-Targeted Cell Uptake. *ACS Appl. Mater. Interfaces* **2015**, *7* (20), 10677–10683. https://doi.org/10.1021/acsami.5b00093.

(170) Dykman, L. A.; Khlebtsov, N. G. Methods for Chemical Synthesis of Colloidal Gold. *Russ. Chem. Rev.* **2019**, *88* (3), 229–247. https://doi.org/10.1070/RCR4843.

(171) Giljohann, D. A.; Seferos, D. S.; Daniel, W. L.; Massich, M. D.; Patel, P. C.; Mirkin, C. A. Gold Nanoparticles for Biology and Medicine. *Angew. Chem. Int. Ed.* **2010**, *49* (19), 3280–3294. https://doi.org/10.1002/anie.200904359.

(172) Mandal, T. K.; Fleming, M. S.; Walt, D. R. Preparation of Polymer Coated Gold Nanoparticles by Surface-Confined Living Radical Polymerization at Ambient Temperature. *Nano Lett.* **2002**, *2* (1), 3–7. https://doi.org/10.1021/nl015582c.

(173) Aqil, A.; Qiu, H.; Greisch, J.-F.; Jérôme, R.; De Pauw, E.; Jérôme, C. Coating of Gold Nanoparticles by Thermosensitive Poly(N-Isopropylacrylamide) End-Capped by Biotin. *Polymer* **2008**, *49* (5), 1145–1153. https://doi.org/10.1016/j.polymer.2007.12.033.

(174) Sakai, T.; Alexandridis, P. Single-Step Synthesis and Stabilization of Metal Nanoparticles in Aqueous Pluronic Block Copolymer Solutions at Ambient Temperature. *Langmuir* **2004**, *20* (20), 8426–8430. https://doi.org/10.1021/la049514s.

(175) Stöber, W.; Fink, A.; Bohn, E. Controlled Growth of Monodisperse Silica Spheres in the Micron Size Range. *J. Colloid Interface Sci.* **1968**, *26* (1), 62–69. https://doi.org/10.1016/0021-9797(68)90272-5.

(176) Ackerson, C. J.; Jadzinsky, P. D.; Sexton, J. Z. Synthesis and Bioconjugation of 2 and 3 Nm-Diameter Gold Cluster Compounds. 7.

(177) Zhan, N.; Palui, G.; Safi, M.; Ji, X.; Mattoussi, H. Multidentate Zwitterionic Ligands Provide Compact and Highly Biocompatible Quantum Dots. *J. Am. Chem. Soc.* **2013**, *135* (37), 13786–13795. https://doi.org/10.1021/ja405010v.

(178) Huo, S.; Jiang, Y.; Jiang, Z.; Landis, R. F.; Liang, X.-J.; Rotello, V. M. Stable and Oxidant Responsive Zwitterionic Nanoclusters. *Nanoscale* **2018**, *10* (16), 7382–7386. https://doi.org/10.1039/C7NR08951A.

(179) Thakur, N. S.; Mandal, N.; Banerjee, U. C. Esterase-Mediated Highly Fluorescent Gold Nanoclusters and Their Use in Ultrasensitive Detection of Mercury: Synthetic and Mechanistic Aspects. *ACS Omega* **2018**, *3* (12), 18553–18562. https://doi.org/10.1021/acsomega.8b02505.

(180) Liu, X.; Atwater, M.; Wang, J.; Huo, Q. Extinction Coefficient of Gold Nanoparticles with Different Sizes and Different Capping Ligands. *Colloids Surf. B Biointerfaces* **2007**, *58* (1), 3–7. https://doi.org/10.1016/j.colsurfb.2006.08.005.

(181) Freund, G.; Sibler, A.-P.; Desplancq, D.; Oulad-Abdelghani, M.; Vigneron, M.; Gannon, J.; Van Regenmortel, M. H.; Weiss, E. Targeting Endogenous Nuclear Antigens by Electrotransfer of Monoclonal Antibodies in Living Cells. *mAbs* **2013**, *5* (4), 518–522. https://doi.org/10.4161/mabs.25084.

(182) Ackerson, C. J.; Jadzinsky, P. D.; Sexton, J. Z.; Bushnell, D. A.; Kornberg, R. D. Synthesis and Bioconjugation of 2 and 3 Nm-Diameter Gold Nanoparticles. *Bioconjug. Chem.* **2010**, *21* (2), 214–218. https://doi.org/10.1021/bc900135d.

(183) Shimmin, R. G.; Schoch, A. B.; Braun, P. V. Polymer Size and Concentration Effects on the Size of Gold Nanoparticles Capped by Polymeric Thiols. *Langmuir* **2004**, *20* (13), 5613–5620. https://doi.org/10.1021/la036365p.

(184) Chen, T.; Luo, Z.; Yao, Q.; Yeo, A. X. H.; Xie, J. Synthesis of Thiolate-Protected Au Nanoparticles Revisited: U-Shape Trend between the Size of Nanoparticles and Thiol-to-Au Ratio. *Chem. Commun.* **2016**, *52* (61), 9522–9525. https://doi.org/10.1039/C6CC04433F.

(185) Zhou, M.; Zeng, C.; Chen, Y.; Zhao, S.; Sfeir, M. Y.; Zhu, M.; Jin, R. Evolution from the Plasmon to Exciton State in Ligand-Protected Atomically Precise Gold Nanoparticles. *Nat. Commun.* **2016**, *7* (1), 13240. https://doi.org/10.1038/ncomms13240.

(186) Lévy, R.; Thanh, N. T. K.; Doty, R. C.; Hussain, I.; Nichols, R. J.; Schiffrin, D. J.; Brust, M.; Fernig, D. G. Rational and Combinatorial Design of Peptide Capping Ligands for Gold Nanoparticles. *J. Am. Chem. Soc.* **2004**, *126* (32), 10076–10084. https://doi.org/10.1021/ja0487269.

(187) Kalderon, D.; Roberts, B. L.; Richardson, W. D.; Smith, A. E. A Short Amino Acid Sequence Able to Specify Nuclear Location. *Cell* **1984**, *39* (3), 499–509. https://doi.org/10.1016/0092-8674(84)90457-4.

(188) Ribbeck, K.; Görlich, D. Kinetic Analysis of Translocation through Nuclear Pore Complexes. *EMBO J.* **2001**, *20* (6), 1320–1330. https://doi.org/10.1093/emboj/20.6.1320.

(189) Willett, J.; Lawrence, M.; Wilder, J.; Smithies, O. A Tetraethylene Glycol Coat Gives Gold Nanoparticles Long in Vivo Half-Lives with Minimal Increase in Size. *Int. J. Nanomedicine* **2017**, *Volume 12*, 2581–2592. https://doi.org/10.2147/IJN.S121486.

(190) Xiao, W.; Xiong, J.; Zhang, S.; Xiong, Y.; Zhang, H.; Gao, H. Influence of Ligands Property and Particle Size of Gold Nanoparticles on the Protein Adsorption and Corresponding Targeting Ability. *Int. J. Pharm.* **2018**, *538* (1–2), 105–111. https://doi.org/10.1016/j.ijpharm.2018.01.011.

(191) ELLMAN, G. L. A Colorimetric Method for Determining Low Concentrations of Mercaptans. *Arch. Biochem. Biophys.* **1958**, *74* (2), 443–450. https://doi.org/10.1016/0003-9861(58)90014-6.

(192) Eck, W.; Craig, G.; Sigdel, A.; Ritter, G.; Old, L. J.; Tang, L.; Brennan, M. F.; Allen, P. J.; Mason, M. D. PEGylated Gold Nanoparticles Conjugated to Monoclonal F19 Antibodies as Targeted Labeling Agents for Human Pancreatic Carcinoma Tissue. *ACS Nano* **2008**, *2* (11), 2263–2272. https://doi.org/10.1021/nn800429d.

(193) Hong, R.; Han, G.; Fernández, J. M.; Kim, B.; Forbes, N. S.; Rotello, V. M. Glutathione-Mediated Delivery and Release Using Monolayer Protected Nanoparticle Carriers. *J. Am. Chem. Soc.* **2006**, *128* (4), 1078–1079. https://doi.org/10.1021/ja056726i.

(194) Templeton, A. C.; Wuelfing, W. P.; Murray, R. W. Monolayer-Protected Cluster Molecules. *Acc. Chem. Res.* **2000**, *33* (1), 27–36. https://doi.org/10.1021/ar9602664.

(195) Hostetler, M. J.; Wingate, J. E.; Zhong, C.-J.; Harris, J. E.; Vachet, R. W.; Clark, M. R.; Londono, J. D.; Green, S. J.; Stokes, J. J.; Wignall, G. D.; Glish, G. L.; Porter, M. D.; Evans, N. D.; Murray, R. W. Alkanethiolate Gold Cluster Molecules with Core Diameters from 1.5 to 5.2 Nm: Core and Monolayer Properties as a Function of Core Size. *Langmuir* **1998**, *14* (1), 17–30. https://doi.org/10.1021/la970588w.

(196) Leff, D. V.; Ohara, P. C.; Heath, J. R.; Gelbart, W. M. Thermodynamic Control of Gold Nanocrystal Size: Experiment and Theory. *J. Phys. Chem.* **1995**, *99* (18), 7036–7041. https://doi.org/10.1021/j100018a041.

(197) Jiang, D.; Tiago, M. L.; Luo, W.; Dai, S. The “Staple” Motif: A Key to Stability of Thiolate-Protected Gold Nanoclusters. *J. Am. Chem. Soc.* **2008**, *130* (9), 2777–2779. https://doi.org/10.1021/ja710991n.

(198) Hostetler, M. J.; Templeton, A. C.; Murray, R. W. Dynamics of Place-Exchange Reactions on Monolayer-Protected Gold Cluster Molecules. *Langmuir* **1999**, *15* (11), 3782–3789. https://doi.org/10.1021/la981598f.

(199) Guo, R.; Song, Y.; Wang, G.; Murray, R. W. Does Core Size Matter in the Kinetics of Ligand Exchanges of Monolayer-Protected Au Clusters? *J. Am. Chem. Soc.* **2005**, *127* (8), 2752–2757. https://doi.org/10.1021/ja044638c.

(200) Song, Y.; Murray, R. W. Dynamics and Extent of Ligand Exchange Depend on Electronic Charge of Metal Nanoparticles. *J. Am. Chem. Soc.* **2002**, *124* (24), 7096–7102. https://doi.org/10.1021/ja0174985.

(201) Nativo, P.; Prior, I. A.; Brust, M. Uptake and Intracellular Fate of Surface-Modified Gold Nanoparticles. *ACS Nano* **2008**, *2* (8), 1639–1644. https://doi.org/10.1021/nn800330a.

(202) Sun, L.; Liu, D.; Wang, Z. Functional Gold Nanoparticle−Peptide Complexes as Cell-Targeting Agents. *Langmuir* **2008**, *24* (18), 10293–10297. https://doi.org/10.1021/la8015063.

(203) Oh, E.; Delehanty, J. B.; Sapsford, K. E.; Susumu, K.; Goswami, R.; Blanco-Canosa, J. B.; Dawson, P. E.; Granek, J.; Shoff, M.; Zhang, Q.; Goering, P. L.; Huston, A.; Medintz, I. L. Cellular Uptake and Fate of PEGylated Gold Nanoparticles Is Dependent on Both Cell-Penetration Peptides and Particle Size. *ACS Nano* **2011**, *5* (8), 6434–6448. https://doi.org/10.1021/nn201624c.

(204) Hamann, A.; Nguyen, A.; Pannier, A. K. Nucleic Acid Delivery to Mesenchymal Stem Cells: A Review of Nonviral Methods and Applications. *J. Biol. Eng.* **2019**, *13* (1), 7. https://doi.org/10.1186/s13036-019-0140-0.

(205) Cho, E. C.; Au, L.; Zhang, Q.; Xia, Y. The Effects of Size, Shape, and Surface Functional Group of Gold Nanostructures on Their Adsorption and Internalization by Cells. *Small* **2010**, *6* (4), 517–522. https://doi.org/10.1002/smll.200901622.

(206) Kapingidza, A. B.; Kowal, K.; Chruszcz, M. Antigen-Antibody Complexes. *Subcell. Biochem.* **2020**, *94*, 465–497. https://doi.org/10.1007/978-3-030-41769-7_19.

(207) Chiu, M. L.; Goulet, D. R.; Teplyakov, A.; Gilliland, G. L. Antibody Structure and Function: The Basis for Engineering Therapeutics. *Antibodies* **2019**, *8* (4), 55. https://doi.org/10.3390/antib8040055.
(208) Porter, R. R. The Formation of a Specific Inhibitor by Hydrolysis of Rabbit Antiovalbumin. *Biochem. J.* **1950**, *46* (4), 479–484. https://doi.org/10.1042/bj0460479.
(209) Porter, R. R. A Chemical Study of Rabbit Antiovalbumin. *Biochem. J.* **1950**, *46* (4), 473–478. https://doi.org/10.1042/bj0460473.
(210) Persson, H.; Lantto, J.; Ohlin, M. A Focused Antibody Library for Improved Hapten Recognition. *J. Mol. Biol.* **2006**, *357* (2), 607–620. https://doi.org/10.1016/j.jmb.2006.01.004.
(211) Cobaugh, C. W.; Almagro, J. C.; Pogson, M.; Iverson, B.; Georgiou, G. Synthetic Antibody Libraries Focused Towards Peptide Ligands. *J. Mol. Biol.* **2008**, *378* (3), 622–633. https://doi.org/10.1016/j.jmb.2008.02.037.
(212) Almagro, J. C.; Quintero-Hernández, V.; Ortiz-León, M.; Velandia, A.; Smith, S. L.; Becerril, B. Design and Validation of a Synthetic VH Repertoire with Tailored Diversity for Protein Recognition. *J. Mol. Recognit.* **2006**, *19* (5), 413–422. https://doi.org/10.1002/jmr.796.
(213) Dennler, P.; Fischer, E.; Schibli, R. Antibody Conjugates: From Heterogeneous Populations to Defined Reagents. *Antibodies* **2015**, *4* (3), 197–224. https://doi.org/10.3390/antib4030197.
(214) Lyon, R. P.; Setter, J. R.; Bovee, T. D.; Doronina, S. O.; Hunter, J. H.; Anderson, M. E.; Balasubramanian, C. L.; Duniho, S. M.; Leiske, C. I.; Li, F.; Senter, P. D. Self-Hydrolyzing Maleimides Improve the Stability and Pharmacological Properties of Antibody-Drug Conjugates. *Nat. Biotechnol.* **2014**, *32* (10), 1059–1062. https://doi.org/10.1038/nbt.2968.
(215) Billah, Md. M.; Hodges, C. S.; Hays, H. C. W.; Millner, P. A. Directed Immobilization of Reduced Antibody Fragments onto a Novel SAM on Gold for Myoglobin Impedance Immunosensing. *Bioelectrochemistry* **2010**, *80* (1), 49–54. https://doi.org/10.1016/j.bioelechem.2010.08.005.
(216) Sun, M. M. C.; Beam, K. S.; Cerveny, C. G.; Hamblett, K. J.; Blackmore, R. S.; Torgov, M. Y.; Handley, F. G. M.; Ihle, N. C.; Senter, P. D.; Alley, S. C. Reduction−Alkylation Strategies for the Modification of Specific Monoclonal Antibody Disulfides. *Bioconjug. Chem.* **2005**, *16* (5), 1282–1290. https://doi.org/10.1021/bc050201y.
(217) Stimmel, J. B.; Merrill, B. M.; Kuyper, L. F.; Moxham, C. P.; Hutchins, J. T.; Fling, M. E.; Kull, F. C. Site-Specific Conjugation on Serine → Cysteine Variant Monoclonal Antibodies. *J. Biol. Chem.* **2000**, *275* (39), 30445–30450. https://doi.org/10.1074/jbc.M001672200.
(218) Shen, B.-Q.; Xu, K.; Liu, L.; Raab, H.; Bhakta, S.; Kenrick, M.; Parsons-Reponte, K. L.; Tien, J.; Yu, S.-F.; Mai, E.; Li, D.; Tibbitts, J.; Baudys, J.; Saad, O. M.; Scales, S. J.; McDonald, P. J.; Hass, P. E.; Eigenbrot, C.; Nguyen, T.; Solis, W. A.; Fuji, R. N.; Flagella, K. M.; Patel, D.; Spencer, S. D.; Khawli, L. A.; Ebens, A.; Wong, W. L.; Vandlen, R.; Kaur, S.; Sliwkowski, M. X.; Scheller, R. H.; Polakis, P.; Junutula, J. R. Conjugation Site Modulates the in Vivo Stability and Therapeutic Activity of Antibody-Drug Conjugates. *Nat. Biotechnol.* **2012**, *30* (2), 184–189. https://doi.org/10.1038/nbt.2108.
(219) Axup, J. Y.; Bajjuri, K. M.; Ritland, M.; Hutchins, B. M.; Kim, C. H.; Kazane, S. A.; Halder, R.; Forsyth, J. S.; Santidrian, A. F.; Stafin, K.; Lu, Y.; Tran, H.; Seller, A. J.; Biroc, S. L.; Szydlik, A.; Pinkstaff, J. K.; Tian, F.; Sinha, S. C.; Felding-Habermann, B.; Smider, V. V.; Schultz, P. G. Synthesis of Site-Specific Antibody-Drug Conjugates Using Unnatural Amino Acids. *Proc. Natl. Acad. Sci.* **2012**, *109* (40), 16101–16106. https://doi.org/10.1073/pnas.1211023109.
(220) Xiao, H.; Chatterjee, A.; Choi, S.; Bajjuri, K. M.; Sinha, S. C.; Schultz, P. G. Genetic Incorporation of Multiple Unnatural Amino Acids into Proteins in Mammalian Cells. *Angew. Chem. Int. Ed.* **2013**, *52* (52), 14080–14083. https://doi.org/10.1002/anie.201308137.
(221) Levary, D. A.; Parthasarathy, R.; Boder, E. T.; Ackerman, M. E. Protein-Protein Fusion Catalyzed by Sortase A. *PLoS ONE* **2011**, *6* (4), e18342. https://doi.org/10.1371/journal.pone.0018342.
(222) Swee, L. K.; Guimaraes, C. P.; Sehrawat, S.; Spooner, E.; Barrasa, M. I.; Ploegh, H. L. Sortase-Mediated Modification of ADEC205 Affords Optimization of Antigen Presentation and

Immunization against a Set of Viral Epitopes. *Proc. Natl. Acad. Sci. U. S. A.* **2013**, *110* (4), 1428–1433. https://doi.org/10.1073/pnas.1214994110.

(223) Josten, A.; Haalck, L.; Spener, F.; Meusel, M. Use of Microbial Transglutaminase for the Enzymatic Biotinylation of Antibodies. *J. Immunol. Methods* **2000**, *240* (1–2), 47–54. https://doi.org/10.1016/S0022-1759(00)00172-1.

(224) Jeger, S.; Zimmermann, K.; Blanc, A.; Grünberg, J.; Honer, M.; Hunziker, P.; Struthers, H.; Schibli, R. Site-Specific and Stoichiometric Modification of Antibodies by Bacterial Transglutaminase. *Angew. Chem. Int. Ed.* **2010**, *49* (51), 9995–9997. https://doi.org/10.1002/anie.201004243.

(225) Scheck, R. A.; Francis, M. B. Regioselective Labeling of Antibodies through N-Terminal Transamination. *ACS Chem. Biol.* **2007**, *2* (4), 247–251. https://doi.org/10.1021/cb6003959.

(226) Marques, A. C.; Costa, P. J.; Velho, S.; Amaral, M. H. Functionalizing Nanoparticles with Cancer-Targeting Antibodies: A Comparison of Strategies. *J. Controlled Release* **2020**, *320*, 180–200. https://doi.org/10.1016/j.jconrel.2020.01.035.

(227) Farahavar, G.; Abolmaali, S. S.; Gholijani, N.; Nejatollahi, F. Antibody-Guided Nanomedicines as Novel Breakthrough Therapeutic, Diagnostic and Theranostic Tools. *Biomater. Sci.* **2019**, *7* (10), 4000–4016. https://doi.org/10.1039/C9BM00931K.

(228) Hsieh, B.-Y.; Chang, Y.-F.; Ng, M.-Y.; Liu, W.-C.; Lin, C.-H.; Wu, H.-T.; Chou, C. Localized Surface Plasmon Coupled Fluorescence Fiber-Optic Biosensor with Gold Nanoparticles. *Anal. Chem.* **2007**, *79* (9), 3487–3493. https://doi.org/10.1021/ac0624389.

(229) Lopez, A.; Lovato, F.; Hwan Oh, S.; Lai, Y. H.; Filbrun, S.; Driskell, E. A.; Driskell, J. D. SERS Immunoassay Based on the Capture and Concentration of Antigen-Assembled Gold Nanoparticles. *Talanta* **2016**, *146*, 388–393. https://doi.org/10.1016/j.talanta.2015.08.065.

(230) Choi, D. H.; Lee, S. K.; Oh, Y. K.; Bae, B. W.; Lee, S. D.; Kim, S.; Shin, Y.-B.; Kim, M.-G. A Dual Gold Nanoparticle Conjugate-Based Lateral Flow Assay (LFA) Method for the Analysis of Troponin I. *Biosens. Bioelectron.* **2010**, *25* (8), 1999–2002. https://doi.org/10.1016/j.bios.2010.01.019.

(231) Liszbinski, R. B.; Romagnoli, G. G.; Gorgulho, C. M.; Basso, C. R.; Pedrosa, V. A.; Kaneno, R. Anti-EGFR-Coated Gold Nanoparticles In Vitro Carry 5-Fluorouracil to Colorectal Cancer Cells. *Materials* **2020**, *13* (2), 375. https://doi.org/10.3390/ma13020375.

(232) García-Fernández, L.; Garcia-Pardo, J.; Tort, O.; Prior, I.; Brust, M.; Casals, E.; Lorenzo, J.; Puntes, V. F. Conserved Effects and Altered Trafficking of Cetuximab Antibodies Conjugated to Gold Nanoparticles with Precise Control of Their Number and Orientation. *Nanoscale* **2017**, *9* (18), 6111–6121. https://doi.org/10.1039/C7NR00947J.

(233) Mustafaoglu, N.; Kiziltepe, T.; Bilgicer, B. Site-Specific Conjugation of an Antibody on a Gold Nanoparticle Surface for One-Step Diagnosis of Prostate Specific Antigen with Dynamic Light Scattering. *Nanoscale* **2017**, *9* (25), 8684–8694. https://doi.org/10.1039/C7NR03096G.

(234) Alves, N. J.; Kiziltepe, T.; Bilgicer, B. Oriented Surface Immobilization of Antibodies at the Conserved Nucleotide Binding Site for Enhanced Antigen Detection. *Langmuir* **2012**, *28* (25), 9640–9648. https://doi.org/10.1021/la301887s.

(235) Finetti, C.; Sola, L.; Pezzullo, M.; Prosperi, D.; Colombo, M.; Riva, B.; Avvakumova, S.; Morasso, C.; Picciolini, S.; Chiari, M. Click Chemistry Immobilization of Antibodies on Polymer Coated Gold Nanoparticles. *Langmuir* **2016**, *32* (29), 7435–7441. https://doi.org/10.1021/acs.langmuir.6b01142.

(236) Bonavia, R.; Inda, M. M.; Vandenberg, S.; Cheng, S.-Y.; Nagane, M.; Hadwiger, P.; Tan, P.; Sah, D. W. Y.; Cavenee, W. K.; Furnari, F. B. EGFRvIII Promotes Glioma Angiogenesis and Growth through the NF-KB, Interleukin-8 Pathway. *Oncogene* **2012**, *31* (36), 4054–4066. https://doi.org/10.1038/onc.2011.563.

(237) Aubin-Tam, M.-E.; Hwang, W.; Hamad-Schifferli, K. Site-Directed Nanoparticle Labeling of Cytochrome c. *Proc. Natl. Acad. Sci.* **2009**, *106* (11), 4095–4100. https://doi.org/10.1073/pnas.0807299106.

(238) Aubin-Tam, M.-E.; Hamad-Schifferli, K. Gold Nanoparticle−Cytochrome c Complexes: The Effect of Nanoparticle Ligand Charge on Protein Structure. *Langmuir* **2005**, *21* (26), 12080–12084. https://doi.org/10.1021/la052102e.

(239) Aubin-Tam, M.-E.; Hamad-Schifferli, K. Structure and Function of Nanoparticle–Protein Conjugates. *Biomed. Mater.* **2008**, *3* (3), 034001. https://doi.org/10.1088/1748-6041/3/3/034001.

(240) Ackerson, C. J.; Sykes, M. T.; Kornberg, R. D. Defined DNA/Nanoparticle Conjugates. *Proc. Natl. Acad. Sci.* **2005**, *102* (38), 13383–13385. https://doi.org/10.1073/pnas.0506290102.

(241) Bowman, M.-C.; Ballard, T. E.; Ackerson, C. J.; Feldheim, D. L.; Margolis, D. M.; Melander, C. Inhibition of HIV Fusion with Multivalent Gold Nanoparticles. *J. Am. Chem. Soc.* **2008**, *130* (22), 6896–6897. https://doi.org/10.1021/ja710321g.

(242) Morais, T.; Soares, M. E.; Duarte, J. A.; Soares, L.; Maia, S.; Gomes, P.; Pereira, E.; Fraga, S.; Carmo, H.; Bastos, M. de L. Effect of Surface Coating on the Biodistribution Profile of Gold Nanoparticles in the Rat. *Eur. J. Pharm. Biopharm.* **2012**, *80* (1), 185–193. https://doi.org/10.1016/j.ejpb.2011.09.005.

(243) Zhu, D.; Li, X.; Liu, X.; Wang, J.; Wang, Z. Designing Bifunctionalized Gold Nanoparticle for Colorimetric Detection of Pb2+ under Physiological Condition. *Biosens. Bioelectron.* **2012**, *31* (1), 505–509. https://doi.org/10.1016/j.bios.2011.11.026.

(244) Jabir, M. S.; Taha, A. A.; Sahib, U. I.; Taqi, Z. J.; Al-Shammari, A. M.; Salman, A. S. Novel of Nano Delivery System for Linalool Loaded on Gold Nanoparticles Conjugated with CALNN Peptide for Application in Drug Uptake and Induction of Cell Death on Breast Cancer Cell Line. *Mater. Sci. Eng. C* **2019**, *94*, 949–964. https://doi.org/10.1016/j.msec.2018.10.014.

(245) Alexis, F.; Pridgen, E.; Molnar, L. K.; Farokhzad, O. C. Factors Affecting the Clearance and Biodistribution of Polymeric Nanoparticles. *Mol. Pharm.* **2008**, *5* (4), 505–515. https://doi.org/10.1021/mp800051m.

(246) Conic, S.; Desplancq, D.; Ferrand, A.; Fischer, V.; Heyer, V.; Reina San Martin, B.; Pontabry, J.; Oulad-Abdelghani, M.; Babu N., K.; Wright, G. D.; Molina, N.; Weiss, E.; Tora, L. Imaging of Native Transcription Factors and Histone Phosphorylation at High Resolution in Live Cells. *J. Cell Biol.* **2018**, *217* (4), 1537–1552. https://doi.org/10.1083/jcb.201709153.

(247) Hainfeld, J. F.; Dilmanian, F. A.; Slatkin, D. N.; Smilowitz, H. M. Radiotherapy Enhancement with Gold Nanoparticles. *J. Pharm. Pharmacol.* **2008**, *60* (8), 977–985. https://doi.org/10.1211/jpp.60.8.0005.

(248) Vigderman, L.; Zubarev, E. R. Therapeutic Platforms Based on Gold Nanoparticles and Their Covalent Conjugates with Drug Molecules. *Adv. Drug Deliv. Rev.* **2013**, *65* (5), 663–676. https://doi.org/10.1016/j.addr.2012.05.004.

(249) Muyldermans, S. Nanobodies: Natural Single-Domain Antibodies. *Annu. Rev. Biochem.* **2013**, *82* (1), 775–797. https://doi.org/10.1146/annurev-biochem-063011-092449.

(250) Hamers-Casterman, C.; Atarhouch, T.; Muyldermans, S.; Robinson, G.; Hammers, C.; Songa, E. B.; Bendahman, N.; Hammers, R. Naturally Occurring Antibodies Devoid of Light Chains. *Nature* **1993**, *363* (6428), 446–448. https://doi.org/10.1038/363446a0.

(251) Greenberg, A. S.; Avila, D.; Hughes, M.; Hughes, A.; McKinney, E. C.; Flajnik, M. F. A New Antigen Receptor Gene Family That Undergoes Rearrangement and Extensive Somatic Diversification in Sharks. *Nature* **1995**, *374* (6518), 168–173. https://doi.org/10.1038/374168a0.

(252) Desmyter, A.; Transue, T. R.; Ghahroudi, M. A.; Thi, M.-H. D.; Poortmans, F.; Hamers, R.; Muyldermans, S.; Wyns, L. Crystal Structure of a Camel Single- Domain VH Antibody Fragment in Complex with Lysozyme. **1996**, *3* (9), 9.

(253) Beghein, E.; Gettemans, J. Nanobody Technology: A Versatile Toolkit for Microscopic Imaging, Protein–Protein Interaction Analysis, and Protein Function Exploration. *Front. Immunol.* **2017**, *8*, 771. https://doi.org/10.3389/fimmu.2017.00771.

(254) Pleiner, T.; Bates, M.; Trakhanov, S.; Lee, C.-T.; Schliep, J. E.; Chug, H.; Böhning, M.; Stark, H.; Urlaub, H.; Görlich, D. Nanobodies: Site-Specific Labeling for Super-Resolution Imaging, Rapid

Epitope-Mapping and Native Protein Complex Isolation. *eLife* **2015**, *4*, e11349. https://doi.org/10.7554/eLife.11349.

(255) Carrington, G.; Tomlinson, D.; Peckham, M. Exploiting Nanobodies and Affimers for Superresolution Imaging in Light Microscopy. *Mol. Biol. Cell* **2019**, *30* (22), 2737–2740. https://doi.org/10.1091/mbc.E18-11-0694.

(256) Ries, J.; Kaplan, C.; Platonova, E.; Eghlidi, H.; Ewers, H. A Simple, Versatile Method for GFP-Based Super-Resolution Microscopy via Nanobodies. *Nat. Methods* **2012**, *9* (6), 582–584. https://doi.org/10.1038/nmeth.1991.

(257) Platonova, E.; Winterflood, C. M.; Junemann, A.; Albrecht, D.; Faix, J.; Ewers, H. Single-Molecule Microscopy of Molecules Tagged with GFP or RFP Derivatives in Mammalian Cells Using Nanobody Binders. *Methods* **2015**, *88*, 89–97. https://doi.org/10.1016/j.ymeth.2015.06.018.

(258) Mikhaylova, M.; Cloin, B. M. C.; Finan, K.; van den Berg, R.; Teeuw, J.; Kijanka, M. M.; Sokolowski, M.; Katrukha, E. A.; Maidorn, M.; Opazo, F.; Moutel, S.; Vantard, M.; Perez, F.; van Bergen en Henegouwen, P. M. P.; Hoogenraad, C. C.; Ewers, H.; Kapitein, L. C. Resolving Bundled Microtubules Using Anti-Tubulin Nanobodies. *Nat. Commun.* **2015**, *6* (1), 7933. https://doi.org/10.1038/ncomms8933.

(259) Klein, A.; Hank, S.; Raulf, A.; Joest, E. F.; Tissen, F.; Heilemann, M.; Wieneke, R.; Tampé, R. Live-Cell Labeling of Endogenous Proteins with Nanometer Precision by Transduced Nanobodies. *Chem. Sci.* **2018**, *9* (40), 7835–7842. https://doi.org/10.1039/C8SC02910E.

(260) Witte, M. D.; Cragnolini, J. J.; Dougan, S. K.; Yoder, N. C.; Popp, M. W.; Ploegh, H. L. Preparation of Unnatural N-to-N and C-to-C Protein Fusions. *Proc. Natl. Acad. Sci.* **2012**, *109* (30), 11993–11998. https://doi.org/10.1073/pnas.1205427109.

(261) Kijanka, M.; van Donselaar, E. G.; Müller, W. H.; Dorresteijn, B.; Popov-Čeleketić, D.; el Khattabi, M.; Verrips, C. T.; van Bergen en Henegouwen, P. M. P.; Post, J. A. A Novel Immuno-Gold Labeling Protocol for Nanobody-Based Detection of HER2 in Breast Cancer Cells Using Immuno-Electron Microscopy. *J. Struct. Biol.* **2017**, *199* (1), 1–11. https://doi.org/10.1016/j.jsb.2017.05.008.

(262) Ariotti, N.; Hall, T. E.; Rae, J.; Ferguson, C.; McMahon, K.-A.; Martel, N.; Webb, R. E.; Webb, R. I.; Teasdale, R. D.; Parton, R. G. Modular Detection of GFP-Labeled Proteins for Rapid Screening by Electron Microscopy in Cells and Organisms. *Dev. Cell* **2015**, *35* (4), 513–525. https://doi.org/10.1016/j.devcel.2015.10.016.

(263) Martell, J. D.; Deerinck, T. J.; Sancak, Y.; Poulos, T. L.; Mootha, V. K.; Sosinsky, G. E.; Ellisman, M. H.; Ting, A. Y. Engineered Ascorbate Peroxidase as a Genetically Encoded Reporter for Electron Microscopy. *Nat. Biotechnol.* **2012**, *30* (11), 1143–1148. https://doi.org/10.1038/nbt.2375.

(264) Novikoff, A. B.; Novikoff, P. M.; Quintana, N.; Davis, C. Diffusion Artifacts in 3,3'-Diaminobenzidine Cytochemistry. *J. Histochem. Cytochem.* **1972**, *20* (9), 745–749. https://doi.org/10.1177/20.9.745.

(265) Ariotti, N.; Rae, J.; Giles, N.; Martel, N.; Sierecki, E.; Gambin, Y.; Hall, T. E.; Parton, R. G. Ultrastructural Localisation of Protein Interactions Using Conditionally Stable Nanobodies. *PLOS Biol.* **2018**, *16* (4), e2005473. https://doi.org/10.1371/journal.pbio.2005473.

(266) de Beer, M. A.; Kuipers, J.; van Bergen en Henegouwen, P. M. P.; Giepmans, B. N. G. A Small Protein Probe for Correlated Microscopy of Endogenous Proteins. *Histochem. Cell Biol.* **2018**, *149* (3), 261–268. https://doi.org/10.1007/s00418-018-1632-6.

(267) Jiang, Z.; Jin, X.; Li, Y.; Liu, S.; Liu, X.-M.; Wang, Y.-Y.; Zhao, P.; Cai, X.; Liu, Y.; Tang, Y.; Sun, X.; Liu, Y.; Hu, Y.; Li, M.; Cai, G.; Qi, X.; Chen, S.; Du, L.-L.; He, W. Genetically Encoded Tags for Direct Synthesis of EM-Visible Gold Nanoparticles in Cells. *Nat. Methods* **2020**, *17* (9), 937–946. https://doi.org/10.1038/s41592-020-0911-z.

(268) Buser, D. P.; Schleicher, K. D.; Prescianotto-Baschong, C.; Spiess, M. A Versatile Nanobody-Based Toolkit to Analyze Retrograde Transport from the Cell Surface. *Proc. Natl. Acad. Sci.* **2018**, *115* (27), E6227–E6236. https://doi.org/10.1073/pnas.1801865115.

(269) Abdellatif, M. E. A.; Hipp, L.; Plessner, M.; Walther, P.; Knöll, B. Indirect Visualization of Endogenous Nuclear Actin by Correlative Light and Electron Microscopy (CLEM) Using an Actin-Directed Chromobody. *Histochem. Cell Biol.* **2019**, *152* (2), 133–143. https://doi.org/10.1007/s00418-019-01795-3.

(270) Courtoy, P. J.; Picton, D. H.; Farquhar, M. G. Resolution and Limitations of the Immunoperoxidase Procedure in the Localization of Extracellular Matrix Antigens. *J. Histochem. Cytochem.* **1983**, *31* (7), 945–951. https://doi.org/10.1177/31.7.6304184.

(271) Kubala, M. H.; Kovtun, O.; Alexandrov, K.; Collins, B. M. Structural and Thermodynamic Analysis of the GFP:GFP-Nanobody Complex. *Protein Sci.* **2010**, *19* (12), 2389–2401. https://doi.org/10.1002/pro.519.

(272) Rinaldi, A.-S.; Freund, G.; Desplancq, D.; Sibler, A.-P.; Baltzinger, M.; Rochel, N.; Mély, Y.; Didier, P.; Weiss, E. The Use of Fluorescent Intrabodies to Detect Endogenous Gankyrin in Living Cancer Cells. *Exp. Cell Res.* **2013**, *319* (6), 838–849. https://doi.org/10.1016/j.yexcr.2013.01.011.

(273) Vigneron, M.; Dietsch, F.; Bianchetti, L.; Dejaegere, A.; Nominé, Y.; Cordonnier, A.; Zuber, G.; Chatton, B.; Donzeau, M. Self-Associating Peptides for Modular Bifunctional Conjugation of Tetramer Macromolecules in Living Cells. *Bioconjug. Chem.* **2019**, *30* (6), 1734–1744. https://doi.org/10.1021/acs.bioconjchem.9b00276.

(274) Moeremans, M.; Daneels, G.; Van Dijck, A.; Langanger, G.; De Mey, J. Sensitive Visualization of Antigen-Antibody Reactions in Dot and Blot Immune Overlay Assays with Immunogold and Immunogold/Silver Staining. *J. Immunol. Methods* **1984**, *74* (2), 353–360. https://doi.org/10.1016/0022-1759(84)90303-X.

(275) Danscher, G.; Nörgaard, J. O. Light Microscopic Visualization of Colloidal Gold on Resin-Embedded Tissue. *J. Histochem. Cytochem.* **1983**, *31* (12), 1394–1398. https://doi.org/10.1177/31.12.6631001.

(276) Rothbauer, U.; Zolghadr, K.; Tillib, S.; Nowak, D.; Schermelleh, L.; Gahl, A.; Backmann, N.; Conrath, K.; Muyldermans, S.; Cardoso, M. C.; Leonhardt, H. Targeting and Tracing Antigens in Live Cells with Fluorescent Nanobodies. *Nat. Methods* **2006**, *3* (11), 887–889. https://doi.org/10.1038/nmeth953.

(277) Gronenborn, A. M. Ramers of Wild-Type and Mutant P53 No Longer Bind DNA Sequence Specifically or Bind with Much Reduced Affinity. (Iii) The. **1994**, *265*, 7.

(278) Brokx, R. D.; Bolewska-Pedyczak, E.; Gariépy, J. A Stable Human P53 Heterotetramer Based on Constructive Charge Interactions within the Tetramerization Domain. *J. Biol. Chem.* **2003**, *278* (4), 2327–2332. https://doi.org/10.1074/jbc.M208528200.

(279) Zheleva, D. I.; Zhelev, N. Z.; Fischer, P. M.; Duff, S. V.; Warbrick, E.; Blake, D. G.; Lane, D. P. A Quantitative Study of the in Vitro Binding of the C-Terminal Domain of P21 to PCNA: Affinity, Stoichiometry, and Thermodynamics. *Biochemistry* **2000**, *39* (25), 7388–7397. https://doi.org/10.1021/bi992498r.

(280) Warbrick, E. A Functional Analysis of PCNA-Binding Peptides Derived from Protein Sequence, Interaction Screening and Rational Design. *Oncogene* **2006**, *25* (20), 2850–2859. https://doi.org/10.1038/sj.onc.1209320.

(281) Cramer, L. P.; Mitchison, T. J. Myosin Is Involved in Postmitotic Cell Spreading. *J. Cell Biol.* **1995**, *131* (1), 179–189. https://doi.org/10.1083/jcb.131.1.179.

(282) Hirsch, P.; Kässens, M.; Püttmann, M.; Reimer, L. Contamination in a Scanning Electron Microscope and the Influence of Specimen Cooling. *Scanning* **2008**, *16* (2), 101–110. https://doi.org/10.1002/sca.4950160207.

(283) Schumacher, D.; Helma, J.; Schneider, A. F. L.; Leonhardt, H.; Hackenberger, C. P. R. Nanobodies: Chemical Functionalization Strategies and Intracellular Applications. *Angew. Chem. Int. Ed.* **2018**, *57* (9), 2314–2333. https://doi.org/10.1002/anie.201708459.

(284) Helma, J.; Cardoso, M. C.; Muyldermans, S.; Leonhardt, H. Nanobodies and Recombinant Binders in Cell Biology. *J. Cell Biol.* **2015**, *209* (5), 633–644. https://doi.org/10.1083/jcb.201409074.

(285) Leduc, C.; Si, S.; Gautier, J.; Soto-Ribeiro, M.; Wehrle-Haller, B.; Gautreau, A.; Giannone, G.; Cognet, L.; Lounis, B. A Highly Specific Gold Nanoprobe for Live-Cell Single-Molecule Imaging. *Nano Lett.* **2013**, *13* (4), 1489–1494. https://doi.org/10.1021/nl304561g.

(286) van der Heide, S.; Russell, D. A. Optimisation of Immuno-Gold Nanoparticle Complexes for Antigen Detection. *J. Colloid Interface Sci.* **2016**, *471*, 127–135. https://doi.org/10.1016/j.jcis.2016.03.001.

(287) Kanda, T.; Sullivan, K. F.; Wahl, G. M. Histone–GFP Fusion Protein Enables Sensitive Analysis of Chromosome Dynamics in Living Mammalian Cells. *Curr. Biol.* **1998**, *8* (7), 377–385. https://doi.org/10.1016/S0960-9822(98)70156-3.

(288) Kimura, H.; Cook, P. R. Kinetics of Core Histones in Living Human Cells: Little Exchange of H3 and H4 and Some Rapid Exchange of H2B. *J. Cell Biol.* **2001**, *153*, 13.

(289) Hebbrecht, T.; Liu, J.; Zwaenepoel, O.; Boddin, G.; Van Leene, C.; Decoene, K.; Madder, A.; Braeckmans, K.; Gettemans, J. Nanobody Click Chemistry for Convenient Site-Specific Fluorescent Labelling, Single Step Immunocytochemistry and Delivery into Living Cells by Photoporation and Live Cell Imaging. *New Biotechnol.* **2020**, *59*, 33–43. https://doi.org/10.1016/j.nbt.2020.05.004.

(290) Doh, J. K.; White, J. D.; Zane, H. K.; Chang, Y. H.; López, C. S.; Enns, C. A.; Beatty, K. E. VIPER Is a Genetically Encoded Peptide Tag for Fluorescence and Electron Microscopy. *Proc. Natl. Acad. Sci.* **2018**, *115* (51), 12961–12966. https://doi.org/10.1073/pnas.1808626115.

(291) Baake, M. Core Histones and Linker Histones Are Imported into the Nucleus by Different Pathways. *Eur. J. Cell Biol.* **2001**, *80* (11), 669–677. https://doi.org/10.1078/0171-9335-00208.

(292) Padavannil, A.; Sarkar, P.; Kim, S. J.; Cagatay, T.; Jiou, J.; Brautigam, C. A.; Tomchick, D. R.; Sali, A.; D'Arcy, S.; Chook, Y. M. Importin-9 Wraps around the H2A-H2B Core to Act as Nuclear Importer and Histone Chaperone. *eLife* **2019**, *8*, e43630. https://doi.org/10.7554/eLife.43630.

(293) Keck, K. M.; Pemberton, L. F. Histone Chaperones Link Histone Nuclear Import and Chromatin Assembly. *Biochim. Biophys. Acta BBA - Gene Regul. Mech.* **2012**, *1819* (3–4), 277–289. https://doi.org/10.1016/j.bbagrm.2011.09.007.

(294) Arregi, I.; Falces, J.; Bañuelos, S.; Urbaneja, M. A.; Taneva, S. G. The Nuclear Transport Machinery Recognizes Nucleoplasmin–Histone Complexes. *Biochemistry* **2011**, *50* (33), 7104–7110. https://doi.org/10.1021/bi2008867.

(295) Rigort, A.; Bauerlein, F. J. B.; Villa, E.; Eibauer, M.; Laugks, T.; Baumeister, W.; Plitzko, J. M. Focused Ion Beam Micromachining of Eukaryotic Cells for Cryoelectron Tomography. *Proc Natl Acad Sci USA* **2012**, *109* (12), 4449–4454. https://doi.org/10.1073/pnas.1201333109.

(296) Groysbeck, N.; Stoessel, A.; Donzeau, M.; da Silva, E. C.; Lehmann, M.; Strub, J.-M.; Cianferani, S.; Dembélé, K.; Zuber, G. Synthesis and Biological Evaluation of 2.4 Nm Thiolate-Protected Gold Nanoparticles Conjugated to Cetuximab for Targeting Glioblastoma Cancer Cells via the EGFR. *Nanotechnology* **2019**, *30* (18), 184005. https://doi.org/10.1088/1361-6528/aaff0a.

Résumé de thèse français

Conception et synthèse de conjugués de type anticorps-particules d'or pour un marquage à haute résolution de cibles moléculaires du vivant

Introduction

La microscopie électronique (ME) donne la possibilité d'obtenir des images de cellules et tissues à très haute résolution.[116] L'immuno-marquage à l'or permet en outre de localiser une protéine sélectionnée et de mieux connaître l'organisation ultrastructurale d'échantillon biologique.[92] Pour des spécimens denses, constitués d'une quantité importante d'éléments divers, une coloration ou un marquage sélectif d'éléments particuliers contribuent aussi grandement à l'interprétation des images et à discerner les éléments individuels et en faibles concentrations par rapport aux filaments et autres superstructures. L'opacité des nanoparticules d'or (AuNPs) par rapport aux composés organiques s'est révélée utile à cet effet après conjugaison à des anticorps. Ces sondes de AuNP-anticorps sont classiquement composées d'AuNP de 5 à 15 nm, auxquels les anticorps sont liés par adsorption.[97] Ces sondes sont encore couramment utilisées mais les étapes de préparation des échantillons pour la ME (fixation, coupe, coloration) dénaturent les échantillons. Or, au cours des dernières années, les microscopes électroniques pour une observation en condition cryogénique, les méthodologies de préparation des échantillons biologiques et les procédures de traitements d'images, permettent une amélioration extraordinaire des images du vivant à des résolutions au sub-nanomètre. La cryo-microscopie électronique (cryo -ME) et l'ensemble des procédures permettent ainsi de révéler les structures secondaires de larges protéines ou de leurs assemblages lorsque les épaisseurs de l'échantillon demeurent fines. Des méthodes de coupe de cellules en conditions cryogéniques ont aussi été mises au point et au terme d'un processus de très haut vol, des images de l'intérieur du cytosol de cellules à haute résolution ont été obtenues.[295] Une étape suivante serait de détecter des protéines à l'intérieur du noyau avec un marquage sélectif. Le point d'achoppement est que les sondes actuelles d'immunomarquage ne sont pas compatibles avec des processus de préparation des échantillons non dénaturants. D'abord, la membrane plasmique est imperméable à ces sondes et empêche leurs entrées. Des

détergents permettent de ménager des trous dans la membrane plasmique pour une entrée de sondes. Malheureusement, le coût est important en termes de dénaturation du spécimen. Ensuite, la taille des sondes diminue fortement leurs diffusions dans les tissues. Enfin, leurs conceptions ne permettent pas une localisation spatiale très précise de leurs cibles. Pour améliorer les technologies d'immunomarquage et éviter une dénaturation chimique des échantillons, Orlov *et al*. ont utilisé des AuNPs de 0.8 nm conjugués à un anticorps anti RNA polymérase II et une méthode de transfection pour les faire rentrer dans des cellules vivantes.[127] Des images prometteuses ont été obtenues par FIB/STEM. Toutefois, la qualité des sondes et l'efficacité de transfection sont variables d'une cellule à l'autre ne permettent pas d'envisager avec sérénité l'emploi de cette méthode pour la cryo-ME. D'abord, les particules de 0.8 nm ne fournissent pas suffisamment de contraste pour le faisceau d'électrons, car elle repose sur une amplification de taille des AuNP à l'argent. L'objectif principal de mes recherches doctorales a été de travailler la conception des sondes de ME compatibles avec la cryo-fixation non dénaturante, ce qui nécessite aussi leur transfert à l'intérieur de cellules vivantes.

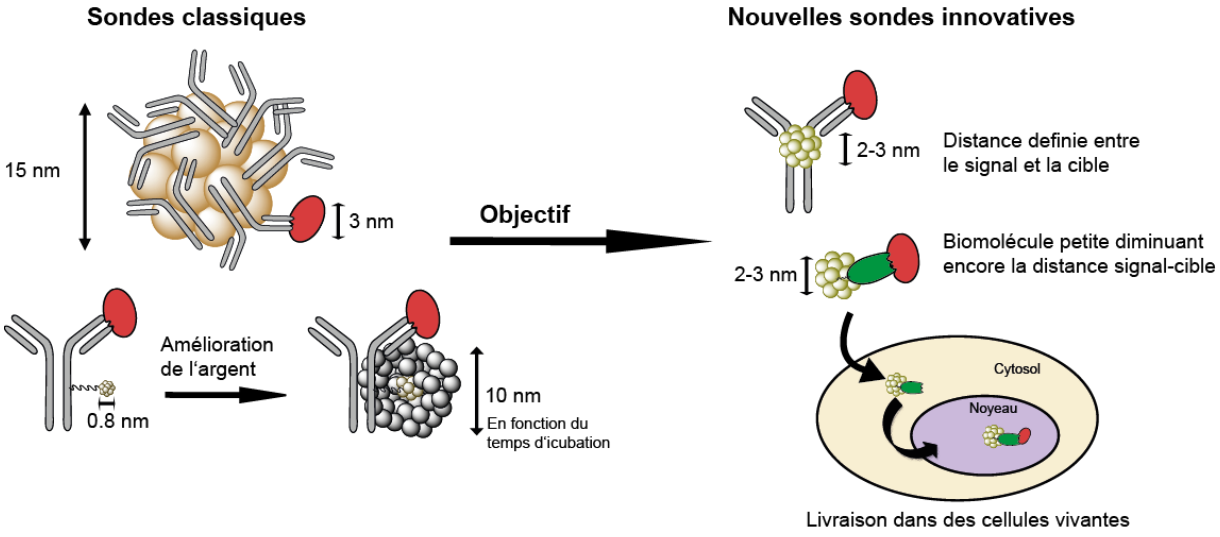

Figure 1. Illustration de l'objectif principal de mes recherches doctorales. À gauche : schéma montrant les propriétés physicochimiques des sondes anticorps-particules d'or actuels et leurs limitations. A droite : proposition pour des nouvelles sondes composées d'AuNP de 1.4 à 2.6 nm conjuguées à un anticorps ou à un nanobody pour diminuer la distance entre la cible et le signal et augmenter la biocompatibilité.

Pour mettre en œuvre cette ambition, nous avons décomposé notre programme de thèse en 3 parties. La première partie était de concevoir des AuNPs faciles à fonctionnaliser, qui sont d'une part, suffisamment grandes pour faciliter une visualisation directe plus aisée à l'intérieur de coupes tissulaires, d'autre part, suffisamment petites pour permettre une diffusion libre à l'intérieur de cellules vivantes qui sont riches en polymères. La deuxième partie était d'établir une conjugaison d'une AuNP sélectivement au niveau de la région charnière d'un anticorps. La

troisième partie était de développer un protocole de conjugaison pour coupler les AuNPs à des nanobodies, qui sont des biomolécules de ciblage plus petites que les anticorps dans l'idée d'améliorer les caractéristiques de diffusion et la localisation spatiale des cibles dans l'échantillon. Dans chacune de ces trois parties du projet, nous avons évalué si les AuNPs/bioconjugués peuvent être transférés dans des cellules vivantes sans les tuées et si leurs propriétés physico-chimiques leur permettent de se diffuser dans l'environnement encombré de cellules vivantes. La Figure 1 illustre l'objectif de cette thèse.

Résultats et discussion

1. Conception synthèse et caractérisation de particules d'or de tailles homogènes, soluble dans l'eau et réactives avec des biomolécules thiolées

Notre objectif était de concevoir des AuNPs de tailles homogènes, solubles dans l'eau et faciles à fonctionnaliser avec des biomolécules thiolées. En nous fondant sur les travaux d'Ackerson[182] et Kornberg,[7] nous avons mis au point la synthèse de nouvelles particules d'or qui sont originales par leurs ligands de surface. La synthèse des AuNPs a été réalisée par une réduction d'un sel d'or ($HAuCl_4$) à l'aide de $NaBH_4$ en présence d'acide dithionitrobenzoïque (DTNB). À la fin de réaction, la DTNB se transforme en thionitrobenzoate (TNB) et thioaminobenzoate (TAB). Ces ligands recouvrent la particule d'or par liaison de coordination Au-S stable mais échangeable avec des thiols exogènes. En modifiant les conditions réactionnelles et notamment le solvant, nous avons mis en place des protocoles pour produire des AuNPs avec des diamètres de 1.4 nm, 2.4 nm et 2.6 nm. La caractérisation des nanoparticules a été effectuée avec les méthodes d'analyse suivantes : électrophorèse sur gel de polyacrylamide en présence de dodecylsulfate de sodium (SDS-PAGE), spectroscopie UV/Visible, spectrométrie de masse et microscopie électronique à transmission. Les analyses montrent clairement que chaque particule a une taille très bien définie. La Figure 2 montre la caractérisation des trois AuNPs par SDS-PAGE, UV-Vis, spectrométrie de masse et microscopie électronique à transmission.

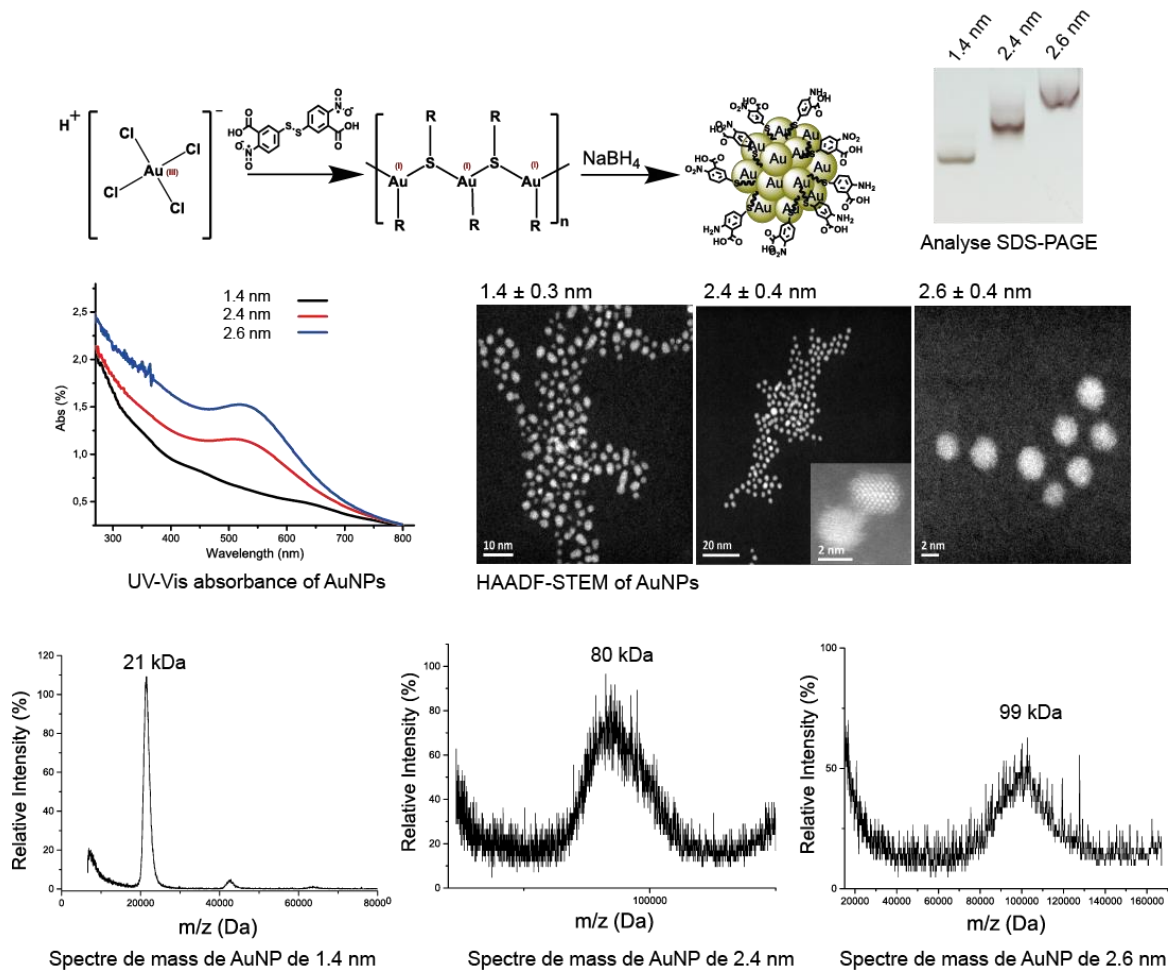

Figure 2. Caractérisation des AuNPs par SDS-PAGE, spectroscopie UV/Visible et microscopie électronique à transmission (high angle annular dark field scanning transmission electron microscopy HAADF-STEM) et spectrométrie de masse.

Les propriétés réactionnelles des AuNPs avec des molécules thiolées dans de l'eau ont été étudiées en utilisant diverses molécules contenant du thiol, telles que la cystéine, le glutathion, des peptides contenant de la cystéine ou un polyéthylène glycol (PEG) thiolé de 2000 Da. L'analyse des réactions par électrophorèse démontre que l'échange des ligands originels de surfaces (TNB et TAB) se produit très bien avec des molécules thiolées exogènes et dans des conditions aqueuses douces. En fonction du rapport molécules thiolées/AuNP et en relation avec la taille initiale de la particule d'or, il est ainsi possible d'obtenir des AuNPs ayant des surfaces fonctionnalisées par des molécules choisies. De plus, nous avons étudié le profil cinétique de l'échange thiolate-thiolate en suivant la libération du TNB dont le coefficient d'absorption à 412 nm est connu et utilisé pour quantifier le thiol libre. Nous avons constaté que l'échange thiolate-thiolate de l'AuNP de 1.4 nm est beaucoup plus rapide que les réactions des plus grosses particules : C'est-à-dire que la surface de l'AuNP de 1.4 nm atteint la saturation

après environ 20 minutes, alors que les réactions d'échange de thiol des AuNPs de 2.4 nm et 2.6 nm ne sont toujours pas terminés après 2 heures.

Nous avons ensuite testé l'influence du revêtement de surface sur le comportement des particules à l'intérieur des cellules vivantes et notamment après réaction avec diverses molécules de passivation, qui bloquent la réactivité des AuNPs aux thiols et modifient les propriétés physicochimiques de surface de la particule. Les particules de tailles différentes et de surfaces variées (glutathione, cysteine, PEG(2000) thiolé, CALNNG) ont été incubées avec des cellules HeLa vivantes puis les cellules ont été soumises à des pulses électriques pour une perméabilisation transitoire des membranes plasmiques. Les cellules vivantes ont ensuite été observées 24h après et les particules d'or détectées par coloration à l'argent. Les résultats montrent que : 1. Les particules enrobées avec du glutathion et de la cystéine accumulent préférentiellement à l'intérieur des vésicules intracellulaires entourant le noyau et ne semblent pas diffuser dans le cytosol; 2. Les particules enrobées avec le PEG de haut poids moléculaire ou le CALNNG diffusent dans toute la cellule sans accumulation préférentielle ; 3. Les AuNP de 2.6 nm enrobées du PEG étaient contrairement aux autres particules majoritairement exclues du noyau. Si la particule de 2.6 nm enrobée du PEG était par ailleurs équipée d'un signal de localisation nucléaire (NLS), les particules étaient localisées exclusivement à l'intérieur du noyau. Il a été observé que le peptide CALNNG n'est un agent de passivation efficace que pour l'AuNP de 1.4 nm. Les AuNPs de 2.4 nm et 2.6 nm demandent une passivation avec du PEG(2000) thiolé pour diffuser dans la cellules. Ces observations montrent ainsi que au-delà de 1.4 nm, une couverture par du PEG(2000) est nécessaire pour empêcher les associations aspécifiques aves les constituants cellulaires (membrane cellulaires et cytosquelette inclus). Enfin, il convient de noter qu'aucune toxicité cellulaire n'a été observée dans les 48 heures après l'électroporation des AuNPs.

2 Synthèse de conjugués anticorps-particules d'or

Nous avons privilégié l'AuNP de 2.4 nm pour une conjugaison à des anticorps car cette taille nous semble offrir le meilleur compris entre opacité aux électrons (contraste en ME) et capacité de diffusion. Pour mettre au point la synthèse de conjugués, nous avons choisi dans un premier temps des anticorps facile à obtenir en grandes quantités. Nous avons aussi choisi comme anticorps modèles deux anticorps thérapeutiques, le Cetuximab (ciblant le récepteur du facteur

de croissance épidermique EGFR) et le Bevacizumab (ciblant le facteur de croissance de l'endothélium vasculaire VEGF), ainsi qu'un anticorps monoclonal le 7G5, ciblant l'ARN polymérase II (RNAP II). Les trois anticorps, qui appartiennent tous à la sous-classe isotypique IgG1, possèdent deux liaisons disulfures dans la région charnière entre le fragment Fab et le fragment Fc. Ces disulfures peuvent être réduit sélectivement en thiols et servir de point d'attache à l'AuNP. La réduction sélective des disulfures de la charnière a été effectuée en condition douce avec du TCEP. Les anticorps réduits ont ensuite été ajoutés à la particule d'or de 2.4 nm pour un échange de quelques ligands de surface. Le reste des ligands a ensuite été neutralisé par passivation avec le CALLNG ou PEG(2000) thiolé. Après ajustement des paramètres (concentrations des différents partenaires, température, pH, tampon de réactions et durée), des conjugués ont été obtenus. L'avancement de la réduction sélective au niveau de la charnière et des réactions ultérieures avec l'AuNP a été facilement suivi par SDS-PAGE, permettant en outre d'évaluer la composition stœchiométrique du conjugué. Pour toutes les réactions, les produits principaux de conjugaison consistaient en un conjugué avec un rapport d'une nanoparticule par IgG. Il convient de noter que les conditions de conjugaison devaient être légèrement modifiées en fonction de chaque anticorps. Notamment, les conditions de réduction devaient être ajustées pour chaque anticorps individuellement, bien que les trois anticorps appartiennent à la même sous-classe, ce qui indique que des changements plus subtils entre les séquences d'anticorps impactent la susceptibilité à la réduction.

La capacité de liaison du AuNP-Cetuximab (Au-Cmab) a ensuite été étudiée sur cellules vivantes exprimant (ou non) l'EGFR. Les résultats montrent que Au-Cmab se comporte de manière très similaire à l'anticorps Cetuximab en termes de capacités de liaison et d'activités, suggérant que la taille et les propriétés physico-chimiques de l'AuNP ne modifient pas de façon importante l'activité et la stabilité de l'anticorps natif. Ces travaux ont déjà été publiés et le manuscrit est joint en annexe (Groysbeck *et al.* 2019).[296] La Figure 3 montre une illustration de la stratégie de conjugaison pour lier l'anticorps Cetuximab à l'AuNP et son analyse par SDS-PAGE. La liaison de Au-Cmab généré à l'EGFR a été évaluée en incubant des cellules vivantes de glioblastome surexprimant l'EGFR et des cellules privées d'expression d'EGFR par silençage de l'ARN si avec Au-Cmab, le conjugué AuNP-Bevacizumab (ciblant le VEGF, contrôle négatif) et Cetuximab (contrôle positif).

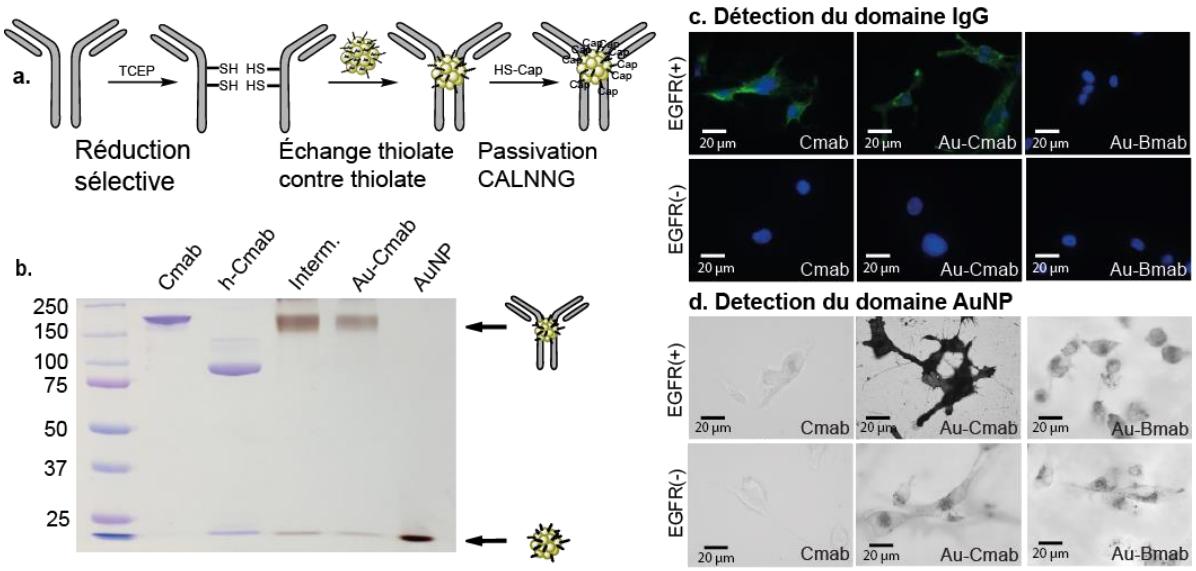

Figure 3. Conjugaison de Cetuximab à l'AuNP de 2.4 nm à la charnière par échange thiolate contre thiolate (a) et la caractérisation par PAGE (b). AuNP visible sous forme de bande brune, bandes de protéines colorées au bleu de Coomassie. La coloration brune de la bande à 150 kDa confirme le succès de la conjugaison à des particules d'or. Evaluation de la liaison de Au-Cmab à l'EGFR en utilisant des cellules vivantes de glioblastome EGFR(+) et des cellules EGFR(-) (c, d). Les cellules ont été incubées avec du Cetuximab (Cmab), AuNP-Cetuximab (Au-Cmab) et AuNP-Bevacizuman (Au-Bmab). La présence de l'Au-Cmab a été déterminée par révélation du domaine IgG (c) et du domaine AuNP (d) par immunofluorescence et coloration des particules d'or avec de l'argent, respectivement. Barre d'échelle : 20 µm

La caractérisation du conjugué AuNP-7G5 (Au-7G5) pour sa capacité à cibler la RNAP II était plus complexe que l'évaluation biologique de Au-Cmab, puisque la RNAP II est localisée à l'intérieur du noyau et nécessite donc le la délivrance cellulaire de Au-7G5 afin de permettre le marquage du complexe multiprotéique dans les cellules vivantes.

Dans une première étape, nous avons testé la capacité du conjugué Au-7G5 passivé avec CALNNG à se lier à la RNAP II en utilisant des cellules fixes et perméabilisées. Bien que nos données aient clairement montré une localisation nucléaire pour le conjugué, une quantité importante de liaison aspécifique à des constituants du cytosol a été observée. Nous avons émis l'hypothèse que la liaison non spécifique observée de Au-7G5 pourrait être entraînée par le revêtement de surface de l'AuNP, qui a été passivé avec CALNNG, puisque nous avons déjà observé lors de l'électroporation de l'AuNP de 2.4 nm que les propriétés stabilisantes du peptide CALNNG sont idéales pour le AuNP de 1.4 nm, mais pas pour le AuNP de 2.4 nm. Dans le cas de Au-Cmab, qui était également passivé avec le peptide CALNNG, nous n'avons pas observé ce degré significatif de marquage non spécifique, mais dans ce cas, la cible était un récepteur extracellulaire et lors de l'étude de liaison à l'EGFR, les membranes plasmiques cellulaires étaient intactes (vivant) et donc le conjugué ne pouvait pas interagir avec les divers composants de l'intérieur des cellules. Pour tester cette hypothèse nous avons resynthétisé le conjugué de

ciblage RNAP II et passivé le domaine AuNP avec PEG. L'étude de liaison de cet 7G5-AuG-PEG sur des cellules fixées et perméabilisées a clairement démontré que le nouveau conjugué Au-7G5-PEG se lie spécifiquement à la RNAP II avec peu de liaisons aspécifiques.

Ensuite, nous voulions évaluer si le conjugué Au-7G5-PEG se lie également à sa cible nucléaire à l'intérieur des cellules vivantes. Par conséquent, nous avons livré le conjugué dans des cellules vivantes en utilisant l'électroporation, comme cela a été effectué pour les AuNPs passivés décrits dans la section précédente. La localisation des AuNPs a été observée 24 h après l'électroporation et les données enregistrées correspondaient à celles de l'étude de liaison utilisant des cellules fixes, démontrant que Au-7G5-PEG est capable de se lier à sa cible nucléaire RNAP II à l'intérieur des cellules vivantes après transduction (Figure 4).

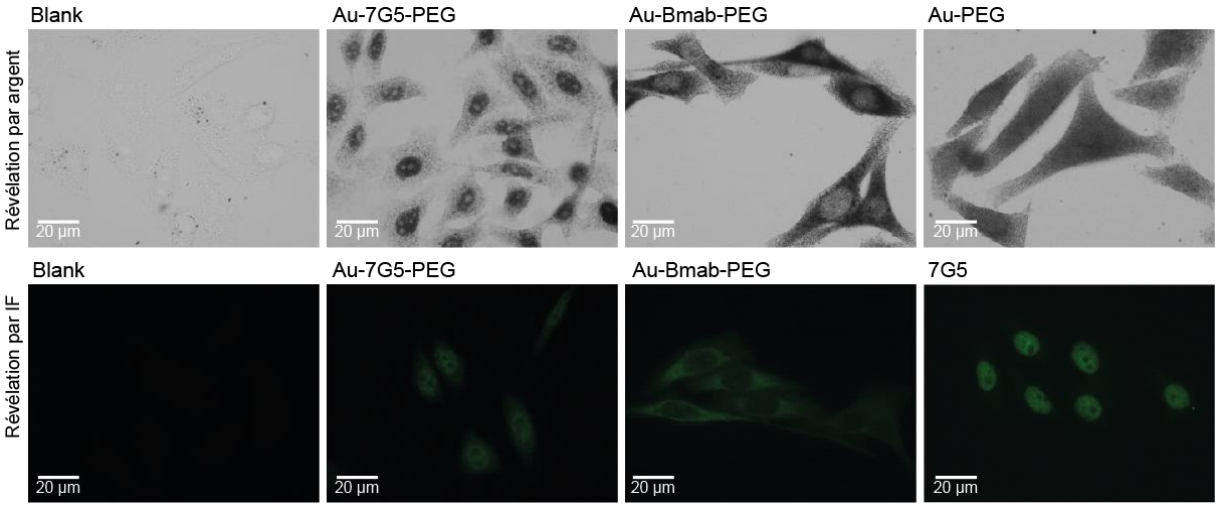

Figure 4. Electroporation de Au-7G5-PEG, Au-Bmab-PEG, AuNPs de 2.4 nm fonctionnalisés avec du PEG (Au-PEG) et anticorps anti-RNAP II (7G5) dans des cellules HeLa vivantes. La localisation des espèces électroporées à l'intérieur des cellules a été révélée par coloration à l'argent, ainsi que par immunofluorescence (IF). Le blanc correspond aux cellules non électroporées. Barre d'échelle: 20 µm.

En tant que contrôle, nous avons également électroporé le conjugué AuNP-Bevacizumab (Au-Bmab-PEG), les AuNPs de 2.4 nm non conjugués et passivés avec PEG (Au-PEG) et l'anticorps 7G5. Alors que Au-7G5-PEG montre clairement un marquage nucléaire typique de celui des RNAP II, le conjugué témoin Au-Bmab-PEG est exclu du noyau et les AuNPs passivés avec PEG sont comme décrit précédemment répartis de manière homogène à l'intérieur des cellules. Etant donné que le complexe de pores nucléaires limite la diffusion passive dans le noyau à des molécules ayant un poids moléculaire inférieur à 60 kDa, les anticorps et par conséquent les anticorps conjugués aux AuNPs ne diffusent pas passivement dans le noyau. Pourtant, comme nous avons observé un marquage spécifique de RNAP II nucléaire après l'électroporation de Au-7G5, nous avons supposé que le conjugué électroporé se lie à RNAP II nouvellement traduit, qui doit voyager des ribosomes (cytoplasme) dans le noyau, et que le conjugué lié à

l'antigène est donc transporté dans le noyau. Ce processus hypothétique connu sous le nom « piggybacking » a déjà été décrit pour les anticorps anti-RNAP II livrés dans les cellules vivantes.[181]

3. Bioconjugaison d'un nanobody à la particule d'or et mis en place d'un protocole d'immunomarquage pour une observation par ME.

Dans un autre registre, nous avons cherché à minimiser la taille globale du bioconjugué anticorps-AuNP et à réduire la distance entre l'AuNP et la protéine ciblée en choisissant un nanobody (15 kDa) au lieu de l'anticorps total (150 kDa), afin d'améliorer la résolution spatiale, ainsi que la capacité de diffusion du conjugué. Nous avons sélectionné un nanobody anti-GFP dont l'excellente association avec la GFP a été déterminée et la structure du complexe déterminé.[271] Pour relier le nanobody à l'AuNP, nous avons poursuivi deux stratégies différentes. La première approche était basée sur la création d'une liaison Au-S directe entre le nanobody thiol modifié et l'AuNP par échange de thiolate-thiolate, ce qui entraînait une distance très proche entre la particule et le nanobody. La deuxième approche impliquait l'addition d'étiquettes sur la particule d'or et sur le nanobody pour une association forte et non covalente des deux éléments par assemblage. La raison de s'attaquer à ces deux stratégies était d'étudier si les différentes approches conduisent à des différences dans la fonction biologique du bioconjugué. Après synthèse et purification de conjugués, qui sont toujours analysables par SDS-PAGE, nous avons testé la capacité de liaison des conjugués à la GFP avec des méthodes classiques de type ELISA ou immunocytochimiques avec des lignes cellulaires exprimant des protéines en fusion avec de la GFP. Les résultats démontraient que la conjugaison directe du nanobody à l'AuNP est plus difficile à réaliser, que la conjugaison directe avec des anticorps. Une diminution importante de la sélectivité et affinité de liaison du conjugué AuNP-nanobody à la GFP par rapport au nanobody seul a été observée. Cette diminution est probablement due à des altérations structurelles du nanobody suite à la proximité étroite entre l'AuNP et la biomolécule. La formation de sondes *via* des étiquettes de liaison non covalentes s'est avérée beaucoup plus facile et plus neutre vis à vis de la liaison du domaine nanobody à sa cible. La Figure 5 montre la liaison des deux conjugués aux cellules HeLa exprimant, ou non exprimant la protéine histone H2B fusionnée à la GFP (conjugaison direct : Au-C7nabo, conjugaison *via* des étiquettes peptidiques : Au-*bind*-nabo), ainsi que des tests d'ELISA utilisant de la GFP purifié.

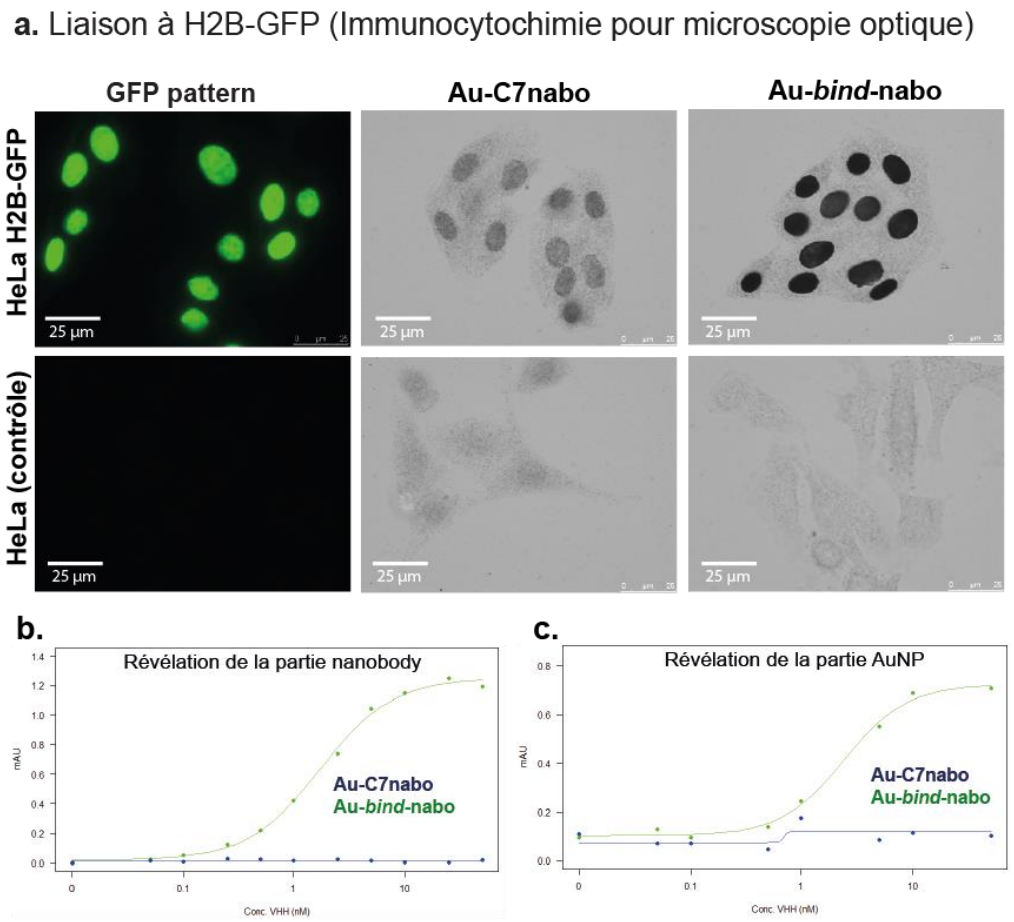

Figure 5. Étude de liaison à la GFP des bioconjugués AuNP-nanobody généré *via* échange thiolate contre thiolate (Au-C7nabo) et via l'emploi des étiquettes peptidiques (Au-*bind*-nabo). (a) Immunocytochimie utilisant des cellules HeLa exprimant ou non exprimant la protéine nucléaire H2B-GFP. (b) Test d'ELISA pour comparer l'affinité des deux bioconjugués (gauche : révélation de la partie nanobody avec IgG secondaires couplé à HRP, droite : révélation de l'or par coloration d'argent). Barre d'échelle : 25 µm

L'utilité du conjugué Au-*bind*-nabo comme sonde pour la localisation de protéines fusionnées avec la GFP a ensuite été évaluée pour différentes protéines fusionnées avec la GFP qui ont été transitoirement exprimées dans les cellules HeLa. Pour le moment, la sonde s'est montrée efficace pour localiser la GFP fusionnée à la protéine histone H2B (cible nucléaire homogène), la GFP-β-galactosidase (cible cytosolique homogène), et la GFP-PCNA, une cible nucléaire directement impliqués dans la réplication et réparation de l'ADN.

Avant de procéder à la livraison cellulaire du bioconjugué pour réaliser un marquage dans les cellules vivantes, nous avons souhaité clarifier si le conjugué Au-*bind*-nabo peut être utilisé comme sonde pour l'immunomarquage classique en ME en utilisant des cellules fixes. Ici, nous utilisons dans un premier temps la ME non cryogénique de type classique dans une expérience de pré-inclusion avec des cellules Hela exprimant H2B-GFP. Étant donné que l'AuNP est directement liée à la molécule de ciblage, ce nouveau protocole d'immunomarquage ne contient

qu'une seule étape de marquage, réduisant ainsi le temps de travail. Pour une première observation des échantillons avec un microscope électronique conventionnel, les AuNPs ont été agrandis par amélioration d'argent pour permettre leur détection (Figure 6). Les images de ME obtenues ont confirmé la liaison sélective du conjugué à la GFP et ont démontré que la sonde est applicable à l'immunomarquage dans un cadre de pré-inclusion.

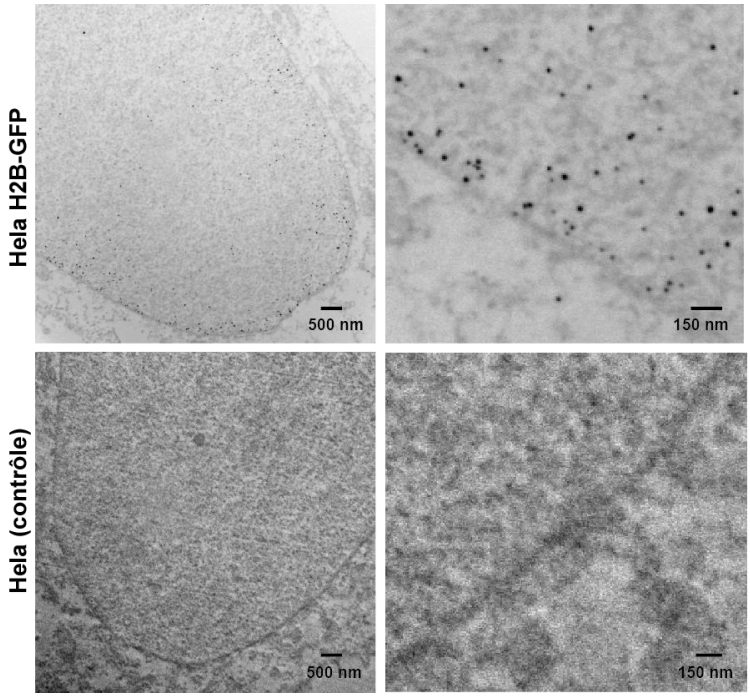

Figure 6. Immunomarquage des cellules HeLa exprimant la protéine histone H2B-GFP (HeLa H2B-GFP) et HeLa (côtrole) avec le conjugué AuNP-nanobody (Au-*bind*-nabo). Les AuNPs (facilement reconnaissable sous forme de points noirs à fort grossissement) sont localisé exclusivement dans le noyau et marquent la protéine H2B-GFP. Barres d'Echelles (images à gauche) : 500 nm, barres d'echelles : (images à droite) : 150 nm.

Sur la base de ces résultats et pour évaluer en outre si les AuNPs de 2.4 nm intégrées dans l'ultrastructure cellulaire peuvent être directement détectées par HAADF-STEM, nous avons préparé les mêmes échantillons qui n'ont pas été colorés à l'argent. Les analyses EDX montrent clairement que les spécimens contiennent des particules d'or. Néanmoins, nous n'avons pas encore été en en mesure de détecter directement des particules d'or de 2.4 nm individuelles. It faut avouer que l'observation de ces particules dans une coupe biologique avec très peu d'agent de contraste est extrêmement challenging même avec le HAADF-STEM

Enfin, la capacité de sondage du conjugué anti-GFP Au-*bind*-nabo a été étudiée pour les cibles intracellulaires dans des cellules vivantes, afin de rendre la sonde compatible avec le flux de travail de la cryo-ME. Comme modèle, nous avons de nouveau utilisé la lignée cellulaire HeLa stable exprimant l'histone H2B fusionnée à la GFP, exigeant ainsi que le conjugué diffuse ou

soit transporté par un mécanisme de « piggybacking » dans le noyau pour permettre le marquage sélectif de la cible. Pour la livraison cellulaire, nous avons utilisé le même protocole d'électroporation qui a permis la transduction des conjugués AuNPs passivées et AuNP-anticorps dans les cellules HeLa. L'observation au microscope des cellules électroporées a révélé que le conjugué Au-*bind*-nabo se retrouvent bien à l'intérieur de cellules HeLa H2B-GFP, mais que la sonde ne diffuse pas passivement dans le noyau. Ces résultats indiquent une fois de plus que Au-*bind*-nabo ne présente pas les propriétés de pénétration et de diffusion bénéfiques attendues pour le bioconjugué.

Afin d'analyser l'impact de la taille des sondes sur leur devenir intracellulaire, nous avons synthétisé le conjugué Au-*bind*-nabo ciblant la GFP en utilisant les particules d'or de 1.4 nm. Ensuite nous avons électroporé le nouveau conjugué de plus petite taille dans les cellules HeLa H2B-GFP. Comme contrôle, nous avons utilisé les AuNPs de 1.4 nm, qui sont fonctionnalisés avec l'étiquette peptidique *bi* et passivés avec du PEG (Au-PEG-*bi*), ainsi qu'un nanobody control (HER-Au-*bind*-nabo). Les images de microscopie optique des cellules électroporées sont représentées sur la Figure 7. Comme attendu, tous les AuNPs/bioconjugués de 1.4 nm diffusait passivement dans le noyau, mais uniquement le 1.4 nm GFP-Au-*bind*-nabo se liait spécifiquement à la protéine histone H2B-GFP.

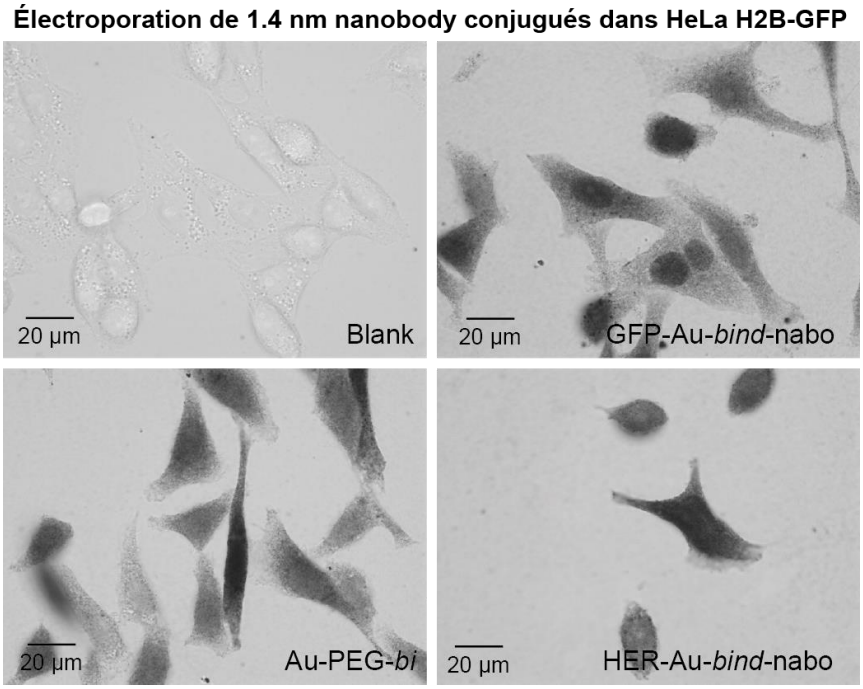

Figure 7. Transduction de 1.4 nm conjugué ciblant GFP (GFP-Au-*bind*-nabo), 1.4 nm conjugué ciblant HER2/neu (HER-Au-*bind*-nabo) et des AuNPs de 1.4 nm fonctionnalisés avec *bi* tag et PEG (Au-PEG-*bi*) dans des cellules HeLa H2B-GFP. Les cellules électroporées ont été cultivées pendant 15 h puis traitées pour la coloration à l'argent et l'observation au microscope optique. Le blanc représente les cellules qui n'ont pas été électroporées. Barre d'échelle : 20 µm.

Pris ensemble, les données obtenues ont révélé que ce type de conjugué Au-*bind*-nabo est stable à l'intérieur des cellules vivantes et si le conjugué est suffisamment petit, il se diffuse dans le noyau et est capable de cibler l'histone H2B marquée par la GFP. Le fait que le conjugué de 2.4 nm ne soit pas capable de se diffuser passivement dans le noyau ou d'être délivré dans le noyau par un mécanisme de « piggybacking » était malheureux et devrait être étudié dans de futures études.

Conclusion générale et perspectives

L'objectif de ce projet était de développer des sondes innovantes pour la ME de spécimens cellulaires permettant le marquage de protéines sélectionnées dans leur contexte natif (cellules vivantes) avec une résolution spatiale accrue, par rapport aux agents de l'immunomarquage à l'or classiques, qui semblent dépassés par rapport au progrès des microscopes électroniques et des procédures de préparation des échantillons. Pour atteindre cet objectif, nous avons développé des AuNPs qui facilitent grandement la préparation de conjugués avec des anticorps et des anticorps recombinants de taille réduite (nanobodies). Nous avons ensuite ajusté la synthèse de conjugués anticorp-AuNP/nanobody-AuNP et travaillé le recouvrement de surface des particules d'or pour minimiser les associations non-spécifiques. Les propriétés de certains conjugués démontrent un bénéfice par rapport aux sondes existantes en termes de stabilité physicochimique et surtout de faciliter d'analyse grâce à leurs mobilités électrophorétiques. Les premières évaluations de ces conjugués comme sondes de microscopie optique montrent que les sondes ont des capacités indéniables pour de l'immunomarquage à l'or. Les images de microscopie électronique à basse résolution sont prometteuses, en attendant des observations plus pointues. De même, les AuNPs montrent une capacité à diffuser dans une cellule vivante après électroporation, indiquant que ces sondes pourraient se lier à leurs cibles avant cryo-fixation. En particulier, les conjugués AuNP-anticorp générés semblent très prometteurs en tant que sondes de cryo-ME, puisque nous avons réalisé le marquage des protéines nucléaires à l'intérieur des cellules vivantes en utilisant un conjugué comprenant l'AuNP de 2.4 nm, qui fournit probablement suffisamment d'opacité aux électrons pour être discernable des composants organiques de la cellule à l'aide de nouveaux cryo-microscopes électroniques. Actuellement, le bioconjugué à base du nanobody synthétisé à partir de l'AuNP de 1.4 nm, qui

diffuse passivement dans le noyau après la délivrance cellulaire, ne répond pas aux exigences des études cryo-ME, à cause de la résolution actuelle des microscopes électroniques adaptés pour les échantillons biologiques. Pourtant, les progrès constants dans le développement des détecteurs de ME et des procédures de préparation d'échantillons pourraient permettre l'utilisation de cette sonde de petite taille à l'avenir, ce qui serait encore plus avantageux que le conjugué d'anticorps mentionné ci-dessus, en raison de sa capacité à diffuser à travers tout le volume cellulaire. Enfin, l'ensemble de ces données tangibles apportent de l'intérêt de ces AuNPs et bioconjugués pour des applications comme sonde d'immunomarquage à l'or mais aussi pour étudier et moduler le vivant, ouvrant ainsi de perspectives d'applications et de collaborations prometteuses.

Références

(1) Parton, R. G. Twenty Years of Traffic: A 2020 Vision of Cellular Electron Microscopy. Traffic 2020, 21 (1), 156–161. https://doi.org/10.1111/tra.12684.

(2) Polishchuk, E. V.; Polishchuk, R. S. Pre-Embedding Labeling for Subcellular Detection of Molecules with Electron Microscopy. Tissue and Cell 2019, 57, 103–110. https://doi.org/10.1016/j.tice.2018.11.002.

(3) Faulk, W Page; Taylor, G Malcom. An Immunocolloid Method for the Electron Microscope. Immunocytochemistry 1971, 1081–1083.

(4) Rigort, A.; Bauerlein, F. J. B.; Villa, E.; Eibauer, M.; Laugks, T.; Baumeister, W.; Plitzko, J. M. Focused Ion Beam Micromachining of Eukaryotic Cells for Cryoelectron Tomography. Proc. Natl. Acad. Sci. USA 2012, 109 (12), 4449–4454. https://doi.org/10.1073/pnas.1201333109.

(5) Orlov, I.; Schertel, A.; Zuber, G.; Klaholz, B.; Drillien, R.; Weiss, E.; Schultz, P.; Spehner, D. Live Cell Immunogold Labelling of RNA Polymerase II. Sci Rep 2015, 5 (1), 8324. https://doi.org/10.1038/srep08324.

(6) Ackerson, C. J.; Jadzinsky, P. D.; Sexton, J. Z.; Bushnell, D. A.; Kornberg, R. D. Synthesis and Bioconjugation of 2 and 3 Nm-Diameter Gold Nanoparticles. Bioconjugate Chem. 2010, 21 (2), 214–218. https://doi.org/10.1021/bc900135d.

(7) Levi-Kalisman, Y.; Jadzinsky, P. D.; Kalisman, N.; Tsunoyama, H.; Tsukuda, T.; Bushnell, D. A.; Kornberg, R. D. Synthesis and Characterization of Au 102 (p -MBA) 44 Nanoparticles. J. Am. Chem. Soc. 2011, 133 (9), 2976–2982. https://doi.org/10.1021/ja109131w.

(8) Groysbeck, N.; Stoessel, A.; Donzeau, M.; da Silva, E. C.; Lehmann, M.; Strub, J.-M.; Cianferani, S.; Dembélé, K.; Zuber, G. Synthesis and Biological Evaluation of 2.4 Nm Thiolate-Protected Gold Nanoparticles Conjugated to Cetuximab for Targeting Glioblastoma Cancer Cells via the EGFR. Nanotechnology 2019, 30 (18), 184005. https://doi.org/10.1088/1361-6528/aaff0a.

(9) Freund, G.; Sibler, A.-P.; Desplancq, D.; Oulad-Abdelghani, M.; Vigneron, M.; Gannon, J.; Van Regenmortel, M. H.; Weiss, E. Targeting Endogenous Nuclear Antigens by Electrotransfer of Monoclonal Antibodies in Living Cells. mAbs 2013, 5 (4), 518–522. https://doi.org/10.4161/mabs.25084.

(10) Kubala, M. H.; Kovtun, O.; Alexandrov, K.; Collins, B. M. Structural and Thermodynamic Analysis of the GFP:GFP-Nanobody Complex. Protein Sci. 2010, 19 (12), 2389–2401. https://doi.org/10.1002/pro.519.

Supporting Information

Additional Figures

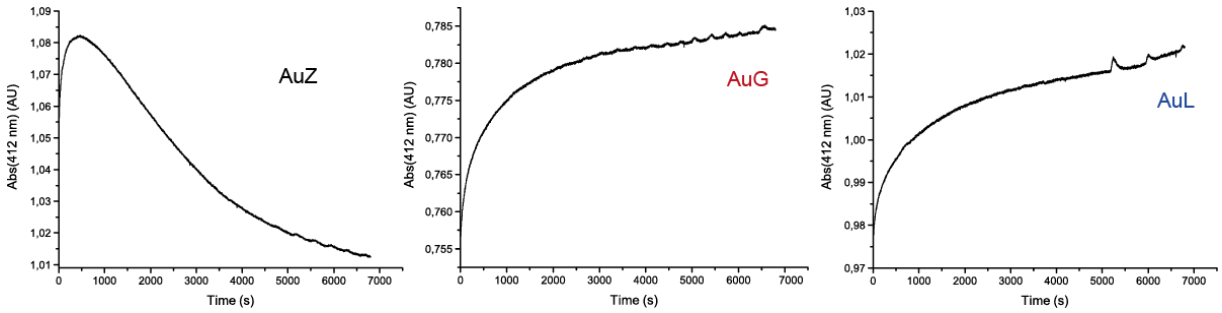

Figure 64. Investigation of thiolate-for-thiolate exchange kinetics of AuZ, AuG and AuL upon addition of excess Cap peptide. The three spectra A(AuZ on the left, AuG in the middle, AuL on the right) show the absorbance at 412 nm (max absorbance of TNB) as a function of time. The maximum absorbance of AuZ is 1.08, the maximum absorbance of AuG is 0.78 and the maximum absorbance of AuL is 1.02, which permit the calculation of the number of moles of released TNB.

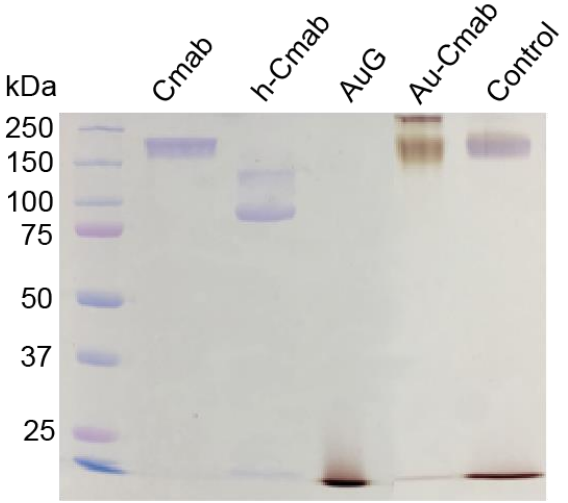

Figure 65. SDS-PAGE analysis to demonstrate that AuG was site-specifically linked to the hinge thiols of reduced Cmab and not simple adsorbed to the non-reduced antibody. Order on the gel from left to right: Cetuximab (Cmab), selectively reduced Cmab (h-Cmab), 2.4 nm AuNP (AuG), conjugation product of AuG and h-Cmab (Au-Cmab), mixture of AuG and intact, non-reduced Cmab (Control). Note that band at 150 kDa in lane of Control is not brown (no reaction with AuG).

a. anti-GFP nanobody DNA sequence which was mutated to C7nabo and CtCnabo

ATGCAGGTTCAACTGGTGGAAAGCGGCGGTGCTCTGGTACAACCGGGCGGTAGTCTGCGCCTG
AGCTGTGCCGCAAGCGGTTTCCCAGTCAACCGCTACTCTATGCGTTGGTATCGCCAGGCGCCTG
GTAAAGAACGTGAATGGGTTGCCGGCATGAGCAGTGCGGGCGATCGTTCTAGTTACGAGGACTC
TGTTAAAGGTCGTTTTACAATTAGCCGTGATGATGCGCGCAATACCGTGTATCTGCAAATGAACA
GTCTGAAGCCGGAGGACACCGCAGTATATTATTGCAATGTCAACGTGGGGTTTGAATATTGGGGC
CAGGGGACTCAGGTGACGGTGAGCTCTAAACATCACCATCACCATCAC

Corresponding amino acid sequence (before mutation to C7nabo and CtCnabo)

MQVQLVESGGALVQPGGSLRLSCAASGFPVNRYSMRWYRQAPGKEREWVAGMSSAGDRSSYEDS
VKGRFTISRDDARNTVYLQMNSLKPEDTAVYYCNVNVGFEYWGQGTQVTVSSKHHHHHH

b. anti-GFP nanobody sequence fused to *nd* tag (*nd*-nabo)

ATGGGGTCCCAGGTTCAGCTGGTTGAAAGTGGTGGTGCACTGGTACAACCGGGCGGTAGTCTGC
GCCTGAGCTGTGCCGCAAGCGGTTTCCCAGTCAACCGCTACTCTATGCGTTGGTATCGCCAGGC
GCCTGGTAAAGAACGTGAATGGGTTGCCGGCATGAGCAGTGCGGGCGATCGTTCTAGTTACGAG
GACTCTGTTAAAGGTCGTTTTACAATTAGCCGTGATGATGCGCGCAATACCGTGTATCTGCAAAT
GAACAGTCTGAAGCCGGAGGACACCGCAGTATATTATTGCAATGTCAACGTGGGGTTTGAATATT
GGGGCCAGGGGACCCAGGTCACCGTCTCCTCAGCGGCCGCAACTAGTGAACAAAAACTCATCTC
AGAAGAGGATCTGAATGCTAGCACGCCACTGGGTGACACGACTCATACCAGCGGTAACAACACC
AGCTCCTCTCCCCAGCCAAAGAAGAAACCACTGGATGGAGAATATTTCACCCTTCAGATCCGTGG
GCGTGAGCGCTTCGAGATGTTCCGAGAGCTGAATGAGGCCTTGGAACTCGAGGATGCCCAGGCT
GGGAAGGAGCCAGGGGGTTCAGGCGGAGCTCCACATCACCATCATCACCAT

Corresponding amino acid sequence (*nd*-nabo)

MGSQVQLVESGGALVQPGGSLRLSCAASGFPVNRYSMRWYRQAPGKEREWVAGMSSAGDRSSYE
DSVKGRFTISRDDARNTVYLQMNSLKPEDTAVYYCNVNVGFEYWGQGTQVTVSSAAATSEQKLISEE
DLNASTPLGDTTHTSGNNTSSSPQPKKKPLDGEYFTLQIRGRERFEMFRELNEALELEDAQAGKEPG
GSGGAPHHHHHH

Figure 66. DNA and corresponding amino acid sequence of anti-GFP nanobody before mutation to C7nabo and CtCnabo in (a). DNA sequence and corresponding amino acid sequence of anti-GFP nanobody fused to *nd*-tag (*nd*-nabo) in (b).

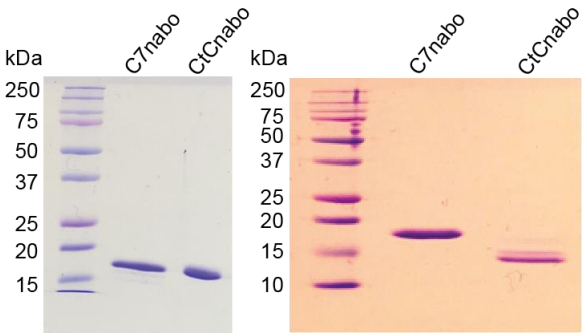

Figure 67. SDS-PAGE analysis of GFP-targeting C7nabo and CtCnabo after purification (left gel) and after three weeks of storage at 4°C (right gel). Left gel: C7nabo and CtCnabo show the expected electrophoretic mobility between 15 kDa and 20 kDa (MW = 15.5 kDa). Right gel: C7nabo band is detectable as expected at MW higher than 15 kDa, CtCnabo does not show the expected migration pattern anymore (one intense and one faint band below 15 kDa), indicating that CtCnabo was degraded by proteolysis.

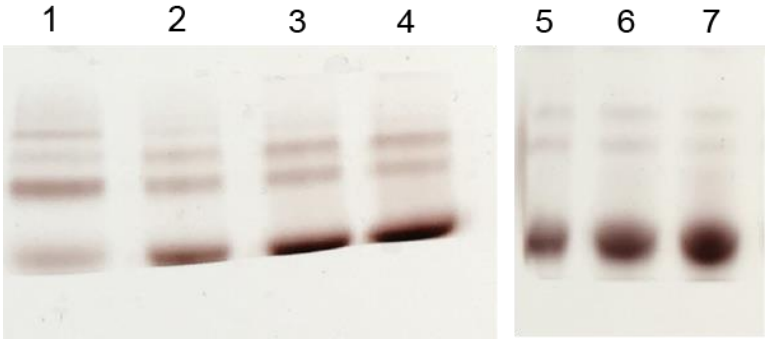

Figure 68. SDS-PAGE analysis of reactions of AuG with C7nabo using increasing amounts of (excess) AuG. The following AuG/C7nabo ratios were used: 1 (lane 1), 2 (lane 2), 3 (lane 3), 4 (lane 4), 5 (lane 5), 7 (lane 6) and 10 (lane 7). Apart from the conjugation using an AuG/C7nabo ratio of 1, all reactions yield 2 conjugate bands (presumably representing Au-$(nabo)_1$ and Au-$(nabo)_2$) and high amount of AuG remains unreacted.

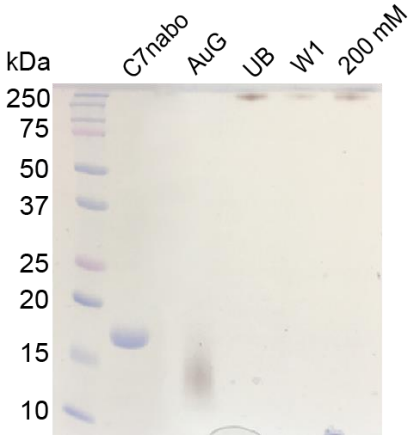

Figure 69. SDS-PAGE analysis of AuP-C7nabo purification by Ni NTA affinity chromatography. From left to right: C7nabo, AuG, UB: fraction remaining unbound to the Ni beads, W1: first wash fraction using PBS, 200 mM: elution of AuP-C7nabo conjugate using 200 mM imidazole. Note that the AuNP species of all fractions have the same electrophoretic mobility, which results from the passivation with PEG.

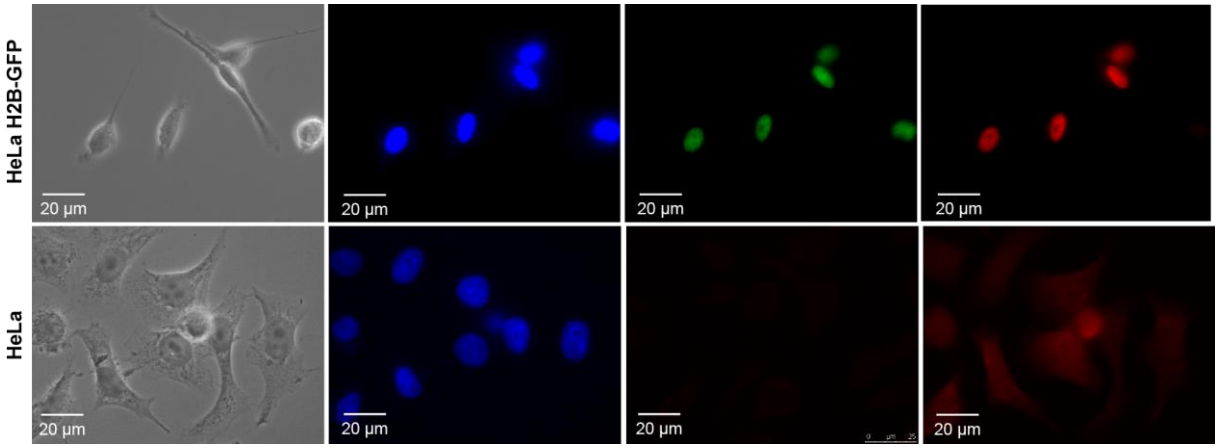

Figure 70. Light and fluorescence microscopy images of HeLa H2B-GFP cells and HeLa cells that were electroporated with anti-GFP *nd*-nabo. Detection of the nanobody by IF was performed 15 h after the

electroporation (blue fluorescence from DAPI staining, green fluorescence from H2B-GFP, red fluorescence from IF revealing localization of *nd*-nabo).

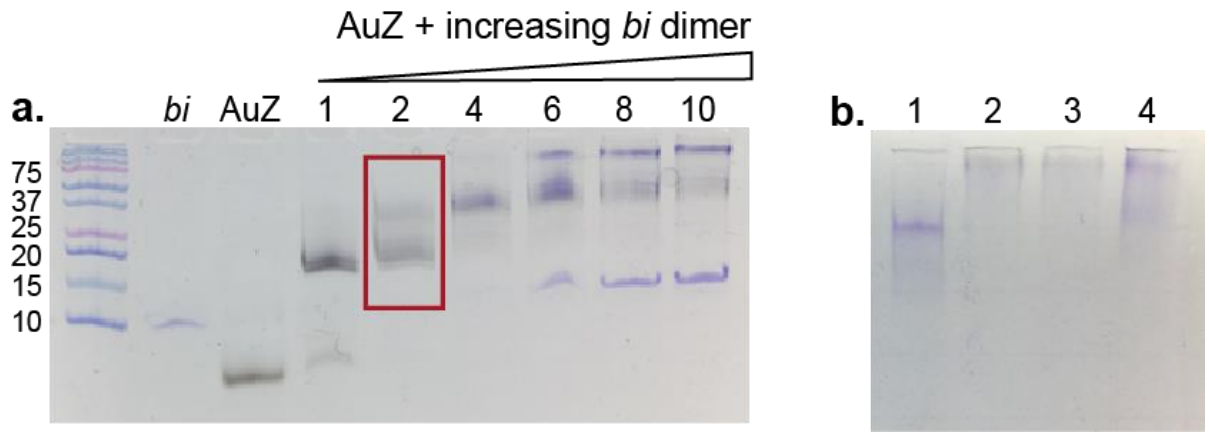

Figure 71. Analysis of non-covalent conjugation of AuZ to GFP-nabo mediated by *bi* and *nd* tags. (a) SDS-PAGE showing reactions of AuZ with increasing equivalents of *bi* dimer. 2 eq. of bi dimer leave no unreacted AuNP and were consequently selected for the conjugation (encircled in red); (b) Native PAGE of test assemble of AuZ-P-*bi* with increasing amounts of *nd*-nabo (lane 1: *nd*-nabo, lane 2: 2 eq. AuZ-P-*bi* + 1 eq. *nd*-nabo, lane 3: 1 eq. AuZ-P-*bi* + 1 eq, *nd*-nabo, lane 4: 2 eq. AuZ-P-*bi* + 1 eq. *nd*-nabo). Equimolar ratio of *bi* dimer and *nd*-nabo were chosen for the conjugation.

Manuscript (published in *Nanotechnology* on February 21, 2019)

Synthesis and biological evaluation of 2.4 nm thiolate-protected gold nanoparticles conjugated to Cetuximab for targeting glioblastoma cancer cells *via* the EGFR

Nadja Groysbeck,[1] Audrey Stoessel,[1] Mariel Donzeau,[1] Elisabete Cruz da Silva,[2] Maxime Lehmann, [2] Jean-Marc Strub,[3] Sarah Cianferani,[3] Kassiogé Dembélé,[4] Guy Zuber[1]

1. Université de Strasbourg - CNRS, UMR 7242, Laboratoire de Biotechnologie et Signalisation Cellulaire, Boulevard Sébastien Brant, F-67400 Illkirch

2. Université de Strasbourg – CNRS, UMR 7021, Laboratoire de Bioimagerie et Pathologies, Faculté de Pharmacie F-67401 Illkirch

3. Université de Strasbourg - CNRS, IPHC UMR 7178, Laboratoire de Spectrométrie de Masse BioOrganique, F-67000 Strasbourg

4. Université de Strasbourg - Institut de Physique et Chimie des Matériaux de Strasbourg (IPCMS) 23 rue du Loess, F-67034 Strasbourg

E-mail: zuber@unistra.fr

Abstract

Therapeutic monoclonal antibodies benefit to patients and the conjugation to gold nanoparticles (AuNPs) might bring additional activities to these macromolecules. However, the behavior of the conjugate will largely depend on the bulkiness of the AuNP and small sizes are moreover preferable for diffusion. Water-soluble thiolate-protected AuNPs having diameters of 2 to 3 nm can be synthesized with narrow polydispersity and can selectively react with incoming organic thiols *via* a S_N2-like mechanism. We therefore synthesized a mixed thionitrobenzoic acid-, thioaminobenzoic acid-monolayered AuNP of 2.4 nm in diameter and developed a site-selective conjugation strategy to link the AuNP to Cetuximab, an anti-EGFR (Epidermal Growth Factor Receptor) antibody used in clinic. The water-soluble 80 kDa AuNP was fully characterized and then reacted to the hinge area of Cetuximab, which was selectively reduced using mild concentration of TCEP. The conjugation proceeded smoothly and could be analyzed by polyacrylamide gel electrophoresis, indicating the formation of a 1:1 AuNP-IgG conjugate as the main product. When added to EGFR expressing glioblastoma cells, the AuNP-Cetuximab conjugate selectively bound to the cell surface receptor, inhibited EGFR autophosphorylation and entered into endosomes like Cetuximab. Altogether, we describe a simple and robust protocol for a site-directed conjugation of a thiolate-protected AuNP to Cetuximab, which could be easily monitored, thereby allowing to assess the quality of the product formation. The conjugated 2.4 nm AuNP did not majorly affect the biological behavior of Cetuximab, but provided it with the electronic properties of the AuNP. This offers the ability to detect the tagged antibody and opens application for targeted cancer radiotherapy.

Key words: Gold nanoparticle, site-directed bioconjugation, antibody, targeted cancer therapy, epidermal growth factor receptor

Introduction

Nanoparticles (NPs) are particles of sizes ranging between 1 and 100 nm that have important biomedical applications [1]. Some NPs can be functionalized with multiple elements, which permits to provide the nanomaterial with new properties. The coalescence of several functions allows dealing with the complexity of biological systems and might help for diagnosing and treating diseases [2, 3]. Several sophisticated systems demonstrated some efficiencies at preclinical stages for imaging modalities [4], nucleic acid delivery [5], protein delivery [6], tissue-targeted drug delivery [7], hyperthermia and photoablation therapy [8]. Gold nanoparticles (AuNPs) have been extensively investigated for biomedical application, because they have a low toxicity profile and their unique optic and electronic properties can trigger cellular damage upon application of light [9] or radiation [10, 11]. Furthermore, AuNPs can be equipped with organic molecules, including antibodies, which facilitate accumulation of the AuNPs within selected tissues or cancer lesions [12]. AuNPs with diameters above 5 nm display a large surface area that can be used for tight adsorption of antibodies and other proteins [13, 14]. For example, El-Sayed *et al.* coated 40 nm AuNPs with monoclonal antibodies targeting the epidermal growth factor receptor (EGFR) by random adsorption in order to target oral squamous carcinoma cells. The antibody-mediated accumulation of these AuNPs into the cancer cells was then used to promote cell death *via* a photothermal treatment [9]. Patra *et al.* synthesized 5 nm AuNPs that were also surface-coated with anti-EGFR antibodies, as well as with gemcitabine for targeting the drug to cancer cells [15]. Although of straightforward practicability, the functionalization of AuNPs *via* adsorption to the particle's surface has limitations. Firstly, a control over the orientation and stoichiometry of the adsorbed molecules onto the AuNP is challenging [16]. Secondly, the physicochemical properties of the antibody and its subsequent cellular response are impacted by the AuNP's size [17, 18]. When the properties of an AuNP-IgG conjugate should resemble the ones of an antibody, AuNPs of smaller sizes should be selected. However, since antibodies do not tightly adsorb to the surface of small-sized AuNPs, the functionalization method must be adjusted by the formation of an Au-S coordination bond.

Small-sized and uniform AuNPs with diameters between 0.8 and 2 nm are easily prepared by reduction of chloroauric acid in the presence of organic thiols [19]. Thiobenzoate-protected AuNPs of such small sizes and of rather precise chemical composition can be directly prepared in aqueous solutions leading to water-soluble AuNPs. These AuNPs can be further grafted with biological macromolecules, such as oligonucleotides, peptides and proteins [20, 21], or viruses [22] by exchanging the thiobenzoate ligands with incoming thiol-containing macromolecules. To diminish unspecific association to cellular constituents and to enhance the ligand exchange reaction, we have previously developed a mixed thionitrobenzoic acid (TNBA), thioaminobenzoic acid (TABA) protected-AuNP of 1.4 nm diameter that showed diffusion abilities inside living cells after grafting with bioactive peptides [23]. This type of AuNP appeared to be particularly suited for the site-directed conjugation to an IgG at the antibody's hinge region. The hinge region of an IgG connects the complement-activating Fc domain to the antigen-binding (Fab) domain and contains disulfide bonds that can be selectively reduced to liberate nucleophilic thiols. These liberated thiols can then react with electrophiles, thereby forming covalent bonds [24, 25]. Moreover, they can also exchange with the ligands of thiolate-protected AuNPs [26]. When the antibody is tagged at the hinge area, the antibody functionality is generally untouched since the Fab and the Fc domain, which both are implicated in the IgG cellular action, remain unmodified [27]. It should be however mentioned that the thiol-specific conjugation of AuNPs [28] and thiolate-protected AuNPs [26] at the hinge area is not always easy to achieve, likely due to steric hindrance.

In the presented study, we first modified a synthetic protocol for making a TNBA-, TABA-protected AuNP of 2.4 nm. Secondly, we evaluated the ability of this AuNP to react with the thiols of reduced IgGs at the hinge region (AuNP synthesis scheme and bioconjugation strategy illustrated in Figure 1). As models, we selected the anti-EGFR antibody Cetuximab (Cmab) and the anti-VEGF (vascular endothelial growth factor) antibody Bevacizumab (Bmab). The direct ligand exchange proceeded seamlessly at near stoichiometric ratio and the AuNP-antibody link remained intact, even after addition of the CALNNG peptide in large excess, which served the purpose of exchanging the remaining reactive TNBA/TABA ligands with a passive CALNNG layer [29]. Thirdly, the ability of the AuNP-Cetuximab conjugate to bind to its cellular target was assayed using cell line models. Biological evaluation using living cells with or without cell surface EGFR demonstrated that the AuNP-Cetuximab conjugate behaved very similarly to Cetuximab, despite being tagged with a 2.4 nm AuNP.

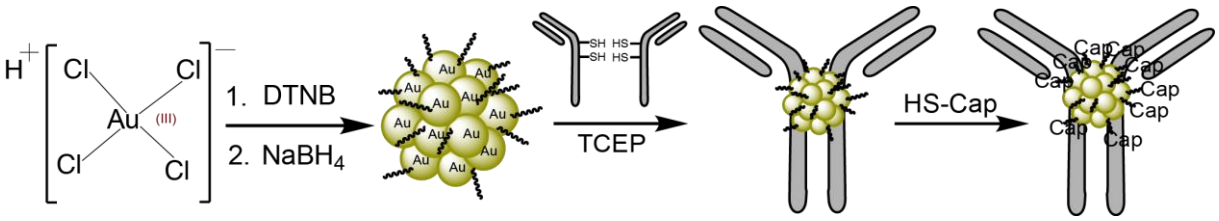

Figure 1. Scheme of gold nanoparticle (AuG) synthesis and bioconjugation to antibody. 1st step: Synthesis of AuG. Reduction of $AuCl_4$*$3H_2O$ to organothiolate gold nanoparticle using $NaBH_4$ in the presence of DTNB (dithionitrobenzoic acid) in CH_3CN/H_2O (80:20) pH = 13. 2nd step: Thiolate-for-thiolate exchange of the selectively reduced antibody's hinge thiols and the AuG-ligands TNBA (thionitrobenzoic acid) and TABA (thioaminobenzoic acid). 3rd step: passivation of the AuNP-IgG conjugate using excess of peptide CALNNG (HS-Cap).

Materials and Methods

Chemicals

Water was purified with a Millipore Q-POD apparatus. The paraformaldehyde (PFA 16% solution) and the glutaraldehyde (25% solution) solutions were of Electron Microscopy quality grade and purchased from Electron Microscopy Sciences. The jet PRIME siRNA transfection reagent was from PolyPlus-transfection. Other chemical reagents and solvents were obtained from commercial sources (Sigma Aldrich, Carl Roth, Honeywell, VWR Chemicals) and used without further purification. The protein ladder for SDS-PAGE analysis was the Precision Plus Protein Standard Dual Xtra (BioRad). Peptides were purchased from GeneCust and the antibodies bevacizumab (Bmab) and cetuximab (Cmab) were provided by Centre de lutte contre le Cancer Paul Strauss (France) and originally purchased from Merck KGaA and Roche laboratory, respectively. The initial buffer solution of the antibodies Cmab and Bmab was changed to PBS using illustra NAP-10 column (GE Healthcare). Antibodies used for the western blot analysis were purchased from Cell Signaling.

Materials

The pH of the solution was measured using a HI 2210 pH meter. Centrifugation of 50 mL tubes was performed with an Eppendorf 5810R centrifuge using an A-4-81 rotor. Centrifugation of smaller volumes (0.2 – 2 mL) was done using an Eppendorf 5415R centrifuge. A Heidolph Rotamax 120 rocking platform was used for mixing the gold reaction solution. Peptide coated AuNPs were purified and

concentrated using Amicon Ultra 0.5 mL centrifugal filter devices (MWCO 10 kDa) if not stated otherwise. UV-Vis spectroscopy was performed on a Varian Cary 100Bio spectrometer.

Synthesis of the AuG gold nanoparticles

Solutions of 0.4 M $HAuCl_4*3H_2O$ (90 µL, 36 µmol) and 50 mM DTNB (5,5'-dithiobis-(2-nitrobenzoic acid), 1.08 mL, 54 µmol) in 0.3 M NaOH were added to 80:20 CH_3CN/H_2O mixture (10.8 mL) under stirring. The mixture was agitated for 6 h at room temperature before addition of a freshly prepared 0.75 M $NaBH_4$ solution in water (240 µL, 180 µmol). The orange colored solution immediately turned to black. After an overnight stirring, the precipitated AuNPs were recovered by centrifugation, washed with acetonitrile and then dried to yield the AuNP (named AuG) as a black powder.

Synthesis of AuNP-antibody conjugate

A 2 mg/mL antibody solution (225 µL, 0.45 mg) was treated with a 7 mM Tris(2-carboxyethyl)phosphine-HCl (TCEP) solution, pH 7.0 (90 µL, 0.63 µmol) for 1.5 h at 37°C. The AuG (73 µL of a 42 µM, 3.06 nmol) was then added to the reduced antibody (297 µL, 0.42 mg) in 0.1 M HEPES buffer, pH 7.5 at 25°C and the reaction was let to proceed overnight. The next day the AuNP-antibody conjugate was passivated with a 1 mM solution of peptide CALNNG (123 µL, 123 nmol or 40 molar eq. of AuNP-antibody conjugate) for 4 h at 25°C in 0.1 M HEPES buffer, pH 7.5. The exchanged AuG-ligands (TNBA and TABA) and excess CALNNG peptides were removed by ultrafiltration using Amicon 100 K ultracentrifugal devices.

Mass spectrometry analysis

Mass spectra were recorded with a MALDI-TOF MS operating in positive ion mode on an Autoflex™ system (Bruker Daltonics GmbH, Bremen, Germany). The system was used at an accelerating potential of 20 kDa in linear and reflector mode. The nitrogen laser (337 nm) was used at a frequency of 5 Hz and the acquisition mass range was set to 5000 – 30000 m/z with a matrix suppression deflection of 500 m/z. Samples were prepared by the dried droplet method. The matrix solution consisted of a saturated solution of α-cyano-4-hydroxycinnamic acid in H_2O/CH_3CN (50:50), which was threefold diluted in H_2O/CH_3CN/TFA (50:49.9:0.1).

Electron microscopy and EDX analysis

Images of the AuNPs were obtained by performing microscopy experiments using a C_s-corrected JEOL JEM-2100F Scanning Transmission Electron Microscope operating at 200 keV. Energy dispersive X-ray (EDX) analysis was carried out on the same instrument, being equipped with an EDX detector. Samples were prepared by adding 10 µL of a 5 µM AuNP solution onto the Carbon film support of a ultrathin carbon 400 mesh Cu grid (Ted Pella Product No 01822-F, Redding, CA). After 2 min, excess liquid was blotted with a filter paper and the grid was dried for 48h.

FTIR analysis

Fourier-transform infrared (FTIR) spectrum of AuNPs was recorded using a Nicolet 380 FTIR spectrometer and a diamond ATR by Thermo Fisher Scientific (Supporting Information, Figure S1).

SDS-PAGE

SDS-PAGE was performed according to a published protocol of Laemmli *et al.* on 10% and 15% acrylamide gels [30]. The gels were pre-run for 20 min in a tris-glycine buffer (0.25 M Tris, 1.92 M glycine, 1%SDS, pH 8.5) at 20 mA. For loading 50% (v/v) glycerol solution was added to the AuNP solutions to a 5% final proportion. After electrophoresis, the AuNPs were seen as black-brown bands. Few amounts of AuNPs could be further visualized by silver enhancement. Proteins were revealed by Coomassie blue staining.

Cell culture

Cell lines were maintained in a 37°C humidified incubator with 5% CO_2. The human U87 glioblastoma cells (U87 MG, ATCC HTB-14) and the human fibrosarcoma cells (HT-1080, ATCC CCL-121) were maintained in Eagle's Minimum Essential Medium (EMEM) containing 10% fetal bovine serum (FBS), 1% sodium pyruvate and 1% nonessential amino acids. Human foreskin fibroblast (HFF) cells (HFF-1, ATCC SCRC-1041) were cultured in Dulbecco's Modified Eagle Medium (DMEM) supplemented with 2 mM L-glutamine, HEPES buffer, 10% heat inactivated fetal calf serum (FCS) and 50 µg/mL gentamycine. The U87 and HFF cells co-culture was done in Opti-MEM cell culture medium containing 10% FCS. The EGFR(+) U87 cell line was a gift from Professor Furnari [31]. The MTT assay was performed according to a published procedure [32].

Downregulation of EGFR expression in U87 cells

Expression of EGFR was down-regulated using the synthetic interfering RNAs (siRNAs) methodology. The U87 cell line was seeded in 6-well plates at 250 000 cells/well the day before the siRNA transfection experiment. For one well, a 50 nM siRNA solution (200 µL jetPrime buffer, 10 pmol siEGFR) was mixed with 4 µL of jetPrime reagent. After 10 min incubation at room temperature, the complexes were added to the cells by dilution into the cell culture medium. To ensure maximum gene silencing the cells were incubated for 48h before use [33]. The human EGFR siRNA solution (siGENOME Human EGFR(1956) siRNA Smart pool) was purchased from Dharmacon. The solution contained 4 siRNA molecules, which target the following mRNA sequences. Sequence 1: CCGCAAAUUCCGAGACGAA, sequence 2: CAAAGUGUGUAACGGAAUA, sequence 3: GUAACAAGCUCACG-CAGUU, sequence 4: GAGGAAAUAUGUACUACGA.

EGFR binding assay

Cells were seeded in 24-well plates and let to adhere on fibronectin-coated (20 µg/mL) glass coverslips the day before the assay. The cell culture medium was then replaced with a serum-free cell culture medium and the cells were incubated at 37°C for 30 min. This starvation step aimed at optimizing EGFR presentation on the cell surface [34]. Culture medium was then carefully removed and replaced with a serum-free medium containing the AuNP-antibody conjugate. After 30 min of incubation, the cell culture medium was removed. Cells were washed with PBS and then fixed with either 4% PFA in PBS (10 min) or 2.5% glutaraldehyde in Sorenson's Buffer (1h).

Assay of EGFR-mediated endocytosis

Cells were seeded in 24-well plates and let to adhere on fibronectin-coated (20 µg/mL) glass coverslips the day before the assay. The cell culture medium was then replaced with serum-depleted culture medium and the cells were let in this medium for 30 min at 37°C. After serum-depletion, cells were incubated in ice-cooled serum-free medium containing 167 nM of the AuNP-antibody conjugate. After 30 min of incubation on ice, the cell culture medium was replaced with pre-warmed serum-containing cell culture medium and the cells were incubated at 37°C for different time periods. The cell surface-bound antibodies were detached with a 0.2 M sodium acetate solution (pH 2.7). The cells were then washed with PBS and fixed with 4% PFA.

P**reparation of the cell specimen for AuNP detection**

The AuNPs were detected using a modified Danscher method [23, 35]. Briefly, after the 2.5% glutaraldehyde fixation step, the cells were incubated with a 0.1 M Sorenson's buffer, pH 7.4 containing 50 mM glycine for 20 min. The cell membrane was then permeabilized using a Sorenson's buffer, pH 7.4 containing 0.05% (w/v) saponine. The buffered solution was then replaced by a 0.1 M citrate solution, pH 6.7 containing 2% (w/v) sucrose. Development of the AuNPs was done in a dark room for 8 min using a freshly prepared 6 mM silver acetate solution in 0.16 M sodium citrate, pH 6.7 containing 2 mM propyl gallate and 20% (w/v) gum arabic. Development of the silver-mediated AuNP staining was stopped by washing the cell specimen with 0.16 M sodium citrate solution, pH 6.7.

Western blot

Cells were lysed in Laemmli loading buffer, the lysate was fractionated by SDS-PAGE and transferred onto a polyvinylidene difluoride (PVDF) membrane. The anti-EGFR D38B1, anti-pEGFR Tyr1068 and anti-GAPDH antibodies were used to detect EGFR, phosphorylated EGFR and GAPDH respectively.

Results

Gold nanoparticle synthesis and characterization

We previously described the synthesis of a TNBA-,TABA- protected AuNP of circa 102 gold atoms that could be grafted with thiolated peptides by exchanging most of the TNBA-ligands, leaving a surrounding zwitterionic protecting shell consisting of gold-coordinated TABAs [23]. In an initial stage, we explored the possibility of preparing the same type of TNBA-, TABA-protected AuNP, but of larger diameter. The nature and proportion of the solvents were seen to dramatically alter the production of thiolate-protected AuNPs [36]. We therefore assayed the reduction of $HAuCl_4$ with $NaBH_4$ and DTNB in various co-solvents. It was observed that a $HAuCl_4$/DTNB/$NaBH_4$ ratio of 1:1.5:5 in a solvent mixture of CH_3CN/H_2O (80:20) yielded to a AuNP population migrating as a discrete band when subjected to a sodium dodecyl sulfate polyacrylamide gel electrophoresis (SDS-PAGE) analysis, suggesting a homogenous population (Figure 2a). This AuNP population (named AuG) was further characterized by UV-Vis spectroscopy (Figure 2b). Data showed that the absorption gradually increases for decreasing wavelengths. The spectrum contains a hump with a maximum absorption at 520 nm, corresponding to the weak surface plasmon resonance absorption of 2 nm diameter AuNPs [37]. The Scanning

Transmission Electron Microscopy (STEM) analysis of the AuNP revealed a homogenous population of spherical particles (Figure 2c) with a mean diameter of 2.4 ± 0.28 nm (n= 61). The observation of a crystalline lattice at high resolution (inset image in Figure 2c) confirmed that the metallic core of AuG was massive (Au^0). A MALDI-TOF mass spectrometry analysis of the AuNP (Figure 2d) displayed a narrow distribution of masses at 80 kDa, confirming the SDS-PAGE and EM data. By combining the different data and a volumetric density of 19.3 g/cm^3 for Au, we estimated that the AuNP contains on average about 420 gold atoms and 130 ligands. Further calculations and a test reaction using increasing ratios of a thiol-containing cationic peptide to the AuNP suggested that the ligand to peptide substitution saturates at about 35 exchanges per particle (Figure S2, Supporting Information). Energy Dispersive X-ray (EDX) analysis was also performed (Figures 2e and 2f). The spectrum displayed the characteristic peaks of gold ($Au_{M\alpha}$ at 2.12 keV; $Au_{L\alpha}$ at 9.712 eV) along with peaks corresponding to carbon and copper resulting from the carbon film-coated copper grid, on which the AuNPs were deposited for the analysis.

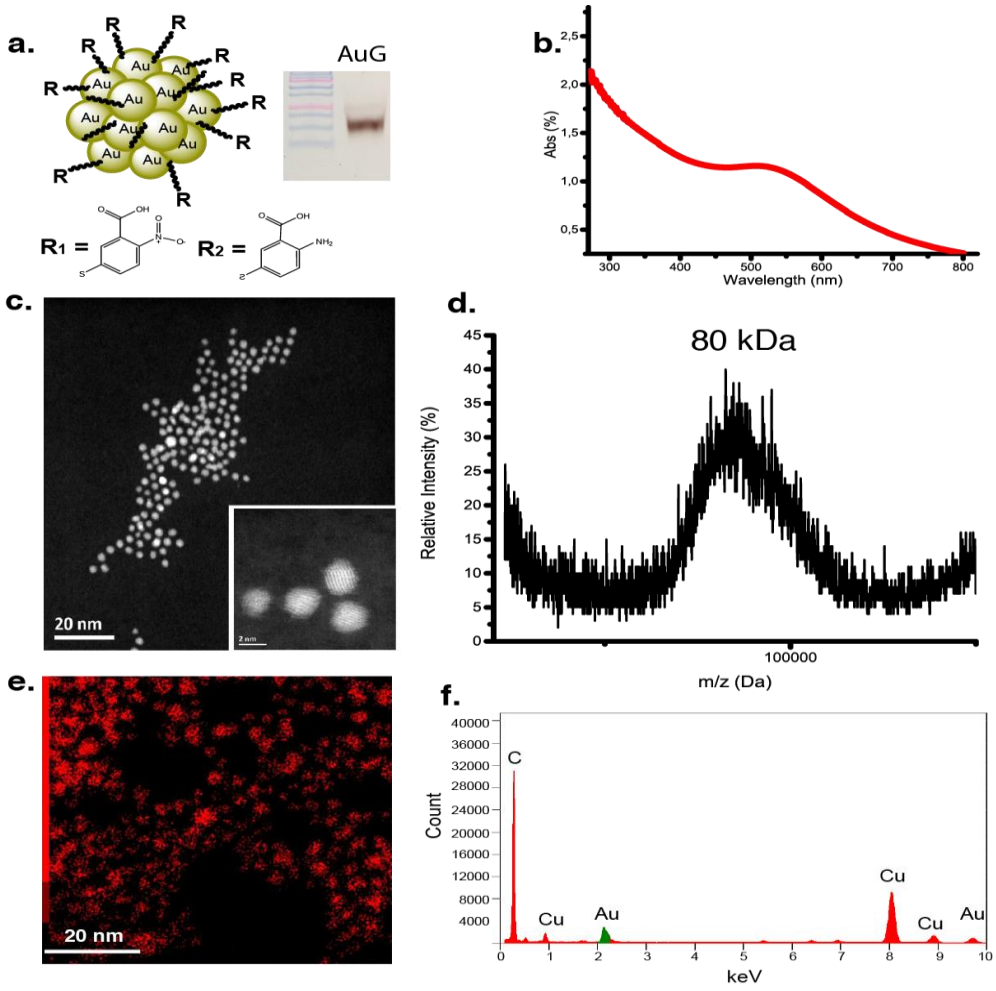

Figure 2. Characterization of 2.4 nm AuNP (AuG) **(a)** Structure and SDS-PAGE analysis of AuG (15% acrylamide gel). Structure of organothiolate ligands building the surface coating of AuG are depicted below the nanoparticle: R_1 = TNBA (thionitrobenzoic acid), R2 = TABA (thioaminobenzoic acid); **(b)** UV-Vis spectrum of AuG (small peak at 520 nm corresponding to weak surface plasmon resonance absorption); **(c)** Scanning transmission electron microscopy image of AuG particles. Inset image in right corner shows magnification (scale bar of main image: 20 nm, scale bar of inset image: 2 nm); **(d)** MALDI-TOF Mass spectrum of AuG (MW^{obs} = 80 kDa); **(e)** Elemental EDX mapping of AuG (scale bar: 20 nm); **(f)** EDX spectrum of AuG ($C_{K\alpha}$ = 0.277 keV, $Cu_{L\alpha}$ = 0.93 keV, $Au_{M\alpha}$ = 2.12 keV, $Cu_{K\alpha}$ = 8.04 keV, $Cu_{K\beta}$ = 8.9 keV, $Au_{L\alpha}$ = 9.71 eV).

Conjugation to antibodies

The weakly nucleophilic and thiol-free reducing agent TCEP was used to reduce the antibody disulfide bridges [38]. For optimizing the reduction condition, the Cetuximab antibody (Cmab) was incubated with increasing TCEP concentrations and the reactions were monitored by SDS-PAGE analysis using non-reducing conditions (Supporting Information, Figure S3). Data showed that a final 2 mM TCEP concentration produced a complete reduction of the 150 kDa band to the expected 75 kDa band. Cmab was hence reduced with 2 mM TCEP in PBS for 90 min and the water-soluble 2.4 nm AuNP (AuG) was then directly added to the TCEP-reduced antibody mixture at a 1:1.2 (Cmab:AuNP) stoichiometry. The formation of the AuNP-Cetuximab conjugate (Au-Cmab) was monitored by SDS-PAGE using 10% acrylamide gels (Figure 3). To enable dual detection of the protein and the AuNP, the gel was firstly stained using Coomassie blue and then silver ions.The conjugation reaction based on the substitution of an AuG ligand with a thiol group of the antibody's hinge area proceeded seamlessly, which could be concluded from the observation of a black colored 150 kDa band and no remaining band at 75 kDa in the lane of Au-Cmab (Figure 3, lane 5). An apparent 250 kDa band was also observed suggesting dimerization of the IgG, but the proportion was estimated to be lower than 10%. We assumed that the major apparent 150 kDa band corresponds to a 1:1 AuNP-IgG conjugate, whereas the 250 kDa species possibly represents either a AuNP-$(IgG)_2$ product or an aggregate of two 1:1 AuNP-IgGs. The observation that the electrophoretic mobility of the main Au-Cmab conjugate was similar to the one of unreacted 150 kDa Cmab is puzzling. However, the AuNP migrated within the migration front and not as classical 80 kDa protein. This high electrophoretic mobility likely results from the high volumetric mass density of gold (19.3 g/cm^3) and the electronegative charge of AuG. A small amount of unreacted AuG was still detectable in the crude Au-Cmab solution (Figure 3, lane 5, faint band at the bottom of the gel), which likely resulted from the slight excess of AuG used for the reaction. Finally, the released ligands, as well as excess peptides and AuNPs were removed using a 100 kDa cut-off ultracentrifugation device. At the present stage, we were unable to remove all the AuNPs as judged by SDS-PAGE analysis, but obtained a batch with less than 5% of free AuNPs. The conjugation of AuG to Bmab and the purification procedure were performed in a similar manner, but using a TCEP concentration of 0.1 mM for reduction of the hinge disulfide bonds (Supporting Information, Figure S4).

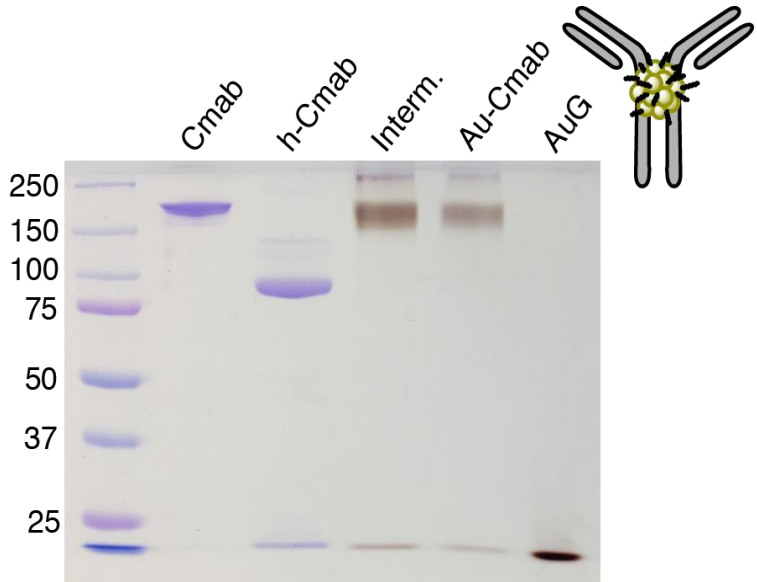

Figure 3. SDS-10% PAGE of gold nanoparticle-antibody-conjugate (Au-Cmab) formation under non-reducing conditions. Order on the gel from left to right: Cetuximab (Cmab), selectively reduced Cetuximab (h-Cmab), AuNP-Cetuximab conjugate before passivation (Interm.), AuNP-Cetuximab conjugate after passivation with peptide CALNNG (Au-Cmab), gold nanoparticle AuG

Biological evaluation of the Au-Cmab conjugate

The ability of the Au-Cmab to bind to EGFR, present on the surface of various cancer cells, was examined using a U87 glioblastoma cell line overexpressing the EGFR [31], hereafter referred to as EGFR(+) U87 cells. The Au-Bmab conjugate, which does not target the EGFR, but the vascular endothelial growth factor (VEGF), was used as the control. In a parallel control experiment, the EGFR expression of U87 wild type cells was almost abolished using the siRNA-mediated gene silencing technology to obtain EGFR(-) U87 cells (western blot confirming the successful downregulation of EGFR depicted in Figure S5, Supporting Information). The Cmab, Au-Cmab and Au-Bmab were added to living cells at a concentration of 167 nM by dilution into the cell culture medium. After 30 min of incubation, the cells were fixed and each domain of the conjugate was separately tracked (Figure 4). The antibody was detected by immunofluorescence (IF) [39] (Figure 4a). Green fluorescence (IgG) was only observed when Cmab and Au-Cmab were added to EGFR(+) U87 cells. Next, the AuNP moiety was revealed by gold-induced silver staining (Figure 4b). Analogous to the IF results, the strongest silver staining pattern was only seen for Au-Cmab-treated EGFR(+) U87 cells. Some silver staining was nonetheless observed within the endosomes of EGFR(-) and EGFR(+) cells for Au-Bmab and for Au-Cmab, suggesting that the AuNP domain somehow favors adherence to cell surfaces and subsequent endocytosis. It should be however mentioned that the silver-enhancement procedure is highly sensitive and not a quantitative method.

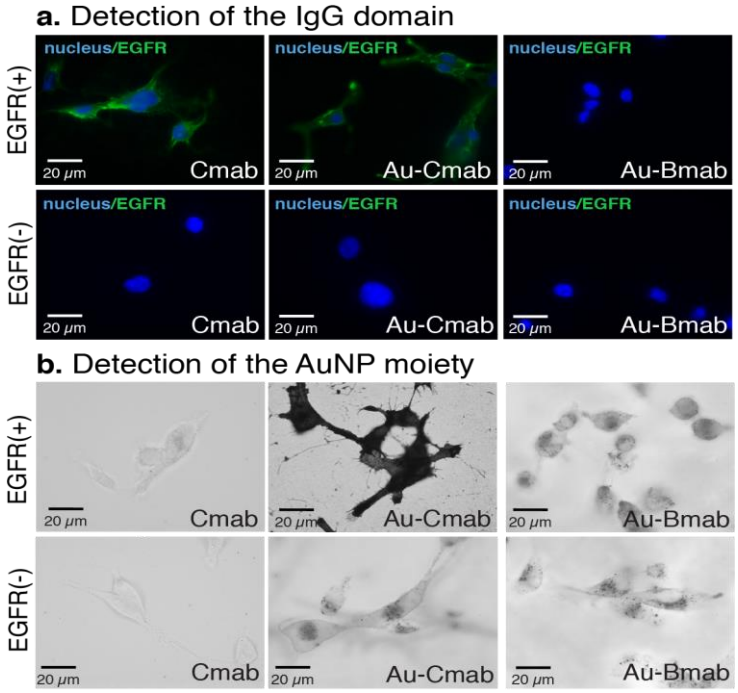

Figure 4. Analysis of the EGFR binding ability of the anti-EGFR Cmab, Au-Cmab and Au-Bmab to living EGFR(+) U87 glioblastoma cells and EGFR(-) U87 cells. **(a)** Detection of the antibody domain of the nanomaterial by immunofluorescence; **(b)** Detection of the AuNP domain by silver staining. Cells were incubated with 167 nM of antibody or AuNP-antibody conjugate for 30 min at 37°C. Scale bar: 20 µm

The ability of Au-Cmab to bind to EGFR-overexpressing cells was confirmed using an other EGFR-expressing cancer cell line (human fibrosarcoma cells, HT-1080; Supporting Information, Figure S6). As previously described for binding experiments using EGFR(+) U87 cells, the Au-Cmab bound to the surface of HT-1080 cells, whereas the control conjugate Au-Bmab did not show this pattern. Here again, we noticed some silver staining of the cells incubated with Au-Bmab, reinforcing the assumption that the AuNP domain slightly promotes adherence to the cell surface and subsequent endocytosis.

These experiments convincingly demonstrated that Cmab and the Au-Cmab conjugate selectively bind to EGFR of living EGFR-presenting cells. We then evaluated the impact of the AuNP on the ability of Cmab to bind to the cell surface receptors. Cmab and Au-Cmab were incubated with the EGFR(+) U87 cells at concentrations ranging from 0.67 pM to 167 nM. The cells were fixed and the cell-attached antibodies were qualitatively detected by IF. An on/off fluorescence detection threshold was used and the on/off detection data were plotted as a function of the initial material concentration (Supporting Information, Figure S7). This rough quantitative analysis showed that the detection of the EGFR onto the cells required 10 times more of the Au-Cmab conjugate, than of Cmab, suggesting that appending the 2.4 nm AuNP at the hinge area may not be fully innocuous.

Next, we assayed the ability of the Au-Cmab to get internalized into cells, as it is described for Cmab [40]. Both compounds (Cmab and Au-Cmab) were incubated with living serum-starved EGFR(+) U87 cells for 30 min on ice to allow for receptor binding, but not for internalization. Afterwards, the sample- and non-serum-containing medium was exchanged for serum-containing cell culture medium and the cells were incubated at 37°C for 30 and 60 min, to allow internalization. At the end of the incubation, the nanomaterials bound to the cell surface receptors were washed away using a mild acidic treatment [41]. The cells were then fixed, the plasma membrane permeabilized with detergent, and the components detected by IF (Figure 5). The time-course experiment showed that binding of Cmab and Au-Cmab to the cell surface receptors is followed by internalization into intracellular vesicular compartments. Although the intracellular fate of Cmab and Au-Cmab was similar, slight differences were observed at the 30 min incubation time-point. Cmab mainly localized into perinuclear compartments, whereas the Au-Cmab was still seen inside vesicles closer to the plasma membrane.

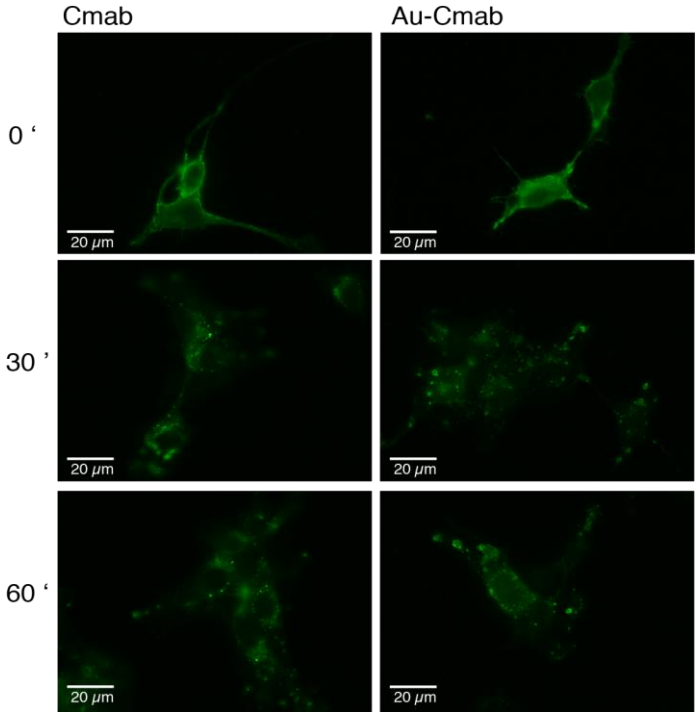

Figure 5. Assay of EGFR-mediated endocytosis. Cetuximab (Cmab) and AuNP-Cetuximab conjugate (Au-Cmab) were added to living EGFR(+) U87 cells for 30 min (37°C) at concentrations of 167 nM. The cell endocytosis was then evaluated immediately (image on top: 0’), as well as after 30 min and 60 min of further incubation in complete medium (not containing antibody and conjugate samples). The nanomaterial was detected by immunofluorescence. Scale bar: 20 µm

To further examine whether the biological function of Cmab was affected by the conjugation to AuG, we compared the ability of Cmab and Au-Cmab to inhibit EGFR autophosphorylation after induction with EGF. The serum-starved EGFR(+) U87 cells were incubated with Cmab and Au-Cmab together with EGF for 15 min at 37°C. Afterwards, the cells were lysed and the cell extracts were fractionated by SDS-PAGE to quantify the intracytosolic levels of EGFR and EGFR-pTyr1068 by western blot analysis (Figure 6). Data showed that the Au-Cmab inhibited the phosphorylation of EGFR similarly to Cmab [42]. Even though Cmab and the Au-Cmab inhibited EGFR phosphorylation, their addition to EGFR(+) U87 cells at a concentration of 167 nM did not apparently impact the cellular viability, as judged by a MTT assay (Supporting Information, Figure S8).

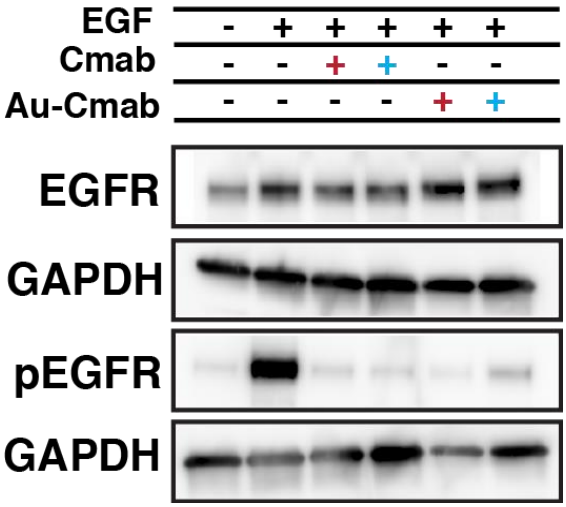

Figure 6. Western blot analysis of EGFR and phosphorylated EGFR (pEGFR) levels after addition of Cmab and AuCmab to EGF-stimulated EGFR(+) U87 cells. GAPDH was used as a loading control. Cmab and Au-Cmab were used at concentrations of 787 nM (left red +) and 394 nM (right blue +). EGF was used at a concentration of 8 nM.

Finally, we examined whether the Au-Cmab conjugate is able to distinguish between EGFR-overexpressing cancer cells and non-cancerous cells. The EGFR(+) U87 cells were co-cultured with the non-cancerous human foreskin fibroblast (HFF) cells and the Au-Cmab was then added to the cell culture medium. After 30 min the cells were fixed and the presence of the Au-Cmab conjugate was revealed by IF and silver staining (Figure 7). The two cell types were easily distinguishable by their cell morphology. EGFR(+) U87 cells (Figure 7a: black arrows) are much smaller and thinner than HFF cells (Figure 7a: red arrow; Figure 7b: cells encircled in red). Only the EGFR(+) U87 cells were engulfing a large proportion of Cmab and Au-Cmab, confirming that the Au-Cmab conjugate might be useful to selectively target EGFR-overexpressing tumor cells while not affecting non-cancerous cells.

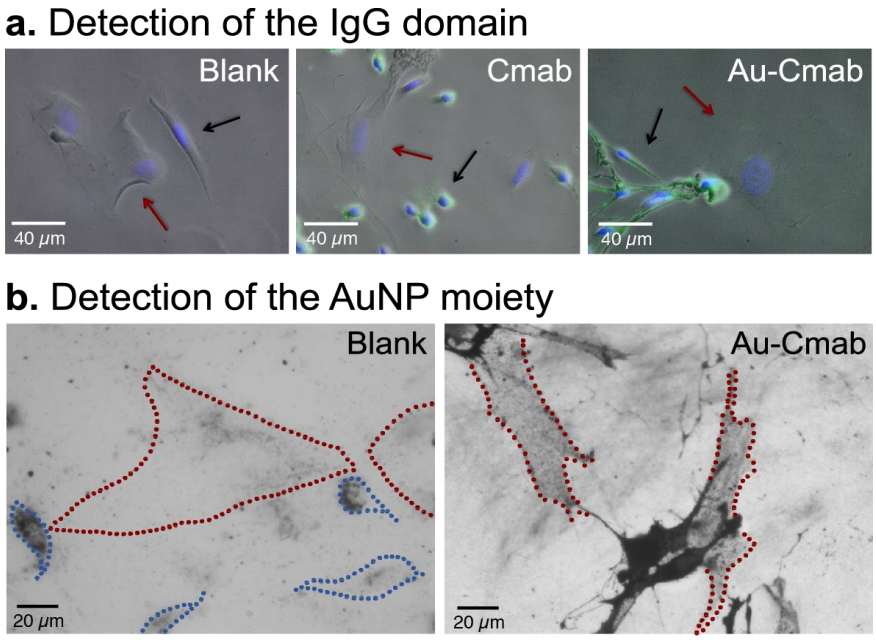

Figure 7. Evaluation of cell selectivity towards EGFR using a co-culture of EGFR(+) U87 cancer cells and non-cancerous human foreskin fibroblast (HFF) cells. Cmab or Au-Cmab were added to the co-culture by dilution in the cell culture medium. After 30 min incubation at 37°C the antibody domain and the AuNP moiety were detected by immunofluorescence **(a)** and silver staining **(b)**. The nuclei were stained in blue (DAPI). (**a)** HFF cells indicated by red arrow, EGFR(+) U87 cells indicated by black arrow. **(b)** HFF cells are encircled in red, EGFR(+) U87 cells are encircled in blue (in blank image only). Cmab and Au-Cmab concentrations used for incubation: 167 nM. Scale bar in **(a):** 40 µm, scale bar in **(b) :** 20 µm

Discussion

NPs, including AuNPs, can be prepared at various sizes and be equipped with functional organic components, which makes them useful for a multitude of different applications [43-48]. For biological applications, the AuNP size plays a major role. Particles having sizes above 4 – 5 nm offer the advantage to be easily detectable by electron microcopy and they can also be easily surface-coated with several antibodies using strong non-covalent binding or be coordination to organic molecules *via* an Au-S coordination [49, 50]. However, presentation of a large surface to macromolecules present in the solvent is not without consequence. When AuNPs are mixed with serum, a large protein corona is forming around the AuNPs [51] that can impact cellular interactions [52]. Beside these variations in physicochemical properties, the size plays an important role for the ADME (absorption, distribution, metabolism, excretion) profile of the particles [53-55]. Another parameter that is clearly impacting the ADME profile of NPs, such as elimination from the body, is the particle's coverage [56-58]. For inorganic non-biodegradable AuNPs, renal excretion should be undoubtedly favored, giving priority to the development of small AuNPs. Based on the work of Ackerson [59] we have prepared a novel type of AuNPs containing a mixed TABA, TNBA layer of circa 102 gold atoms that showed extremely promising usage for biological application, due to its abilities to be functionalized with peptides and to be stabilized with zwitterionic ligands [23]. Although we could have used this AuNP for conjugation, we wished to prepare slightly larger NPs for increasing the quantity of gold atoms within the system on

the one side, but also to increase the conjugation challenge as bulkiness provides steric hindrance and unspecific interactions [60, 61]. While it is well described that increasing the NP size can increase the formation of protein corona [62], the size-threshold for the occurrence of protein corona for thiolate-protected AuNPs and the associated change in the particle's physicochemical properties, is unknown. To start answering to this question, we have hence privileged to work with AuNPs of 2.4 nm, instead of with AuNPs of 1.4 nm.A previous investigation showed that mercaptobenzoic acid-protected AuNPs can be prepared at various sizes by adjusting the type and composition of the solvent mixture used for the particle synthesis [36]. In our case, a solvation of the gold-DTNB complex in an acetonitrile/water (80:20) mixture led to 2.4 nm AuNPs showing a high degree of monodispersity that could be characterized by SDS-PAGE analysis, MALDI-TOF mass spectrometry, STEM, EDX and UV-Vis spectroscopy.

The site-directed bioconjugation of the antibodies Cmab and Bmab to the AuG *via* simple thiolate-for-thiolate ligand exchange proceeded smoothly and could be monitored by non-reducing SDS-PAGE. Until today there are very few reports about the controlled conjugation of large biomolecules to small-sized AuNPs. Ackerson and coworkers attempted the "direct" labeling of cysteine-containing proteins with Au_{144}NPs, however the reaction seemed to require a large excess of NPs, as a large quantity of unreacted AuNPs could be detected on the SDS gels, indicating that the reaction did not proceed as straightforward as it was the case in the present study [26]. The following reason could be hypothesized. The AuNPs produced by Ackerson *et al.* were coated with mercaptobenzoic acid, while the particles of the present study contained zwitterionic thioaminobenzoate ligands. This zwitterionic coating might diminish unspecific associations between the nanoparticle and the biomolecule, thereby favoring the accessibility of the AuNP to the antibody's hinge thiols and consequently the S_N2-like substitution.

The ability of Au-Cmab to selectively bind to EGFR present on living cells was assayed using U87 glioblastoma cells that were engineered to overexpress the EGFR, as well as using the human HT-1080 fibrosarcoma cell line, which also overexpresses the EGFR. The glioblastoma cell model system was chosen, because 40% of all glioblastoma patients overexpress the EGFR, however the response to any EGFR-based therapeutic treatment is extremely low, an issue, which remains unresolved until today [63-65]. As a consequence approaches have been developed to use the anti-EGFR antibody Cmab as a cancer targeting agent to deliver active payloads [63]. These active payloads can hence induce cell damage of the targeted cells, without relying on a "normal functioning" EGFR signaling pathway. The data obtained from the EGFR binding assays of the present study showed that the Au-Cmab conjugate selectively binds to the EGFR on living cells in an analogous, but not identical manner than Cmab. The following AuNP-mediated differences were observed. First, an AuNP-mediated endocytosis was noted, suggesting that the 2.4 nm AuNPs slightly bind by themselves to cell surfaces. The association of the AuNP to the cell membrane was moreover promoting a small change in the intracellular trafficking of the Au-Cmab, confirming some AuNP-mediated non-selective associations to cell surface membranes. The relevance of this slight, but apparent difference between Cmab and AuCmab is unclear but deserves careful attention. Finally, the conjugation of the AuNP decreased the apparent binding affinity. However, it should be emphasized that we have not comprehensively optimized the quality of the Au-Cmab conjugate and the magnitude in decrease of binding affinity, which we have observed (10 times difference), might be reduced.

The cell viability of the EGFR(+) U87 cells was not diminished by incubation with Cmab or Au-Cmab. This absence of toxicity has already been reported for cultured glioblastoma cells [66] and we hypothesize that this issue has the same background as the resistance of glioblastoma tumors to EGFR-based therapies.

Altogether, we reported a synthesis of highly uniform 2.4 nm AuNPs that can be site-directly conjugated to the antibodies Cmab and Bmab *via* a straightforward thiolate-for-thiolate exchange mechanism. Data

from *in vitro* studies showed that the Au-Cmab conjugate was able to specifically bind and internalize into glioblastoma cells after binding to EGFR, demonstrating that a targeted accumulation of AuNPs within cancerous cells is achievable. Since AuNPs allow for radiosensitization [67, 68], can be readily conjugated to drugs [69], or can be prepared from β-emitting radioactive gold-189 [70, 71], the Au-Cmab conjugate holds promise for targeted anticancer therapy of glioblastoma tumors, which are resistant to traditional EGFR-based therapeutic treatments.

At the present stage of investigation and knowledge, antibodies and by extension "antibody-like" conjugates should circulate in the blood after intravenous injection. Assuming that, the pharmacokinetic properties of Au-Cmab are identical to the ones of Cmab, a blood half-life of 18 – 21 days can be expected with an elimination by intracellular catabolism [72], rather than by renal filtration or hepato-biliary mode [73]. This pharmacokinetic behavior should facilitate targeted accumulation of the conjugate at cancer lesions, but raises issues about the reminiscence of AuNPs inside the body after degradation of the antibody moiety. Although it is generally accepted that particles having a hydrodynamic diameter <6 nm are rapidly cleared from the body by renal filtration [73], the elimination of the 2.4 nm AuNPs need to be examined by *in vivo* studies. Moreover, *in vivo* experiments should be performed to study the route of administration, the biodistribution and the fate of the Au-Cmab conjugate.

Conclusion

A highly defined 2.4 nm AuNP, displaying an inner metallic core and an Au-S coordinated organic ligand shell, was synthesized by $NaBH_4$ reduction of chloroauric acid in the presence of the Ellman's reagent in a 80:20 acetonitrile/water mixture. This 2.4 nm AuNP could be characterized using several methods including MALDI-TOF mass spectrometry, SDS-PAGE, UV-Vis spectroscopy, electron microscopy, FTIR and EDX analysis, thereby facilitating the reproducibility of production. The AuNP was subsequently functionalized with the anti-EGFR antibody Cmab *via* a simple thiolate-for-thiolate exchange of the AuG ligands (TNBA and TABA) and the hinge thiols of the selectively reduced antibody – a site-directed conjugation strategy, which has not been explored before for antibodies and small-sized AuNPs. To minimize the formation of protein corona and to prevent NP aggregation, the Au-Cmab conjugate was passivated with peptide CALNNG in a second step. To demonstrate that the conjugation strategy is generally applicable, the AuNP was also conjugated to the VEGF-targeting antibody Bmab. Besides, the Au-Bmab conjugate served as control in the EGFR binding assays. The conjugation reactions could be readily visualized using non-reductive SDS-PAGE analysis, from which it was assessed that the major conjugation products consist of one IgG and one AuNP. The generated Au-Cmab conjugate was seen to behave similarly to Cmab when added to living cells, suggesting that the site-directed conjugation to the AuNP did not destroy the biological activity of the antibody, thereby demonstrating the value of the designed functionalization strategy. The possibility to produce very defined AuNP-IgG conjugates opens now new ways to assay the Au-Cmab conjugate for cancer therapy, either for sensitizing tumor cells to external radiation [10], or as a vehicle for the delivery of radioactive gold isotopes to tumor sites [70, 71, 74].

Acknowledgement

This research was supported by the ANR-10-LABX-0026_CSC and the French Proteomic Infrastructure (ProFI, ANR-10-INBS-08-03). N.G. received a Ph.D. fellowship from the IdEX Unistra (Université de Strasbourg and Investissements d'Avenir).

The authors and co-authors have no conflicts of interest.

References

1. McNamara, K. and S.A.M. Tofail 2016 Nanoparticles in biomedical applications. Advances in Physics: X. 2(1) 54-88.
2. Ma, X., Y. Xiong, and L.T.O. Lee 2018 Application of Nanoparticles for Targeting G Protein-Coupled Receptors. Int J Mol Sci. 19(7).
3. Muhamad, N., T. Plengsuriyakarn, and K. Na-Bangchang 2018 Application of active targeting nanoparticle delivery system for chemotherapeutic drugs and traditional/herbal medicines in cancer therapy: a systematic review. Int J Nanomedicine. 13 3921-3935.
4. Tong, L., et al. 2009 Gold nanorods as contrast agents for biological imaging: optical properties, surface conjugation and photothermal effects. Photochem Photobiol. 85(1) 21-32.
5. Zuber, G., M. Dontenwill, and J.P. Behr 2009 Synthetic viruslike particles for targeted gene delivery to alphavbeta3 integrin-presenting endothelial cells. Mol Pharm. 6(5) 1544-52.
6. Chiper, M., K. Niederreither, and G. Zuber 2018 Transduction Methods for Cytosolic Delivery of Proteins and Bioconjugates into Living Cells. Adv Healthc Mater. 7(6) e1701040.
7. Farooq, M.U., et al. 2018 Gold Nanoparticles-enabled Efficient Dual Delivery of Anticancer Therapeutics to HeLa Cells. Sci Rep. 8(1) 2907.
8. Dykman, L. and N. Khlebtsov 2012 Gold nanoparticles in biomedical applications: recent advances and perspectives. Chem Soc Rev. 41(6) 2256-82.
9. El-Sayed, I.H., X. Huang, and M.A. El-Sayed 2006 Selective laser photo-thermal therapy of epithelial carcinoma using anti-EGFR antibody conjugated gold nanoparticles. Cancer Lett. 239(1) 129-35.
10. Hainfeld, J.F. and F.R. Furuya 1991 Gold Nanoparticles for Radiation Enhancement in Vivo. J Histochem Cytochem. 40(2) 177-184.
11. Chattopadhyay, N., et al. 2013 Molecularly targeted gold nanoparticles enhance the radiation response of breast cancer cells and tumor xenografts to X-radiation. Breast Cancer Res Treat. 137(1) 81-91.
12. Nie, S. 2010 Understanding and overcoming major barriers in cancer nanomedicine. Nanomedicine (Lond). 5(4) 523-8.

13. Dixit, V., et al. 2006 Synthesis and grafting of thioctic acid-PEG-folate conjugates onto Au nanoparticles for selective targeting of folate receptor-positive tumor cells. Bioconjug Chem. 17(3) 603-9.

14. Haller, E., W. Lindner, and M. Lammerhofer 2015 Gold nanoparticle-antibody conjugates for specific extraction and subsequent analysis by liquid chromatography-tandem mass spectrometry of malondialdehyde-modified low density lipoprotein as biomarker for cardiovascular risk. Anal Chim Acta. 857 53-63.

15. Patra, C.R., et al. 2008 Targeted delivery of gemcitabine to pancreatic adenocarcinoma using cetuximab as a targeting agent. Cancer Res. 68(6) 1970-8.

16. Montenegro, J.M., et al. 2013 Controlled antibody/(bio-) conjugation of inorganic nanoparticles for targeted delivery. Adv Drug Deliv Rev. 65(5) 677-88.

17. Jiang, W., et al. 2008 Nanoparticle-mediated cellular response is size-dependent. Nat Nanotechnol. 3(3) 145-50.

18. Bhattacharyya, S., et al. 2010 Nanoconjugation modulates the trafficking and mechanism of antibody induced receptor endocytosis. Proc Natl Acad Sci U S A. 107(33) 14541-6.

19. Brust, M., et al. 1994 Synthesis of thiol-derivatised gold nanoparticles in a two-phase Liquid–Liquid system. J. Chem. Soc., Chem. Commun. 0(7) 801-802.

20. Ackerson, C.J., et al. 2010 Synthesis and bioconjugation of 2 and 3 nm-diameter gold nanoparticles. Bioconjug Chem. 21(2) 214-8.

21. Levi-Kalisman, Y., et al. 2011 Synthesis and Characterization of Au102(p-MBA)44 Nanoparticles. J Am Chem Soc. 133(9) 2976-2982.

22. Marjomaki, V., et al. 2014 Site-specific targeting of enterovirus capsid by functionalized monodisperse gold nanoclusters. Proc Natl Acad Sci U S A. 111(4) 1277-81.

23. Desplancq, D., et al. 2018 Cytosolic Diffusion and Peptide-Assisted Nuclear Shuttling of Peptide-Substituted Circa 102 Gold Atom Nanoclusters in Living Cells. ACS Applied Nano Materials. 1(8) 4236-4246.

24. Yao, H., et al. 2016 Methods to Design and Synthesize Antibody-Drug Conjugates (ADCs). Int J Mol Sci. 17(2).

25. Billah, M.M., et al. 2010 Directed immobilization of reduced antibody fragments onto a novel SAM on gold for myoglobin impedance immunosensing. Bioelectrochemistry. 80(1) 49-54.

26. Ackerson, C.J., R.D. Powell, and J.F. Hainfeld 2010 Site-Specific Biomolecule Labeling with Gold Clusters. Methods Enzymol. 481 195-230.

27. Diebolder, C.A., et al. 2014 Complement is activated by IgG hexamers assembled at the cell surface. Science. 343(6176) 1260-3.

28. He, W., et al. 2007 A freeze substitution fixation-based gold enlarging technique for EM studies of endocytosed Nanogold-labeled molecules. J Struct Biol. 160(1) 103-13.

29. Lévy, R., et al. 2004 Rational and Combinatorial Design of Peptide Capping Ligands for Gold Nanoparticles. J Am Chem Soc. 126(32) 10076-10084.

30. Laemmli, U.K. 1970 Cleavage of Structural Proteins during the Assembly of the Head of Bacteriophage T4. Nature. 227 680.

31. Bonavia, R., et al. 2012 EGFRvIII promotes glioma angiogenesis and growth through the NF-kappaB, interleukin-8 pathway. Oncogene. 31(36) 4054-66.

32. Chiper, M., et al. 2017 Self-aggregating 1.8kDa polyethylenimines with dissolution switch at endosomal acidic pH are delivery carriers for plasmid DNA, mRNA, siRNA and exon-skipping oligonucleotides. J Control Release. 246 60-70.

33. Pinel, S., et al. 2014 Quantitative measurement of delivery and gene silencing activities of siRNA polyplexes containing pyridylthiourea-grafted polyethylenimines. J Control Release. 182 1-12.

34. Fraser-Pitt, D.J., et al. 2011 Phosphorylation of the epidermal growth factor receptor (EGFR) is essential for interleukin-8 release from intestinal epithelial cells in response to challenge with Escherichia coli O157 : H7 flagellin. Microbiology. 157(Pt 8) 2339-47.

35. Danscher, G. and J.O.R. Nörgaard 1983 Light microscopic visuaization of colloidal gold on resin-embedded tissue. J Histochem Cytochem. 31(12) 1394-1398.

36. Wong, O.A., W.S. Compel, and C.J. Ackerson 2015 Combinatorial Discovery of Cosolvent Systems for Production of Narrow Dispersion Thiolate-Protected Gold Nanoparticles. ACS Combinatorial Science. 17(1) 11-18.

37. Amendola, V. and M. Meneghetti 2009 Size Evaluation of Gold Nanoparticles by UV−vis Spectroscopy. J Phys Chem C. 113(11) 4277-4285.

38. Makaraviciute, A., et al. 2016 Considerations in producing preferentially reduced half-antibody fragments. J Immunol Methods. 429 50-6.

39. Desplancq, D., et al. 2016 Targeting the replisome with transduced monoclonal antibodies triggers lethal DNA replication stress in cancer cells. Exp Cell Res. 342(2) 145-58.

40. Okada, Y., et al. 2017 EGFR Downregulation after Anti-EGFR Therapy Predicts the Antitumor Effect in Colorectal Cancer. Mol Cancer Res. 15(10) 1445-1454.

41. Sorkin, A. and J.E. Duex 2010 Quantitative analysis of endocytosis and turnover of epidermal growth factor (EGF) and EGF receptor. Curr Protoc Cell Biol. Chapter 15 Unit 15 14.

42. Brand, T.M., M. Iida, and D.L. Wheeler 2011 Molecular mechanisms of resistance to the EGFR monoclonal antibody cetuximab. Cancer Biol Ther. 11(9) 777-792.

43. Bowman, M.C., et al. 2008 Inhibition of HIV fusion with multivalent gold nanoparticles. J Am Chem Soc. 130(22) 6896-7.

44. Hainfeld, J.F., et al. 2013 Gold nanoparticle imaging and radiotherapy of brain tumors in mice. Nanomedicine (Lond). 8(10) 1601-9.

45. Polyakov, A., et al. 2018 Gold Decoration and Photoresistive Response to Nitrogen Dioxide of WS2 Nanotubes. Chemistry.

46. Choi, B.J., et al. 2018 A gold nanoparticle system for the enhancement of radiotherapy and simultaneous monitoring of reactive-oxygen-species formation. Nanotechnology. 29(50) 504001.

47. Cole, L.E., et al. 2018 Effects of Bisphosphonate Ligands and PEGylation on Targeted Delivery of Gold Nanoparticles for Contrast-Enhanced Radiographic Detection of Breast Microcalcifications. Acta Biomaterials. 82 122-132.

48. Mahmoodzadeh, F., et al. 2018 A novel gold-based stimuli-responsive theranostic nanomedicine for chemo-photothermal therapy of solid tumors. Mater Sci Eng C Mater Biol Appl. 93 880-889.

49. Chattopadhyay, N., et al. 2010 Design and characterization of HER-2-targeted gold nanoparticles for enhanced X-radiation treatment of locally advanced breast cancer. Mol Pharm. 7(6) 2194-206.

50. Qian, Y., et al. 2014 Enhanced cytotoxic activity of cetuximab in EGFR-positive lung cancer by conjugating with gold nanoparticles. Sci Rep. 4 7490.

51. Monopoli, M.P., et al. 2012 Biomolecular coronas provide the biological identity of nanosized materials. Nat Nanotechnol. 7(12) 779-86.

52. Walkey, C.D., et al. 2014 Protein corona fingerprinting predicts the cellular interaction of gold and silver nanoparticles. ACS Nano. 8(3) 2439-55.

53. Perrault, S.D., et al. 2009 Mediating tumor targeting efficiency of nanoparticles through design. Nano Lett. 9(5) 1909-15.

54. Wong, O.A., et al. 2013 Structure-activity relationships for biodistribution, pharmacokinetics, and excretion of atomically precise nanoclusters in a murine model. Nanoscale. 5(21) 10525-33.

55. Choi, H.S., et al. 2007 Renal clearance of quantum dots. Nat Biotechnol. 25(10) 1165-70.

56. Shah, N.B., et al. 2012 Blood-nanoparticle interactions and in vivo biodistribution: impact of surface PEG and ligand properties. Mol Pharm. 9(8) 2146-55.

57. Storm, G., et al. 1995 Surface modification of nanoparticles to oppose uptake by the mononuclear phagocyte system. Adv Drug Deliv Rev. 17(1) 31-48.

58. Morais, T., et al. 2012 Effect of surface coating on the biodistribution profile of gold nanoparticles in the rat. Eur J Pharm Biopharm. 80(1) 185-93.

59. Jadzinsky, P.D., et al. 2007 Structure of a thiol monolayer-protected gold nanoparticle at 1.1 A resolution. Science. 318(5849) 430-3.

60. Piella, J., N.G. Bastus, and V. Puntes 2017 Size-Dependent Protein-Nanoparticle Interactions in Citrate-Stabilized Gold Nanoparticles: The Emergence of the Protein Corona. Bioconjug Chem. 28(1) 88-97.

61. Saha, K., et al. 2016 Regulation of Macrophage Recognition through the Interplay of Nanoparticle Surface Functionality and Protein Corona. ACS Nano. 10(4) 4421-30.

62. Al-Jawad, S.M.H., et al. 2018 Synthesis and characterization of small-sized gold nanoparticles coated by bovine serum albumin (BSA) for cancer photothermal therapy. Photodiagnosis Photodyn Ther. 21 201-210.

63. Westphal, M., C.L. Maire, and K. Lamszus 2017 EGFR as a Target for Glioblastoma Treatment: An Unfulfilled Promise. CNS Drugs. 31(9) 723-735.

64. Hatanpaa, K.J., et al. 2010 Epidermal Growth Factor Receptor in Glioma: Signal Transduction, Neuropathology, Imaging, and Radioresistance. Neoplasia. 12(9) 675-684.

65. Zhu, J.J. and E.T. Wong 2013 Personalized medicine for glioblastoma: current challenges and future opportunities. Curr Mol Med. 13(3) 358-67.

66. Kaluzova, M., et al. 2015 Targeted therapy of glioblastoma stem-like cells and tumor non-stem cells using cetuximab-conjugated iron-oxide nanoparticles. Oncotarget. 6(11) 8788-8806.

67. Hainfeld, J.F., et al. 2008 Radiotherapy enhancement with gold nanoparticles. J Pharm Pharmacol. 60(8) 977-85.

68. Her, S., D.A. Jaffray, and C. Allen 2017 Gold nanoparticles for applications in cancer radiotherapy: Mechanisms and recent advancements. Adv Drug Deliv Rev. 109 84-101.

69. Vigderman, L. and E.R. Zubarev 2013 Therapeutic platforms based on gold nanoparticles and their covalent conjugates with drug molecules. Adv Drug Deliv Rev. 65(5) 663-76.

70. Chanda, N., et al. 2010 Radioactive gold nanoparticles in cancer therapy: therapeutic efficacy studies of GA-198AuNP nanoconstruct in prostate tumor-bearing mice. Nanomedicine. 6(2) 201-9.

71. Shukla, R., et al. 2012 Laminin receptor specific therapeutic gold nanoparticles (198AuNP-EGCg) show efficacy in treating prostate cancer. Proc Natl Acad Sci U S A. 109(31) 12426-31.

72. Ryman, J.T. and B. Meibohm 2017 Pharmacokinetics of Monoclonal Antibodies. CPT Pharmacometrics Syst Pharmacol. 6(9) 576-588.

73. Longmire, M., P.L. Choyke, and H. Kobayashi 2008 Clearance properties of nano-sized particles and molecules as imaging agents: considerations and caveats. Nanomedicine (Lond). 3(5) 703-17.

74. Rovais, M.R.A., et al. 2018 Internalization capabilities of gold-198 nanoparticles: Comparative evaluation of effects of chitosan agent on cellular uptake into MCF-7. Appl Radiat Isot. 142 85-91.

UNIVERSITÉ DE STRASBOURG

Nadja GROYSBECK

Development of novel probes for high-resolution electron microscopy based on small-sized gold nanoparticle-antibody conjugates

Résumé

L'imagerie par microscopie électronique (ME) des cellules nécessite des agents de contraste, car les cellules sont constituées d'éléments de faible numéro atomique. Des nanoparticules d'or (AuNPs) de 5 à 15 nm se sont avérées utiles à cet effet et fonctionnalisées avec des anticorps, elles permettent le marquage de protéines cellulaires. En raison d'une augmentation de la résolution d'image en ME et l'avènement de la cryo-ME permettant l'imagerie de cellules dans des conditions proches du natif, les sondes classiques d'anticorps-AuNP (ca. 25 nm de diamètre, non compatible avec les conditions cryogéniques) semblent obsolètes. Pour surmonter ces limitations, nous avons développé de nouvelles sondes basées sur des AuNPs de 1.4 à 2.4 nm qui ont été conjugués de manière sélective à des anticorps et des nanobodies. Les sondes ont été caractérisées pour leur capacité de ciblage et certaines des sondes se sont avérées se lier spécifiquement à leurs cibles à l'intérieur de cellules vivantes. Ces résultats jettent les bases pour localiser des protéines cellulaires à haute résolution dans des conditions quasi-natives par cryo-ME.

Nanoparticule d'or, conjugaison sélective, cryo-microscopie électronique, anticorps, cellules vivantes

Résumé en anglais

Electron microscopy (EM) imaging of cells requires contrast agents, since cells consist of low atomic number elements. 5 – 15 nm gold nanoparticles (AuNPs) providing high opacity to electrons have proven valuable for this purpose and functionalized with antibodies, they permit the labeling of selected cellular proteins. Due to the technical advances of electron microscopes, which resulted in a drastic increase in image resolution, as well as the advent of cryo-EM allowing the imaging of cells under close-to-native conditions, the classical AuNP-antibody probes (ca. 25 nm in diameter, not compatible with cryogenic conditions) appear outdated. To overcome these limitations, we developed novel EM probes based on AuNPs of 1.4 – 2.4 nm that were site-selectively conjugated to antibodies and nanobodies. The probes were intensively characterized for their targeting ability and delivered into living cells to examine their fate. Certain of the probes proved to specifically bind to their targets inside living cells, which builds the ground for future cryo-EM studies permitting the pinpointing of cellular proteins at high resolution under quasi-native conditions.

Gold nanoparticles, site-selective conjugation, cryo-electron microscopy, antibody, live cells